



Age and morphotype influence on thoracic mechanical response: in vivo experimental study and numerical analysis using personalized human body FE models

David Poulard

► To cite this version:

David Poulard. Age and morphotype influence on thoracic mechanical response: in vivo experimental study and numerical analysis using personalized human body FE models. Mechanics [physics]. Université Claude Bernard - Lyon I, 2012. English. NNT : 2012LYO10332 . tel-01077963

HAL Id: tel-01077963

<https://theses.hal.science/tel-01077963>

Submitted on 27 Oct 2014

HAL is a multi-disciplinary open access archive for the deposit and dissemination of scientific research documents, whether they are published or not. The documents may come from teaching and research institutions in France or abroad, or from public or private research centers.

L'archive ouverte pluridisciplinaire **HAL**, est destinée au dépôt et à la diffusion de documents scientifiques de niveau recherche, publiés ou non, émanant des établissements d'enseignement et de recherche français ou étrangers, des laboratoires publics ou privés.

THÈSE DE L'UNIVERSITE DE LYON

en vue de l'obtention du diplôme de

Docteur de l'Université Claude Bernard Lyon 1

Spécialité : **Génie Mécanique**

préparée au **Laboratoire de Biomécanique et Mécanique des Chocs (UMR_T 9406)**

dans le cadre de l'École Doctorale **MEGA (ED 162)**

présentée et soutenue publiquement
par

David POULARD

le 19 Décembre 2012

Titre:

Influence de l'âge et du morphotype sur la réponse mécanique du thorax : étude expérimentale *in vivo* et analyse numérique à l'aide de modèles EF personnalisés du corps humain

Directrice de thèse: **Mme Karine BRUYERE**

Jury

M. François BERMOND, Chargée de Recherche IFSTTAR, LBMC, Bron

Mme Karine BRUYERE, Chargée de Recherche IFSTTAR, LBMC, Bron

Mme Sabine COMPIGNE, Industriel, Toyota Motor Europe, Belgique

M. Richard KENT, Professeur, Université de Virginie, USA

M. Sébastien LAPORTE, Professeur des Universités, ENSAM, Paris

M. Jean-Michel MOREAU, Professeur des Universités, Université Claude Bernard Lyon 1

Age and morphotype influence on thoracic mechanical response: in vivo experimental study and numerical analysis using personalized human body FE models

Préambule

Ce travail a été réalisé au sein du Laboratoire de Biomécanique et Mécanique des Choc (LBMC), unité mixte de l’Institut Français des Sciences et Technologies des Transports, de l’Aménagement et des Réseaux (Ifsttar) et de l’Université Claude Bernard Lyon 1 (UCBL), dans le cadre d’un projet de recherche en partenariat avec Toyota Motor Europe.

Ce rapport de thèse a été rédigé en anglais afin de faciliter son utilisation au près du partenaire industriel et dans le but d’intégrer des personnes non francophones dans le comité de jury. Un résumé en français se trouve à la fin du manuscrit.

Foreword

This work was carried out in the Biomechanics and Impact Mechanics Laboratory (LBMC), a joint unit of French institute of science and technology for transport, development and networks (Ifsttar) and the Université Claude Bernard Lyon 1 (UCBL), as part of a research project in partnership with Toyota Motor Europe.

This PhD report has been written in English in order to facilitate its use for the industrial partner and in order to integrate non-French speakers in the PhD committee. A French summary can be found at the end of the manuscript.

« Pour guérir quelque chose qui ne marche pas ou qui fait trop de bruit, il faut et il suffit de taper dessus avec quelque chose qui marche mieux ou qui fait plus de bruit. »

Les Shadoks

« Toute certitude est par essence contradictoire avec la philosophie de la recherche. »

Pierre Joliot

ACKNOWLEDGEMENTS

I would like to thank my advisor - Dr. Karine Bruyère - for her help and useful experience, for her kindness and her availability, especially during the reviewing of this manuscript.

This work and the overall project would not have been possible without Dr. Sabine Compigne from Toyota Motor Europe.

I'd like to acknowledge all the volunteers who participated in this study and Dr. Francois Bermond, Patrick Joffrin, Alain Maupas, Jean-Luc Russo, Sophie Serindat, Loretta Leoni-Duplessy, Alain Gilibert, Richard Roussillon, Dr Georges Baraton, Yaël Perricard, Bilal Boussouar for their contribution and the Desgenettes Hospital for providing bone density examinations.

I owe to acknowledge Professor Sébastien Laporte and Professor Richard Kent for accepting the review of my work, as well as Professor Jean-Michel Moreau, Dr. Sabine Compigne and Dr. François Bermond for taking part in the jury committee.

I'd also like to thank the students and staff of the Biomechanics and Impact Mechanics Laboratory. They have been both friends and colleagues, and I will always be grateful for having been a part of this team.

Finally, to my parents, my brother, my friends for their moral support, over the past three years and for helping me to overcome my doubts, thank you again...

TABLE OF CONTENTS

Introduction	25
Chapter I - State of the art	27
1. Anatomy of the human thorax.....	27
1.1 Ribcage.....	27
1.2 Intercostal muscles	33
1.3 Viscera.....	33
2. Thoracic trauma in frontal impact	34
2.1 Abbreviated Injury Scale (AIS).....	34
2.2 Accidentology	34
2.3 Thoracic injuries mechanisms.....	36
3. Thorax mechanical response during frontal loading	39
3.1 Blunt impact tests.....	39
3.2 Compression tests.....	39
3.3 Sled tests.....	40
3.4 Influence of loading conditions	42
4. Thoracic injury assessment based on dummy responses	42
4.1 Anthropomorphic test devices.....	43
4.2 Thoracic injury criteria.....	44
5. Potential of in-vivo experiments for thorax mechanical response assessment	52
5.1 Influence of physiology.....	52
5.2 Influence of age	53
5.3 Influence of corpulence	56
6. Potential of numerical human models for personalize injury risk prediction	56
6.1 Introduction	56
6.2 FE models.....	58
6.3 Existing personalized FE models	58
7. Conclusion.....	64
Chapter II - In vivo analysis of thorax mechanical response under belt loading.....	67
1. Introduction	67
2. Materials and methods	67

2.1 Test device.....	67
2.2 Definition of the deceleration pulse	68
2.3 Tested volunteers.....	69
2.4 Conventional instrumentation	71
2.5 3D trajectories of body markers	71
2.6 Data analysis	75
3. Results	79
3.1 Definition of an individual thoracic mechanical response	79
3.2 Comparison with literature.....	80
3.3 Comparison of thoracic mechanical response from different age and BMI groups...	83
3.4 Definition of thoracic mechanical response groups	92
4. Discussion	100
 Chapter III - Geometrical personalization of human FE model	103
1. Introduction	103
2. Materials and methods	103
2.1 Human body model	103
2.2 Geometrical personalization process.....	105
2.3 Software	113
3. Assessment of the geometrical personalization process	113
3.1 Assessment of the thoracic geometrical personalization.....	113
3.2 Assessment of the whole body geometrical personalization.....	116
4. Discussion	120
 Chapter IV - Injury risk on vulnerable individuals with personalized human body finite element models.....	121
1. Introduction	121
2. Material and methods	121
2.1 Geometrically personalized FE models of human body	121
2.2 Material properties personalization considering aging	123
2.3 Solver and software.....	125
2.4 Sled configuration	125
2.5 Simulation matrix	127
2.6 Measurements.....	128

2.7 Rib injury assessment.....	129
3. Responses of geometrically personalized models at low speed	131
4. Influence of personalization levels on thoracic injury risk prediction	136
4.1 Influence of geometrical personalization	136
4.2 Influence of material property modifications.....	144
5. Discussion	151
Conclusion.....	153
Bibliography	159
Publications.....	171
Conferences.....	171
Appendix 1: Definition of a non-injurious low deceleration pulse protocol for analysis of thorax response under belt loading	173
Appendix 2: Definition of palpable landmarks	179
Appendix 3: Definition of body coordinates systems used in geometrical personalization process	187
Appendix 4: The Radial Basis Functions (RBF), a non-rigid transformation method for scaling an initial mesh using a set of control points (Buhmann, 2000).....	191
Appendix 5: French summary of the manuscript	194

TABLE OF FIGURES

Fig. 1. Ribcage anatomy (Gray, 1918).....	27
Fig. 2. The parts of the rib (Gray, 1918)	30
Fig. 3. Internal structure of the rib.	30
Fig. 4. Typical thoracic vertebra (Gray, 1918).	31
Fig. 5. Rib's axes of rotations (Kapandji, 2009).....	32
Fig. 6. Intercostal muscles (Gray, 1918).....	33
Fig. 7. Anatomy of pleural cavity and mediastinum (Gray, 1918)	34
Fig. 8. Type of thoracic injuries AIS ≥ 2 by genders and age (Ndiaye and Chiron, 2009).	35
Fig. 9. Site of rib fractures depending on impact surface shape (Schmitt et al., 2009).	36
Fig. 10. Compression of the heart (Schmitt et al., 2009)	38
Fig. 11. Thoracic mechanical responses on PMHS using impactor (Kroell C.K., 1971; Nahum A.M., 1975; Neathery, 1974).....	39
Fig. 12. Supine belt loading setup and instrumentation (Cesari and Bouquet, 1990).....	40
Fig. 13. Sled tests on PMHS with belt restraint system in a real world crash environment (Kuppa and Eppinger, 1998).	41
Fig. 14. Typical force-time histories (left, center) and chest contours (right) of a driver restrained by belt or airbag in frontal impact (Kallieris et al., 1994; Yoganandan et al., 1991).....	41
Fig. 15. Examples of injury pattern in sled tests by using 3-point belt and airbag (Kallieris et al., 1994).....	41
Fig. 16. Force at 20% chest deflection for a 50th male as a function of loaded area (Kent et al., 2004).....	42
Fig. 17. Examples of injury risk curves for different severities.....	45
Fig. 18. Probability of AIS ≥ 3 thoracic injury versus age and shoulder belt load (Foret-Bruno et al., 1998).....	46

Fig. 19. Risk of thoracic injuries as a function of sternal deflection for a mid-size adult male (left) and as a function of Hybrid III sternal deflection (right) (Mertz et al., 1991).....	47
Fig. 20. Risk curve for AIS \geq 4 chest injury based on Viscous Criterion for blunt frontal impact (Lau and Viano, 1986).....	48
Fig. 21. Illustration of the Combined deflection on a deformed thorax (Song et al., 2010).....	50
Fig. 22. Chest compression during relaxed (left) and braced (right) conditions (Kemper et al. 2011).....	52
Fig. 23. Ratios for age changes in the ultimate tensile strength of soft tissues (Yamada, 1970).....	54
Fig. 24. Age-related change in rib slope (Gayzik et al., 2008; Kent et al., 2003).	55
Fig. 25. Illustration of mechanism by which increased rib angle increases thoracic stiffness while decreasing chest deflection tolerance (Kent et al., 2005).	55
Fig. 26. Overview of the HUMOS2 scaling tool (Vezin and Verriest, 2005).	60
Fig. 27. Sled configuration based upon a standard sedan car environment of a front passenger restrained by a 3-point belt.....	68
Fig. 28. Comparison of sled pulses applied in vivo.	69
Fig. 29. Distribution of tested subjects compared to the initial targets based upon anthropometry charts (Jürgens et al., 1990).	70
Fig. 30. Landmarks spread over volunteer during belt loading.	72
Fig. 31. Overview of camera location and field of view.....	72
Fig. 32. Reconstruction of an object in space from the images taken by several cameras. Adapted from (Compigne et al., 2004).	73
Fig. 33. Calibration of the sled scene with the calibration object	73
Fig. 34. Comparison of different methods of interpolations of mid-sternum landmark trajectory for the computation of mid-sternum deflection.	74
Fig. 35. Definition of the thoracic coordinates system used in sled tests.	75

Fig. 36. Computation of the resulting shoulder belt load F_{Res} (adapted from Eickhoff et al., 2011).....	76
Fig. 37. Standard deviation ellipse on force-deflection curve (adapted from Shaw et al., 2006).....	77
Fig. 38. Definition of Dynamic Stiffness (DS) and Effective Stiffness (ES) on experimental force-deflection curve.....	78
Fig. 39. Comparison of mid-sternum compression corridors for 50th percentile male from the present study ($n=3$) and Kemper et al. (2011; $n=5$).....	80
Fig. 40. Time history of the external shoulder belt force FB3 for age group and BMI group.....	84
Fig. 41. Time history of the lower shoulder belt force FB4 for age group and BMI group.....	85
Fig. 42. Time history of the lap belt force FB6 for age group and BMI group.	85
Fig. 43. Time history of the resultant shoulder belt force FRes for age group and BMI.....	86
Fig. 44. Time history of mid-sternum compressions for different age and BMI groups.	87
Fig. 45. Maximum belt loads for different age and BMI groups.	87
Fig. 46. Maximum compression for different age and BMI groups.	88
Fig. 47. Comparison of sternal relative trajectories in sagittal plane for age and BMI group.....	89
Fig. 48. Maximum sagittal excursion for different age and BMI groups.	89
Fig. 49. Thoracic force-deflection curve for different age and BMI groups.	91
Fig. 50. Maximum force-deflection characteristics for different age and BMI groups.	91
Fig. 51. Thoracic force-deflection curve computed from model parameters for different age and BMI groups.	92
Fig. 52. Correlation of K, μ parameters with age and BMI. The coefficient of determination R^2 for linear regression was displayed when correlation was found significant ($p<0.05$).	92
Fig. 53. Pareto chart of the percent variability explained by each principal component from PCA.	94

Fig. 54. Projection of the variables (blue line) and the subjects (red symbol) against the selected principal components.	95
Fig. 55. Age and BMI group factor maps for the first three principal components.....	96
Fig. 56. Dendrogram illustrating the arrangement of the clusters produced by AHC.	97
Fig. 57. AHC group factor maps for the first three principal components.	98
Fig. 58. THUMS features (Toyota Central R&D Labs Inc.).	104
Fig. 59. Thorax and spine mesh (Toyota Central R&D Labs Inc.).....	104
Fig. 60. Synthesis of the personalization process.	106
Fig. 61. Segmentation of the 50th percentile male THUMS model.	107
Fig. 62. Generation of initial surface nodes of the left forearm.....	107
Fig. 63. Personalization of thoracic surface points by RBF with the 42 thoracic anatomical points.....	109
Fig. 64. Definition of thoracic anatomical landmarks for thoracic geometry personalization.	109
Fig. 65. Personalization of left arm surface points by homothety with limb length and circumference.....	110
Fig. 66. Definition of lateral anatomical landmarks used for posture personalization.	112
Fig. 67. Rotation of target surface nodes according to volunteer's posture.....	112
Fig. 68. Mesh interpolation by RBF using surface nodes.	113
Fig. 69. MRI-scans used for the assessment of the thoracic geometrical personalization....	114
Fig. 70. View of the distance d_i found for skin point of the reference geometry CT-scan to the closest point of the personalized thorax mesh using <i>thoracic skin set</i>	115
Fig. 71. Six geometrically personalized FE models.....	122
Fig. 72. Distribution of tested subjects compared to the initial targets based upon anthropometry charts (Jürgens et al., 1990).	123
Fig. 73. Generic interior vehicle model with a personalized THUMS human body model.....	125

Fig. 74. Low speed (gray) and high speed (black) pulses used for the sled test simulations.....	127
Fig. 75. Definition of the points used for chest deflection measurement during simulation.....	129
Fig. 76. Prediction of bone fractures in simulation.....	129
Fig. 77. Comparisons of external shoulder belt load FB3 between geometrically personalized models and in-vivo sled tests at low speed (4 g, 8 km/h).	133
Fig. 78. Comparisons of internal shoulder belt load FB4 between geometrically personalized models and in-vivo sled tests (4 g, 8 km/h).	133
Fig. 79. Comparisons of the lap shoulder belt load FB6 between geometrically personalized models and in-vivo sled tests (4 g, 8 km/h).	134
Fig. 80. Comparisons of the resultant shoulder belt load FRes between geometrically personalized models and in-vivo sled tests (4 g, 8 km/h).	134
Fig. 81. Comparisons of mid-sternum deflections between geometrically personalized models and in-vivo sled tests (4 g, 8 km/h).....	135
Fig. 82. Comparisons of mid-sternum compression between geometrically personalized models and in-vivo sled tests (4 g, 8 km/h).....	135
Fig. 83. Comparisons of the thoracic forces-deflection responses between geometrically personalized models and volunteers (4 g, 8 km/h).	136
Fig. 84. Maximum outputs for different geometrically personalized models.....	138
Fig. 85. Force-deflection obtained for geometrically personalized models at high speed (IJ40).	140
Fig. 86. Von Mises stress contour obtained for geometrically personalized models in high speed sled tests at maximum bony midsternal deflection time (upper: cortical, lower: cartilage & trabecular).	141
Fig. 87. Significant correlations of outputs with the number of fractured ribs.....	143
Fig. 88. Maximum outputs for different personalized models considering aging.	145
Fig. 89. Force-deflection obtained for personalized models considering aging at high speed (13 g, 40 km/h).	147

Fig. 90. Von Mises stress contour obtained for personalized models considering aging in high speed sled tests at maximum bony midsternal deflection time (upper: cortical, lower: cartilage & trabecular)	148
Fig. 91. Autochoc, crash simulator of MACIF	174
Fig. 92. Testochoc, crash simulator of French Road Safety.	174
Fig. 93. Ifsttar sled.	174
Fig. 94. Mean deceleration pulses of the three devices.	177
Fig. 95. HIII AM50 (black) and HIII AF 05 (grey) sternal deflection measured by internal dummy sensor (solid lines) and stereovision (dotted lines).	177
Fig. 96. Thorax mechanical responses of two volunteers (S01 in grey, S03 in black) overlayed with Dummy ones. (thick lines)	177
Fig. 97. Side view of spine kinematics of S01 (left) and S03 (right) subjects relative to the sled. 2D trajectory of T8 is shown in black line.....	177
Fig. 98. External anthropometric measurements taken on volunteers.	184
Fig. 99. Body coordinates system.	187
Fig. 100. Anatomie de la cage thoracique (Gray, 1918)	195
Fig. 101. Réponses mécaniques du thorax évaluées sur impacteurs (Kroell C.K., 1971) ; (Nahum A.M., 1975; Neathery, 1974).	195
Fig. 102. Relèvement costal chez les personnes agées (Gayzik et al., 2008; Kent et al., 2003).....	197
Fig. 103. Vue globale du dispositif.	199
Fig. 104. Définition des raideurs thoraciques DS et ES.....	199
Fig. 105. Comparaison de corridors de compressions pour des volontaires proche du 50ème percentile homme entre cette étude (n=3) et Kemper et al. (2011; n=5).....	200
Fig. 106. Courbe de force-déflexion thoracique pour different groups d'âge et de BMI.	200
Fig. 107. Dendrogramme illustrant la répartition des groupes produit par la classification hiérarchique ascendante.	201
Fig. 108. Données invivo utilisés pour personnaliser le modèle EF.....	202

Fig. 109. Synthèse du processus de personnalisation géométrique.	203
Fig. 110. IRM utilisés dans l'évaluation du processus de personnalisation géométrique.	204
Fig. 111. Modèles personnalisés géométriquement soumis à un pulse similaire aux essais invivo	206
Fig. 112. Modélisation d'un intérieur générique adapté au modèle THUMS personnalisé géométriquement placé en position passager.	206
Fig. 113. Modèles personnalisés géométriquement pour l'étude de l'influence de la personnalisation géométrique.....	207
Fig. 114. Contraintes d Von Mises stress obtenus pour quatre modèles personnalisés géométriquement soumis à un pulse de 13g à 40 km/h (haut: cortical, bas: cartilage & traveculae)	208

LIST OF TABLES

Table 1. Material properties of the cortical bone (Yamada, 1970).....	31
Table 2. Thoracic tolerance reduction ratio with age at the injury level of AIS3 (Zhou et al., 1996).....	35
Table 3. AIS rating for skeletal and soft tissue thoracic injuries (Schmitt et al., 2009).....	38
Table 4. Key dimensions and weights for various sizes of dummies (Nahum and Melvin, 2002).....	43
Table 5. Frontal impact criteria and tolerances for the thorax (Schmitt et al., 2009).....	51
Table 6. Volunteer studies on thorax mechanical response in antero-posterior loading.....	53
Table 7. Material property of the cortical rib in an elderly thoracic model based on the 50th percentile male THUMS (Tamura et al., 2005).	60
Table 8. Material property of the ribcage for adult and elderly model (Ito et al., 2009).....	61
Table 9. Overview of recent thorax FE model from (Charpail, 2006; Yang et al., 2006).....	62
Table 10. Anthropometric characteristics of volunteers subjected to sled tests.....	70
Table 11. Thoracic mechanical characteristics dataset obtained from in vivo sled tests.	81
Table 12. Thoracic mechanical characteristics dataset from in vivo sled tests: different age and BMI groups.	82
Table 13. Reduced thoracic mechanical dataset used for PCA and ACH.	93
Table 14. The principal component coefficient for each variable obtained using PCA. Markers variables are underlined.	94
Table 15. AHC group description according to age, genders and BMI groups	98
Table 16. AHC group description according to anthropometries.....	98
Table 17. AHC group description according to markers variables.	99
Table 18. Surface nodes extracted for each body part.....	106
Table 19. External anthropometric measurements used in the personalization process.	111
Table 20. Results of woman personalized models with different candidate nodes as thoracic palpable points compared to MRI-scans.	115

Table 21. Optimum set candidate nodes as thoracic palpable points	117
Table 22. Results of man and woman personalization for different combination candidate nodes as thoracic palpable points on global anthropometry dimensions.....	118
Table 23. Results of man and woman personalization for different combination candidate nodes as thoracic palpable points on thoracic anthropometry dimensions... ...	118
Table 24. Results of man and woman personalization for different combination candidate nodes as thoracic palpable points on weight.....	119
Table 25. Results of man and woman personalization for different combination candidate nodes as thoracic palpable points on mesh quality.	119
Table 26. Anthropometric characteristics of volunteers subjected to THUMS personalization process.	121
Table 27. Thoracic anthropometries of volunteer 948 and 118.....	123
Table 28. Ratio for personalization of material properties according to age from Ito et al. (2009).	124
Table 29. Material properties of the initial THUMS model (1) and the aged THUMS model (2).	126
Table 30. Cortical thickness of the initial THUMS model (1) and the aged THUMS model (2).	126
Table 31. Level of material property personalization and associated versions of personalized THUMS models.	126
Table 32. Simulation tests matrix.....	128
Table 33. Computation of Torso Abbreviated Injury Scale (TOAIS) according to the number of fractured ribs and their location (AIS 2005).	130
Table 34. Thoracic mechanical characteristics obtained on geometrically personalized models and volunteers at low-speed (4g, 8km/h).....	132
Table 35. Thoracic mechanical characteristics dataset obtained on geometrically personalized models at high-speed (13g, 40km/h).	139
Table 36. Fractures summarize for geometrically personalized models at high speed (IJ40).	142

Table 37. Computation of Torso Abbreviated Injury Scale (TOAIS) according to the number of fractured ribs and their location for geometrically personalized models at high speed (IJ40)	143
Table 38. Thoracic mechanical characteristics dataset obtained on personalized models considering aging at high-speed (13g, 40km/h)	146
Table 39. Fractures summarize for the personalized models considering aging	149
Table 40. Computation of Torso Abbreviated Injury Scale (TOAIS) according to the number of fractured ribs and their location for the personalized models considering aging	150
Table 41. Definition of landmarks acquired on volunteer (front & back) during sled tests (1/3)	179
Table 42. Definition of the anatomical landmarks acquired on left side of the volunteer during sled tests	181
Table 43. Definition of the thorax anatomical landmarks acquired on thorax volunteer for geometrical personalization process	182
Table 44. Definition of the anatomical landmarks acquired on THUMS geometry	183
Table 45. Definition of the anthropometric measurements taken on volunteers	185
Table 46. Résultats des modèles personnalisés géométriquement pour différents jeux de noeuds comme marqueurs palpable thoraciques comparés aux IRMs	204

INTRODUCTION

Although significant improvements have been achieved in mitigating road traffic fatalities, frontal impacts play a predominant role in the frequency of road traffic fatalities as they account for up to 46% of the mortality (Klanner, 2001). This impact configuration often causes bony fractures mainly in the thoracic region. In particular, several studies have reported that elderly people are susceptible to sustain sternum and rib fractures, thereby, leading to high mortality and morbidity rates (Lafont and Laumon, 2003; Ndiaye and Chiron, 2009).

Yet, age is a global parameter, strongly linked to corpulence and it seems important to define their influence on intrinsic parameters explaining thorax mechanical response in dynamic loading: properties of biological tissues (bone, cartilage), costo-vertebral and costo-chondral joint stiffness and joint limits, thorax morphotypes (spine curvature, rib angle).

Work schedule n° 2 “Thorax vulnerability of elderly car users” project was conducted at Ifsttar in partnership with Toyota Motor Europe. It aimed to quantify the influence of age on thorax mechanical response and its consequences on injury mechanisms in frontal impacts. For that, two steps were defined:

- First, to identify the age specificities on thorax mechanical response by performing a in vivo parametric study
- Secondly, to show the ability of personalized FE human body model to predict increased injury risk.

First objective of the thesis is to develop and implement an in vivo test protocol to analyse the link between subject intrinsic parameters (gender, age, corpulence, morphology of the thorax) and thorax mechanical response under belt loading. This analysis should answer the following questions:

- What are the parameters explaining the thorax mechanical response during an antero-posterior loading?
- What is the influence of age genders and BMI on these parameters?

In addition, there are no injury assessment tools accounting for differences in anatomical features and biological material properties that are observed between adults and elderly.

Compare to ATD, human numerical models have the potential to predict local physical variables that can be related to injury. Moreover, they offer a large potential of customization in term of geometry, material and joint properties. Nevertheless, the choice of the level of customization and its sensibility to predict thoracic injury risk is still a scientific obstacle.

Thus, the second objective of the thesis is to use customize FE models to do the same analysis in the injurious domain. For that, first step aims at implementing a geometrical personalisation process in order to adapt the geometry and the posture of a human FE model to various cases. Second is based on simulations in the injurious domain to isolate the role of geometrical parameters possibly linked to the thorax mechanical response under dynamic loading and their role in severity.

In **Chapter 1**, after some anatomical description of the thorax, thoracic injury mechanisms are summarized. Then, a state of the art of thorax mechanical response in antero-posterior loading and thoracic injury criteria is presented. Their limitations to account for differences in anatomical features and material properties between adults and elderly were listed. Finally, the benefit of in vivo experiments to enlarge the limited amount of available response data and the potential of personalized numerical model to predict personalize risk injury were also presented.

Chapter 2 presents first the in vivo protocol for the analysis of thorax mechanical response under belt loading carried out on adults of various anthropometries and age. Then, the influence of age and overweight on thorax mechanical response is analyzed.

Chapter 3 describes the methodology used to personalize the geometry and posture of the THUMS model using external landmarks and anthropometric dimensions taken on volunteers. The process was assessed on one subject by comparing computed thorax geometry and IRM data and on other subjects by comparing anthropometric dimensions.

Chapter 4 provides the analysis of simulations of personalized models of six specific subjects. First, a validation of the models under a low pulse is presented. Then, simulations of more severe pulse are used to compare different levels of personalization in the injury risk.

CHAPTER I - STATE OF THE ART

1. Anatomy of the human thorax

The human thorax is the upper part trunk between the neck and the abdomen. The thoracic region is bounded above by the shoulder girdle and the first pair of ribs, posteriorly by the thoracic spine and the posterior arch of the ribs, laterally by the ribs and anteriorly by the sterno-costal plastron.

The thoracic segment consists of:

- the bony structure of the thorax or ribcage which protects the viscera contained therein,
- the musculature and the skin which constitute the outer shell of this segment,
- the intra-thoracic viscera (heart, lungs, vessels ...).

1.1 Ribcage

The ribcage is formed by the sternum, twelve pairs of ribs with cartilage and twelve thoracic vertebrae (Fig. 1). The main role of the rib cage is to maintain and protect vital organs and visceral structures.

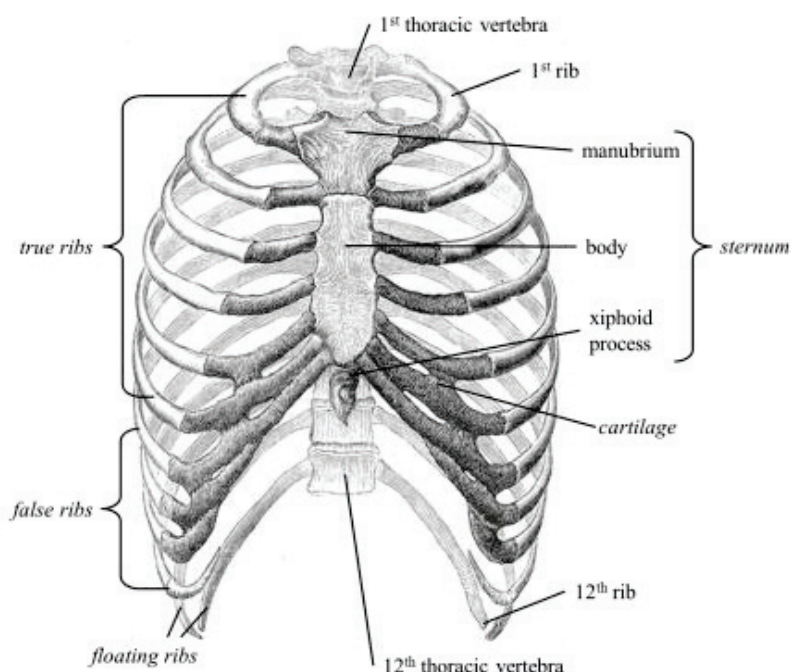


Fig. 1. Ribcage anatomy (Gray, 1918).

The ribs are posteriorly attached to the thoracic vertebrae. Anteriorly, the upper seven pairs of ribs are directly fixed to sternum by the mean of an elastic cartilage, the costal cartilage. The 8th, 9th and 10th pairs of ribs join indirectly the sternum with the costal cartilages of the ribs above. The two last (11th and 12th) pairs of ribs, called floating ribs, are attached to the posterior abdominal wall muscles.

1.1.1 Sternalum

The sternum is a symmetrical long flat bony plate where the ribs are attached. Although it is fused, the sternum consists of three main parts: manubrium, body of sternum and xiphoid process. The sternal angle is located at the point where the body joins the manubrium. While manubrium and the body are constituted of bone, the xiphoid process is cartilaginous for youth, but more or less ossified for the adult.

1.1.2 Costal cartilages

The costal cartilages are bars of hyaline cartilage that connect ribs 1-10 to the sternum (either directly for the true ribs or indirectly for the false ribs). The junction between costal cartilage and rib is termed the costo-chondral junction. All costo-chondral junctions are hyaline cartilage joints which firmly bind the rib to the cartilage via continuity of the perichondrium (the fibrous outer layer of the cartilage) with the periosteum (the fibrous outer layer of the rib bone). No relative motion occurs between the rib and the cartilage at the costo-chondral junction (Moore and Dalley 1999). The junctions between costal cartilage and sternum are called the sterno-costal junctions. The sterno-costal junction of the first rib consists of a primary cartilaginous joint which do not allow motion between the cartilage and the manubrium (Forman, 2010). The sterno-costal junctions of the second through seventh ribs consist of synovial joints which allow some relative rotation between the cartilage and the sternum during respiration (Moore and Dalley 1999).

During the inspiration, the elevation of ribs leads the costal cartilages to undergo a movement of rotation relatively to the sternum (chondrosternal joint) and torsion around their longitudinal axis. The energy expended on the inspiration is stored by the cartilages thanks to their elastic deformation. At the time of muscle relaxation, the cartilages via their elasticity take part in the return of thorax to its initial position (Kapandji, 2009).

The costal cartilages contribute very materially to the elasticity of the walls of the thorax especially the perichondrium, that surrounds the costal cartilage (Forman, 2010).

Limited studies have investigated the material properties of the costal cartilage. Yamada et al. (1970) provided a Young's moduli of costal cartilage of 26 MPa often used in simulation (Yamada, 1970). Nevertheless, Yamada found a strain-softening in tension and a greater stiffness in compression, contrary to nearly all other data available on the mechanical behaviors of hyaline cartilages (Forman, 2010). These differences are likely due to a difference in test methods, and it is difficult to resolve these differences due to the absence of a test method description in Yamada reference (Forman, 2010).

1.1.3 Rib anatomy

The rib is described as elastic flat and long bone with two faces (internal / external) and two edges (top / bottom), and with three curvatures in space:

- A curvature along the faces: a medially concave curvature with two bends which are called posterior angle (costal angle) and anterior angle.
- A curvature along the edges: it gives the appearance of an S-shape with a back end and one end rose ventral plunging.
- A curvature along the axis: it corresponds to the torsion on the rib, and explains that the side of the dorsal segment of the rib is directed downward and backward, while that of the ventral segment is oriented upward and forward.

The rib consists of three parts:

- The posterior or vertebral extremity: it consists of a head, a neck and a tuberosity. The head is composed of two facet joints that come to articulate with the thoracic vertebrae. The tubercle is protruding rib back; its articular surface meets the articular surface of the transverse process of thoracic vertebra of same number.
- The body is the main part of the rib that takes origin in the tubercle, follows the direction of the neck on a short ride, then bent inwards, forming the costal angle. The body is flattened from within.
- The ventral or anterior extremity: it consists of an excavation that receives the outer end of costal cartilage (costo-chondral junction).

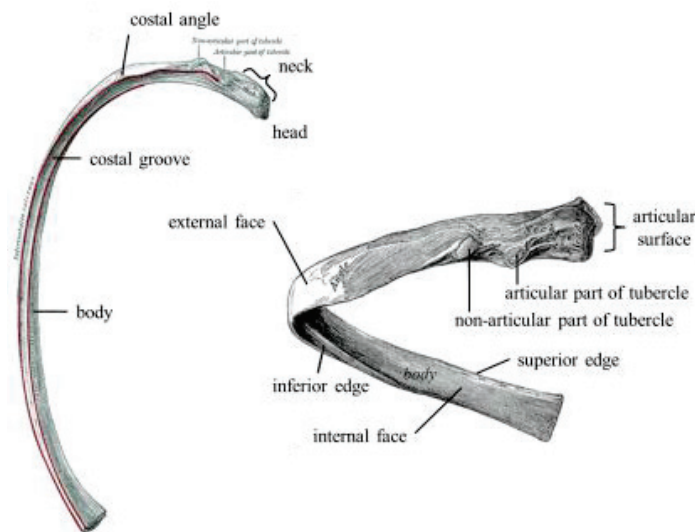
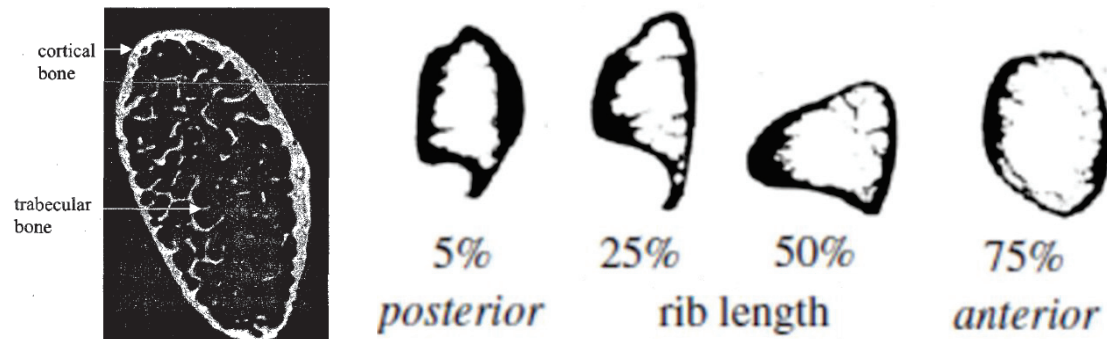


Fig. 2. The parts of the rib (Gray, 1918).

The body of the rib is made of highly vascular trabecular (or "spongy") bone (with interstitial bone marrow), surrounded by a thin outer layer of dense cortical bone (**Fig. 3**). It was found that the distribution of cortical bone was non-uniform and the geometry of cross section very variable as showed in **Fig. 3** (Mohr et al., 2007).



a) Cross-sectional view of rib body from a μ CT scan (Forman, 2010)
b) Variation of rib cross-section along the longitudinal axis (Mohr et al., 2007).

Fig. 3. Internal structure of the rib.

Cortical bone consists of layers of an arrangement of cylindrical structures called osteons. It is composed of mineral salts (for about 60% by mass), water (25%) and collagen. This structure is heterogeneous, anisotropic and viscoelastic. Young's modulus varies from 15000 to 35000 MPa (Burstein et al., 1976; Yamada, 1970). The behaviour of compact bone is different in tension and compression. Although it has a lower modulus of elasticity in compression than in tension, the ultimate stress and strain at failure are greater for a bone subjected to compression (Cowin, 2001). This observation suggests that the breaking of the compact bone is determined

by its ability to withstand tensile loading (Charpail, 2006). Some material properties of the cortical bone are given in **Table 1**.

Table 1. Material properties of the cortical bone (Yamada, 1970).

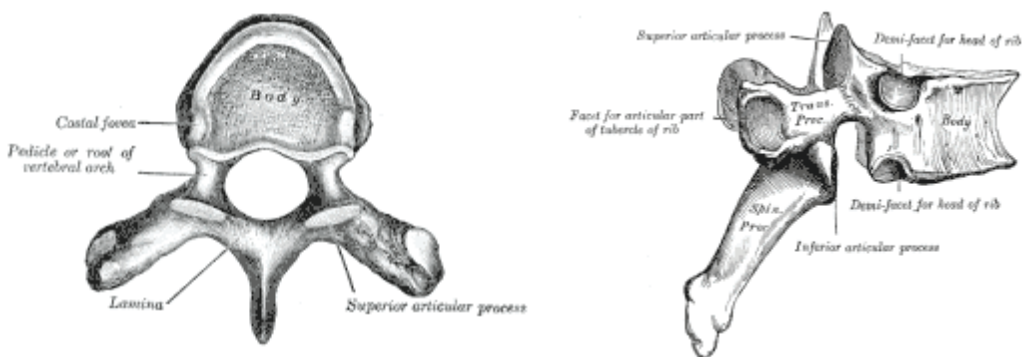
$\sigma_{\text{failure}} \text{ in}$ traction (MPa)	$\varepsilon_{\text{failure}} \text{ in}$ traction (%)	$\sigma_{\text{failure}} \text{ in}$ compression (MPa)	$\varepsilon_{\text{failure}} \text{ in}$ compression (%)	$\sigma_{\text{failure}} \text{ in flexion}$ (MPa)
109	1.35	162	1.8	160

Trabecular bone is composed of bone (or trabeculae) and marrow. Its structure has an important role in terms of damping due to the bone marrow that contains therein (Charpail, 2006). It is heterogeneous, viscoelastic and anisotropic. The trabecular bone may be considered as a material having an elastic phase, a phase of compaction in compression and a damage phase in tension. Its mechanical behaviour is very sensitive to the shear rate: the modulus of elasticity increases with the strain rate (Charpail, 2006). Density also plays an important role on the behaviour (Charpail, 2006). Young's modulus varies from 1.4 to 9800 MPa and the failure stress varies from 0.2 to 25 MPa (Charpail, 2006).

1.1.4 Thoracic vertebrae

Thoracic vertebrae known also as dorsal vertebrae compose the middle segment of the vertebral column, between the cervical vertebrae and the lumbar vertebrae. They are each composed of a vertebral body, two transverse apophyses and a spinous process (**Fig. 4**). The twelve thoracic bones and their transverse processes have surfaces that articulate with the ribs.

Laterally, the vertebral bodies contain, mostly two facet joints, each of which constitutes half of an articular surface for articulation with the head of a rib. Some rotation can occur between the thoracic vertebrae, but their connection with the rib cage prevents much flexion or other excursion. In this manuscript, we designate the thoracic vertebrae with the letter T followed by the number of the vertebra: for example T7 symbolizes the thoracic vertebra number 7.



a) Inferior view

b) Lateral view

Fig. 4. Typical thoracic vertebra (Gray, 1918).

1.1.5 Costovertebral joints

On each level of the thoracic spine, a pair of ribs articulates with the vertebrae by two joints:

- the costovertebral joint between the rib head and the intervertebral disc and the vertebral bodies.
- the costo-transverse joint between the rib tubercle and the transverse process of the underlying vertebra.

Kapandji hypothesizes that the costovertebral joint, on the one hand, and the costo-transverse joint, on the other hand, are mechanically linked (Kapandji, 2009). Their combined movement during breathing is a rotation around a common axis passing through the center of each of these two joints (**Fig. 5**). For the lower ribs, this axis is closer to the sagittal plane (a), consequently the thoracic cavity space increases along the transversal axis during rib elevation. For the upper ribs, the axis coincides with the frontal plane (b) which increasing the thoracic cavity space along the anterior-posterior direction. In the case of a frontal quasi-static loading of the ribcage, it has been showed that this axis of rotation migrates to remain parallel to the direction imposed (Eckert et al., 2000).

During inspiration, the elevation of the ribs implies the rotational movement of the costal cartilage relatively to the sternum (chondro-sternal joint) and torsion about the longitudinal axis. The costal cartilage stores potential energy due to the inspiration and releases it, to return to its original position during expiration.

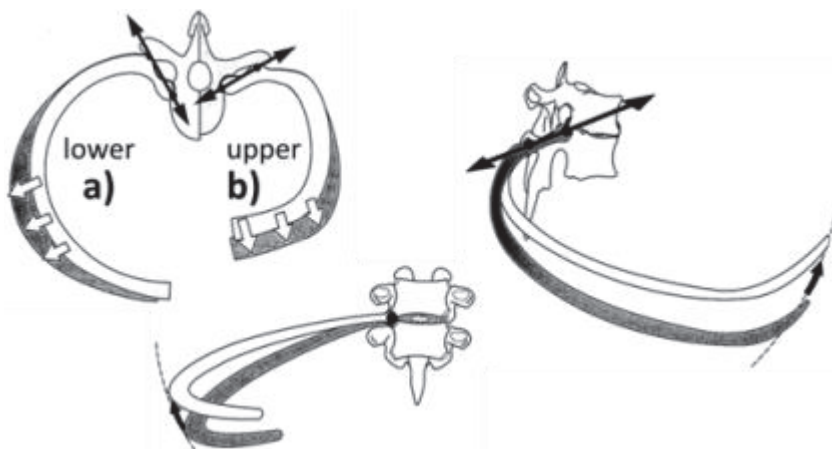


Fig. 5. Rib's axes of rotations (Kapandji, 2009).

1.2 Intercostal muscles

Ribs are interconnected by the intercostal muscle group, forming a solid but flexible barrier between the ribs (**Fig. 6**). Intercostal muscles are:

- external intercostal muscles are attached from the lower border of one rib to the upper border of the rib immediately below, with their fibers orientated obliquely forward and downward. During the inspiration, the external intercostal muscles are tensed in order to produce an upward movement of the anterior thorax;
- internal intercostal muscles are attached similarly but their fibers are orientated obliquely backward and downward. The tensing of the internal intercostal muscles results in the outward movement of the anterior thorax, contributing to the expiration.

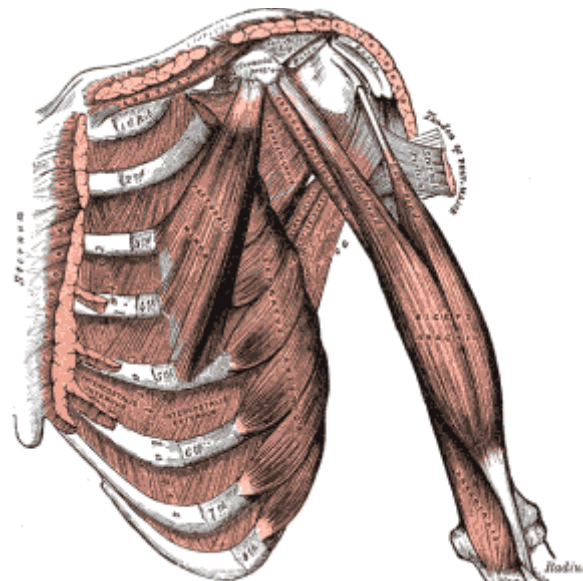


Fig. 6. Intercostal muscles (Gray, 1918).

1.3 Viscera

The ribcage protects vital organs from injuries involved in respiration and blood circulation. Thoracic cavity can be divided into three cavities:

- the right and the left outer cavities contain the lungs. Each lung is surrounded by a thin membrane called visceral pleura. The entire volume of the rib cage is covered by another thin membrane, the parietal pleura.
- the center cavity, called mediastinum, contains the heart, the esophagus, the trachea and large vessels.

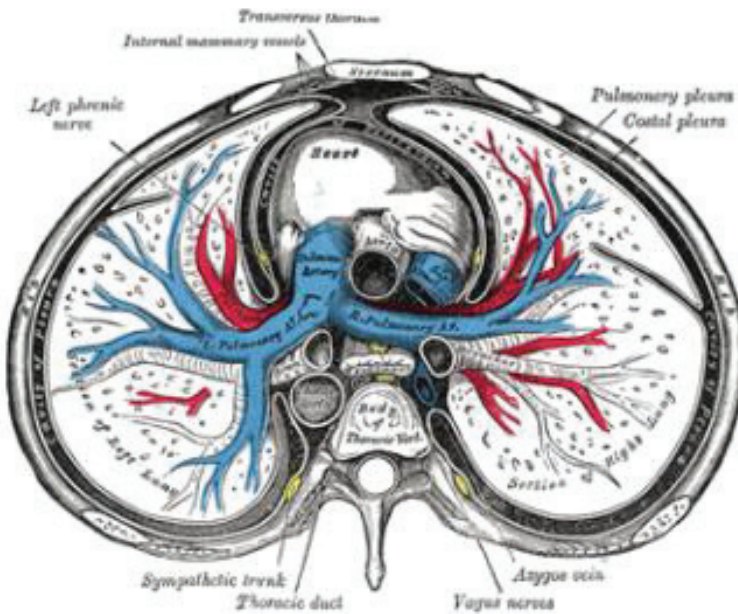


Fig. 7. Anatomy of pleural cavity and mediastinum (Gray, 1918).

2. Thoracic trauma in frontal impact

2.1 Abbreviated Injury Scale (AIS)

Traumatic injuries referencing and severity are performed with the Abbreviated Injury Scale (AIS). The AIS was developed to provide to researchers a simple numerical method for ranking and comparing injuries by severity and to standardize the terminology describing the lesions. The values of AIS quantify injuries and not their consequences. AIS can be used as an intrinsic ²evaluation of the severity of the injury and not as a measure of disability that may result.

At the end of this section, **Table 3** provides an overview of different injuries and their according AIS.

2.2 Accidentology

Various parts of the vehicle interior (like the steering wheel, safety belt, or the dashboard) can be in contact with the thorax in frontal collisions. In these conditions, sharp impact to the thorax is rare, occurring only due to obstacles inside or when the occupant is ejected from the vehicle. Consequently, most thorax injuries caused by contact mechanisms are caused by blunt impact.

Statistics showed that thoracic injuries were the main source of serious casualties of elderly ones (Lafont and Laumon, 2003). Considering AIS ≥ 2 thoracic injuries in the elderly population, it was observed that it was mainly rib and sternum fractures as showed in **Fig. 8** (Ndiaye and Chiron, 2009).

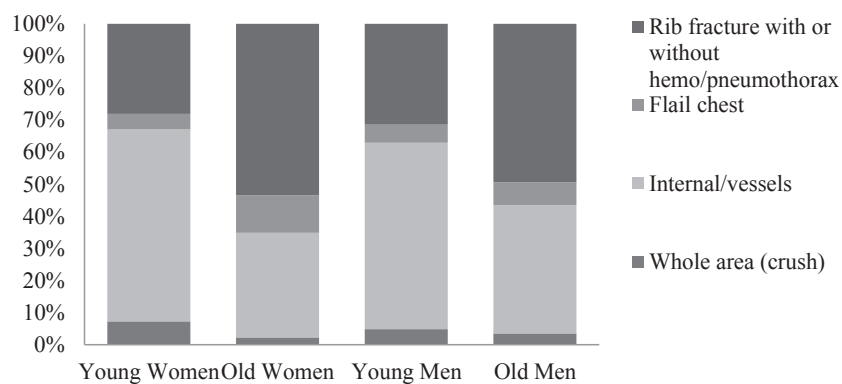


Fig. 8. Type of thoracic injuries AIS ≥ 2 by genders and age (Ndiaye and Chiron, 2009).

It is well established that tolerance of the human thorax under dynamic loading decreases as age increases (Zhou et al., 1996). Using the published data of PMHS tests under 3-point belt, the injury severity of each age group was assessed by the mean number of thoracic fractures normalized by the value of the 20-29 age group. Under same loading conditions, the injury severity increases substantially as age increases. From these results, it was assumed that the number of rib fractures increases linearly by approximately 0.33 rib fracture per year based on age at the time of death (Petitjean et al., 2003). By using the number of fractured ribs of the young group as a standard, **Table 2** synthetises the recommended reduction ratios at the injury level of AIS3.

Table 2. Thoracic tolerance reduction ratio with age at the injury level of AIS3 (Zhou et al., 1996).

Age range	16-35	36-65	66-85
Reduction ratio	1	0.47	0.28

Three different injury mechanisms can be occurred when the thorax is injured in blunt impact: compression, viscous loading and inertia loading of the internal organs. Furthermore any combination of these three basic phenomena can occur (Schmitt et al., 2009).

The resulting injuries can be categorized as skeletal injuries and soft tissue injuries. Most often the thoracic wall and the lung are injured together with rib fractures, sternum fractures and pleura ruptures. American epidemiological studies have highlighted that internal thoracic

vital organ injuries are relatively infrequent in 3-point belt restrained victims in frontal collisions (Yoganandan et al., 1991).

2.3 Thoracic injuries mechanisms

2.3.1 Rib fractures

The rib fracture is the complete rupture of one or more ribs. The fracture can be closed if the skin and the soft tissue overlaying the fracture remain intact or open if the chest wall is perforated by sharp edges of broken ribs. In less serious cases, the rib fracture is self-healing and causes localized pain, discomfort during breathing and sleeping.

However, when the chest wall is perforated by sharp edges of broken ribs, life threatening complications may appear. In particular, when multi rib fractures occurred, a portion of the chest wall is released from the entire skeleton. These phenomena called flail chest makes it difficult to expel the air out of the lung.

Generally, sagittal loading of the ribcage is more likely to cause single rib fracture, while lateral impact more often results in multi rib fractures. Rib fracture occurs at the maximum point of curvature or at the location where a force is applied. As the ribs have a stronger curvature in the lateral part with less soft tissues that cover the ribs, lateral fractures are more usual.

The site of lateral rib fractures depends on the shape of the impacting body (**Fig. 9**). According to PMHS studies (Melvin et al., 1975; Stalnaker and Mohan, 1974), the number of rib fractures depends on the magnitude of rib deflection rather than on the rate of deflection. However, due to the viscous nature of the thorax, the maximal force depends on the loading rate. Maximal force appears to be related to the number of rib fractures for a given loading rate.

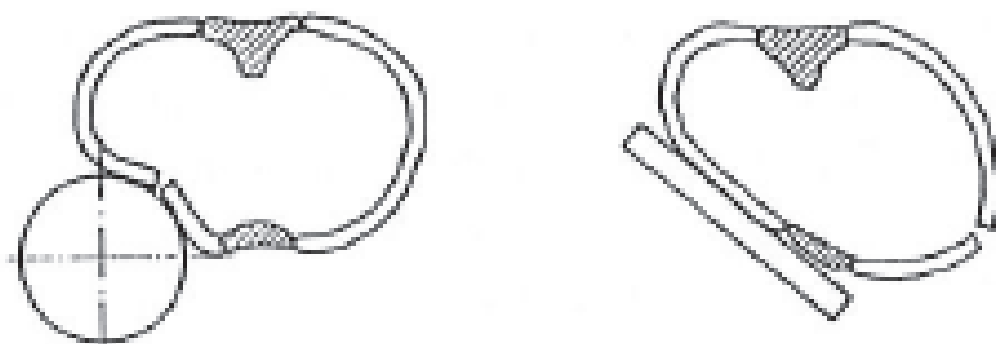


Fig. 9. Site of rib fractures depending on impact surface shape (Schmitt et al., 2009).

2.3.2 Lung injuries

The most frequent lung injuries are lung contusions. Lung contusions appeared with excessive thorax compression. This often happens with combination with flail chest but can occur without any rib fracture. Unlike bone fractures, lung contusion is rate-dependent (Fung and Yen, 1984). At high velocities, a shock wave is transmitted to the lung tissue and can cause microscopic ruptures of vessels.

However, the laceration and lung perforation traumas caused by fractured ribs are more critical to life (Schmitt et al., 2009). This may result in a pneumothorax or a hemothorax. The pneumothorax is an abnormal presence of air in the pleural cavity which is due to the perforations of the pleura and the lung producing a loss of air from the lung tissue to the pleural cavity. During the inspiration, the pleural cavity fills with air whereas during the expiration, the laceration in the lung tissue is compressed preventing the air in the pleural cavity to be expelled. Therefore, the lung progressively deflates. The hemothorax is an accumulation of blood in the pleural cavity due to bleeding injuries in the thorax, e.g. lacerations of blood vessels running between the intercostal muscle layers in each intercostal space. As blood is incompressible, the volume in which the lung can expand is reduced.

2.3.3 Other injuries

The space between the sternum and the thoracic vertebrae is particularly minimal, thus the compression of the anterior chest wall can cause the direct traumatic impact of the sternum with internal anatomical components or the displacement and the possible tearing of the mediastinum structures. A significant thorax deceleration results in a difference in kinetic energy between the mediastinum components which is responsible for shearing, tearing or impact of the organ tissues (Schmitt et al., 2009).

In case of frontal collision implying thoracic impact, the heart can be subjected to several injuries including contusion and laceration (**Fig. 10**). Contusions appear with heart crushing on the anterior face of the sternum. The lacerations of the pericardial sac, which enclosed the heart, are caused by broken part of the bony structure. Likewise, the perforation of the heart can arise in case of high thoracic compression magnitude. Another life threatening complication due to a thoracic impact at high velocity is a disorder of the heart electric conduction bringing about a cardiac fibrillation or even a cardiac arrest (Schmitt et al., 2009).

Furthermore, major thoracic blood vessels like the aorta can be injured. Rupture and laceration are the most likely mechanisms resulting front blunt impact trauma to the thorax.

Cavanaugh reports that arterial injury account for 6% to 8% of AIS>2 only, but represent 30% of the estimated harm (Cavanaugh, 1993). It should be noticed that the majority of the victims sustaining an aortic trauma die at the scene of the accident.

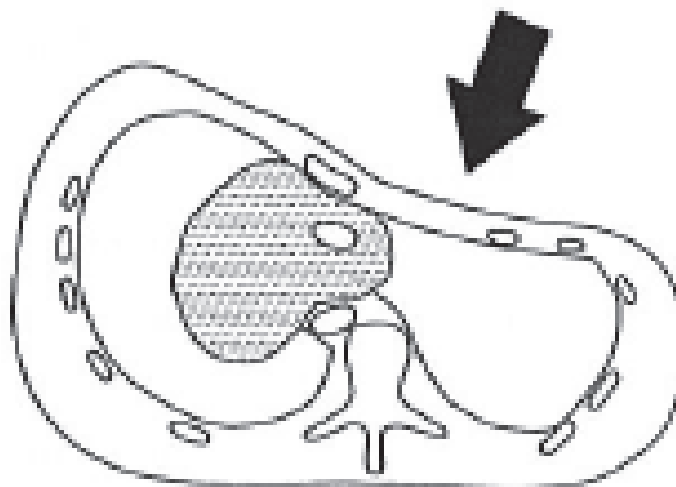


Fig. 10. Compression of the heart (Schmitt et al., 2009).

The most vulnerable aortic region is located at the junction of the aortic arch and the descending thoracic aorta (Creasy et al., 1997). The rupture or the light fissure of this anatomical part occurs either from the traction or the shearing generated between a movable group composed by the heart and the aortic arch, and the immovable descending portion of the aorta which is joined to the thoracic wall, or simply due to the direct compression over the vertebral column. An excessive sudden increase of the intraluminal pressure is also a possible injury mechanism.

Table 3. AIS rating for skeletal and soft tissue thoracic injuries (Schmitt et al., 2009).

AIS	Injury severity	Skeletal injury	Soft tissue injury
1	Minor	1 rib fracture	Contusion of bronchus
2	Moderate	2-3 rib fractures Sternum fracture	Partial thickness bronchus tear
3	Serious	4 or more rib fracture on one side 2-3 rib fractures with hemo/pneumothorax Flail chest	Lung contusion Minor heart contusion
4	Severe	4 or more rib fractures on each side 4 or more rib fractures with hemo/pneumothorax	Bilateral lung laceration Minor aortic laceration Major heart contusion
5	Critical	Bilateral flail chest	Major aortic laceration Lung laceration with tension pneumothorax
6	Untreatable		Aortic laceration with haemorrhage not confined to mediastinum

3. Thorax mechanical response during frontal loading

3.1 Blunt impact tests

Numerous tests with different configurations were conducted in laboratory on PMHS to assess thorax biomechanical response in frontal impacts. First understanding of thoracic biomechanical response to antero-posterior loading was assessed in the past on Post Mortem Human Surrogates (PMHS) using blunt hub impactor tests (Kroell C.K., 1971; Lobdell et al., 1973; Nahum A.M., 1975; Neathery, 1974). These blunt impact tests were representative simulations of the impact from the steering wheel to an unrestrained occupant (due to the low rates of seatbelt use in the 1960's and 1970's).

PMHS were subjected to dynamic, antero-posterior blunt loading of the thorax, involving a 15 cm diameter circular rigid impactor (Kroell C.K., 1971). The impact was accomplished by an impacting mass travelling at constant velocity (4.3 m/s - 10 m/s) in the horizontal direction and striking the thorax of an upright-seated surrogate (**Fig. 11**).

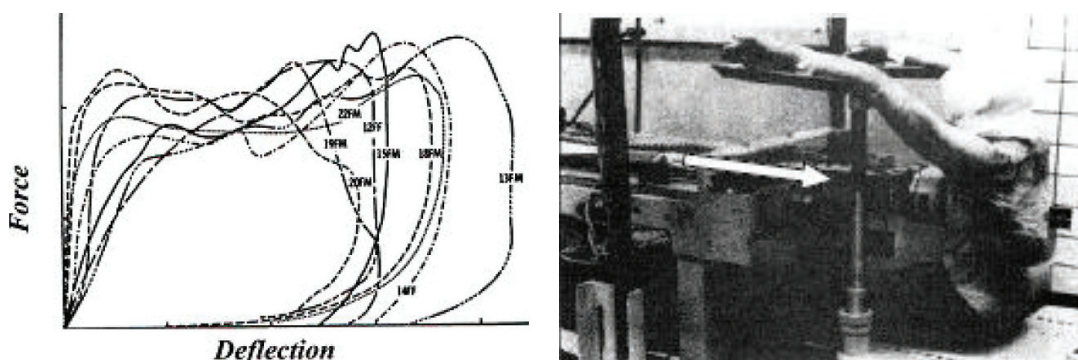


Fig. 11. Thoracic mechanical responses on PMHS using impactor (Kroell C.K., 1971; Nahum A.M., 1975; Neathery, 1974).

Corridors were formed by bounding the individual force-deflection responses at several impact velocities in order to illustrate the rate-related changes in thorax behaviour (Neathery, 1974). These corridor responses were used for the validation standard Hybrid III dummies (Schneider et al., 1989).

3.2 Compression tests

Several authors carried out series of PMHS positioned supine on a table and subjected to a seatbelt-like loading as described in **Fig. 12** (Cesari and Bouquet, 1990; Kent et al., 2004; L'Abbe et al., 1982). The analysis of thoracic deflection showed that the most extensive deformations is situated at the point 8 which is on a relatively soft part of the thorax, as well

as at the point 1 which is more deflected than the two other points on the sternum. Moreover, these results strongly support the fact that the lower region of the human thorax is more compliant than the upper region, because of changes in the overall geometry and individual rib geometry.

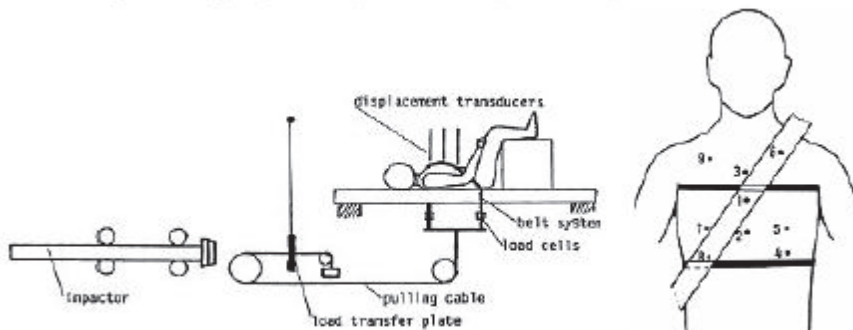


Fig. 12. Supine belt loading setup and instrumentation (Cesari and Bouquet, 1990).

In compression tests, the thorax is loaded between the table and the belt. The advantage of this protocol is to provide a fixed reference plane in the analysis of the thorax deformation. The authors support the idea that the interactions between the ribs and the table have a negligible effect on the thoracic deflection. The main limitation of the compression tests is the possible restriction of rib rotation due to the supine position. This could virtually increase the thoracic stiffness due to constraints in costovertebral joints. In this test configuration, the subject is put in a different situation than that of a belted car occupant in a frontal collision where the belt loading is only due to the occupant inertia.

3.3 Sled tests

In sled test, forward motion of the subject is stopped by the belt like in real-world crashes (**Fig. 13**). In the 1990's, sled tests were carried out on PMHS in order to quantify thoracic deformations in simulated frontal impacts with several kinds of restraint system (Crandall et al., 1994; Kallieris et al., 1995; Kallieris et al., 1994; Yoganandan et al., 1993; Yoganandan et al., 1991). **Fig. 14** illustrates the typical belt force-time histories obtained during sled tests in which the subject was restrained by a standard 3-point belt (Kallieris et al., 1994; Yoganandan et al., 1991). In addition, the pattern of thoracic deformation contours obtained from Chestband indicated considerable local compressions of the thorax at the belt path (**Fig. 14**).

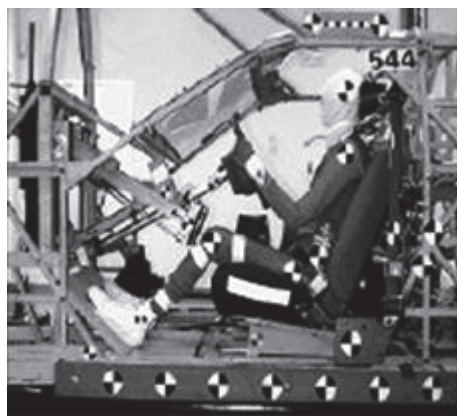


Fig. 13. Sled tests on PMHS with belt restraint system in a real world crash environment (Kuppa and Eppinger, 1998).

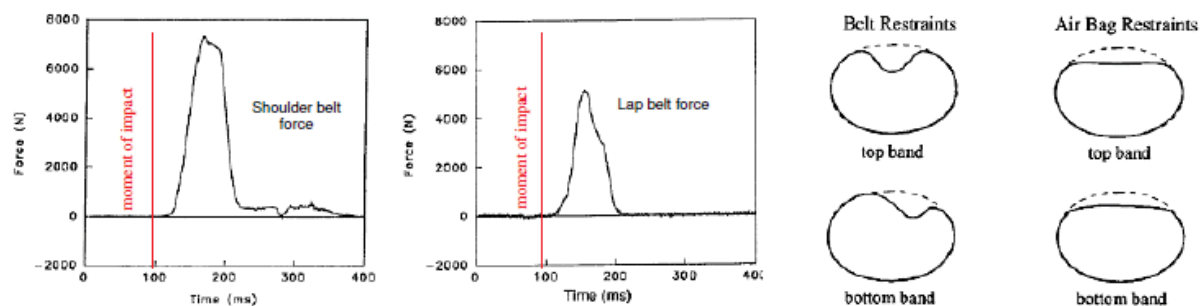


Fig. 14. Typical force-time histories (left, center) and chest contours (right) of a driver restrained by belt or airbag in frontal impact (Kallieris et al., 1994; Yoganandan et al., 1991).

In this configuration, the most common thorax injuries were fractures, especially rib fractures. The thoracic injury severity seems to be influenced by the age of the occupant, the impact severity and the restraint condition. The type of restraint system used causes specific patterns of rib fractures, whereas the number of rib fractures seems to vary depending on both the subject's age and the impact velocity (**Fig. 15**).

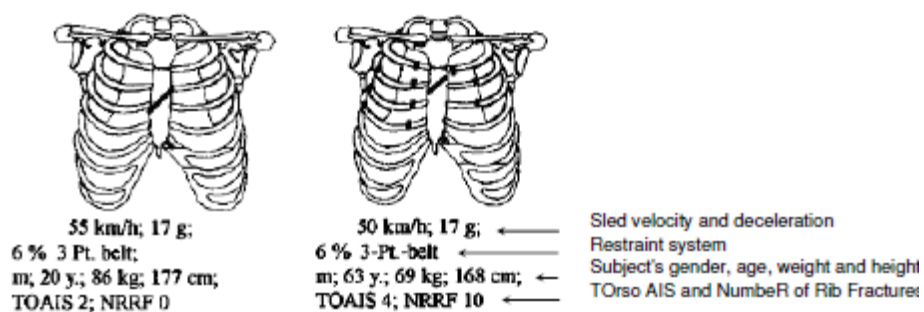


Fig. 15. Examples of injury pattern in sled tests by using 3-point belt and airbag (Kallieris et al., 1994).

3.4 Influence of loading conditions

Although blunt impact tests allowed the increase in the understanding of the thorax behavior, the current automotive environment is different than the environment when the hub impact tests were being conducted. In particular, injuries from belt or air bag loading are becoming more important as their uses are standard in recent vehicles (Kent et al., 2003).

Kent et al. conducted several PMHS tests, with different protocols (Kent et al., 2004). The human cadavers were subjected to four loading conditions on the anterior thorax (single belt loading, double belt loading, distributed loading and hub loading). He demonstrated that the calculated effective stiffness of the thorax is strongly dependent on the load distribution. The distributed loading condition generates the highest effective stiffness whereas the hub load generates a lower effective stiffness than the other conditions.

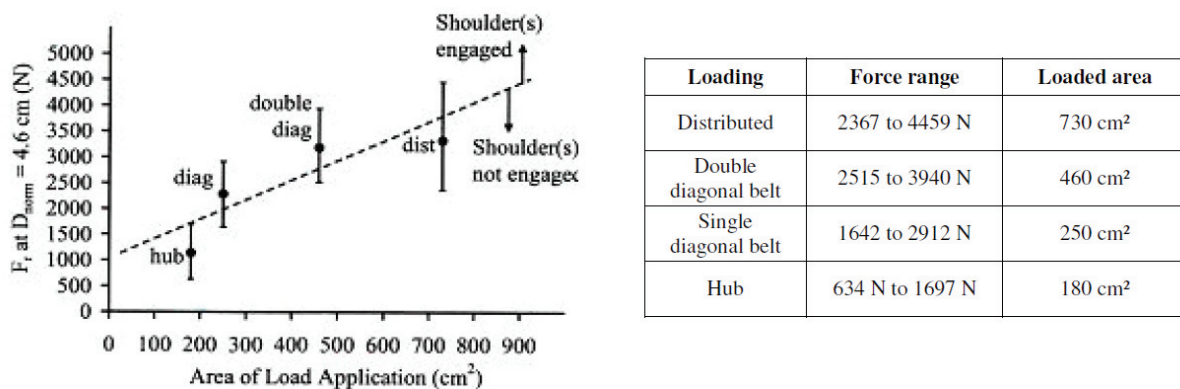


Fig. 16. Force at 20% chest deflection for a 50th male as a function of loaded area (Kent et al., 2004).

The force required to generate an injurious level of deflection is strongly dependent on the load distribution on the thorax (Kent et al., 2004). Thus, corridors defined using impactors should not be used to assess thorax mechanical response under belt loading.

4. Thoracic injury assessment based on dummy responses

Anthropomorphic test devices (ATD), commonly termed crash test dummies are mechanical surrogates of the human body that simulate its dimensions, weight proportions and joints (Mertz, 1993). They are used in the field of transport safety to assess the injury risk and thus to assess the effectiveness of various restraints systems and car designs. ATD are instrumented with transducers that measure accelerations, deformations and loads of main body parts. These measurements are analyzed to compute specific injury criteria that are linked to injury risk.

4.1 Anthropomorphic test devices

ATD are classified according to size, age, sex and impact direction. The midsize adult male dummy is the most utilized size in automotive restrain testing. It approximates the median height and weight of the 50th percentile adult male population. The height and weights of the small female and large male adult dummies are approximately those of the North American 5th percentile female and the North American 95th percentile male respectively. Key dimensions and weights for various sizes of dummies are given in **Table 4**.

Table 4. Key dimensions and weights for various sizes of dummies (Nahum and Melvin, 2002).

Key dimensions and weights	Infants			Children		Adults (percentile)		
	6 mo	12 mo	18 mo	3 yr	6 yr	5 th female	50 th male	95 th male
Dimensions (mm)								
Erect sitting height	439	480	505	546	635	812	907	970
Buttocks to knee	170	198	221	284	381	521	589	638
Knee to floor	125	155	173	221	358	464	544	594
Shoulder to elbow	130	150	160	193	234	305	366	381
Elbow to fingertip	175	198	213	254	310	399	465	503
Standing height	671	747	813	953	1168	1510	1751	1873
Weights (kg)								
Head	2.11	2.49	2.72	3.05	3.48	3.68	4.54	4.96
Neck	0.29	0.34	0.35	0.43	0.41	0.81	1.54	2.04
Torso	3.04	4.38	5.22	6.61	10.76	24.14	40.23	53.00
Upper extremity	0.85	1.18	1.31	1.79	1.98	4.67	8.53	10.94
Lower extremity	1.53	1.31	1.60	2.63	4.28	13.52	23.36	31.79
Total weight	7.82	9.70	11.20	14.51	20.91	46.82	78.20	102.73

The first crash test dummy used by the domestic automobile industry for restraint was Sierra Sam, a 95th percentile adult male dummy that was developed by Sierra Engineering in 1949 for ejection seat testing by the U.S. Air Force (Mertz, 1993). The most used of the early frontal impact dummies was the Hybrid II midsize adult male dummy, developed by General Motors in 1972 to assess 3-point belt systems. In addition to midsize male, small adult female and large adult male were developed. Hybrid II dummy family was known to have lack in head and neck biofidelity and had little instrumentation (Nahum and Melvin, 2002).

Hybrid III dummy family was developed to improve the biofidelity and instrumentation drawbacks of the Hybrid II family (Mertz, 1993). These dummies consist of a small adult (5th percentile) female adult, a midsize adult (50th percentile) male dummy, a large adult (95th percentile) male dummy and a 3-year-old and a 6-year-old child dummy. The midsize male dummy which made its first appearance in 1976, is the standard crash test dummy in frontal impact. Hybrid III are limited in their biofidelity and in their application type. Indeed, the

Hybrid III chest is two times stiffer than the thorax of PMHS (Cesari and Bouquet, 1994). In addition, the Hybrid III dummy does not adequately assess the risk thoracic lesion (Foret Bruno et al., 1998). It comes in contradiction with the accidentology in the evaluation of the restraint belt with force limiter 4 kN and airbag (Petitjean et al., 2002). Similarly, crash test dummies which are extremely simplified depiction of human anatomy cannot take into account physiology.

Hybrid IIIs are designed to research the effects of frontal impacts, and are less valuable in assessing the effects of other sorts of impacts, such as side impacts. The SID (Side Impact Dummy) family of test dummies has been designed to measure rib, spine, and internal organ effects in side collisions. An international consortium was established to oversee the development of a universal side impact dummy termed WorldSID (Moss et al., 2000).

The successor of Hybrid III dummy, THOR (Test device for Human Occupant Restraint) has been developed to become the successor of Hybrid III dummy. This development program, undertaken by GESAC Inc. in 1995 and overseen by National Highway Traffic Safety Administration (NHTSA), resulted in the design and development of an advanced frontal crash test dummy that incorporates improved biofidelity and significantly expanded instrumentation (Shams et al., 2005). Other companies had recently started developing their own version of the THOR dummy.

4.2 Thoracic injury criteria

An injury criterion is defined as a physical parameter (acceleration, force, penetration) or a function of several physical parameters which correlates well with the injury severity of a body region for a specific type of lesion. Injury criteria are measurable engineering parameters which have the highest injury predictive ability among all others.

Injury risk curves are used to define the injury risk for a given human body response. They are mostly based on data from tests using animals, Post Mortem Human Surrogates (PMHS) or human volunteers. Examples of risk curves are shown in **Fig. 17**. The injury criterion is presented along the horizontal axis, while the injury risk is presented along the vertical axis. It should be noted that depending on the shape (which is related to the mathematical method used) of the risk curve, a small difference for the injury criterion value could result in large differences for the injury risk.

A protection criterion is defined as a threshold value of the criterion which is associated with a chosen percentage of the risk of sustaining injury.

In the following part, the thorax injury criteria used in automotive regulations are described, along with the emerging criteria proposed for future standards. A synthesis is given in **Table 5**.

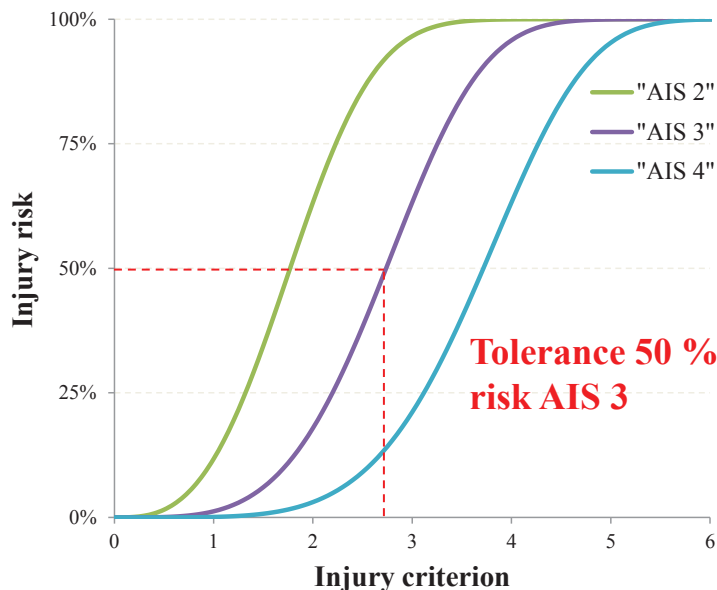


Fig. 17. Examples of injury risk curves for different severities.

4.2.1 Acceleration

In the U.S., the earliest chest injury criterion to enter a crash test regulation which was specified in the Federal Motor Vehicle Safety Standards (FMVSS) 208 was the whole body deceleration tolerance criterion. Mertz and Gadd recommended that the peak chest acceleration measured at the mass centre of the chest does not exceed the value of 60 g for acceleration pulses of 100 ms and shorter, in order to avoid severe thorax injuries (Mertz and Gadd, 1971). Nowadays, the FMVSS 208 injury criteria specify that the 3-ms clip value of resultant chest acceleration at the gravity centre of the upper thorax of the Hybrid III dummy should be limited to 60 g in 48-km/h frontal impact tests against a rigid barrier.

4.2.2 Force

Foret-Bruno studied the possible relationship between the risk of injury and the force applied by the belt to the shoulder (Foret-Bruno et al., 1998). They examined the statistics of 256 car accidents in frontal impact including the textile load limiters and 6 kN limiters. The analysis of the limiter value in relation to the occupant injuries led to the thoracic injury risk curves according to age as function of the shoulder belt force (**Fig. 18**).

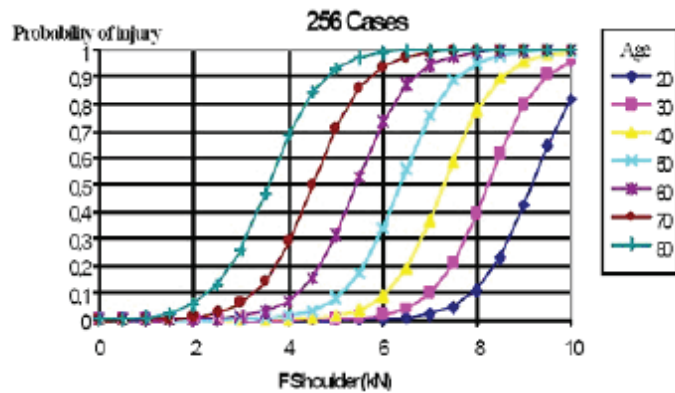


Fig. 18. Probability of AIS ≥ 3 thoracic injury versus age and shoulder belt load (Foret-Bruno et al., 1998).

In addition, a statistical model was developed from these injury risk curve correlating the risk of severe injury (AIS3+) with the effort in the shoulder F_{shoulder} and the age:

$$p(\text{AIS} \geq 3) = \frac{1}{1 + e^{20.6 - \frac{\text{age}}{6.2} \frac{F_{\text{shoulder}}}{0.529}}} \quad \text{Equation I-1}$$

4.2.3 Compression criterion

Chest compression C is defined as the chest deformation divided by the initial thickness of the thorax. Analysing blunt impact tests, Kroell concluded that the maximum chest compression correlated well with AIS (Kroell C.K., 1971). The following relationship was established:

$$\text{AIS} = -3.78 + 19.56 \times C \quad \text{Equation I-2}$$

Compressions of 30% and 40% correspond respectively to a thorax injury rated AIS2 and AIS4. A compression of 40% represents 92 mm of chest deflection on a 50th percentile male thorax (229 mm) likely cause multiple skeletal injury, especially flail chest (**Fig. 19**). A tolerated maximum compression of 33% corresponding to a 50% probability of an AIS ≥ 3 thoracic injury was extrapolated in the 50th percentile male Hybrid III dummy to be a maximum allowable sternal deflection of 75 mm (represented for a 45 year old male in blunt frontal impact). Mertz developed thoracic injury risk curves, for AIS ≥ 3 thoracic injury on the basis of the sternal deflection responses of the Hybrid III 50th adult male dummy restrained by a 3-point belt load system (Mertz et al., 1991).

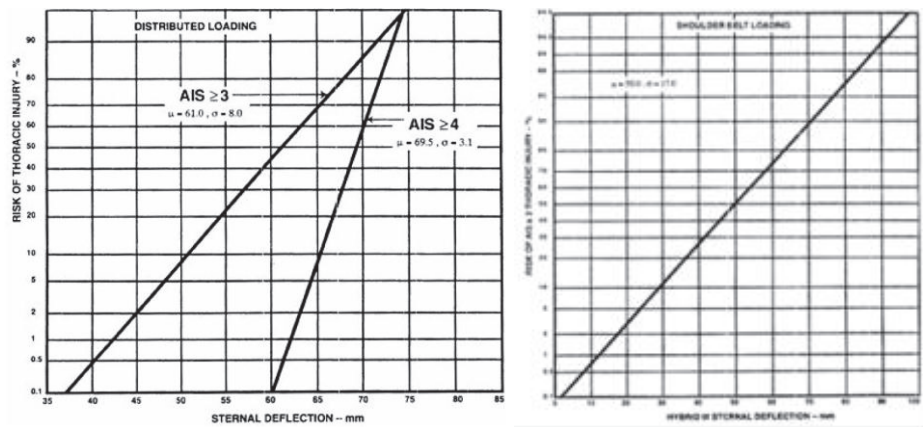


Fig. 19. Risk of thoracic injuries as a function of sternal deflection for a mid-size adult male (left) and as a function of Hybrid III sternal deflection (right) (Mertz et al., 1991).

In FMVSS 208, the deflection of the sternum relative to the spine measured by the central rotary potentiometer in the 50th percentile Hybrid III male dummy cannot exceed 75 mm during the specified crash tests. Afterwards, Mertz suggested that the threshold value of 75 mm was maintained for airbag loading, but the 50 mm of sternum deflection (22 % of chest compression) should be recommended as the limit for shoulder belt loading (Mertz et al., 1991). The European and Canadian frontal impact regulations accepted this limit, but the U.S. automotive regulations continued with 75 mm of sternal deflection (33% of chest compression) regardless of the restraint system used.

4.2.4 Viscous criterion

Since the vital organs contained in the mediastinum are soft tissues, the understanding of their injury mechanisms is critical to the improvement of occupant protection systems. On the basis of 123 frontal impact experiments on anaesthetized rabbits, Lau and Viano proposed the concept of Viscous Criterion for predicting thoracic soft tissue injury (Lau and Viano, 1986).

A viscous response was defined by a time dependent function formed by the product of the instantaneous velocity of deformation, $V(t)$, and the instantaneous compression, $C(t)$, defined as the chest deformation divided by the initial thickness of the thorax. According to the authors, the viscous response peak $[VC]_{max}$, occurs generally earlier than the maximum compression and seems to happen at about the same time as the initiation of skeletal damage. This maximum value of the time function is consequently considered as a potential biomechanical index of injury and is called Viscous criterion.

The injury risk curve associated with $[VC]_{max}$, was developed by carrying out a probity analysis of the thoracic AIS values and the corresponding $[VC]_{max}$. A frontal impact

producing a $[VC]_{max}$ of 1.3 m/s had consequently a 50% chance of causing a thoracic AIS ≥ 4 injury severity (**Fig. 20**). The threshold level of 1 m/s which corresponds to a 25% probability of AIS ≥ 4 has often been chosen as a human chest tolerance threshold in vehicle regulations.

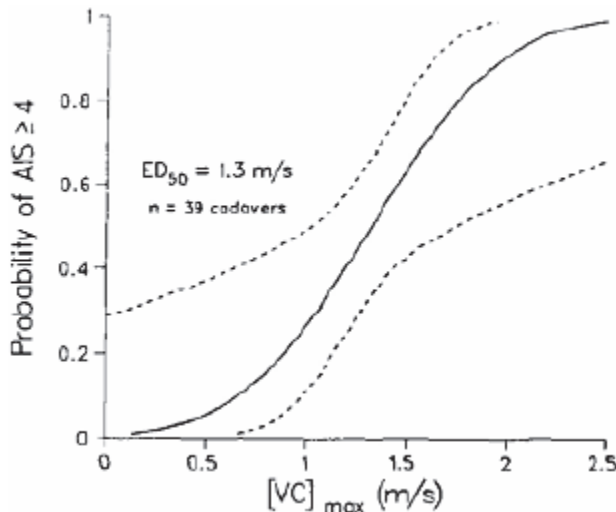


Fig. 20. Risk curve for AIS ≥ 4 chest injury based on Viscous Criterion for blunt frontal impact (Lau and Viano, 1986).

Viscous criterion is a good indicator of soft tissue injury for chest deformation velocities ranging from 3 to 30 m/s (Lau and Viano, 1986). Below 3 m/s, the influence of impact velocity on soft tissue gradually diminishes. In this case, the soft tissue injuries are essentially induced by crushing of the tissue. In consequence, the prediction capability of VC is diminished and the compression criterion becomes a better indicator of soft tissue injury risk and tolerance to rib cage damage. When the velocity of deformation approaches 30 m/s, the impact velocity becomes a predominant factor in determining injury outcome. In conditions of high-velocity impact exposures with very little chest deformation, the blast injury begins to occur first in the lung, then to other hollow organs.

In Hybrid III dummy, the viscous response is computed from the chest internal deflection sensor. However, the proposed human tolerance was derived from cadaver data which measured the antero-posterior deformation externally. A scaling factor is applied from the VC values given by the sensor to achieve the external VC values by using the following relationship:

$$[VC]_{ext} = 1.3 \times [VC]_{int} \quad \text{Equation I-3}$$

4.2.5 Combined Thoracic Index

The Combined Thoracic Index (CTI) represents an injury criterion in frontal impact combining compression and acceleration criteria (Eppinger et al., 1999; Kleinberger and Administration, 1998). It is defined as the evaluated 3ms value from the 3-ms clip value of T1 acceleration and the maximum normalized chest deflection

$$CTI = \frac{A_{max}}{A_{int}} + \frac{D_{max}}{D_{int}} \quad \text{Equation I-4}$$

where A_{max} is the maximum value of spinal acceleration, D_{max} is the maximum value of the dummy deflection, and A_{int} and D_{int} are equal to 90 g and 103 mm respectively.

The CTI was developed based on cadavers tests and correlated with the probability of an AIS ≥ 3 injury. To date, the CTI was included in FMVSS 208 even if several car manufacturers preferred to maintain the current criteria which limit the chest acceleration and the chest deflection independently (Eppinger et al., 1999).

4.2.6 Thoracic deflection

The thoracic deflection is a criterion used by the ES-2re dummy and the worldSID dummy to evaluate the protection level for side impacts (Cavanaugh et al., 1993). The relevance of thoracic deflection as an independent thorax injury criterion was evaluated in different loading conditions including frontal impacts (Song et al., 2009). In this study, simulations with a modified HUMOS FE human body model was validated versus a database constructed on PMHS tests literature review covering different impact directions (frontal, lateral and oblique), different loading configurations (impactor, belt and airbag) and different injury levels (number of fractured ribs). The antero-lateral deflection seems representing better the deformation shape of the thorax. Since this variation does not significantly change from one loading to another, thoracic deflection can be considered as a relevant indicator of ribcage damage level.

4.2.7 Combined Deflection

Some authors proposed a new thoracic injury criterion which should be valid in all thorax restraint configurations (Song et al., 2010). Various injury criteria were tested on different directions of impact (0° , 60° and 90°), different loading types (impactor, belt and harness, airbag, sled with belt-only restraint and sled with combined belt and airbag restraint), investigating different loading severities (sub-injury to numerous rib fractures) with a FE human body model based on HUMOS model. The Combined Deflection D_c defined below was judged the most relevant by the authors:

$$D_c = D_s + C_f [(\Delta D - L_c) + |\Delta D - L_c|] \quad \text{Equation I-5}$$

where D_s is the mid-sternum deflection, ΔD a lower thorax differential deflection, C_f : a correction factor based on the simulation and L_c : the characteristic length.

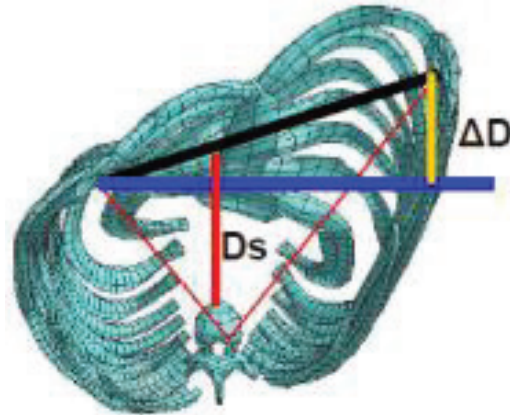


Fig. 21. Illustration of the Combined deflection on a deformed thorax (Song et al., 2010).

After analysis, the relationship between the Number of Fractured Ribs (NFR) and the Combined deflection doesn't change significantly versus loading type. The analysis of the NFR threshold led to thoracic injury curves according to loading type as a function of the Combined deflection. However, the proposed C_f correction factor was defined from the simulations performed with HUMOS model. This correction factor may be different with another FE model and for dummy.

Table 5. Frontal impact criteria and tolerances for the thorax (Schmitt et al., 2009).

Tolerance level	Injury level	Reference
Force: 3.3. kN to sternum 8.8 kN to chest and shoulders	minor injury major injury	(Foret-Bruno et al., 1998; Foret-Bruno et al., 2001) (Foret-Bruno et al., 1998; Foret-Bruno et al., 2001)
Acceleration 60 g	3ms value for Hybrid III	FMVSS 208
Deflection: 50 mm 58 mm 75 mm	no rib fracture no rib fracture limit for Hybrid III	ECE R94 (Stalnaker and Mohan, 1974) FMVSS 208
Compression: 20% 40%	Rib fractures flail chest	(Kroell C.K., 1971) (Kroell C.K., 1971)
Viscous criterion 1.0 m/s 1.3 m/s	25% probability of AIS \geq 4 50% probability of AIS \geq 4	(Lau and Viano, 1986) (Lau and Viano, 1986)
CTI: Amax/60g + Dmax/76mm	50% probability of AIS>3 in cadavers	(Eppinger et al., 1999; Kleinberger and Administration, 1998)

5. Potential of in-vivo experiments for thorax mechanical response assessment

Most of the studies on thorax injuries are based on PMHS tests. The drawback with the use of PMHS as experimental subjects is the differences in dynamic response characteristics with the living humans. These differences which have been observed between the PMHS sled tests and the field accident data may be attributed to several factors that are listed below.

5.1 Influence of physiology

In crashworthiness, more than half of the driver may be tensing prior to impact (Kent et al., 2006). Some series of human volunteer tests were carried out in the 1970's and the 1980's, in order to quantify the influence of the muscle tensing on the force-deflection response of the thorax. These studies show an increase of thorax stiffness in tensed state. The increasing of thorax stiffness varies in different studies, its effect decreases at higher compression. Pig tests show that the peak force increases with muscle tensing for chest deflection levels up to about 20%, after which the peak force changes negligibly when the muscles are tensed (Kent et al., 2006).

Compression tests were carried out with 10 volunteers (L'Abbe et al., 1982; Backaitis and St-Laurent, 1986). In relaxed state, the largest amplitude occurred at mid-sternum location (40 mm). In tensed state, largest amplitude was registered at mid-sternum location (35 mm).

Recently, a total of 10 low-speed frontal sled tests (5.0g, 9.7kph) were performed with 5 male human volunteers similar to the 50th percentile male, in a driver configuration (Kemper et al. 2011). Volunteers were asked to adopt a relaxed state in one test and a braced state in the other tests. Mid-sternum compressions were computed using a chestband placed at the nipple level. Bracing have significant effect on thorax mechanical response (Fig. 22).

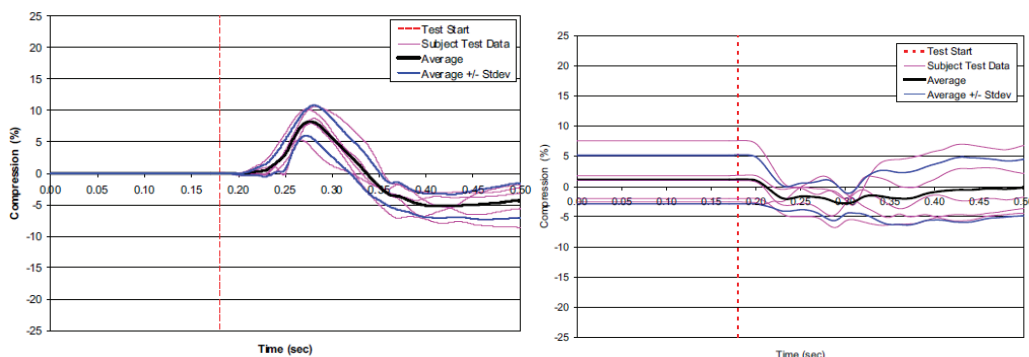


Fig. 22. Chest compression during relaxed (left) and braced (right) conditions (Kemper et al. 2011).

Table 6. Volunteer studies on thorax mechanical response in antero-posterior loading.

Reference	Methodology	Objective	Limitations
(Armstrong et al., 1968)	30 US Air Force Personnel on sled test 8-20 km/h, 3-15g	Influence of subject restraint on kinetic subject absorption	Experienced volunteers No chest deflection data High peak pulses
(Lobdell et al., 1973)	7 human volunteers subjected to static hub loading (11% chest deflection) 1 human volunteer impacted at 2.4 m/s with a 10 kg padded hub impactor (18% chest deflection) 11 volunteers	Chest deflection	Loading conditions
(Patrick, 1981)	Impacted at 2.4 m/s with a 10 kg padded hub impactor (18% chest deflection) 11 volunteers	Chest deflection	Unique volunteer Impactor loading type
(Tsitlik et al., 1983)	Quasi-static loading of the sternum with a rubber plate (48 x 64 mm) Volunteers dynamically loaded	Chest deflection	Loading conditions
(Backaitis and St-Laurent, 1986)	by diagonal belts Belt load 2.8-3.2 kN (14 % chest deflection, 35 mm)	Volunteer vs. dummy chest response	Higher stiffness from back restrained
(Arbogast et al., 2009)	5 male volunteers on sled test in front crash conditions 8 km/h, 4 g	Child difference of neck and head response	No thorax study Focused on child
(Kemper et al. 2011)	5 male volunteers in front crash conditions 10 km/h, 5 g	Effects of bracing on chest compression	Volunteer close to 50th percentile No data on belt forces

5.2 Influence of age

The PMHS population used in sled test differs from the real-world population at risk because most of the PMHS used in the studies were over fifty years-old whereas the mean age of the driving population is thirty years. Similarly, crash test dummies as mechanical devices do not have versions according to age groups. About age-related changes occurred in the thorax, the degeneration of human ribs and soft tissues is an important factor which modified significantly thorax mechanical response.

5.2.1 Rib and soft tissues mechanical properties modifications

It was assumed that proportion of cortical bone in rib cross-section and the moduli of both cortical and trabecular bone decrease by 20% from age 20 to age 90 (Kent et al., 2004; Stein and Granik, 1976).

A decrease in bone density is observed at the age between 30 and 40 because the metabolism is unable to maintain a positive balance between the removal of old bone and the replacement of new one. Furthermore, the change in porosity seems to play a greater role in the reduction in strength than the change in mineral content (McCalден et al., 1993). After 55 years old, the decrease in bone density becomes more pronounced, and increases significantly between age of 60 to 70 (Zhou et al., 1996).

These changes result in a greater reduction in ability of the bone to absorb the impact energy than the static strength and elastic modulus changes (Burstein et al., 1976).

The progressive calcification of the costal cartilage may tend to increase the global thoracic stiffness and consequently decrease the chest deflection tolerance. The mechanical properties of some typical soft tissues decrease with aging (Yamada, 1970) especially costal cartilage strength are show in **Fig. 23**.

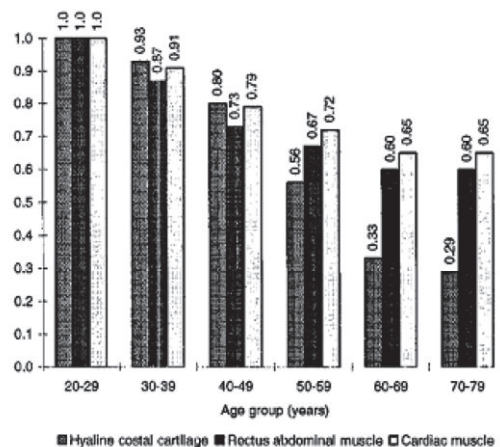


Fig. 23. Ratios for age changes in the ultimate tensile strength of soft tissues (Yamada, 1970).

The effects of age on the modulus of the thoracic soft tissues and organs are not as well documented as for bone. The reduction of ultimate tensile strength of human arterial tissues in the longitudinal direction is about 20% between the young adult group and elderly group (Yamada, 1970). On the other hand, the coronary artery wall is twice stiffer for age 70 than age 20 due to collagen reinforcement of the arterial wall (Bass et al., 2001).

5.2.2 Ribcage structural modifications

Studies suggested that the slope of ribs in the sagittal plane decreases with ageing (Gayzik et al., 2008; Kent et al., 2005; Kent et al., 2003). A significant association between the angle of the ribs and age was identified, with the ribs become perpendicular to the spine as age increased (**Fig. 24**).

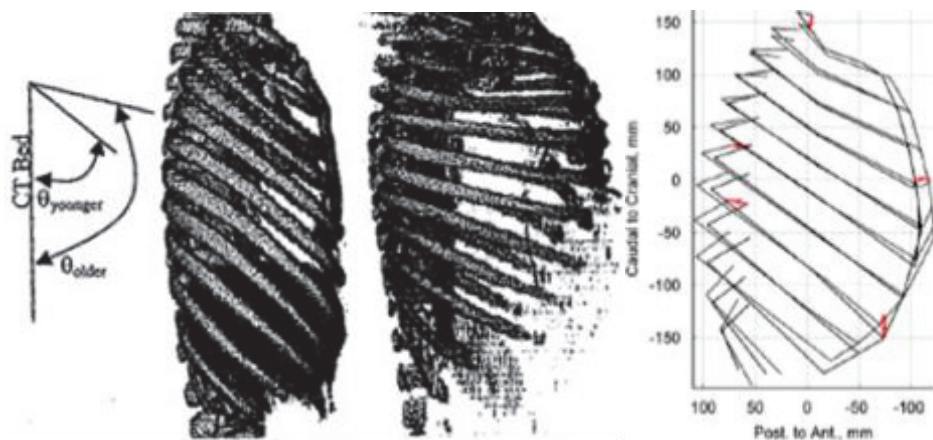


Fig. 24. Age-related change in rib slope (Gayzik et al., 2008; Kent et al., 2003).

It was assumed that according to the rib orientation, the applied force causes rib deformations and rotations at various degrees (Kent et al., 2005). Specifically, for an individual with “vertical” rib cage, typically a young subject, an antero-posterior loading produces joint ribs rotations and bone deformation. Whereas, for individual with “horizontal” rib cage, typically an ageing subject, the load force acts straight in the plane of the ribs and imply primarily bony deformation. Thus, the increase in angle between ribs and spine results in an increase in the structural stiffness and a reduction of thoracic deflection tolerance. This phenomenon is illustrated in Fig. 25. A link was found between the initial slope and the amount of rotation and deformations (Vezin and Berthet, 2009).

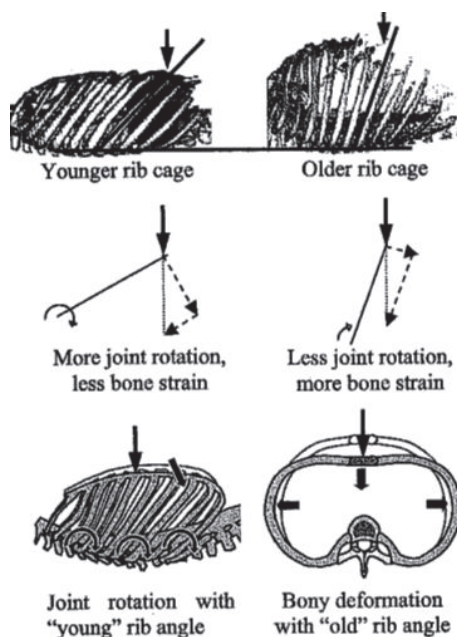


Fig. 25. Illustration of mechanism by which increased rib angle increases thoracic stiffness while decreasing chest deflection tolerance (Kent et al., 2005).

5.3 Influence of corpulence

Some authors found a correlation between Body Mass Index (BMI) and the thorax shape (Berthet et al., 2005; Gayzik et al., 2008). BMI was associated with increased risk of mortality and increased risk of severe injury with a predominant occurrence for rib fractures and pulmonary contusions (Boulanger et al., 1992; Mock et al., 2002), Shankuan et al. 2006). Obese subjects were linked to unfavorable kinematics (greater head and pelvis excursion) and may be linked to higher chest compression (Forman et al., 2009).

In the vast majority of developed countries, the prevalence of overweight and obesity in older adult population is very high (Gutierrez-Fisac et al., 2004). The association between BMI and fatality rate did not change significantly with age. Yet, the role of obesity, age, for crash fatality is not clearly known.

Moreover, the existing mechanical dummies represent only the population through 3 sizes (50th percentile male, 5th percentile female and 95th percentile male). These sizes were based on anthropometric charts extract from the North American population which can slightly differ in other countries (De Onis and Habicht, 1996). Therefore, the crash test dummies produce important shortcomings with respect to a real crash situation.

6. Potential of numerical human models for personalize injury risk prediction

6.1 Introduction

Numerical human models have been developed to produce biofidelic predictions of human response in crash and to improve the understanding of human impact response and injury mechanisms (Yang et al., 2006). Limited by technology, earlier mathematical models tended to simplify the system using a set of differential equations.

In the 1970's, Lobdell et al. developed a spring-dashpot-mass model of the thorax describing its behavior in frontal impact (Lobdell et al., 1973). The model was tuned to match the low and high velocity corridors determined experimentally in blunt frontal impact (Kroell C.K., 1971; Lobdell et al., 1973). With this model, they attempted to assign the inertial, elastic and viscous characteristics of the load-deflection response obtained from blunt impact tests. Due to inherent limitations, lumped mass modeling can only predict the gross motion of the human

thorax in one direction. They are unable to simulate detailed anatomical structures of the thorax or complex loading conditions.

Advances in computing simulations allow the development of many sophisticated models and numerical methods. Their primary benefit is the ability to provide detailed insight into impact response at the tissue level, depending on the level of detail in the model, and to identify the importance of different tissues in terms of response and the potential for injury. At the organ/tissue level, trauma is associated with stress, deformation, strain rate, and wave phenomena. Numerical methods include specific computer codes written to solve a series of dynamics equations. The explicit finite element method is the most commonly used numerical method in impact crash biomechanics.

The finite element method (FEM) is a numerical approach used to solve partial differential equations. It is an approximation to the original problem, where a volume is discretized into smaller sub-volumes termed elements with a prescribed mass distribution and material behavior. FEM can deal with complex geometry, nonlinear materials, collision and contact, material damage, and failure. The explicit formulation is used to simulate dynamic problems like frontal crashes. In this formulation, the equations are solved at discrete time increments (time step) using a central difference integration scheme. The base time step is determined from the Courant condition, the time required for a stress wave to cross an element in the model. Time step must be sufficiently small (order of nanoseconds to microseconds) to avoid divergence of the solution. Thus, explicit formulation requires many computation cycles over very small time increments but benefits of a faster processor, or the use of multiple processors. Nevertheless, it should be noted that verification tests based on relevant experimental tests are essential for any model to ensure that the assumptions are reasonable.

In the future, human FE models are called to play an important role in the development and validation of safety solutions through the use of virtual testing. This advanced approach requires more efficient, complex and biofidelic human substitutes. It implies to develop a global human body model simulating the response of a human being and predicting injuries in all impact cases (frontal, rear, side). Since all road users need to be correctly protected by the safety devices during a collision, it is necessary to develop personalized models which represent all the population in corpulence and in age.

6.2 FE models

In the 70's, the first 3D finite element models of the thorax appear (Chen et al., 1978; Roberts and Chen, 1972; Sundaram and Feng, 1977). The rib cage was represented by beam elements and the overall geometry is based on direct measurements made by the authors on a human thorax. Elastic material properties were applied on bone and cartilage and were taken from Yamada (1970). These models were not validated with PMHS tests, but demonstrated the feasibility of a 3D representation of the thorax in different type of loading (first static, then dynamic).

Plank and Eppinger (1989) developed a model with the individual ribs modeled and the internal organs considered as a lumped viscoelastic whole solid. This model was verify with PMHS tests and used for restraint system investigations. Huang (1994) developed a thoracic model with representations of the internal organs, validated with PMHS tests. Shah (2001) implements blood circulation to evaluate aortic injury in crash scenarios. A detailed description of recent human body model developments is provided in **Table 9**.

The level of detail in thorax and human body models has increased over due to the availability of detailed anatomical information and increased computing power (Yang et al., 2006). Significant advances have also been made in terms of material constitutive models (viscoelastic, viscoplastic), their implementation in finite element codes, and the required data to validate them.

At present, several whole body and detailed thorax models exist including: the Total Human Model for Safety (THUMS) (Iwamoto et al., 2002; Iwamoto et al., 2000), the Wayne State University torso model (Zhao and Narwani, 2005), the Johns Hopkins University model (Roberts et al., 2005), L3 Communications thorax model (Shen et al., 2010), the ESI Group H-model (Haug et al., 2004) and the Human Model for Safety (HUMOS) (Robin, 2001; Vezin and Verriest, 2005). Many of the current models contain more than 100K elements, with corresponding element sizes below 5 mm.

6.3 Existing personalized FE models

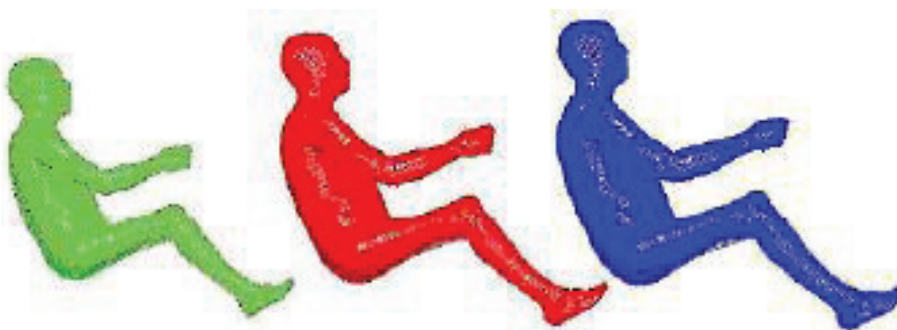
6.3.1 Models of adult extreme anthropometries

In FE model, model geometry is available from different sources including online databases such the Visible Human Project or directly developed from CT scans. In general, these

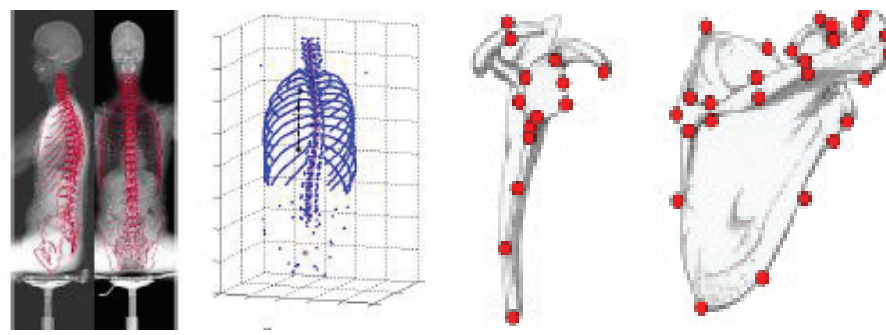
methods provide surfaces and are converted to volumes. Thus, specific models of different populations were developed.

A finite element model of a small female (AF05, 152cm, 46.4kg) has been developed by scaling down the mid-size adult male model of THUMS (Kimpara et al., 2002; Kimpara et al., 2005). The anthropometrical data was obtained from AF05 data defined at the University of Michigan (Schneider, 1983). This model was a combination of the small female Total HUman Model for Safety (THUMS-AF05) (Kimpara et al. 2002) and the Wayne State University Human Thoracic Model (Shah et al., 2001). The model incorporated geometrical genders differences, such as location of the internal organs and structure of the bony skeleton and biomechanical differences of the ribs due to gender. Detailed description of the model is available in **Table 9**. This model was validated against a series of PMHS experiments on the small female (Kroell et al., 1974; Nahum et al., 1970; Talantikite et al., 1998; Viano, 1989; Wilhelm, 2003). Results predicted by the model were well-matched to these experimental data for a range of impact speeds and impactor masses. However, this model still needs validation in sled tests, more representative of real world distributed loading.

In the EC funded HUMOS2 project, methods allowing the personalization in geometry and posture were developed to create the small female and the large male models (a) from the HUMOS 50th percentile male model (**Fig. 26**; (Vezin and Verriest, 2005). They include a scaling tool enabling to derive from the original geometry through mesh control points and statistical relationships between external and internal dimensions. These control points were established from geometric data collected on standing and sitting human volunteers (b) with a low dose bi-plane X ray system but also directly measured on isolated bone parts (c).



a) 5th female, 50th and 95th percentile male obtained from HUMOS mesh.



b) X-ray picture of a seated volunteer and control points obtained. **c)** 3D control points measured on the scapula

Fig. 26. Overview of the HUMOS2 scaling tool (Vezin and Verriest, 2005).

6.3.2 Elderly thoracic model

An elderly thoracic model based on the THUMS mid-sized adult male model was validated in four table-top loading conditions (Tamura et al., 2005). Material properties of the cortical rib in an elderly male were determined based on experimental test data (Stitzel et al., 2003). The material property of the cortical rib used this model was summarized in **Table 7**. By adjusting the material properties of the anterior, lateral and superior part of the cortical ribs to account for aging, the predicted force-deflection characteristics by the model matched the PMHS responses for distributed, hub, single and double diagonal belt loading conditions.

Table 7. Material property of the cortical rib in an elderly thoracic model based on the 50th percentile male THUMS (Tamura et al., 2005).

	σ_y (MPa)	ϵ_y	YM (GPa)	Etan (GPa)	ϵ_p	ϵ_{max}
Anterior part	121.6	0.0145	8.394	3.792	0.0055	0.020
Lateral part	135.3	0.0111	12.211	4.610	0.0089	0.020
Posterior part	112.9	0.0103	10.998	6.332	0.0097	0.020

σ_y : yield stress, ϵ_y : yield strain, YM: Young's modulus, Etan: plastic hardening modulus, ϵ_p : plastic strain, ϵ_{max} : ultimate strain.

Recently, two human thorax FE models for evaluating thoracic skeletal injuries on adult and elderly were developed from H-model (Ito et al., 2009). The rib cage geometries were generated based on the medical CT images and the literature (Gayzik et al., 2008). The material properties of the rib, costal cartilage were estimated based on the literature, and for the sternum, the material property of the rib was used. **Table 8** described material parameters used in this study. The models were validated against isolated rib bending test and chest impact tests from the literature. However, these models still need further validation in at the ribcage model and ultimately in sled tests.

Table 8. Material property of the ribcage for adult and elderly model (Ito et al., 2009).

Cortical bone				
	σ_y (MPa)	ϵ_y	σ_{max} (MPa)	ϵ_{max}
Adult (35 yo)	64.1	0.0246	79.9	0.0246
Elderly (70 yo)	54.0	0.0212	68.3	0.0212
Trabecular bone				
	σ_y (MPa)	ϵ_y	σ_{max} (MPa)	ϵ_{max}
Adult (35 yo)	-	-	3.31	0.0696
Elderly (70 yo)	-	-	1.25	0.0776
Cartilage				
	σ_y (MPa)	ϵ_y	σ_{max} (MPa)	ϵ_{max}
Adult (35 yo)	-	-	9.41	0.018
Elderly (70 yo)	-	-	7.16	0.0139

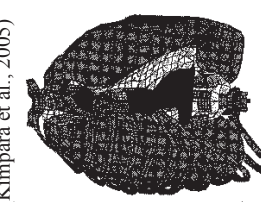
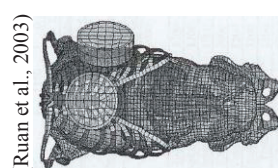
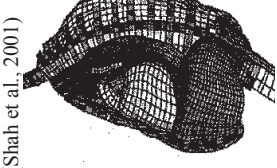
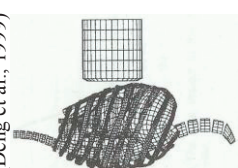
σ_y : yield stress, ϵ_y : yield strain, σ_{max} : ultimate stress, ϵ_{max} : ultimate strain.

Similarly to Ito et al., two human thorax FE models for evaluating thoracic skeletal injuries on adult (35 yr) and elderly (75 yo) were developed from Ford Human Body Model (FHBM) -- an FE model which approximates the geometry and mass of a mid-sized male (El-Jawahri et al., 2010). The geometry of the thorax and the parameters of the material models of long bones, ribs, skin, flesh and intercostal muscles were modified to match those of 35 and 75 yr using literature (Yamada, 1970; Mohr et al., 2007; Dokko et al., 2009). The isolated rib of the age-dependent models was validated against human rib specimens and whole rib tests, under tensile, 3-point bending, and front loading, with and without modeled fracture. In addition, the resulting three age-dependent models were validated against published thoracic pendulum impact, rigid bar abdominal impact, sled impacts and isolated ribcage frontal loading tests. The responses of the models, in general, were within the cadaveric response corridors. When compared to peak responses from individual cadavers similar in size and age to the age-dependent models, some responses were within one standard deviation of the test data. All the other responses, but one, were within two standard deviations.

Table 9. Overview of recent thorax FE model from (Charpail, 2006; Yang et al., 2006)

Reference	Size and model	Elements	Material properties	Validation
(Plank and Eppinger, 1989)	50th percentile man	solid at 8 nodes	Model used in frontal impact with impactor according to Kroll et al. (1971) and 1974)	
(Plank and Eppinger, 1991)	Modelization of ribs, sternum, vertebrae, discs, cartilage, ligaments, muscles and internal organs	(code DYNA3D)	Response in force-deflection corridors of Neathery (1974).	
(Plank et al., 1994)	50th percentile man	bricks (8 nodes)	E = 12304 MPa = 0.3, $\rho = 4790 \text{ kg.m}^{-3}$	
	Ribcage based on anatomical sections	(code DYNA3D)	Response does not longer fit to corridors of Neathery (1974), because the thorax is more compliant than the previous due to geometry change	
(Huang et al., 1994)				The answer is in the corridor defined by Neathery (1974).
(Lizée et al., 1998)	50th percentile man	Soft tissue: bricks (8 nodes)	Bone : elastic Soft tissues : viscoelastic	The model is validated from PMHS tests with impactor (Kroell et al., 1971; Bouquet et al., 1994; Viano, 1989) and belt (Cesari et al., 1990) in frontal and lateral impact.
	Complete model of a human being in a position to lead (based on chest CT scans)	Ribcage: shell (3 nodes)	rib / sternum / spine: $E = 9 \text{ GPa} = 0.3, \rho = 4790 \text{ kg.m}^{-3}$ cartilage : $E = 3 \text{ GPa}, v = 0.42, \rho = 2768 \text{ kg.m}^{-3}$	
		(code RADIOSS)	rib / sternum / spine: $E = 2.5 \text{ GPa} = 0.3, \rho = 1800 \text{ kg.m}^{-3}$ cartilage : not reported	

Reference	Size and model	Elements	Material properties	Validation
(Deng et al., 1999)	50th percentile man Thorax model with detailed geometry of organs and skeletal	bricks (8 nodes)	Rib : elastoplastic with failure Soft tissues/viscera: viscoelastic. Rib E= 26 GPa ; σyield= 110 MPa ; σult= 125 MPa). Cartilage E= 1.2 GPa ; p= 5.0 g.cm⁻³ ; v= 0.2)	The model is validated from PMHS tests with impactor (frontal and lateral) (Kroell et al., 1971 and 1974; Neatherly, 1974)
(Shah et al., 2001)	50th percentile man	Bone : shells (cortical) and solids (trabecular) Cartilage: solids Ligament/Muscle: shells Spine :solids Viscera: solids	Bone : elastic Cartilage: elastic Ligament/Muscle: elastic Spine :elastic Viscera: nonlinear foam	Frontal and lateral pendulum tests
	Thorax model with detailed geometry of organs and skeletal	Rib (cortical) E = 15 GPa = 0.3, ρ = 2000 kg.m⁻³ Rib (trabecular) E = 98.8 MPa = 0.3, ρ = 1000 kg.m⁻³		
	Blood circulation	Cartilage: E = 22.7 MPa = 0.35, ρ = 2000 kg.m⁻³		
(Ruan et al., 2003)	50th percentile man Whole body model in driving position with detailed internal organs	Bone : shells (cortical) and solids (trabecular) Cartilage: solids Ligament/Muscle: shells Spine :solids Viscera: solids	Bone : viscoelastic Cartilage: viscoelastic Ligament/Muscle: viscoelastic Spine :viscoelastic Viscera: viscoelastic	Validation using pendulum tests in frontal and lateral (Kroell et al. 1971 Viano, 1989) and belt (Cesari and Bouquet, 1990)
		Rib ρ = 2000 kg.m⁻³, K= 9.6 GPa, G₀ = 4.4 GPa, G∞ = 1.8 GPa Sternum ρ = 2000 kg.m⁻³, K= 9.6 GPa, G₀ = 4.4 GPa, G∞ = 2.3 MPa		
(Kimpala et al., 2005)	5th percentile female Issue from THUMS model	Cartilage : ρ = 1500 kg.m⁻³, K= 53 MPa, G₀ = 9 MPa, G∞= 96 kPa Bone : elastic Cartilage: elastic Ligament/Muscle: elastic Spine :elastic Viscera: nonlinear foam	Cartilage : ρ = 1500 kg.m⁻³, K= 53 MPa, G₀ = 9 MPa, G∞= 96 kPa Bone : elastic Cartilage: elastic Ligament/Muscle: elastic Spine :elastic Viscera: nonlinear foam	Frontal, lateral, oblique pendulum impacts on small female Ballistic breast impact on small female
		Rib (cortical) E = 9.86 GPa = 0.3, ρ = 2000 kg.m⁻³ Rib (trabecular) E = 40 MPa = 0.45, ρ = 1000 kg.m⁻³		
		Cartilage: E = 49 MPa = 0.4, ρ = 2000 kg.m⁻³		(Kroell et al., 1974; Nahum et al., 1970; Talantikite et al., 1998; Viano, 1989; Wilhelmi, 2003).



7. Conclusion

Statistics show that in France thoracic injuries are a main cause of death among victims of car frontal collisions and the main source of serious casualties of elderly occupants. Moreover, if we focus on moderate injuries sustained by the elderly population, rib and sternum fractures are mainly observed.

First studies on Post Mortem Human Surrogates (PMHS) focused on generating thoracic force-deflection corridors using a hub-impact test condition. These corridors were used in the development of frontal impact dummies. However, force-deflection corridors of the thorax were found to be strongly dependent on the load distribution, and particularly on the anatomical area that supports the load. Thorax mechanical response depends strongly on the geometrical characteristics of the ribcage and on its biological material properties. Authors agree that the deformation of the rib cage under an antero-posterior loading is divided into rib rotation relative to the vertebrae and sternum, and rib deflection. More accurately, it is assumed that according to the rib orientation, the applied force causes rib deformations and rotations at various degrees. Specifically, for an individual with a “vertical” rib cage, an applied antero-posterior load produces rotations of the rib joints and bone deformation whereas, for individual with a “horizontal” rib cage, the load force acts straight in the plane of the ribs and implies primarily bone deformation. A link was found between the initial rib slope and the amount of rotation and deformation. Thus, it seems that geometrical characteristics of the ribcage may predispose ribs to fracturing.

In addition, it was well established that tolerance of the human thorax under dynamic loading decreases as age increases. Physiological phenomena of ageing could be described as the combination of mechanical and structural modifications associated with a decrease of the chest deflection tolerance. The elastic modulus and the tensile strength of human bones decreased with age. Similarly, a decrease in the tensile strength of hyaline rib cartilage and cortical thickness in the rib sections was observed. The age-related changes in thorax shape were also studied and authors assumed that the ribs became more horizontal with age and the slope of ribs in sagittal plane decreased with age. Yet, some authors also found a correlation between BMI and the thorax shape. Body Mass Index (BMI) was associated with increased risk of mortality and increased risk of severe injury with a predominant occurrence for rib fractures and pulmonary contusions. Obese subjects were linked to unfavorable kinematics (greater head and pelvis excursion) and may be linked to higher chest compression. In the vast

majority of developed countries, the prevalence of overweight and obesity in older adult population is very high.

Thus, in order to study the variability of the population in age, anthropometry and for both gender, *in vivo* experiments seem necessary. Except early *in-vivo* experimental studies which brought knowledge on the human body tolerance, most of them were used to analyze the physiology influence on the body response to dynamic loading - muscle tone or to assess the response of specific populations such as children for non-injurious levels.

Currently, the role of geometrical parameters possibly linked to the thorax mechanical response under dynamic loading is not clearly understood and isolated. In particular, the assessment of influence of age and overweight on these parameters is missing.

In addition, there are no injury assessment tools accounting for differences in anatomical features and material properties between adults and elderly. Crash tests dummies differ significantly from the real human body and are only available for a limited set of body sizes. Moreover, the criteria used have been defined from PMHS tests. PMHS have significant differences in dynamic response characteristics with the living humans and their age and corpulence variability are limited too.

Human body models offer some promising advantages including the prediction of injury mechanisms and injury criteria and a large potential of customization. Nevertheless, the choice of the level of customization and its sensibility to predict thoracic injury risk is still a scientific obstacle.

In addition, there are still few amounts of experimental data that can be used to validate these personalized models in real-world loading.

In this context, it seems necessary to perform experiments with adults of various anthropometries and age to understand thorax mechanical response and then to use customize FE models to do the same analysis in the injurious domain.

Chapter 2 presents first the *in vivo* protocol for the analysis of thorax mechanical response under belt loading carried out on adults of various anthropometries and age. Then, the influence of age and overweight on thorax mechanical response is analysed.

Chapter 3 describes the methodology used to personalize the geometry and posture of the THUMS model using external landmarks and anthropometric dimensions taken on volunteers.

The process was assessed on one subject by comparing computed thorax geometry and MRI data and on other subjects by comparing anthropometric dimensions.

Chapter 4 provides the analysis of simulations of personalized models of six specific subjects. First, a validation of the models under a low pulse is presented. Then, simulations of more severe pulse are used to compare different levels of personalization in the injury risk.

CHAPTER II - IN VIVO ANALYSIS OF THORAX MECHANICAL RESPONSE UNDER BELT LOADING

1. Introduction

In the present chapter, we present the analysis of thoracic mechanical response under belt loading of adults of various anthropometries and age subjected to a low deceleration pulse. In particular, the influence of age and overweight ($BMI \geq 25 \text{ kg/m}^2$) on thoracic mechanical response will be assessed.

2. Materials and methods

This in vivo protocol was reviewed and approved by the French ethical committee Comité de Protection des Personnes Sud-Est II at Lyon in February 2011.

2.1 Test device

The sled configuration is based upon a standard sedan car environment of a front passenger restrained by a 3-point belt (**Fig. 27**). Posterior support consisted of a belt band tensed between the two backseat rods. Weight is added to the sled according to the weight of the subject (up to 110 kg) in order to maintain a constant sled mass (640 kg).

The propelling system of the sled is chosen to allow low impact velocities with a good repeatability in pulses and to limit the maximum impact speed; it is made of two rubber bands of diameter 20 mm mounted on each side of the sled.

The sled is pulled rearward by an electrical winch until reaching a length of the two rubber bands so that a desired impact speed is reached.

The stopping system uses the energy of deformation of an elastomeric tube penetrated by a spear to dissipate the kinetic energy of the sled. Elastomeric tubes are conserved in a fridge when not used to maintain their characteristics.



Fig. 27. Sled configuration based upon a standard sedan car environment of a front passenger restrained by a 3-point belt.

2.2 Definition of the deceleration pulse

Two public crash simulators were investigated for establishing the pulse used in the protocol. The longitudinal deceleration of each device was recorded by using an uniaxial accelerometer mounted on it. The deceleration of the first public crash simulator (Autochoc, owned by the French insurer MACIF) reached a peak of 0.97 ± 0.38 g with a pulse duration of 200 ms and an impact speed of 5 km/h. The deceleration of the second one (Testochoc, owned by the French Road Safety) reached a peak of 9.98 ± 0.44 g with a pulse duration of 45 ms and an impact speed of 7 km/h.

Several tube configurations were applied to replicate a pulse between the two pulses with 3.8 g peak and 120 ms duration. This pulse was found similar to the one applied in a recent study on children (Arbogast et al., 2009).

The sled is pulled rearward by an electrical winch until reaching 165% of the two rubber bands' initial length so that an impact speed of 8 km/h is reached. One elastomeric tube (hardness 95 SHA) and a 46.5 mm diameter spear are needed to stop the sled at a maximum deceleration of 4 g and during 120 ms. Deceleration pulses are shown in **Fig. 28**.

More details are available in **Appendix 1**.

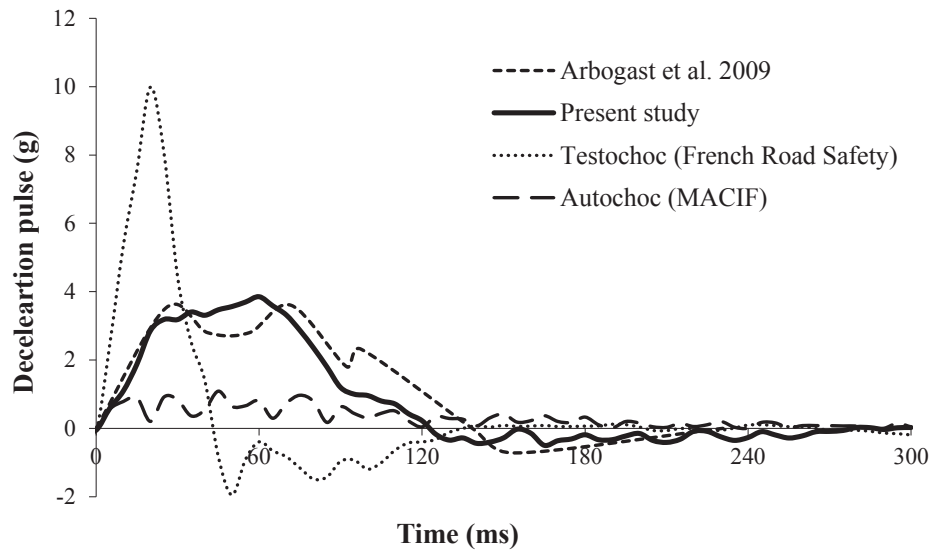


Fig. 28. Comparison of sled pulses applied in vivo.

2.3 Tested volunteers

30 volunteers were tested. They were between 19 and 65 years of age and consisted of both males and females and were chosen on target of height and weight, between 5th and 95th percentile based upon anthropometries charts (Jürgens et al., 1990). Volunteer's main characteristics are listed in **Table 10** sorted with BMI. Distribution of tested subjects for men (a) and women (b) are available in **Fig. 29**.

For physiological issues, subjects with existing endocrine disorders, mediastinal pathology, previous or current diseases of the head, neck and spine were excluded from the tests. Only volunteers over 40 years of age with no osteopenia (total femoral and lumbar T_{score}>-1) were planned for sled testing. Prior to the testing, a medical doctor conducted an exam of each subject to confirm eligibility.

Two sled tests were performed on each volunteer. For each test, they were asked to adopt a relaxed posture.

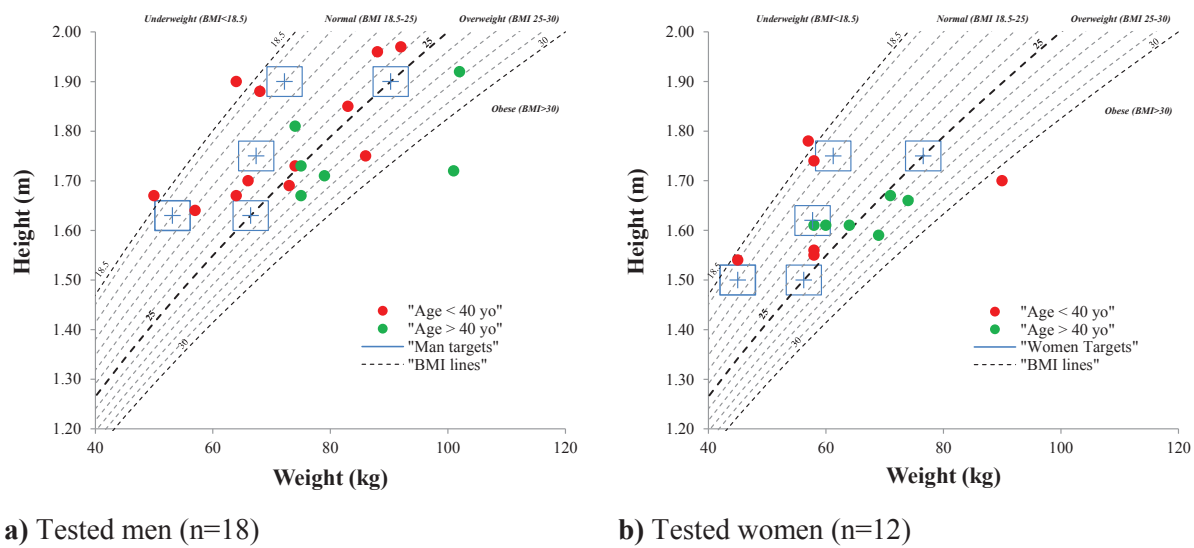


Fig. 29. Distribution of tested subjects compared to the initial targets based upon anthropometry charts (Jürgens et al., 1990).

Table 10. Anthropometric characteristics of volunteers subjected to sled tests.

ID	Gender	Age (yo)	Height (m)	Weight (kg)	BMI (kg/m ²)	Midsternal thickness (mm)
582	M	21	1.90	64	17.8	196
951	F	22	1.78	57	18.0	179
101	M	18	1.67	50	18.1	190
771	F	23	1.54	45	18.7	184
135	M	20	1.88	68	19.2	159
200	F	22	1.74	58	19.3	179
607	M	32	1.64	57	21.1	223
862	F	41	1.61	58	22.2	224
375	M	63	1.81	74	22.6	230
438	M	39	1.70	66	22.9	229
484	F	45	1.61	60	22.9	176
806	M	21	1.96	88	23.1	217
869	M	19	1.67	64	23.1	226
733	M	34	1.97	92	23.6	233
635	F	28	1.56	58	23.8	181
225	M	32	1.85	83	24.2	210
957	F	23	1.55	58	24.5	187
551	F	50	1.61	64	24.7	212
329	M	38	1.73	74	24.8	213
128	M	52	1.73	75	25.1	234
247	F	56	1.67	71	25.5	228
948	M	25	1.69	73	25.6	225
620	M	64	1.71	79	27.0	264
118	M	65	1.67	75	27.0	234
981	F	54	1.66	74	27.1	235
573	F	63	1.59	69	27.3	222
741	M	58	1.92	102	27.7	263
442	M	35	1.75	86	28.0	258
370	F	20	1.70	90	31.1	219
431	M	56	1.72	101	34.1	264

2.4 Conventional instrumentation

The longitudinal deceleration of the sled was recorded by a sled-mounted uniaxial accelerometer.

Load cells were installed on the external and internal ends of the shoulder belt (respectively $FB3$ and $FB4$) and on the lap belt ($FB6$). Maximum value of $FB3$ and $FB4$ are noted $FB3_{max}$ and $FB4_{max}$ respectively.

Reaction forces were measured by 1-axis load cells placed under each footrest and under the seat pan.

Data were acquired at 20 kHz from -3 s to 2 s after the shock and filtered using CFC Butterworth filters according to the standard norm SAE J211.

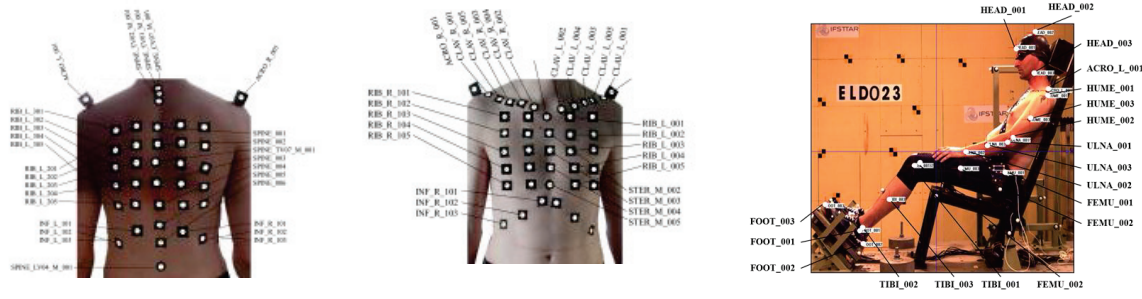
Three markers were placed on the pillar close to seat belt external anchorage points, in order to follow sled displacement.

2.5 3D trajectories of body markers

2.5.1 *Markers definition*

Body markers were placed on volunteer at anatomical landmarks (**Fig. 30**). The subjects were asked to wear light shirt and bra (for women) to facilitate their placement. Markers were placed on the following location:

- Head : nasion, vertex, gonion of the mandible
- Left arm : humerus greater tubercle, lateral epicondyle, middle of the humerus, ulnar styloid process, olecranon posterior face superior border, middle of the ulna,
- Left lower limb : greater trochanter, femoral lateral condyle, middle of the femur, tibia lateral condyle, lateral malleolus, middle of the tibia, lateral malleolus, ankle, anterior extremity of shoes, ball of foot (on shoes)
- Spine : spinous processes of the 7th cervical vertebrae, 1st thoracic vertebrae, 7th thoracic vertebrae, 4th lumbar vertebrae and all along the spine
- Torso: on left and right acromion and clavicles, jugular notch, mid-sternum, xiphoid process and all along the sternum. Additional landmarks were additionally placed 5 cm and 10 cm to the left and right side of chest and on the inferior contour of the ribcage.



a) Back view

b) Front view

c) Lateral view

Fig. 30. Landmarks spread over volunteer during belt loading.

2.5.2 Video recording and reconstruction

Four high speed cameras were positioned around the sled for recording the position of markers placed on subjects and sled at 1000 frames per second (**Fig. 31**). 6 projectors of 10kW were used to light the scene. Time zero was given by a flash visible by all cameras and synchronized with the data acquisition system.

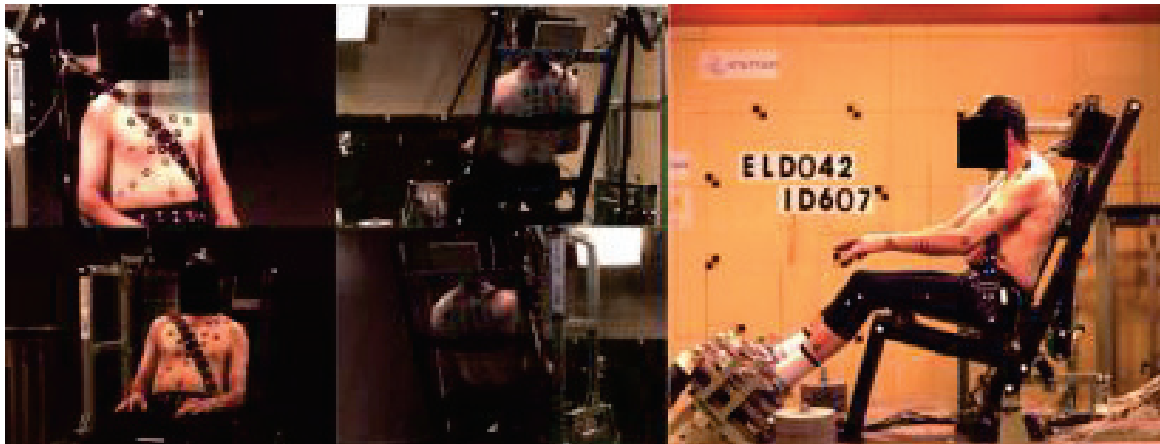


Fig. 31. Overview of camera location and field of view.

The position of each landmark for all cameras was extracted in pixel using MotionTrack® (Vannier Photelc, France). The three dimensional coordinates of the subjects markers were computed using the Direct Linear Transformation method also called stereovision (Abdel-Aziz and Karara, 1971). This method can reconstruct the 3D coordinates (x, y, z) of a point using the 2D coordinates (u, v) collected on two cameras or more (**Fig. 32**).

For each point, each camera introduces a system of two equations (below) to eleven coefficients (also called DLT coefficients) corresponding to the camera position, orientation, and focal length:

$$\begin{cases} u = \frac{L_1x + L_2y + L_3z + L_4}{L_9x + L_{10}y + L_{11}z + 1} \\ v = \frac{L_5x + L_6y + L_7z + L_8}{L_9x + L_{10}y + L_{11}z + 1} \end{cases} \quad \text{Equation II-1}$$

The calculation of these coefficients requires a calibration procedure using an object with a known geometry. Six known markers (6x2 equations) on the object are necessary to calculate the eleven calibration coefficients of each camera. The use of more markers in the object introduces a redundancy that increases the method accuracy. The object used in the tests included 17 spherical markers encompassing a volume of 800x500x400 mm³ (**Fig. 33**). It was positioned in the motion space of the markers of the chest subject during shock. The 3D position of each sphere was measured in a laboratory coordinate system with a standard deviation accuracy of $\pm 50 \mu\text{m}$ using an articulated measuring arm FaroArm®. The object was filmed simultaneously by the four cameras. DLT was applied between (u,v) image coordinates system and (x,y,z) laboratory coordinates system in order to calculate the DLT coefficients for each camera.

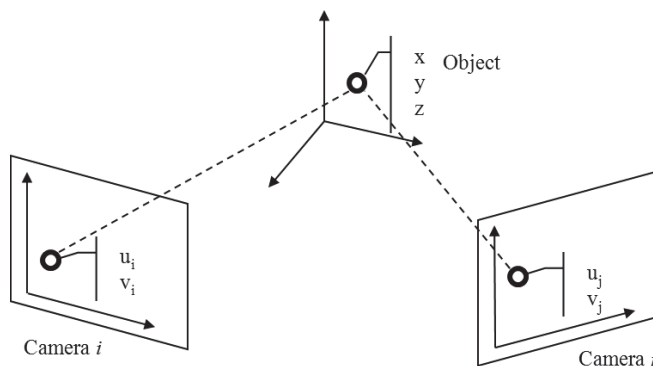


Fig. 32. Reconstruction of an object in space from the images taken by several cameras. Adapted from (Compigne et al., 2004).

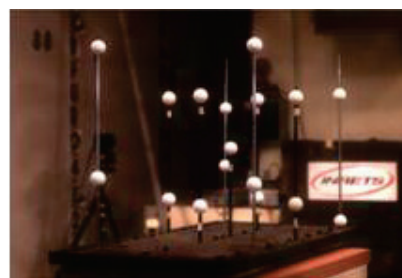


Fig. 33. Calibration of the sled scene with the calibration object.

Then, the determination of the position (x, y, z) of any landmark in the laboratory coordinates system implied the images of two cameras (u, v) and was resolved for each frame by the redundant system below:

$$\begin{bmatrix} L_1^1 - L_9^1 u_1 & L_2^1 - L_{10}^1 u_1 & L_3^1 - L_{11}^1 u_1 \\ L_5^1 - L_9^1 v_1 & L_6^1 - L_{10}^1 v_1 & L_7^1 - L_{11}^1 v_1 \\ L_1^2 - L_9^2 u_2 & L_2^2 - L_{10}^2 u_2 & L_3^2 - L_{11}^2 u_2 \\ L_5^2 - L_9^2 v_2 & L_6^2 - L_{10}^2 v_2 & L_7^2 - L_{11}^2 v_2 \end{bmatrix} \begin{bmatrix} x \\ y \\ z \end{bmatrix} = \begin{bmatrix} u_1 - L_4^1 \\ v_1 - L_8^1 \\ u_2 - L_4^2 \\ v_2 - L_8^2 \end{bmatrix} \quad \text{Equation II-2}$$

Accuracy of the optical method was assessed in [Appendix 1](#). 3D trajectories were filtered at CFC-60 Butterworth.

2.5.3 Trajectories interpolation

Anatomical landmarks were obstructed from view during some frames during the test, and thus, the 3D reconstruction by stereovision was not possible during these frames. In these cases, two methods were investigated to estimate the missing part of the marker trajectory. First method was a time-based interpolation, based upon cubic interpolation of the anterior and posterior frames available. Second method was a geometrical-based interpolation, based on dual-kriging method (Krige, 1951) using other landmarks available at the same frame.

The two methods were assessed on a known mid-sternum (*STER_M_003*) trajectory during which 30 successive frames were deliberately hidden. The reconstructed MS trajectories were directly used in the computation of mid-sternum deflection. [Fig. 34](#) shows the comparison of the sternal deflections computed from the reference mid-sternum (*STER_M_003*) trajectory and from the interpolated ones. The second method appeared more suitable since numerous successive frames interpolation could be applied without loss of the deflection peak pattern.

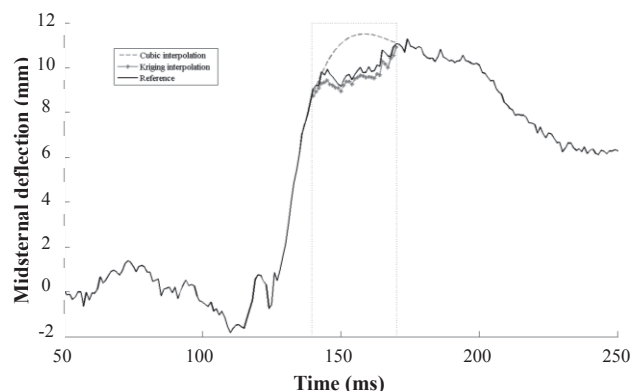


Fig. 34. Comparison of different methods of interpolations of mid-sternum landmark trajectory for the computation of mid-sternum deflection.

2.6 Data analysis

2.6.1 Thoracic coordinates system

A thoracic coordinate system was defined as Ot , Xt , Yt , Zt :

- Ot : The origin coincident with *SPINE_TV01_M_001*
- Zt : The line connecting *SPINE_TV01_M_001* and *SPINE_TV07_M_001*, pointing downward.
- xt : The line connecting *SPINE_TV01_M_001* to the jugular notch (*STER_M_001*), pointing forward
- Yt : The common line perpendicular to the Zt and xt -axis, pointing to the right.
- Xt : The common line perpendicular to the Yt and Zt -axis, pointing to forward.

In this local system, Xt , Yt and Zt correspond respectively to the antero-posterior axis, to the lateral axis and the crano-caudal one.

Mid-sternum trajectories were computed in the antero-posterior – crano-caudal plane Xt - Zt , (saggital plane) in order to follow its excursion. An antero-posterior excursion Δ_{AP} was calculated as the position variation between initial mid-sternum Xt -axis coordinate and the extreme one. $\%_{AP}$ was defined as the ratio of Δ_{AP} to the mid-sternum thickness. Similarly, in the crano-caudal direction, Δ_{CC} and $\%_{CC}$ were calculated in the Zt -axis coordinate.

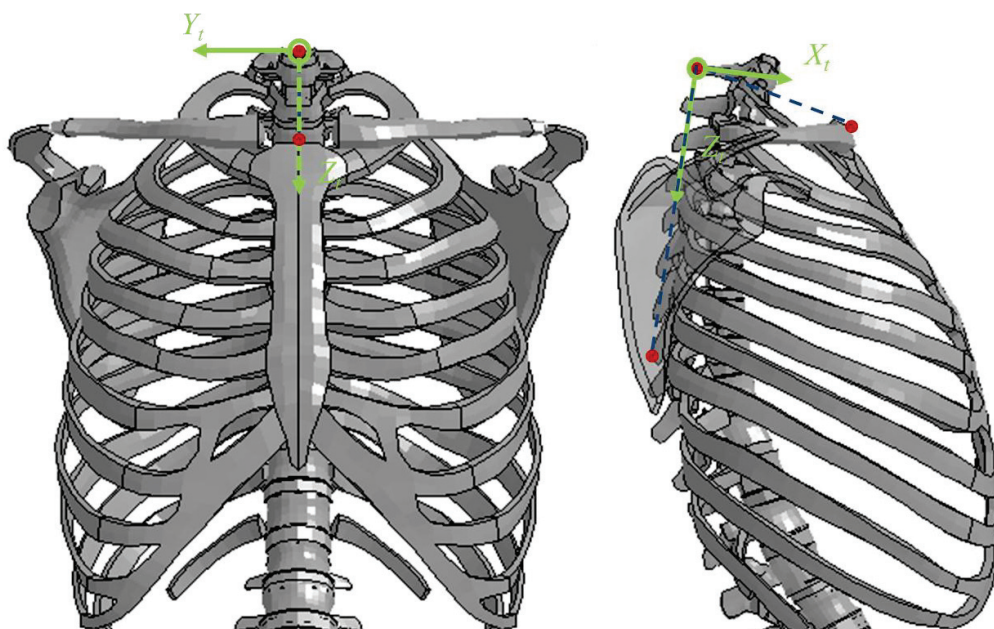


Fig. 35. Definition of the thoracic coordinates system used in sled tests.

2.6.2 Mid-sternum deflection and compression

The mid sternal deflection D was calculated as the distance variation between markers placed at mid-sternum (*STER_M_003*) and the 7th thoracic vertebra spinous process of the subject (*SPINE_TV07_M_001*). The initial zero of deflection was defined as the mid-sternum thickness measured after reaching 5% of the maximum value of external shoulder belt load (see mid-sternum thickness in **Table 10**). Mid-sternum compression C was defined as the ratio of the mid sternal deflection to the mid-sternum thickness. Maximum values of D and C are noted D_{max} and C_{max} respectively.

2.6.3 Resulting shoulder belt load

Resulting shoulder belt force F_{Res} is defined in **Equation II-3** as a combination of the external shoulder belt load F_{B3} , the internal shoulder belt load F_{B4} and the angle made by the belt α calculated using the extreme markers of the belt. This parameter F_{Res} was already used in a recent study (Eickhoff et al., 2011). A time-interpolation of F_{B3} and F_{B4} was performed for combining angles values and loads values. Maximum value of F_{Res} is noted F_{Resmax} .

$$F_{Res} = \sqrt{F_{B3}^2 + F_{B4}^2 - 2 \times F_{B3} \times F_{B4} \cos(\pi - \alpha)} \quad \text{Equation II-3}$$

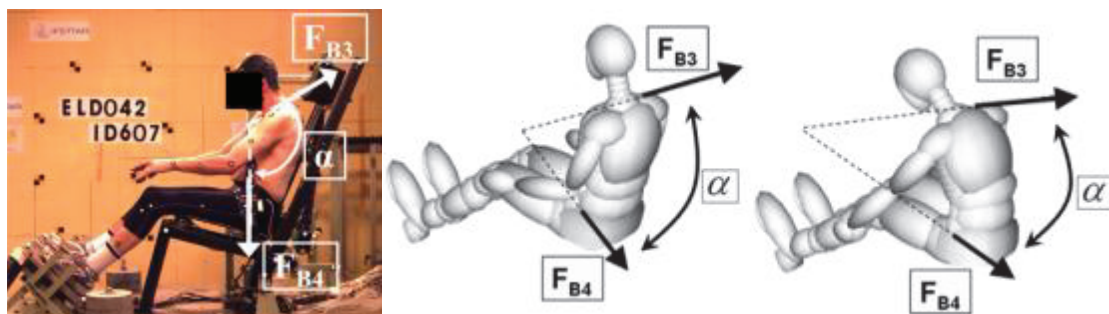


Fig. 36. Computation of the resulting shoulder belt load F_{Res} (adapted from Eickhoff et al., 2011).

2.6.4 Force-deflection corridor

Force-deflection curves of each volunteer were built using F_{Res} and mid-sternum deflection D . Force versus deflection response corridors were generated using the two-dimensional standard deviation ellipse (Shaw et al., 2006). At each point in time, the mean force can be plotted versus the mean deflection. At each point the two-dimensional standard deviation ellipse can also be plotted using **Equation II-4**. The result is Mean force versus deflection curve and a graphical representation of the two-dimensional variance at each point.

$$k^2 = \frac{(f - \bar{f})^2}{\sigma_f^2} + \frac{(d - \bar{d})^2}{\sigma_d^2}$$
Equation II-4

where $k^2 = 1$ for the one standard deviation ellipse.

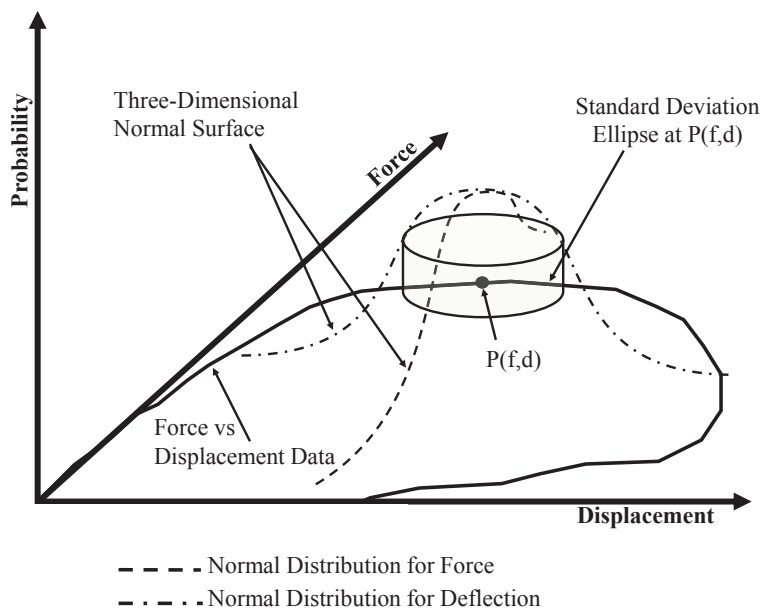


Fig. 37. Standard deviation ellipse on force-deflection curve
(adapted from Shaw et al., 2006).

2.6.5 Force-deflection stiffness and mathematical model

Dynamic Stiffness (DS) was computed as the interpolated ratio of the resulting shoulder belt load force $FRes$ over the mid-sternum deflection D before $FRes_{max}$ was reached. Effective Stiffness (ES) was computed from the ratio of $FRes$ over mid-sternal deflection D when D_{max} was reached (Kent et al., 2005; Sandoz et al., 2009). While DS represents the thoracic behaviour during the beginning of the load, ES represents its behaviour without taking account of this part. Both stiffness definitions are shown in **Fig. 38**.

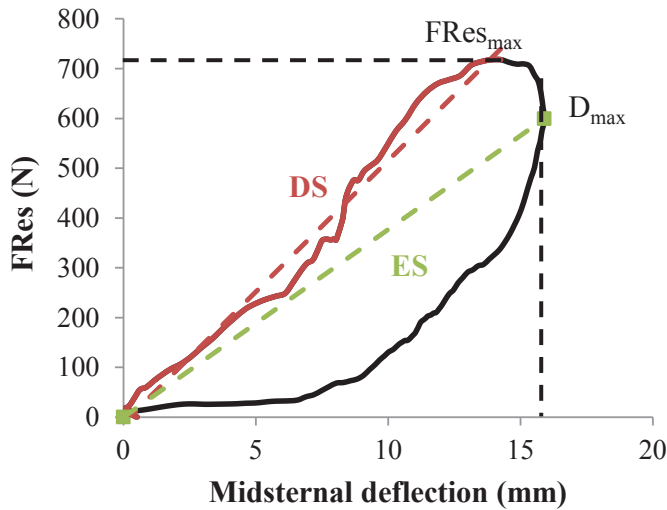


Fig. 38. Definition of Dynamic Stiffness (DS) and Effective Stiffness (ES) on experimental force-deflection curve.

In addition a spring-dashpot-model of the thorax was identified on the force-deflection curves. The model is of the following form:

$$F_{Res}(t) = K \times D(t) + \mu \times V(t) \quad \text{Equation II-5}$$

where K and μ are respectively the linear stiffness and the damping extract from the model; $D(t)$ and $V(t)$ are the mid-sternum deflection and the rate of mid-sternum deflection respectively.

F_{Res} was considered as reference and the differential equation above was resolved with a Runge-Kutta method. K and μ were optimized for each test to minimize the difference between calculated mid-sternum deflection and the experimental one. A least-square errors criterion J was used for the optimisation:

$$J = \min \left(\sum_{t_0}^{t_{end}} (D_{exp} - D_{model})^2 \right) \quad \text{Equation II-6}$$

where t_0 and t_{end} correspond to the time when $F_{Res} \geq \frac{5}{100} \times F_{Res_{max}}$.

2.6.6 Statistics

The statistical analysis was carried out on thoracic mechanical response quantities (**Table 11**) with the package Statistical Toolbox of Matlab. Numerical values were given as mean \pm standard deviation (SD). Age and BMI groups were compared with permutation Student t-test. Comparisons were considered as significant for $p < 0.05$.

In addition, a principal component analysis (PCA) was applied on a reduced dataset extract from in-vivo experiments. This dataset is constituted of variables (C_{max} , K , and so on) and observations (subjects). Prior to the treatment, dataset were standardized as the variables were in different units.

PCA is an orthogonal linear transformation that transforms the data to a new coordinate system. The coordinates of this new coordinate system, termed the principal components are sorted according to the greatest variance (that is, accounts for as much of the variability in the data as possible). In many situations, the first few principal components are able to represent a large percentage of the variability in the variables.

We selected a number of principal components so that the cumulative variance was up to 80 %. Thus, each principal component will be constructed from linear combinations of the variables. For each principal component, the most contributory variables, i.e. with the highest coefficients, are the "marker variables" of the component and give sense to it.

PCA also projects the observations towards the new coordinate system defined by the selected principal components. 2-D plots are used to examine the observations onto the selected principal components.

Agglomerative hierarchical clustering method (AHC) was applied on the PCA dataset. AHC uses a "bottom up" approach: it begins by placing each observation in a separate cluster and then combining clusters based on their distance from each other. The Euclidian distance procedure was used for measuring the distance between two items because it is invariant against transformations of the coordinates. The process continues until the desired number of clusters is formed. The Ward's method also termed Ward's minimum variance criterion was used to agglomerate clusters by minimizing the total within-cluster variance. Ward's method always gives the best clustering results with PCA-data and Euclidian distance.

3. Results

3.1 Definition of an individual thoracic mechanical response

Two sled tests were performed for each volunteer. The force-deflection responses obtained in these two successive tests were found significantly different. The results of the test for which the highest D_{max} was measured, was only considered. Thoracic mechanical characteristics for each volunteer are synthetized in **Table 11**. Mean values for different age and BMI groups are synthetized in **Table 12**.

3.2 Comparison with literature

The pulse applied in the present study is similar to the one applied on 5 men close to 50th percentile subjected to sled test (Kemper et al., 2011). In this study, volunteers were asked to adopt a relaxed state in one test and a braced state in the other. As bracing effect have significant effect on thoracic mechanical response obtained by Kemper et al. (2011) we selected only their corridor of thoracic mechanical response corresponding to the relaxed state.

From our side, we selected 3 men (ID: 329, 128, 375) close to 50th percentile (age: 51 ± 12.5 yo; height: 1.76 ± 0.05 m, weight: 74.3 ± 0.58 kg) and we developed a corridor of midsternum compression. Our 50th percentile male corridor was compared to the corridor obtained by Kemper in **Fig. 39**. Mean midsternal compression peak C_{max} was similar in both studies (7.4% vs. 8%) even if mid-sternum compressions in the present study rose and dropped slower due to the difference in deceleration pulse characteristics, (4 g, 8 kph vs. 5 g, 9.7 kph).

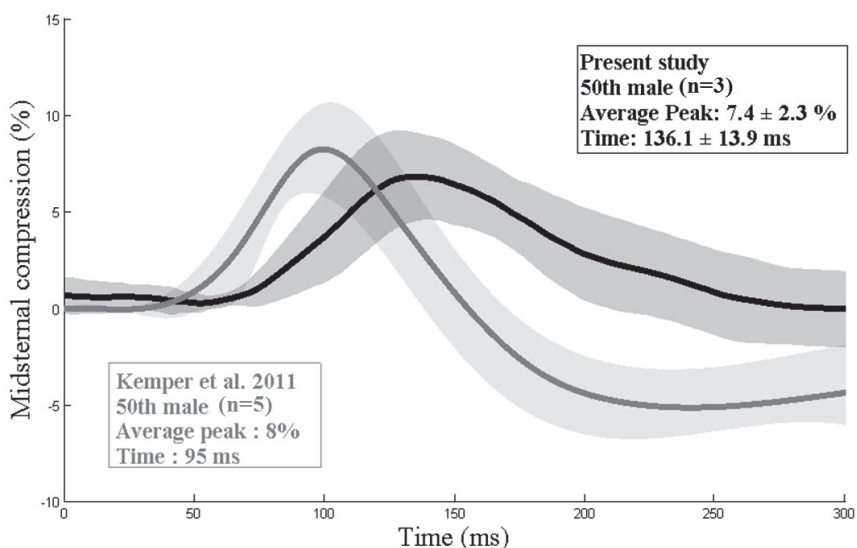


Fig. 39. Comparison of mid-sternum compression corridors for 50th percentile male from the present study ($n=3$) and Kemper et al. (2011; $n=5$).

Table 11. Thoracic mechanical characteristics dataset obtained from in vivo sled tests.

ID	FB3_{max} (N)	FB4_{max} (N)	FB6_{max} (N)	FRes_{max} (N)	Foot_{max} (N)	Seat_{max} (N)	D_{max} (mm)	Thickness (mm)	C_{max} (%)	ΔAP (mm)	ΔCC (mm)	%AP (%)	%CC (%)	ES (N/m)	DS (N/m)	K (N/m)	μ (Ns/m)
582	858	922	986	495	887	1140	10.4	196	5.3%	10.9	4.7	5.6%	2.4%	26053	54412	16681	1325
951	730	880	760	582	972	1005	15.8	179	8.8%	34.6	11.1	19.4%	6.2%	10426	56304	7773	1385
101	770	892	712	337	796	801	16.2	190	8.6%	23.6	10.0	12.5%	5.3%	17377	21600	12709	373
771	760	662	447	544	914	795	14.5	184	7.9%	24.0	18.8	13.0%	10.2%	21838	27309	36628	546
135	949	983	635	600	1152	1237	9.7	159	6.1%	9.5	18.2	6.0%	11.4%	29809	124813	31461	2241
200	560	669	684	357	1049	1086	12.5	179	7.0%	30.1	11.6	16.9%	6.5%	13301	89407	15146	1181
607	616	682	433	417	1030	737	22.4	223	10.0%	31.3	18.9	14.0%	8.4%	16627	62325	13910	326
862	803	860	449	609	900	1133	12.1	224	5.4%	22.3	26.7	9.9%	11.9%	28785	59071	38044	913
375	1362	1177	758	776	1277	1858	13.4	230	5.9%	17.0	18.0	7.4%	7.8%	32053	76074	43390	977
438	1340	1098	892	929	1163	1274	8.6	229	3.7%	20.4	23.8	8.9%	10.4%	58706	122877	56753	2431
484	994	659	689	666	1131	1011	9.2	176	5.2%	30.1	23.5	17.1%	13.3%	67632	83763	93060	830
806	986	1113	529	526	1275	1392	14.1	217	6.5%	24.1	23.2	11.1%	10.7%	30936	46151	46416	1000
869	1036	911	477	547	879	822	16.4	226	7.3%	22.2	11.0	9.8%	4.9%	15974	54400	20396	872
733	1288	1439	909	558	850	1582	12.9	233	5.5%	18.6	18.0	8.0%	7.7%	7295	73051	9351	1969
635	867	948	549	606	709	1177	13.0	181	7.2%	15.6	20.0	8.6%	11.1%	15377	82145	11183	1481
225	883	1023	560	544	1288	1251	10.7	210	5.1%	16.1	8.0	7.7%	3.8%	29950	68926	51430	1137
957	1090	1126	913	721	869	1438	22.5	187	12.0%	32.5	27.4	17.4%	14.7%	14287	40866	20635	656
551	953	863	587	692	1096	1448	14.2	212	6.6%	20.9	25.0	9.9%	11.8%	26100	118094	41466	1695
329	1045	1121	705	602	1042	1813	11.7	213	5.5%	22.8	9.1	10.7%	4.3%	37737	42878	37761	991
128	1189	1112	733	781	1249	1401	14.4	234	6.1%	21.4	28.0	9.1%	11.9%	47366	50642	52276	245
247	975	972	686	614	1173	1658	10.9	228	4.8%	25.9	27.5	11.4%	12.1%	43211	74219	61773	1038
948	1092	1138	546	821	1048	982	23.3	225	10.4%	21.5	18.2	9.6%	8.1%	24971	42829	24689	593
620	1060	995	803	682	1303	1925	16.6	264	6.3%	24.5	5.6	9.3%	2.1%	8837	38554	15893	1421
118	1067	1253	641	726	824	1254	16.7	234	7.2%	30.3	23.6	13.0%	10.1%	36879	47176	29488	730
981	1116	964	711	770	1223	1362	12.3	235	5.2%	20.8	13.7	8.9%	5.8%	14920	79466	28740	1948
573	951	667	460	638	1282	1617	11.2	222	5.0%	27.1	30.0	12.2%	13.5%	12618	110372	17667	2524
741	1580	881	972	1148	1995	1781	14.3	263	5.4%	18.5	25.2	7.0%	9.6%	21586	154143	7773	3914
442	856	930	396	582	1082	1111	26.5	258	10.3%	56.5	37.7	21.9%	14.6%	15796	31423	17628	362
370	1181	1588	897	884	1028	1980	19.5	219	8.9%	41.3	24.8	18.9%	11.3%	33890	54337	13442	403
431	1192	662	857	828	1525	1726	10.3	264	3.9%	30.8	29.3	11.6%	11.1%	38376	123302	56689	2393

Table 12. Thoracic mechanical characteristics dataset from in vivo sled tests: different age and BMI groups.

	FB3_{max} (N)	FB4_{max} (N)	FB6_{max} (N)	FRes_{max} (N)	Foot_{max} (N)	Seat_{max} (N)	D_{max} (mm)	Thickness (mm)	C_{max} (%)	ΔAP (mm)	ACC (mm)	%AP (%)	%CC (%)	ES (N/m)	DS (N/m)	K (N/m)	μ
Non overweight subjects (BMI < 25 kg/m ² , n=19)																	
Mean	942	949	667	585	1015	1211	13.7	203	6.80%	22.5	17.2	11.30%	8.60%	26330	68656	31800	1175
SD	223	204	172	140	171	324	3.8	23	2.00%	7	6.9	4.10%	3.50%	15494	29824	21411	586
c _v	0.24	0.21	0.26	0.24	0.17	0.27	0.28	0.11	0.29	0.31	0.40	0.36	0.41	0.59	0.43	0.67	0.50
Overweight subjects (BMI ≥ 25 kg/m ² , n=11)																	
Mean	1114	1015	700	770	1248	1527	16	241	6.70%	29	24	12.10%	10.00%	27132	73315	29642	1416
SD	187	262	181	158	307	329	5.3	18	2.20%	11.1	8.7	4.50%	3.60%	13392	39867	18759	1162
c _v	0.17	0.26	0.26	0.21	0.25	0.22	0.33	0.07	0.33	0.38	0.36	0.37	0.36	0.49	0.54	0.63	0.82
Young subjects (Age < 40 yr, n=18)																	
Mean	939	1007	668	592	1002	1201	15.6	206	7.60%	25.3	17.5	12.20%	8.40%	23353	60892	24666	1071
SD	215	240	189	161	158	345	5.2	25	2.20%	11.3	8.2	4.90%	3.60%	12336	29069	15155	646
c _v	0.23	0.24	0.28	0.27	0.16	0.29	0.33	0.12	0.29	0.45	0.47	0.40	0.43	0.53	0.48	0.61	0.60
Older subjects (Age ≥ 40 yr, n=12)																	
Mean	1103	922	695	744	1248	1514	13	232	5.60%	24.1	23	10.60%	10.10%	31530	84573	40522	1552
SD	208	198	151	145	299	292	2.4	25	0.90%	4.7	7.2	2.70%	3.30%	16654	35231	23527	1015
c _v	0.19	0.21	0.22	0.19	0.24	0.19	0.18	0.11	0.16	0.20	0.31	0.25	0.33	0.53	0.42	0.58	0.65
All subjects (n=30)																	
Mean	1005	973	679	653	1100	1327	14.5	216	6.80%	24.8	19.7	11.60%	9.10%	26624	70364	31008	1263
SD	224	225	173	170	252	356	4.5	28	2.00%	9.1	8.2	4.20%	3.50%	14526	33247	20174	832
c _v	0.22	0.23	0.25	0.26	0.23	0.27	0.31	0.13	0.29	0.37	0.42	0.36	0.38	0.55	0.47	0.65	0.66
Min	560	659	396	337	709	737	8.6	159	3.70%	9.5	4.7	5.60%	2.10%	7295	21600	7773	245
Max	1580	1588	986	1148	1995	1980	26.5	264	12.00%	56.5	37.7	21.90%	14.70%	67632	154143	93060	3914

3.3 Comparison of thoracic mechanical response from different age and BMI groups

3.3.1 Seat belt loads

Time histories of the seat belt for each age and BMI group are shown in **Fig. 40**, **Fig. 41**, **Fig. 42** and **Fig. 43**. Maximum belt loads, for each group, are presented in **Fig. 45**. As expected, maximum belt loads were linked to maximum subjects weights. The maximum reaction forces also increase with subject mass.

No significant difference were found in $FB4_{max}$, $FB6_{max}$ between overweight subjects ($BMI \geq 25 \text{ kg/m}^2$, $n=11$) and normal ones ($BMI < 25 \text{ kg/m}^2$, $n=19$). Mean $FB3_{max}$ was significantly higher ($p=0.03$) for overweight subjects than for the subjects in the normal group. Mean $FRes_{max}$ was significantly higher ($p<0.02$) for overweight subjects than for the subjects in the normal group. Maximum resultant shoulder load peak $FRes_{max}$ of the overweight volunteers was higher by about 30% than the normal ones.

No significant difference were found in $FB4_{max}$, $FB6_{max}$ between older subjects ($Age \geq 40 \text{ yr}$, $n=12$) and young ones ($Age < 40 \text{ yr}$, $n=18$). Mean $FB3_{max}$ and $FRes_{max}$ were significantly higher ($p=0.047$; $p<0.02$) for older subjects than for young group. Maximum resultant shoulder load peak $FRes_{max}$ of the older volunteers was higher by about 25% than the young ones.

3.3.2 Mid-sternum compressions

Time histories of mid-sternum compressions for BMI and aged groups are shown in **Fig. 44**. Boxplots of maximum mid-sternum deflection peak D_{max} and compression peak C_{max} are shown in **Fig. 46**.

There are no significant differences between overweight subjects ($BMI \geq 25 \text{ kg/m}^2$, $n=11$) and normal subjects ($BMI < 25 \text{ kg/m}^2$, $n=19$) in D_{max} ($p=0.31$) nor C_{max} ($p=0.57$).

There are no significant differences between older subjects ($Age \geq 40 \text{ yr}$, $n=12$) and young subjects ($Age < 40 \text{ yr}$, $n=18$) in D_{max} ($p=0.11$). Mean C_{max} was significantly different for young subjects than for older group ($p<0.01$); C_{max} for the older volunteers was lower by about 27% than the young ones.

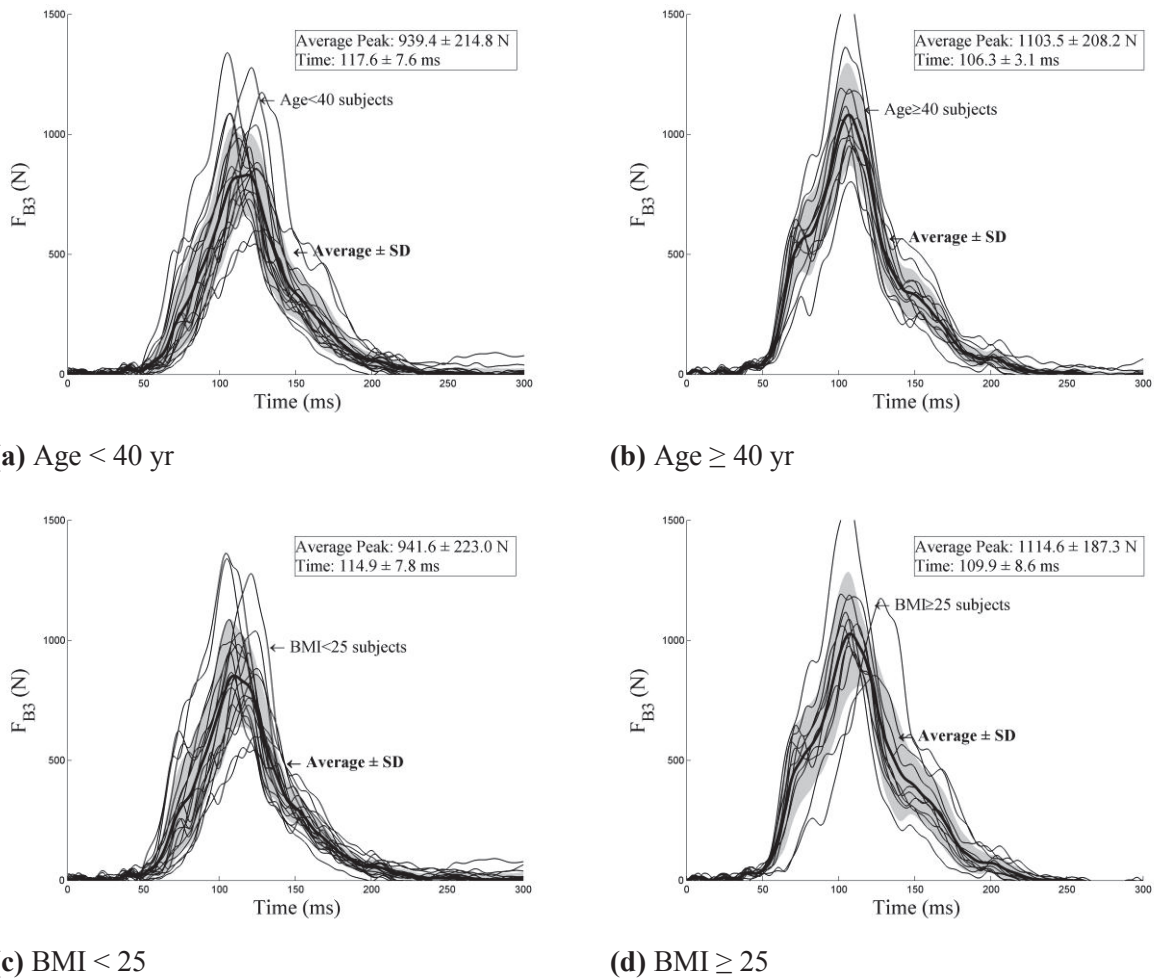
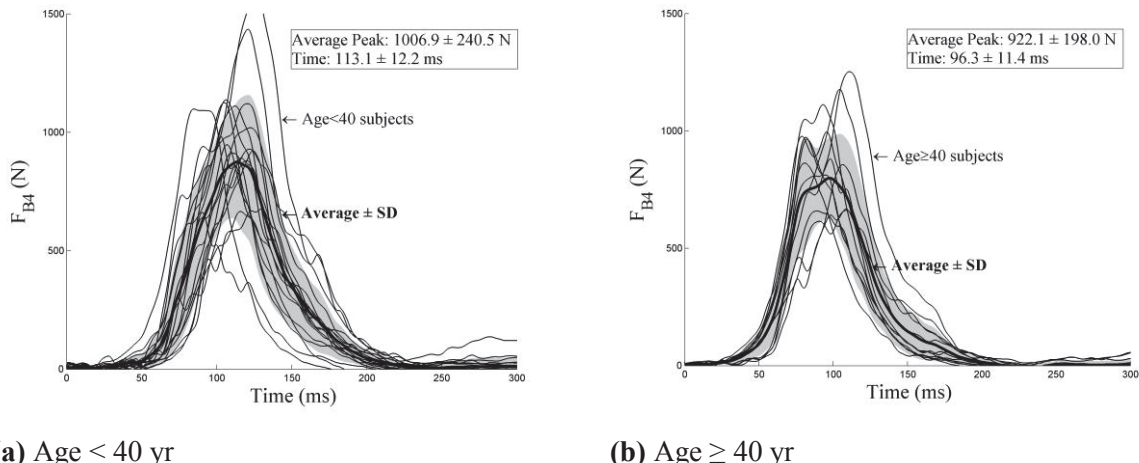
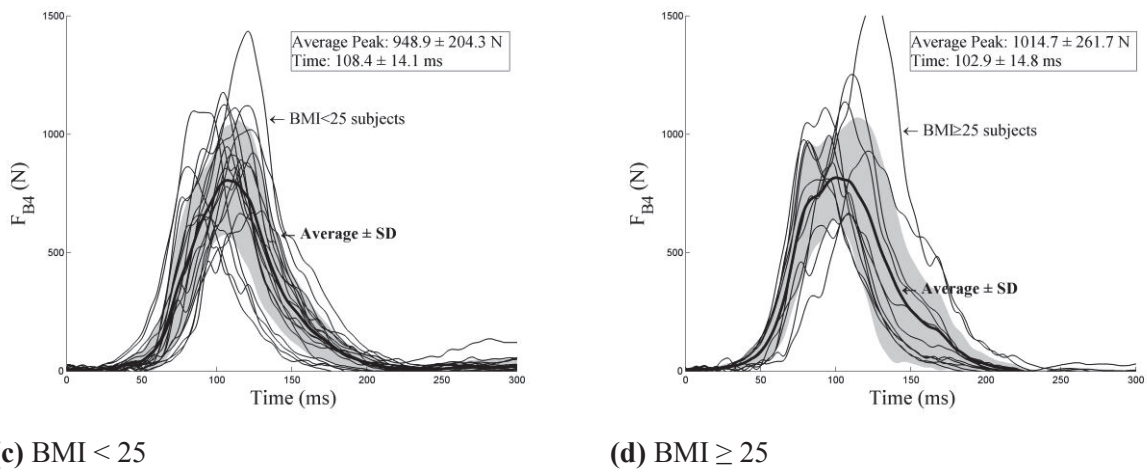


Fig. 40. Time history of the external shoulder belt force F_{B3} for age group and BMI group.

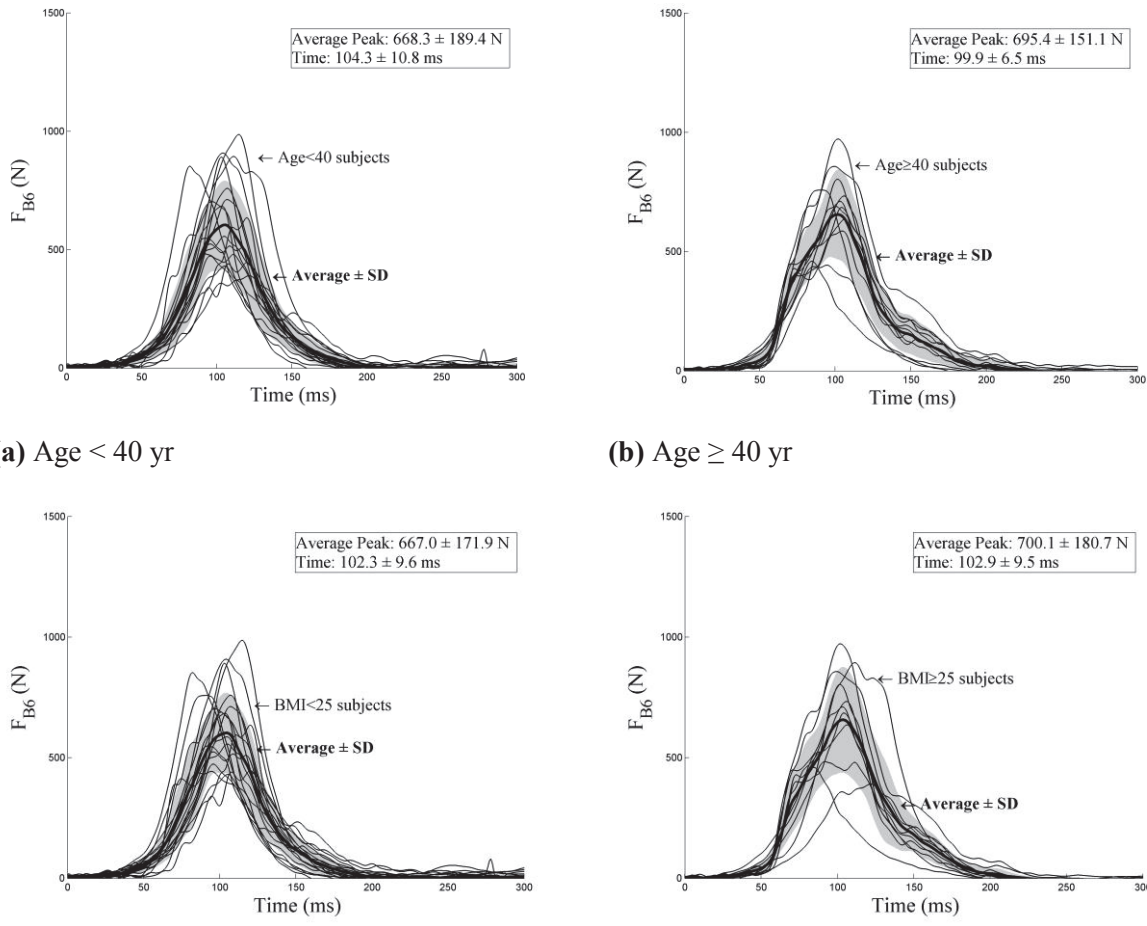




(c) $BMI < 25$

(d) $BMI \geq 25$

Fig. 41. Time history of the lower shoulder belt force $FB4$ for age group and BMI group.



(a) $Age < 40$ yr

(b) $Age \geq 40$ yr

(c) $BMI < 25$

(d) $BMI \geq 25$

Fig. 42. Time history of the lap belt force $FB6$ for age group and BMI group.

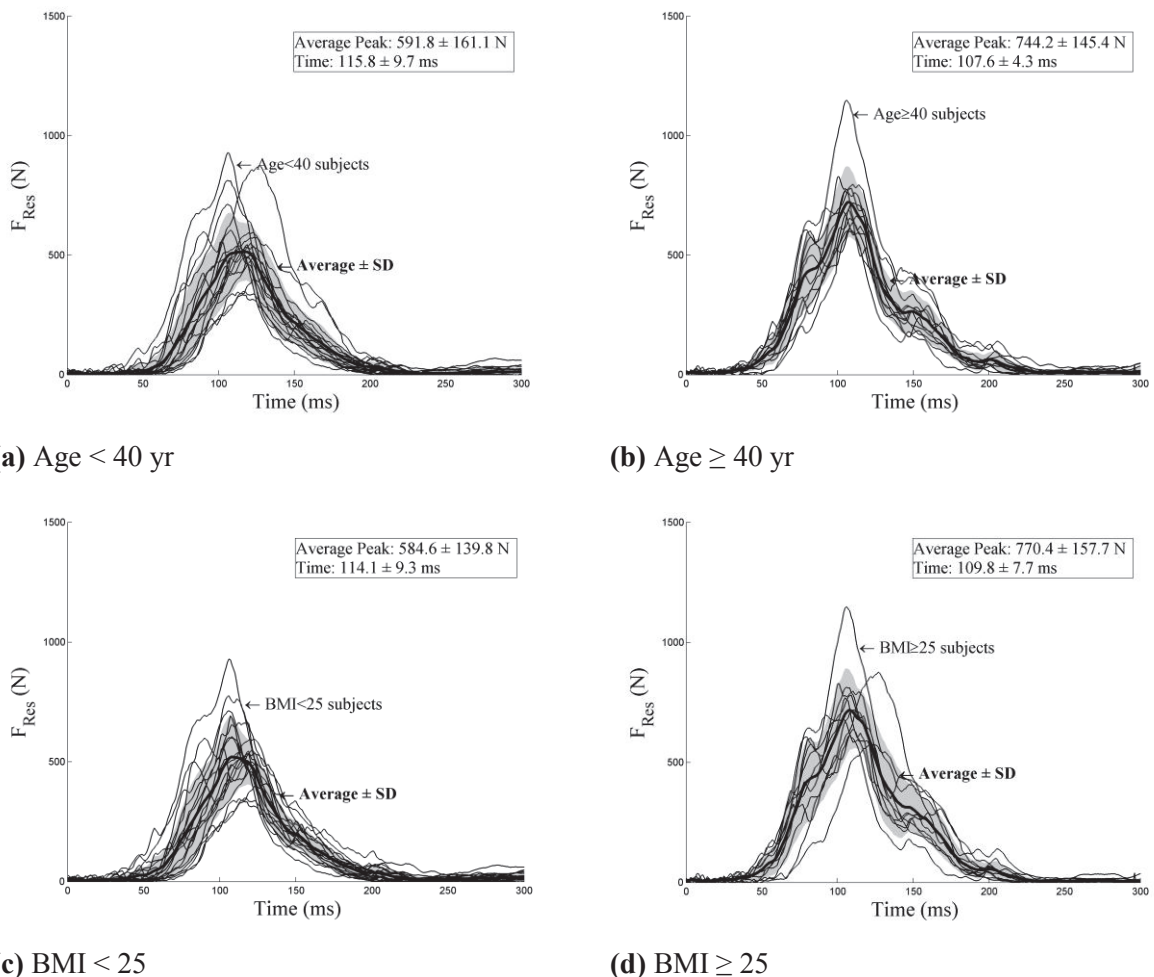
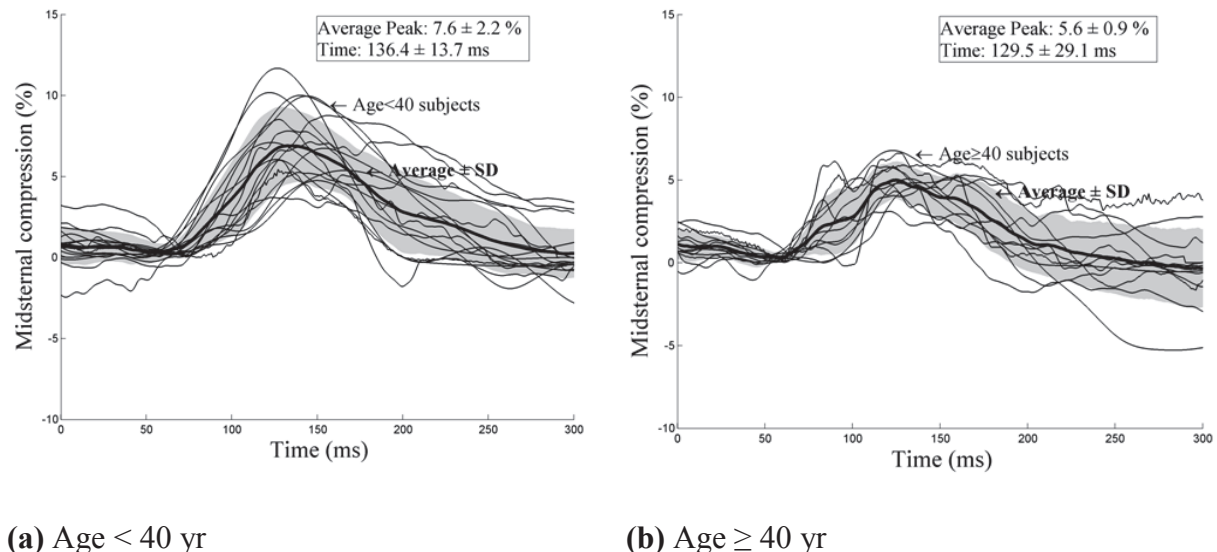


Fig. 43. Time history of the resultant shoulder belt force F_{Res} for age group and BMI.



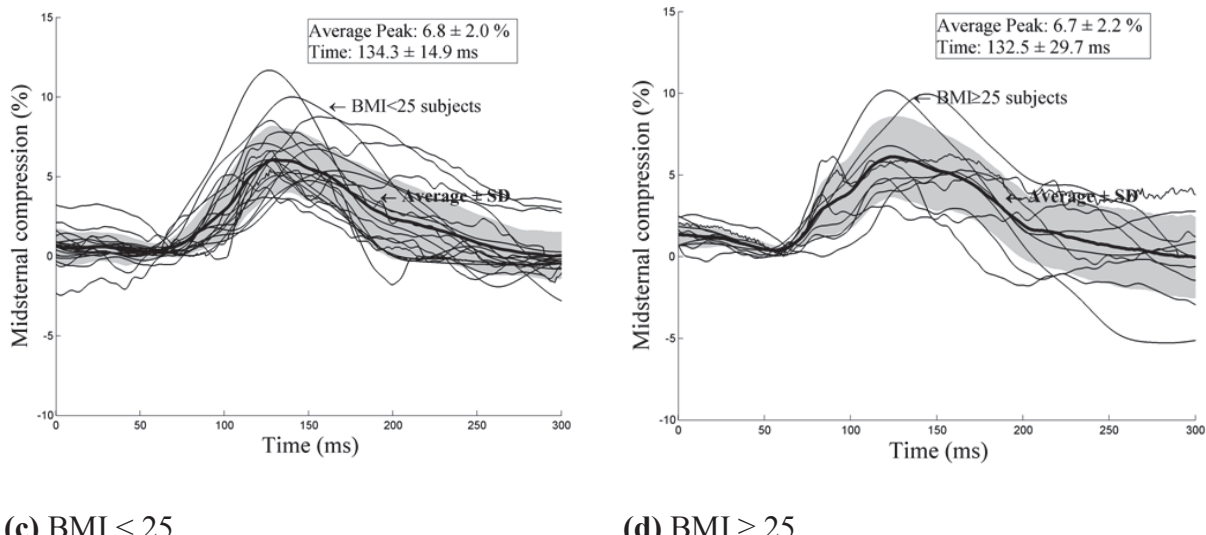


Fig. 44. Time history of mid-sternum compressions for different age and BMI groups.

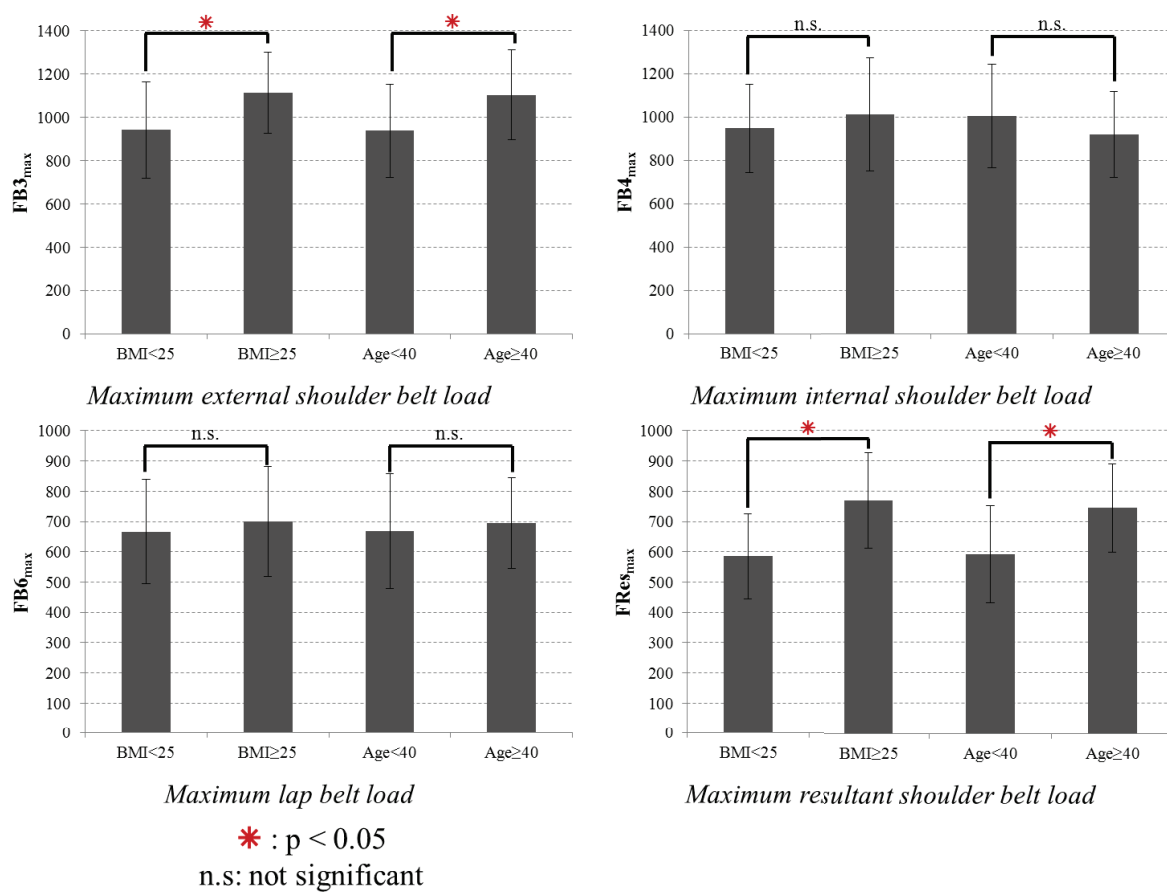


Fig. 45. Maximum belt loads for different age and BMI groups.

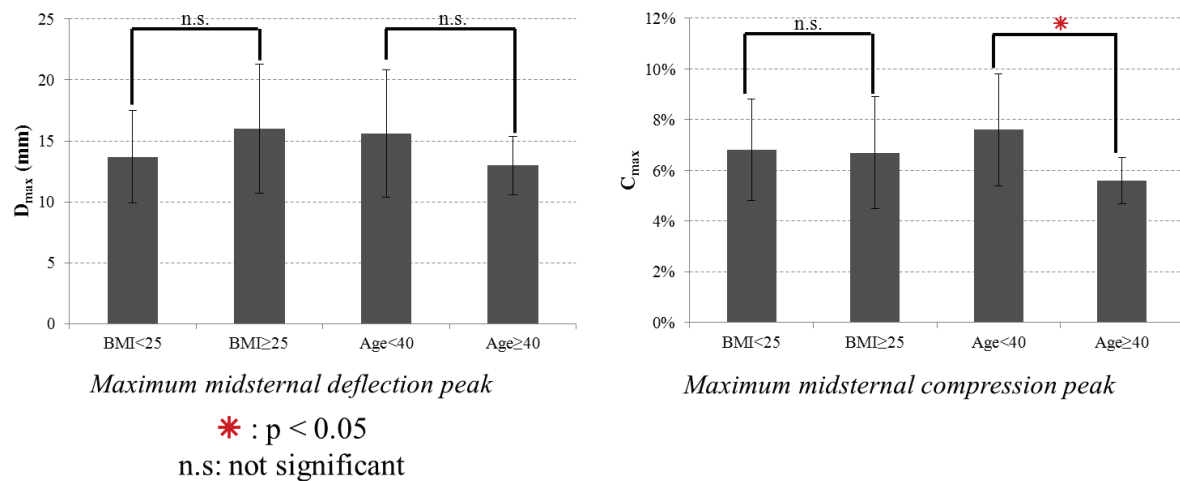


Fig. 46. Maximum compression for different age and BMI groups.

3.3.3 Mid-sternal trajectories in sagittal plane

Generally, mid-sternal landmark tends to move along the posterior direction and along the cranial direction during the shock. Relative trajectories of mid-sternal in saggital plane for the different age and BMI groups are shown in **Fig. 47**. Boxplots of maximum antero-posterior excursions ΔAP and craniocaudal excursion ΔCC and relative ones $\%AP$ and $\%CC$ are shown in **Fig. 48**.

Mean ΔCC was significantly higher for overweight subjects than for normal subjects ($p=0.03$). Thus, maximum crano-caudal excursion for the overweight volunteers was higher by about 40% than the normal ones. There are no significant differences between overweight subjects and normal ones in maximum antero-posterior excursion ΔAP ($p=0.058$), in relative antero-posterior excursion $\%AP$ ($p=0.61$) and relative crano-caudal excursion $\%CC$ ($p=0.21$).

There are no significant differences between young subjects and older subjects in ΔAP ($p=0.73$), in ΔCC ($p=0.07$), in relative antero-posterior excursion $\%AP$ ($p=0.29$) and relative crano-caudal excursion $\%CC$ ($p=0.22$).

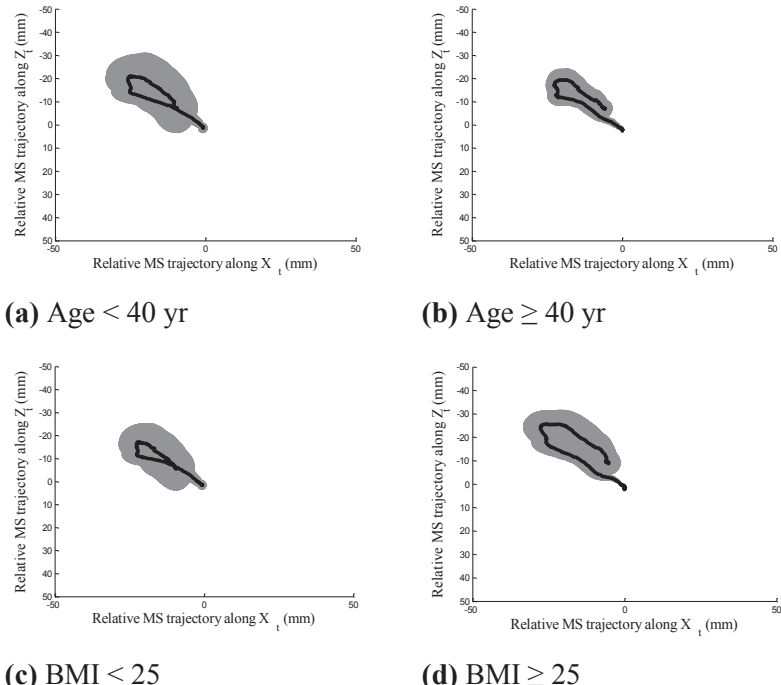


Fig. 47. Comparison of sternal relative trajectories in sagittal plane for age and BMI group.

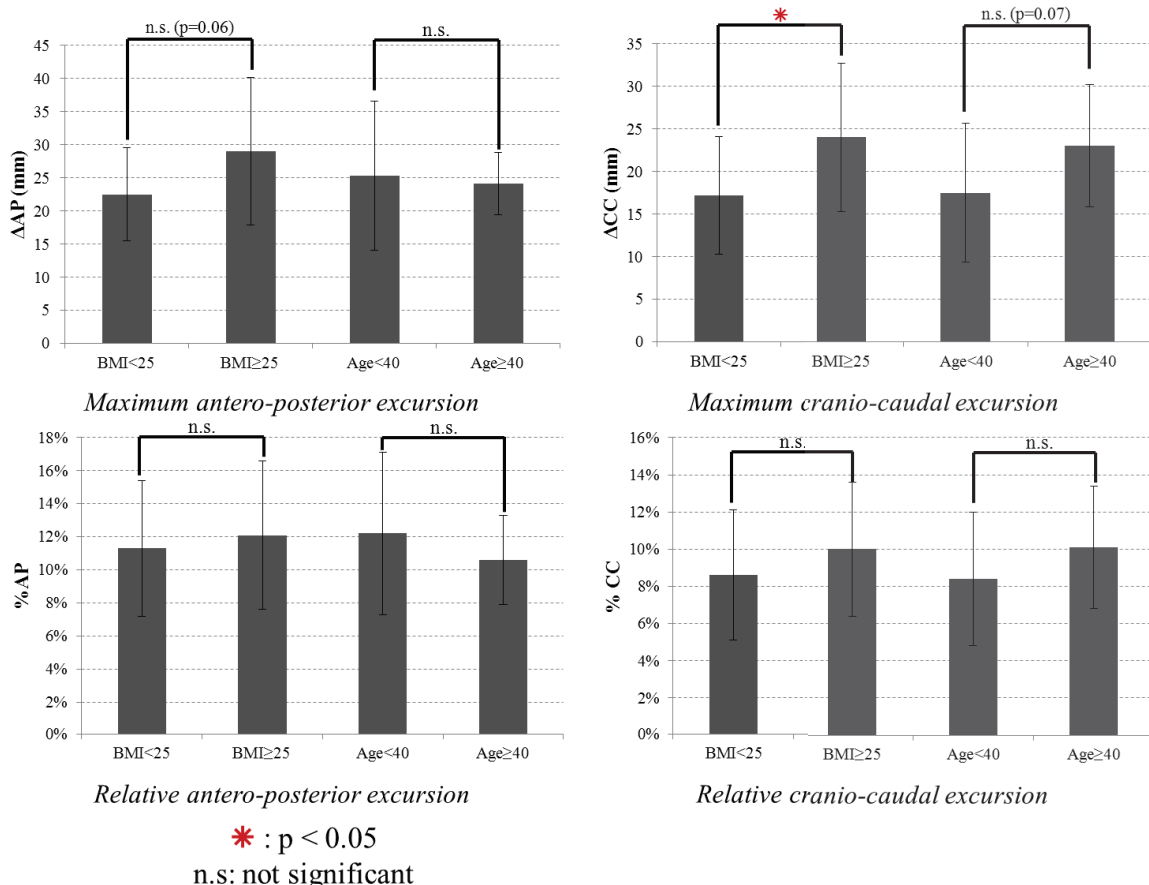


Fig. 48. Maximum sagittal excursion for different age and BMI groups.

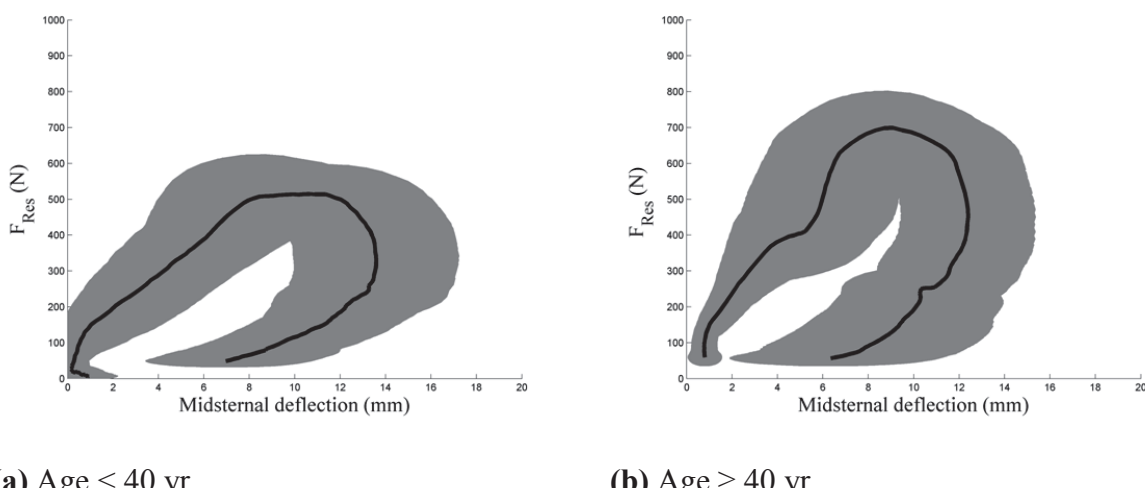
3.3.4 Force-deflection characteristics

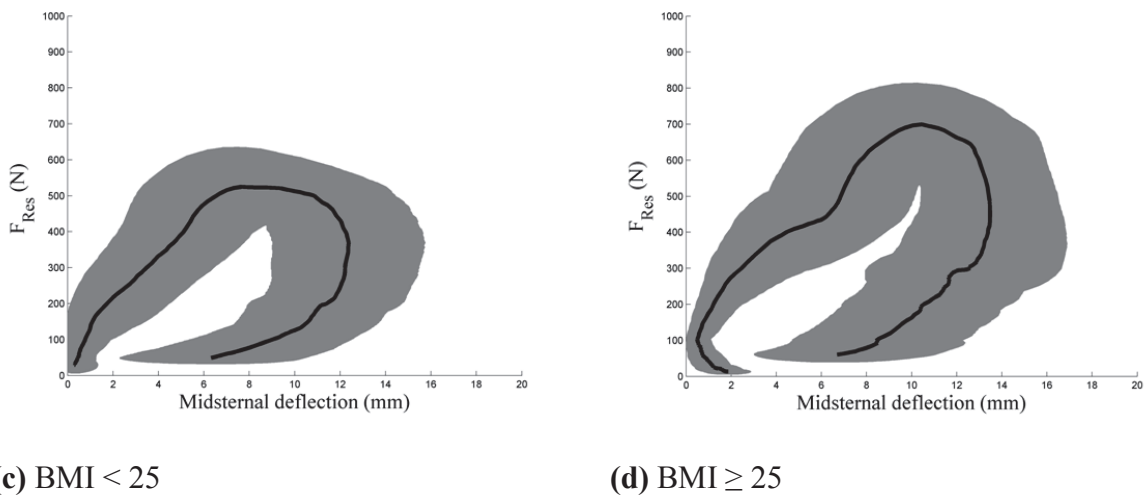
Fig. 49 shows the relationship between the resultant shoulder belt load F_{Res} and the mid-sternum deflection D for different age and BMI groups. Boxplots of thoracic stiffnesses and model parameters are shown in **Fig. 50**. **Fig. 51** shows typical force-deflection curves. While F_{Res} was calculated as the average curve for each group, mid sternal deflection was computed from the mathematical model using the associated average K, μ parameters.

No significant difference was found between overweight and normal subjects in effective stiffness ES ($p=0.40$), dynamic stiffness DS ($p=0.35$), linear stiffness K ($p=0.22$) and damping μ ($p=0.07$). As illustrated in **Fig. 51**, with similar values for model parameters, typical thoracic mechanical response of overweight volunteers is mainly lead by inertia (F_{Res}).

No significant difference was found between older and young subjects in effective stiffness ES ($p=0.13$), dynamic stiffness DS ($p=0.06$), and damping μ ($p=0.12$). Mean linear stiffness K is significantly different between young subjects and older subjects ($p=0.04$). Linear stiffness for the older volunteers is higher by about 60% than the young ones. As illustrated in **Fig. 51**, typical thoracic mechanical responses for age group are mainly lead by model parameters.

In addition, K, μ parameters seem influenced by age and BMI as shows in **Fig. 52**. In this figure, K and μ are displayed crossed age and BMI according to the respective age and BMI groups. The coefficient of determination R^2 for linear regression is displayed when correlation was found significant ($p<0.05$). There is a link ($R^2=0.28, p< 0.02$) between K and age for $BMI<25$ group while not for the overweighed. In addition, there is a link ($R^2=0.28; p=0.05$) between μ and age for $BMI\geq 25$ group while not for the lower BMI.





(c) $BMI < 25$

(d) $BMI \geq 25$

Fig. 49. Thoracic force-deflection curve for different age and BMI groups.

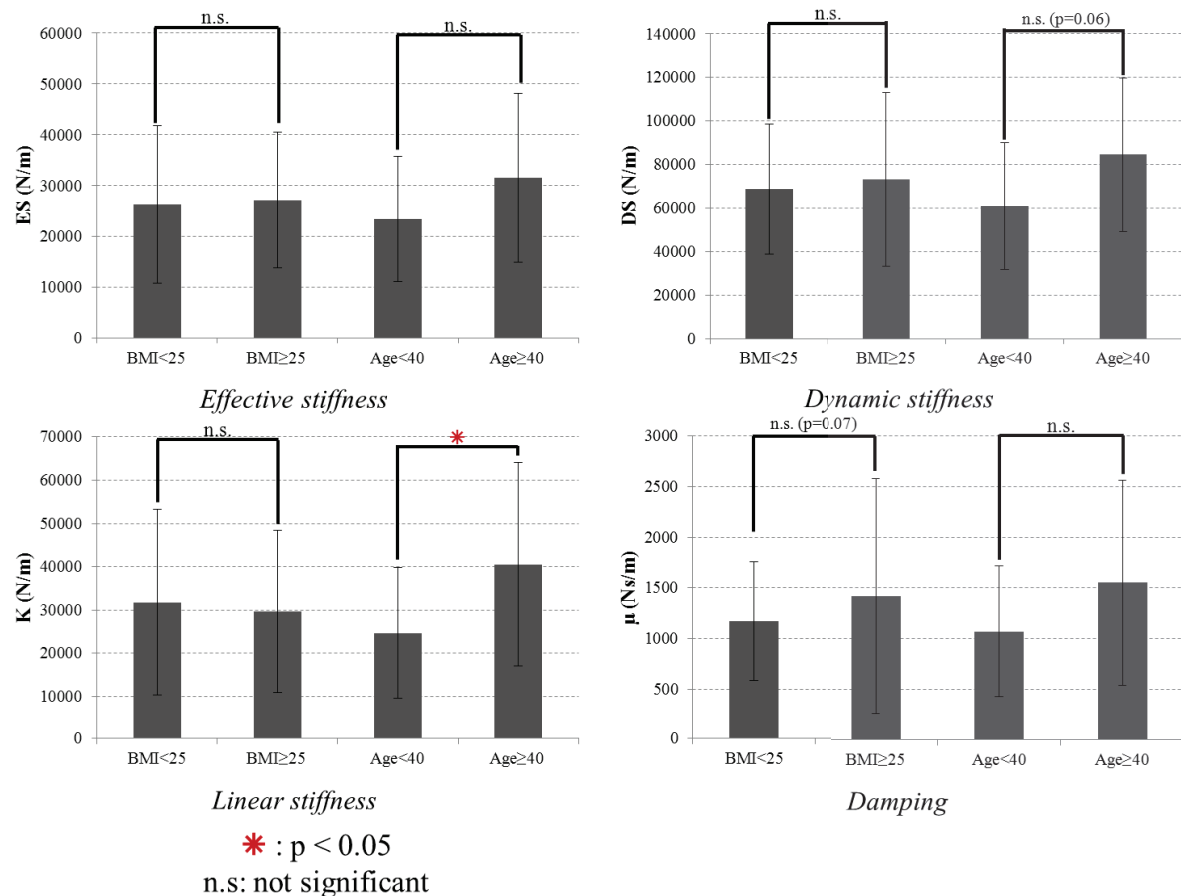


Fig. 50. Maximum force-deflection characteristics for different age and BMI groups.

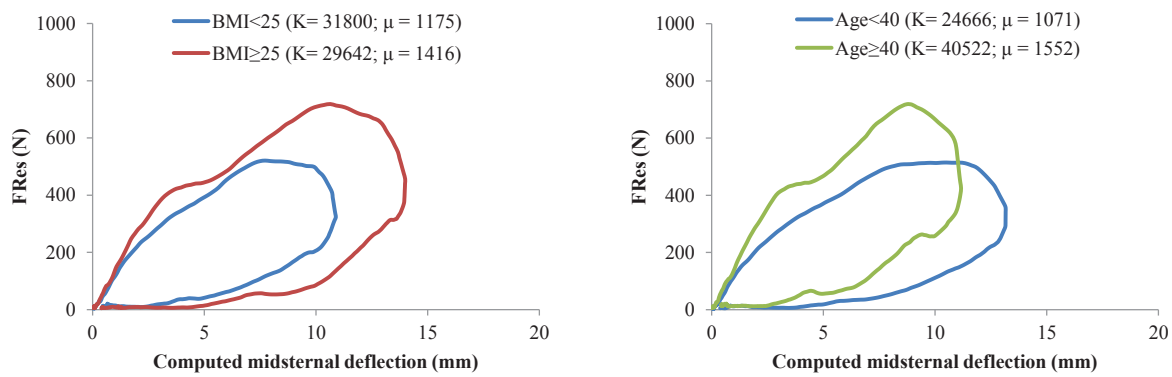


Fig. 51. Thoracic force-deflection curve computed from model parameters for different age and BMI groups.

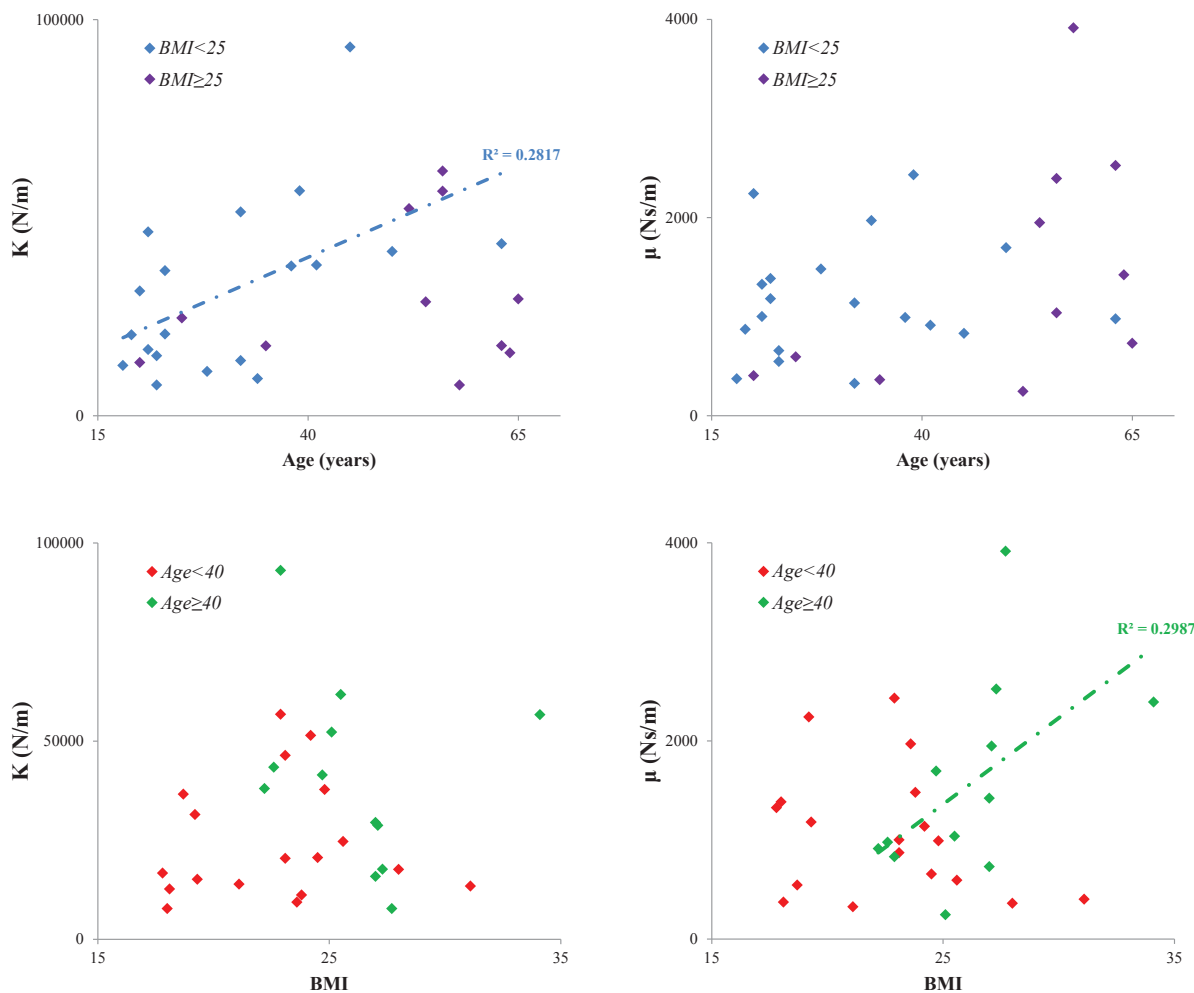


Fig. 52. Correlation of K, μ parameters with age and BMI. The coefficient of determination R^2 for linear regression was displayed when correlation was found significant ($p < 0.05$).

3.4 Definition of thoracic mechanical response groups

3.4.1 Principal Component Analysis (PCA)

Principal component analysis (PCA) was applied on the dataset displayed in **Table 13**. From this dataset, only five variables intrinsically linked to volunteers were studied: C_{\max} , %AP, %CC, K, μ . As described in Materials & Methods part, data were standardized before PCA treatment.

Table 13. Reduced thoracic mechanical dataset used for PCA and ACH.

ID	C_{\max} (%)	%AP	%CC	K (N/m)	μ (Ns/m)
582	5.3%	5.6%	2.4%	16681	1325
951	8.8%	19.4%	6.2%	7773	1385
101	8.6%	12.5%	5.3%	12709	373
771	7.9%	13.0%	10.2%	36628	546
135	6.1%	6.0%	11.4%	31461	2241
200	7.0%	16.9%	6.5%	15146	1181
607	10.0%	14.0%	8.4%	13910	326
862	5.4%	9.9%	11.9%	38044	913
375	5.9%	7.4%	7.8%	43390	977
438	3.7%	8.9%	10.4%	56753	2431
484	5.2%	17.1%	13.3%	93060	830
806	6.5%	11.1%	10.7%	46416	1000
869	7.3%	9.8%	4.9%	20396	872
733	5.5%	8.0%	7.7%	9351	1969
635	7.2%	8.6%	11.1%	11183	1481
225	5.1%	7.7%	3.8%	51430	1137
957	12.0%	17.4%	14.7%	20635	656
551	6.6%	9.9%	11.8%	41466	1695
329	5.5%	10.7%	4.3%	37761	991
128	6.1%	9.1%	11.9%	52276	245
247	4.8%	11.4%	12.1%	61773	1038
948	10.4%	9.6%	8.1%	24689	593
620	6.3%	9.3%	2.1%	15893	1421
118	7.2%	13.0%	10.1%	29488	730
981	5.2%	8.9%	5.8%	28740	1948
573	5.0%	12.2%	13.5%	17667	2524
741	5.4%	7.0%	9.6%	7773	3914
442	10.3%	21.9%	14.6%	17628	362
370	8.9%	18.9%	11.3%	13442	403
431	3.9%	11.6%	11.1%	56689	2393

Fig. 53 showed the percent variance explained by each principal component (axis) obtained by PCA. The individual percent variance is defined as the individual variance divided by the total variance. Individual percent variability is represented in descending order by bars, and the cumulative percent variability is represented by the line. Only the first 95% of the cumulative distribution is displayed. The first three principal components explain over 80% of the total variability in the standardized ratings, so that it seems reasonable to reduce the PCA dimensions to these three principal components.

Table 14 contains the principal component coefficients (loadings) of the variables. For each component, the underlined values correspond to the highest loadings of each principal component and are termed the "marker variables". A different sign between two "marker variables" of a principal component highlights an antagonist action between them. Markers variables give sense to the principal component and permit to differentiate amongst the different types of subjects.

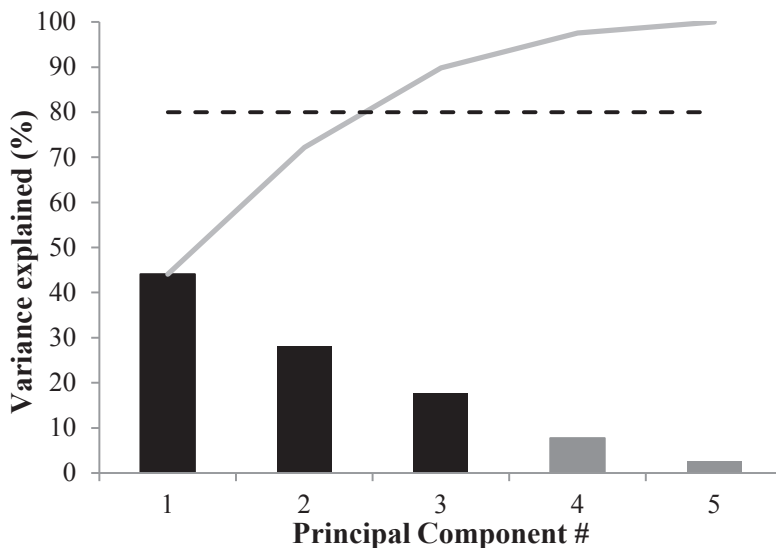


Fig. 53. Pareto chart of the percent variability explained by each principal component from PCA.

Table 14. The principal component coefficient for each variable obtained using PCA. Markers variables are underlined.

Variable	Principal Component #		
	1	2	3
C_{max}	0.61	-0.21	0.08
%AP	0.55	0.21	0.15
%CC	0.20	0.64	0.54
K	-0.21	0.70	-0.44
μ	-0.49	-0.07	0.69

The first three principal components and markers variables are:

- **Principal Component #1:** $C_{max} (>0)$, %AP (>0) and $\mu (<0)$. Considering the coefficients of the markers variables, the first principal component can be defined as a viscous response, strongly opposed to a response with a large relative antero-posterior excursion.
- **Principal Component #2:** %CC (>0), K (>0). This second component can be defined as a stiffness response, associated with a response with a large relative cranio-caudal axis excursion.

- **Principal Component #3:** $\%CC (>0)$, $\mu (>0)$. The third component can be defined as a viscous response, associated with a response with a large relative cranio-caudal axis excursion.

Fig. 54 displays both the observations and the variables projected onto the first three principal components. Each of the five variables is represented in this plot by a vector, and the direction and length of the vector indicates how each variable contributes to the principal components in the plot. For example, we have seen that the first principal component, represented in this left plot by the horizontal axis, has positive coefficients for the markers variables C_{max} , $\%AP$, and negative coefficient for μ . That corresponds to vectors directed into the top and bottom halves of the plot, respectively. This indicates that this component distinguishes between subjects that have high values for the first set of variables and low for the second, and subjects that have the opposite.

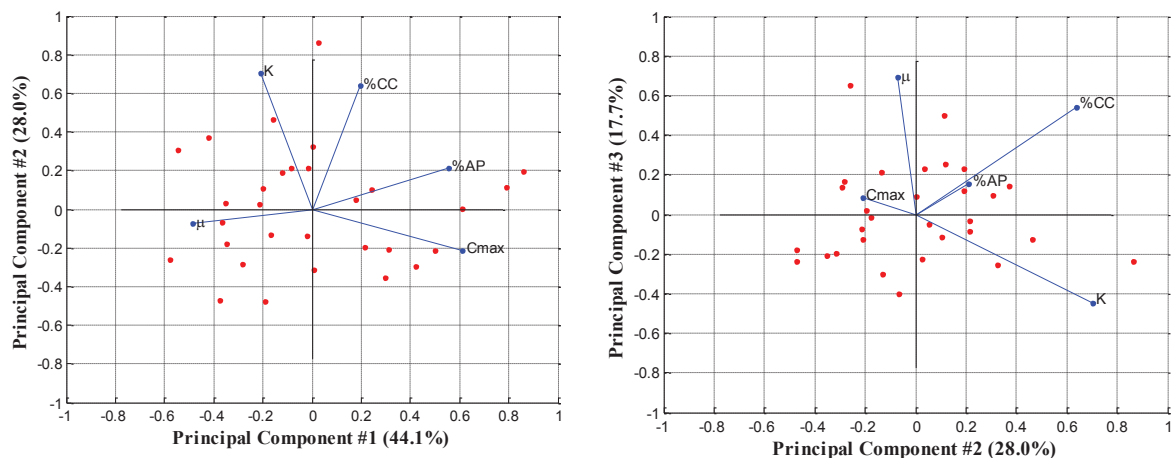


Fig. 54. Projection of the variables (blue line) and the subjects (red symbol) against the selected principal components.

Fig. 55 showed the observations projected against the first three principal components for different age and BMI groups. Older people tend to be in the left side of the 1-2 plane (positive in the **Principal Component #1**). No clear trend can be made for BMI group.

In addition, PCA was also applied on complete thoracic mechanical characteristics dataset. Results are available in **Appendix 3**. It appears that inertia plays an important role in the variability. Similarly, the amount of sternal deflection in antero-posterior and cranio-caudal axis plays an important role. Craniocaudal mobility and thoracic stiffness play lesser role in clustering.

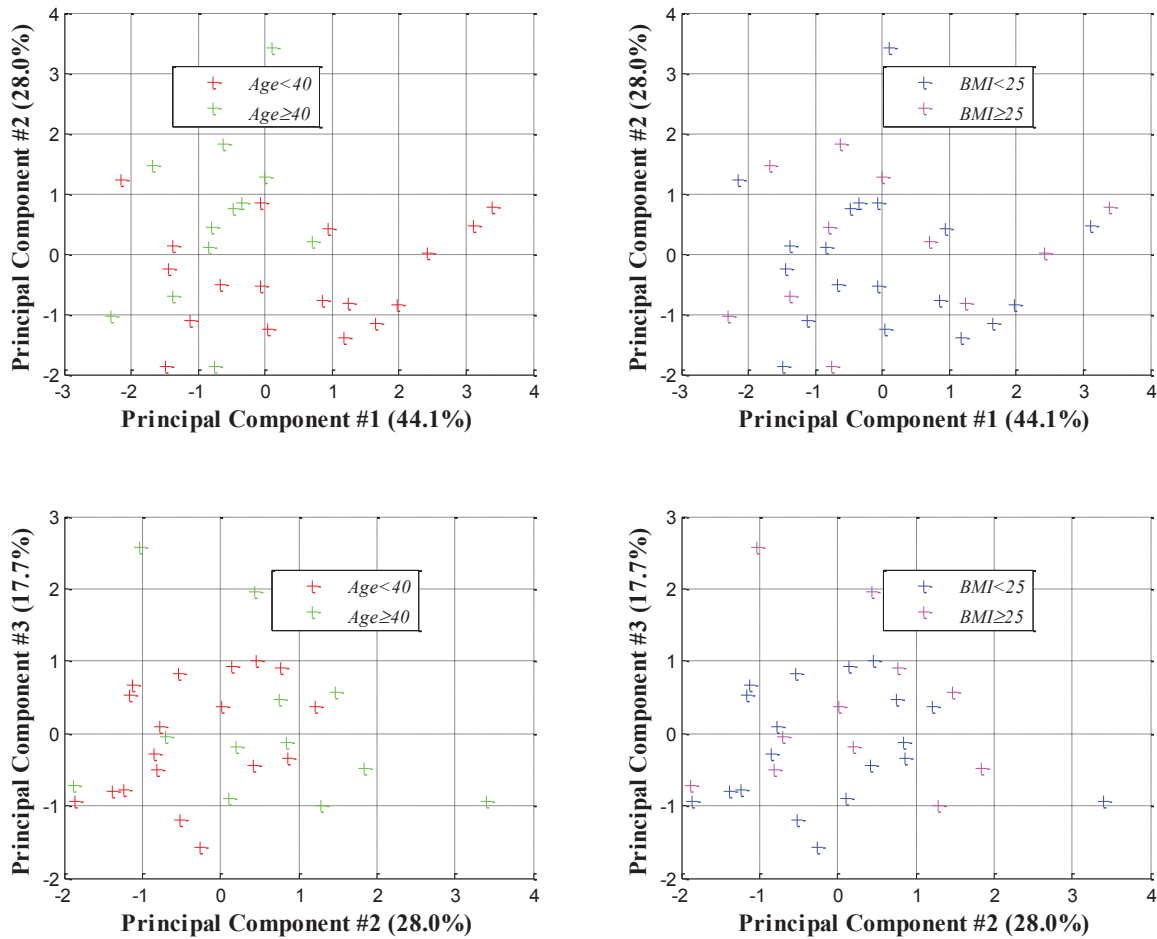


Fig. 55. Age and BMI group factor maps for the first three principal components.

3.4.2 Cluster analysis

Agglomerative hierarchical clustering method (AHC) was applied on the observations dataset projected into the first three principal components. In **Fig. 56**, the dendrogram shows the sequence of joins that were made between clusters. The numbers along the horizontal axis represent the ID of the subjects. The links between objects are represented as upside-down U-shaped lines. The height of the U indicates the distance between the objects.

The general shape of the dendrogram suggests to gather the volunteers into five groups:

- **Group #1:** 862, 806, 551, 128, 247, 771, 118, 484.
- **Group #2:** 582, 620, 375, 329, 225.
- **Group #3:** 135, 573, 733, 981, 635, 741, 438, 431.
- **Group #4:** 951, 607, 101, 948, 200, 869.
- **Group #5:** 657, 442, 370.

Fig. 57 showed the observations projected onto the first three principal components according to these five groups. **Table 15**, **Table 17**, **Table 16** describe the AHC groups according to anthropometries, age and BMI groups and “markers variables”.

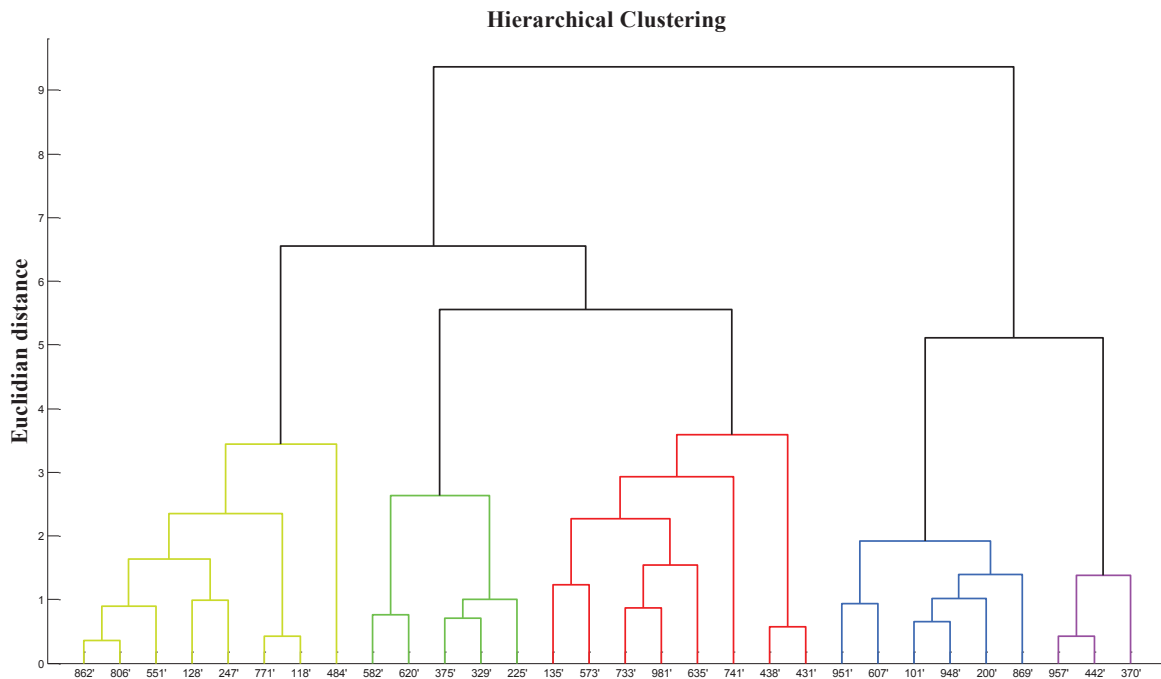


Fig. 56. Dendrogram illustrating the arrangement of the clusters produced by AHC.

Group #1 contains 8 subjects that tend to have higher thoracic stiffness (positive values along **Principal Component # 2**). Typical subjects are women, over 40 years-old with normal corpulence.

Group #2 contains 5 subjects that tend to have low amount of relative crano-caudal excursion (negative values along **Principal Component # 3**). Typical subjects are tall men with normal corpulence.

Group #3 contains 9 subjects that tend to have strong viscous effect in thoracic mechanical response (high values of μ). There is no clear trend in the profile of the typical subjects.

Group #4 contains 8 subjects that tend to have higher midsternal compression and have lower thoracic stiffness (negative values along **Principal Component # 2**). Typical subjects are young with normal corpulence.

Group #5 contains 3 subjects that tend to have higher midsternal compression peak with higher relative sternal excursion both antero-posterior and craniocaudal axis (positive values along **Principal Component # 1**). In addition they tend to have lower thoracic stiffness. Typical subjects are young with overweight.

Group#4 and **Group #5** are very similar. Both groups subjects are young people with similar thoracic behaviour: (low thoracic stiffness and high midsternal compression), even if there are some difference between them in the amount of relative sternal excursion in the saggital plane. **Group #2** and **Group #3** are less similar with higher difference in the amount of viscous effect in thoracic behaviour. **Group #1** is clearly the most outlier group with very stiff thorax from women, over 40 year's old and normal corpulence.

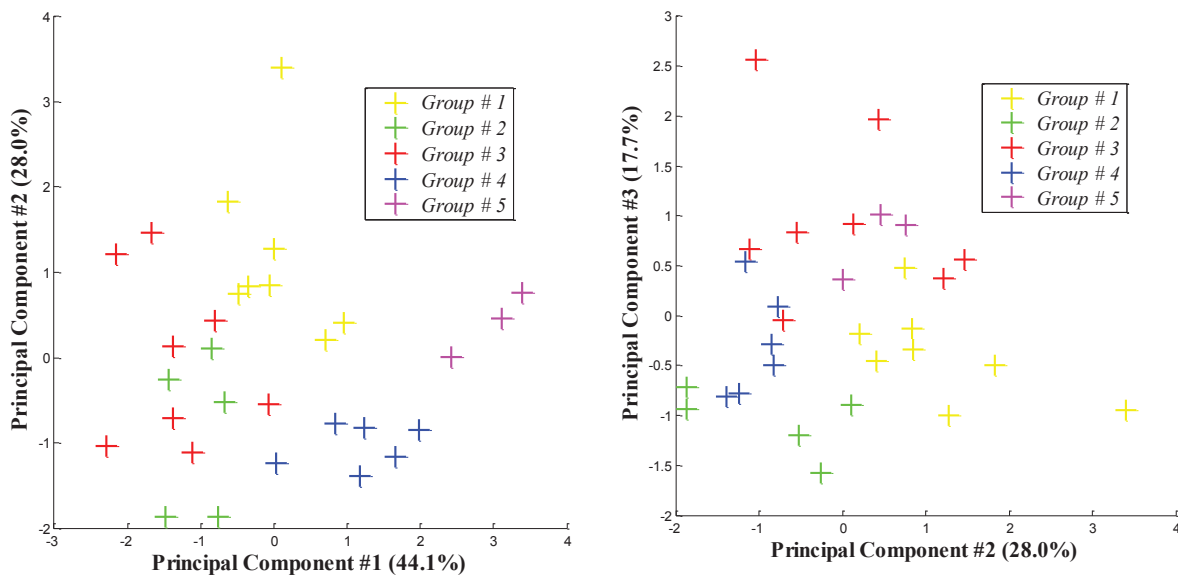


Fig. 57. AHC group factor maps for the first three principal components.

Table 15. AHC group description according to age, genders and BMI groups

	Man	Woman	BMI<25	BMI≥25	Age<40	Age≥40
Group # 1	38% (3/8)	63% (5/8)	63% (5/8)	38% (3/8)	25% (2/8)	75% (6/8)
Group # 2	100% (5/5)	0% (0/5)	80% (4/5)	20% (1/5)	60% (3/5)	40% (2/5)
Group # 3	63% (5/8)	38% (3/8)	50% (4/8)	50% (4/8)	50% (4/8)	50% (4/8)
Group # 4	67% (4/6)	33% (2/6)	83% (5/6)	17% (1/6)	100% (6/6)	0% (0/6)
Group # 5	33% (1/3)	67% (2/3)	33% (1/3)	67% (2/3)	100% (3/3)	0% (0/3)

Table 16. AHC group description according to anthropometries.

	Age		BMI		Height		Weight	
	Group Mean	Group SD						
Group # 1	47.1	10.4	23.7	2.5	1.68	0.13	67.0	13.1
Group # 2	43.6	19.2	23.3	3.4	1.80	0.08	74.8	7.1
Group # 3	44.0	15.8	25.7	4.4	1.75	0.15	78.8	17.1
Group # 4	23.0	5.1	20.9	3.0	1.70	0.05	59.8	7.8
Group # 5	26.0	7.9	27.9	3.3	1.67	0.10	78.0	17.4
Overall	38	16.3	24	3.8	1.72	0.12	71.1	14.3

Table 17. AHC group description according to markers variables.

	Markers	Group Mean	Overall mean	Group SD	Overall SD	p
Group # 1	C _{max}	6.2%	6.8%	1.1%	2.0%	0.46
	%AP	11.8%	11.6%	2.6%	4.2%	0.87
	%CC	11.5%	9.1%	1.1%	3.5%	0.07
	K	49894	31008	20093	20174	0.02
	μ	875	1263	422	832	0.21
	Principal Component #1	0.03	0.00	0.56	1.49	0.96
	Principal Component #2	1.20	0.00	1.02	1.18	0.01
	Principal Component #3	-0.38	0.00	0.47	0.94	0.27
	C _{max}	5.6%	6.8%	0.5%	2.0%	0.22
	%AP	8.1%	11.6%	1.9%	4.2%	0.08
Group # 2	%CC	4.1%	9.1%	2.3%	3.5%	0.00
	K	33031	31008	16041	20174	0.83
	μ	1170	1263	198	832	0.81
	Principal Component #1	-1.04	0.00	0.39	1.49	0.13
	Principal Component #2	-0.88	0.00	0.93	1.18	0.12
	Principal Component #3	-1.06	0.00	0.33	0.94	0.02
	C _{max}	5.3%	6.8%	1.1%	2.0%	0.05
	%AP	8.9%	11.6%	2.1%	4.2%	0.09
	%CC	10.1%	9.1%	2.4%	3.5%	0.47
	K	27452	31008	20023	20174	0.66
Group # 3	μ	2363	1263	713	832	0.00
	Principal Component #1	-1.36	0.00	0.72	1.49	0.02
	Principal Component #2	-0.02	0.00	1.00	1.18	0.97
	Principal Component #3	0.98	0.00	0.86	0.94	0.01
	C _{max}	8.7%	6.8%	1.4%	2.0%	0.04
	%AP	13.7%	11.6%	3.9%	4.2%	0.26
	%CC	6.6%	9.1%	1.4%	3.5%	0.10
	K	15771	31008	5969	20174	0.05
	μ	788	1263	434	832	0.19
	Principal Component #1	1.15	0.00	0.68	1.49	0.07
Group # 4	Principal Component #2	-1.04	0.00	0.26	1.18	0.04
	Principal Component #3	-0.29	0.00	0.52	0.94	0.47
	C _{max}	10.4%	6.8%	1.6%	2.0%	0.01
	%AP	19.4%	11.6%	2.3%	4.2%	0.00
	%CC	13.5%	9.1%	1.9%	3.5%	0.04
	K	17235	31008	3613	20174	0.07
	μ	474	1263	159	832	0.12
	Principal Component #1	2.98	0.00	0.50	1.49	0.00
	Principal Component #2	0.41	0.00	0.38	1.18	0.56
	Principal Component #3	0.76	0.00	0.35	0.94	0.18

4. Discussion

30 volunteers of different anthropometries, genders and ages were subjected to a low deceleration pulse. Thoracic mechanical response quantified using non-invasive techniques was compared to literature and linked to individual characteristics. In particular, the influence of age and overweight on thoracic mechanical response was evaluated.

Resulting shoulder belt force $F_{Res_{max}}$ was significantly linked to individual characteristics while $FB3_{max}$ and $FB4_{max}$ not; the implementation of loading direction in the computation of belt force resultant is important. In addition, spring-dashpot-model parameters K , μ were significantly linked to individual characteristics (age, BMI) while the different stiffness ES, DS not.

Thoracic mechanical responses obtained in the present protocol are similar to those obtained in sled tests (Kemper et al., 2011). The variability of thoracic mechanical response is higher in the present study than in literature where only 50th percentile males were considered.

Overweight volunteers' group shows significantly a higher crano-caudal mid-sternal excursion than the subjects in the normal group. Increased soft tissues artefacts due to increased superficial tissue depth may partly cause the increase in ΔCC observed for overweight subjects. In addition, no significant difference was found in C_{max} for overweight group in the present study. Finally, there may be a trend that overweight volunteers have a higher viscous effect in thoracic behaviour (higher μ -values).

Over 40 years-old group shows significantly a lower midsternal compression C_{max} than younger compression. In addition, thoracic stiffness (higher K -values) was significantly higher for 40-years old group. The higher K value was especially observed for older women with no overweight while the lower K values were found for older people with high BMI. In addition, older people with high BMI seemed to have higher viscous thoracic behaviour than young group than older subjects with no overweight. Young subjects were more compliant (lower K -values) than the others especially the thin ones. Contrary to the older people, there was no trend in viscous effect in thoracic behaviour for young people with high BMI.

Nevertheless, the question of whether these thoracic mechanical differences between volunteers have implications on thoracic injury risk is still open. Thus, the second objective of the thesis is to provide answers by performing the same analysis in the injurious simulations using customize FE models. **Chapter 3** describes the methodology used to implementing a geometrical personalisation process in order to adapt the geometry and the posture of a human

FE model to various cases. **Chapter 4** provides the analysis of simulations simulations in the injurious domain to isolate the role of geometrical parameters possibly linked to the thoracic mechanical response under dynamic loading and their role in severity.

CHAPTER III - GEOMETRICAL PERSONALIZATION OF HUMAN FE MODEL

1. Introduction

In the present chapter, we present the methodology used to personalize the geometry and the posture of the THUMS model using external landmarks and anthropometric dimensions taken on volunteers. The process is assessed on one subject by comparing computed thoracic geometry and MRI data and on two subjects by comparing anthropometric dimensions.

2. Materials and methods

2.1 Human body model

2.1.1 General description

The human body model used was the 50th percentile male THUMS (v3.0, Toyota Central R&D Labs Inc., Nagakute, Aichi, Japan). The THUMS model represents an adult mid-sized male (175cm, 77kg, 30's~40's) in occupant position with respect to anatomical geometry and biomechanical properties such as bone stiffness and skin flexibility (Iwamoto et al., 2002).

Fig. 58 illustrates the main features of THUMS.

2.1.2 Detailed description of the thorax

The model structure and the total number (T.N.) of elements of the THUMS' thorax are described in **Fig. 59**. As for the entire model, the cortical bone of the rib and sternum was modeled using shells made of isotropic elastic plastic material. The trabecular bone and costal cartilage were modeled as isotropic elastic plastic material using solid elements.

Internal organs, abdomen, flesh and fat were modeled as viscoelastic material using solid elements. Internal organs are not separated but merged in “bags”. An improved version of THUMS including individual organs was developed but was validated only for PAM-CRASH® (Iwamoto et al., 2002). The skin was modeled as elastic material using shell elements. Muscles and tendons were modeled as tension-only elastic material using bar elements. Each articular joint was modeled anatomically by bone-to-bone contacts. Each ligament was modeled as tension-only elastic material using membrane or bar elements.

Material properties were taken from Yamada (1970).

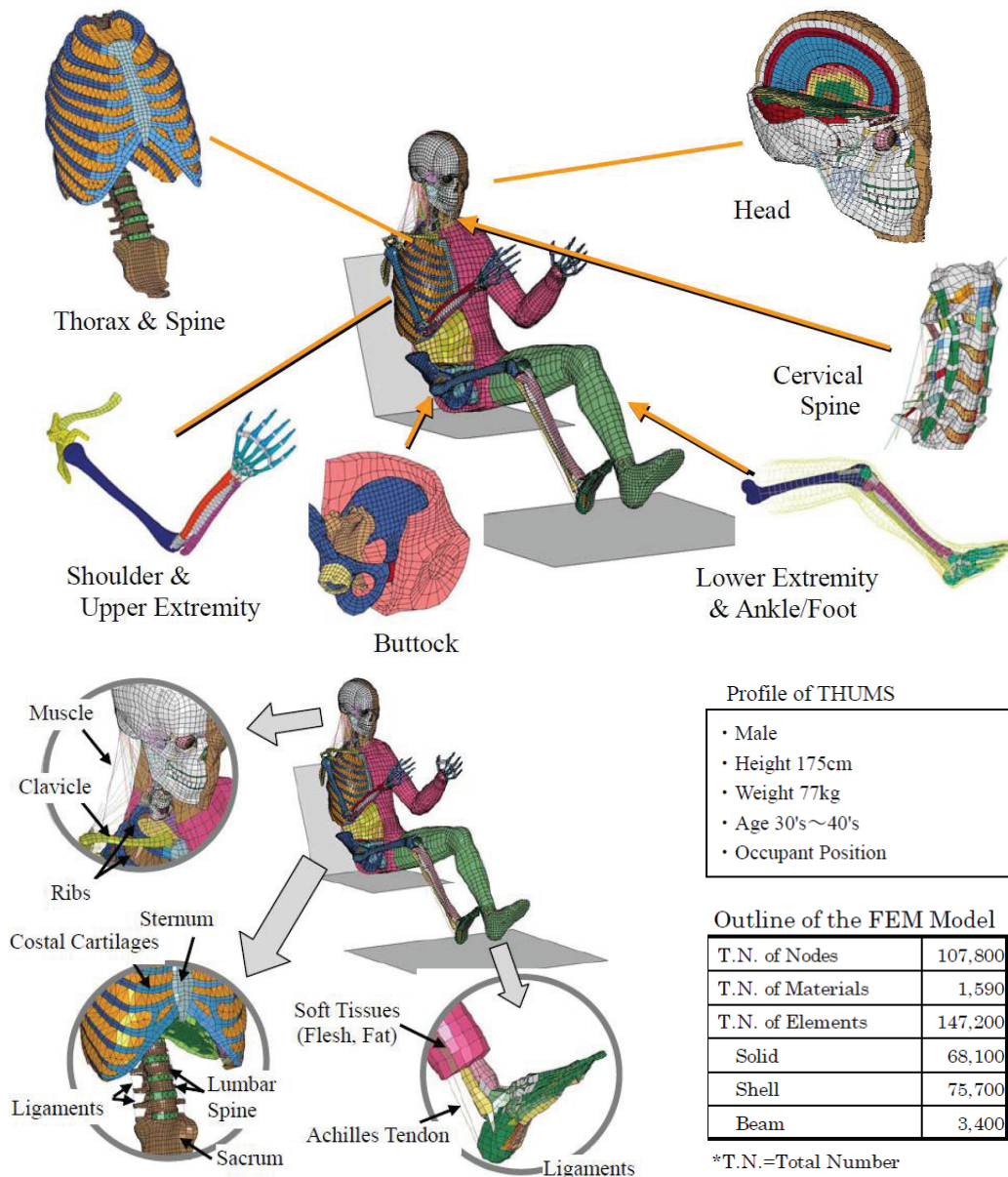


Fig. 58. THUMS features (Toyota Central R&D Labs Inc.).

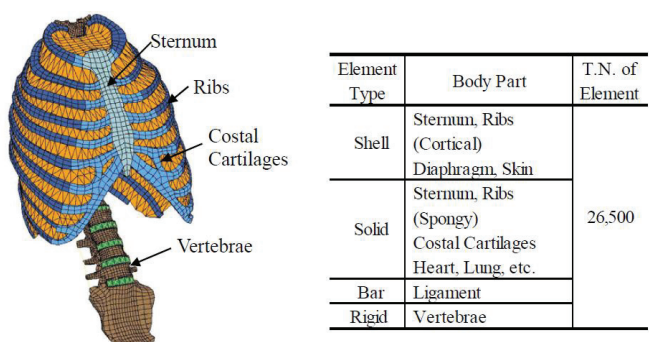


Fig. 59. Thorax and spine mesh (Toyota Central R&D Labs Inc.).

2.1.3 Biofidelity

Validation and development of the THUMS model have been carried out by improving its model predictions from PMHS tests. The THUMS thorax was validated with frontal pendulum impacts (Oshita et al., 2002). The THUMS cervical spine was validated in flexion extension with frontal and rear end loadings (Chawla et al., 2005).

The whole-body kinematics was validated with frontal sled tests for different impact velocity (48 km/h, 29 km/h) and restraint conditions (with/without airbag and pretensioned and load limited belt system) (Pipkorn and Mroz, 2009). The main responses were considered well predicted by THUMS with respect to peak value, time of peak and curve shape (Pipkorn and Mroz, 2009). It indicates that the THUMS model can be used for comparative studies and trend analysis.

2.2 Geometrical personalization process

2.2.1 Overview

The geometrical personalization of THUMS is performed using a method based on the Radial Basis Function (RBF; Buhmann, 2000). This interpolation method is widely spread to personalize FE meshes using control points (Bertrand et al., 2006; Besnault et al., 1998; Serre et al., 2006; Vezin and Berthet, 2009). RBF method allows the personalization of the shape of an initial cloud of nodes towards a new geometry and requires only the coordinates of some control points of the initial geometry and of the new geometry.

The ability of RBF method to generate models of isolated ribcages from direct bony landmarks has been demonstrated (Vezin and Berthet, 2009). During HUMOS2 project, a statistical relationship between anthropometry dimensions were used to create the small female and the large male models from HUMOS2 50th percentile male FE model (Bertrand et al., 2006; Serre et al., 2006).

Our purpose is to modify the initial mesh of THUMS 50th percentile male FE model, using RBF, towards the geometry and the posture of the volunteers tested in **Chapter 2**. Geometry and posture of the volunteers are defined by a set of thoracic palpable points, some anthropometry dimensions and 2D control points from lateral view taken on volunteer during sled tests.

From these data on geometry and posture, control points must be defined to reproduce geometry and posture, to ensure good mesh homogeneity of the model.

Added to thoracic palpable points and 2D view palpable points, virtual control points were created all over the surface of the mesh. All these virtual control points also termed *target surface nodes* were used to personalize the whole body of THUMS using RBF.

Thus, the geometrical personalization of THUMS model was divided into three steps:

- Step 1: Generation of initial surface nodes
- Step 2: Generation of target surface nodes
- Step 3: Mesh personalization using target surface nodes

The whole process is presented in **Fig. 60**.

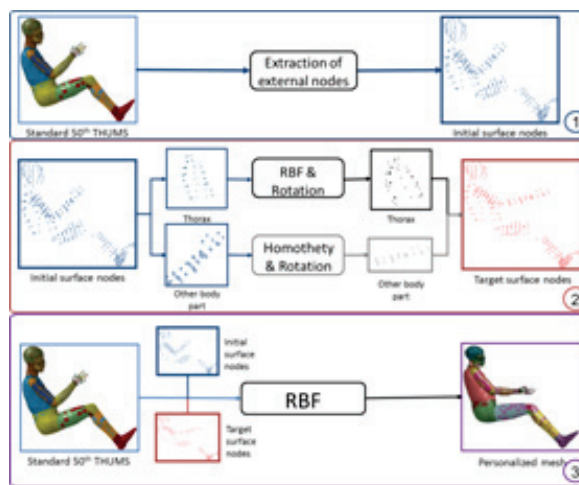


Fig. 60. Synthesis of the personalization process.

2.2.2 Step 1: Generation of initial surface nodes

THUMS is divided according to its body parts as described in **Fig. 61**. Left and right limbs were separated. For each body part, nodes are translated to a local coordinates system. Definitions of local coordinates system are available in **Appendix 5**.

For each body part, a local cylindrical system is defined as shown in **Fig. 62a**. Then, each body part is numerically sliced in 10 slices along its longitudinal axis. In each slice, surface nodes defined as nodes with radial distance above 90% of the maximum radial distance r_{max} found in local slice, are extracted. The extraction process for the 5th slice of the left forearm is illustrated in **Fig. 62b**. Around 1400 surface nodes were extracted on the whole body using this method. **Table 18** describes their repartition among all body parts.

Table 18. Surface nodes extracted for each body part

	Head	Thorax	Arm	Forearm	Thigh	Leg	Foot	Total
Extracted nodes	89	262	120	103	97	108	91	1389

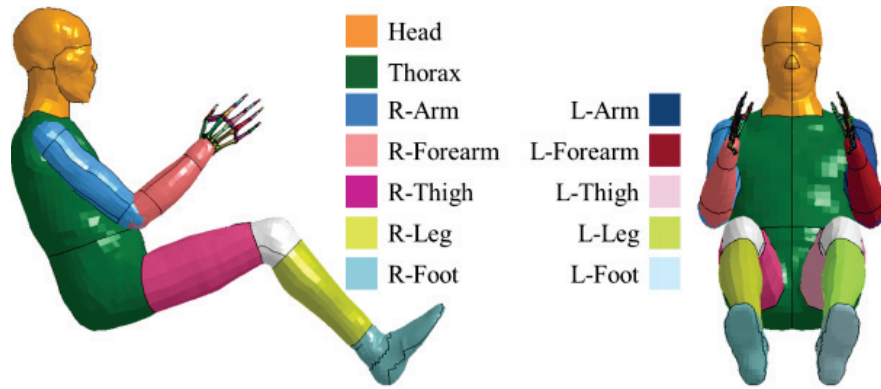
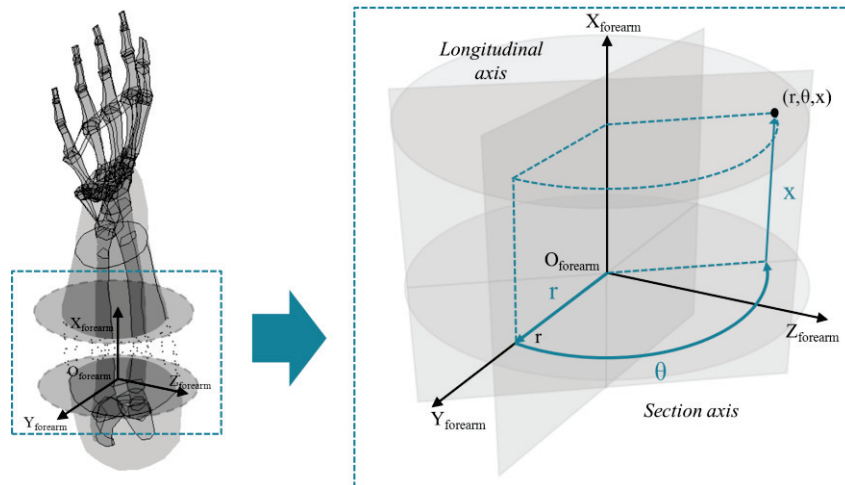
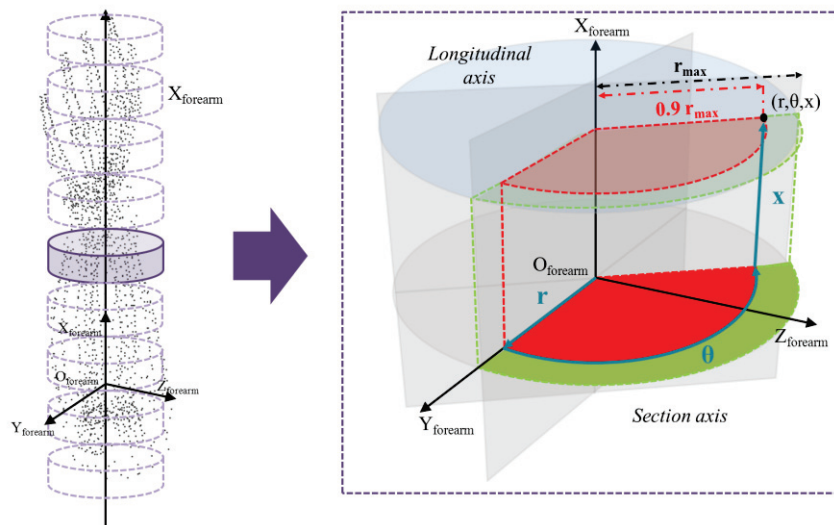


Fig. 61. Segmentation of the 50th percentile male THUMS model.

For each body part, nodes involved in body part coordinate system definition are added to surface nodes. Nodes involved in adjacent local coordinate system definitions are also added to surface nodes.



a) Definition of local cylindrical coordinates system



b) Extraction of surface nodes

Fig. 62. Generation of initial surface nodes of the left forearm

2.2.3 Step 2: Generation of target surface nodes

2.2.3.a Thoracic target surface nodes

Target geometry of each volunteer's ribcage was defined from a reasonable number of thoracic anatomical landmarks quite easy to get on both genders and on both corpulent and thin subjects.

42 thoracic palpable anatomical landmarks were identified. These landmarks are shown in **Fig. 64** and defined in **Table 43**. Their 3D-coordinates were extracted using Vicon® system and expressed in a fixed reference linked to the Vicon® room. Then, the 3D-coordinates of the thoracic anatomical landmarks obtained on volunteer were expressed in the thoracic local coordinate system (**Appendix 2**).

In order to “clean” this set of landmarks, the Z_{thorax} coordinate of the following thoracic anatomical landmarks (CV_M_007, TV_M_001:TV_M_012) was set to 0. Similarly, $X_{\text{thorax}}-Y_{\text{thorax}}-Z_{\text{thorax}}$ coordinates of the left thoracic anatomical landmarks ($Z_{\text{thorax}} < 0$) and of the right thoracic anatomical landmarks ($Z_{\text{thorax}} > 0$) were modified so that similar landmarks of both side were symmetrical wrt the sagittal plane.

These 42 anatomical landmarks were identified on 50th percentile male THUMS mesh. As thoracic anatomical points were not easy to locate on the mesh, three set of candidate nodes were selected on mesh according to their location: nodes on skin, nodes on bone, nodes on bone and skin. Definition of thoracic sets is available in **Appendix 1 (Table 44)**.

To increase the definition of the ribcage target geometry, thoracic target surface nodes were added to the thoracic anatomical landmark set. Thoracic target surface nodes were deformed by RBF method using 42 thoracic anatomical landmarks acquired on thorax volunteer and on 50th percentile male THUMS geometry (**Fig. 63**).

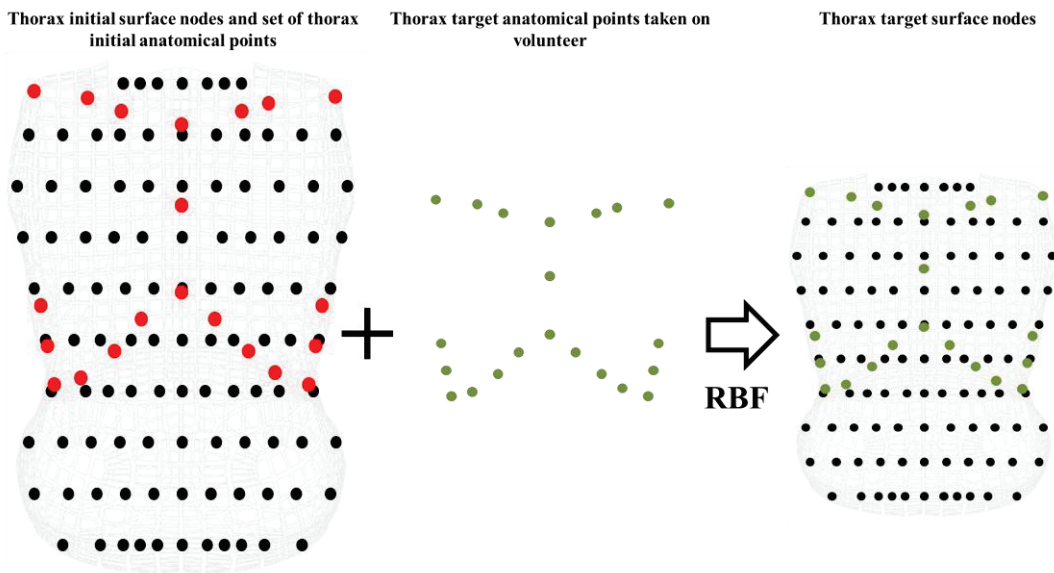


Fig. 63. Personalization of thoracic surface points by RBF with the 42 thoracic anatomical points.

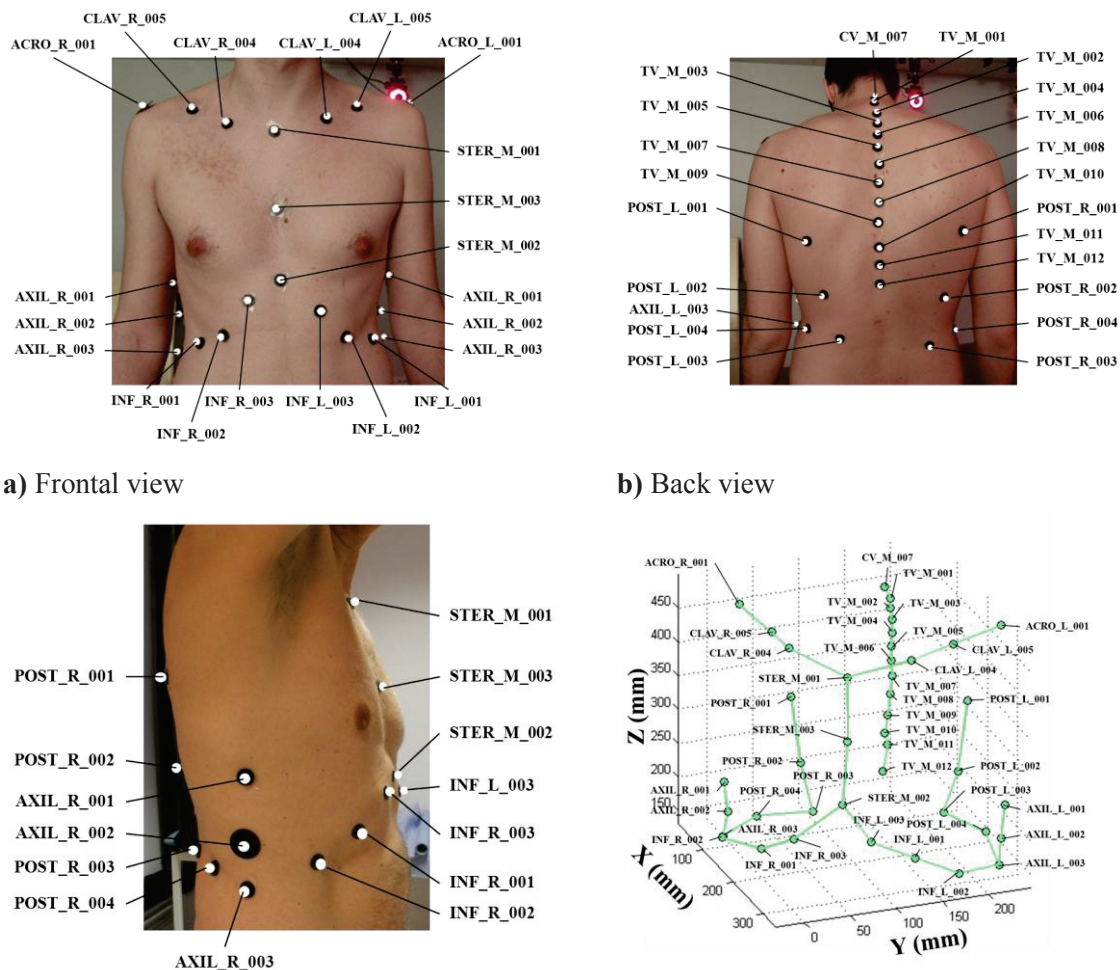


Fig. 64. Definition of thoracic anatomical landmarks for thoracic geometry personalization.

2.2.3.b Other body part target surface nodes

For other body parts, target surface nodes are created from initial surface nodes by homothety based on the length and largest circumference of each body part. This process is illustrated on the left arm in **Fig. 65**.

50 external anthropometric measurements were acquired on volunteer using conventional anthropometric tools (bracket, sliding calliper, meter tape). These external anthropometric measurements are defined in **Appendix 2**. For this step of the personalization, 13 of these external measurements are used (**Table 19**). These 13 pertinent external measurements were also identified on 50th percentile male THUMS mesh. In the local cylindrical reference, 3D coordinates of the target surface nodes of the body part were transformed by homothety to fit the length (longitudinal axis) and circumference ($2\pi \times r$) measured on volunteer. For the specific case of the head, head target surface nodes were transformed according to fit the width, the depth and the height of the head.

As the distances between the body parts has changed due to previous scaling, the distances between the local coordinate systems were modified to fit the length of the limb applied in 2.2.2.b.

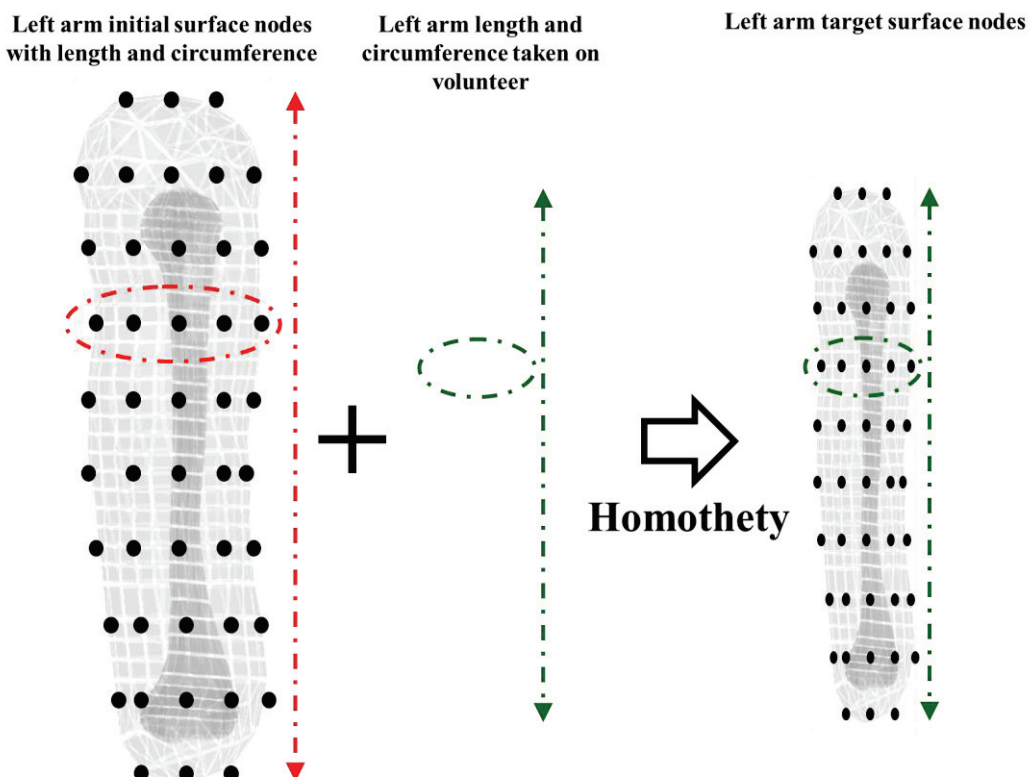


Fig. 65. Personalization of left arm surface points by homothety with limb length and circumference.

Table 19. External anthropometric measurements used in the personalization process.

Code	Description
ANTH_26a	Glabella - occiput lenght
ANTH_26b	Skull height auricular height (porion - vertex)
ANTH_26c	Head width
ANTH_19	Arm lenght (acromion - elbow)
ANTH_44	Arm upper circumference (superior third)
ANTH_18	Ulna length
ANTH_50	Greatest forearm circumference
ANTH_06 - ANTH_07	Greater trochanter top - Knee articular interline spacing
ANTH_36	Thigh upper circumference (superior third)
ANTH_07 -ANTH_43	Knee articular interline spacing – Internal malleolus bottom
ANTH_39	Greatest calf circumference
ANTH_42	Greatest foot lenght
ANTH_43	Greatest foot width

2.2.3.c Posture personalization

Posture of each volunteer was defined using rigid body segmentation and 17 lateral anatomical landmarks placed on the left side of the volunteer during in vivo sled tests.

These lateral anatomical landmarks are illustrated in **Fig. 66** and defined in **Erreur ! Source du renvoi introuvable.**. At the initial time of the shock, 2D-coordinates of the lateral anatomical landmarks were extracted using MotionTrack® (Vannier Photel) and expressed in x-z plane linked to the laboratory reference.

Volunteer's body was divided in 12 segments similar to the THUMS segmentation (2.2.1): Head, Thorax, Arm (L&R), Forearm (L&R), Thigh (L&R), Leg (L&R), Foot (L&R). Relative angles of each segment were computed from the previous segment wrt the following linkage:

- Head → Thorax.
- Upper extremities: Forearm → Arm, Arm → Thorax.
- Lower extremities: Foot → Leg, Leg → Thigh, Thigh → Thorax.

Relative angles on the right extremities were assumed to be identical to those of the left extremities.

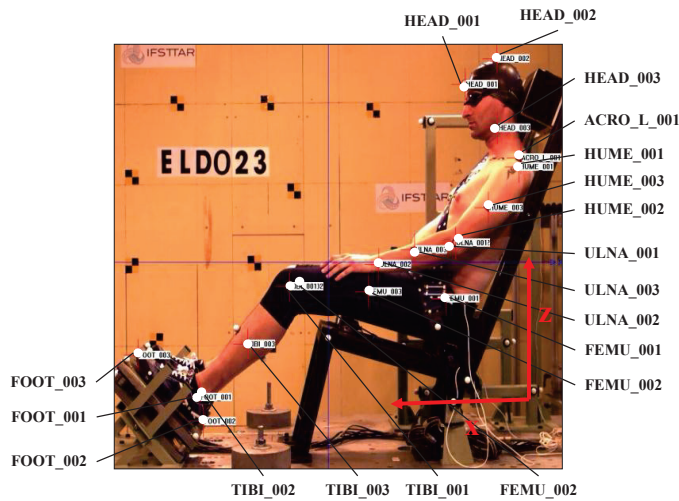


Fig. 66. Definition of lateral anatomical landmarks used for posture personalization.

In addition, these 17 lateral anatomical landmarks were also identified on the 50th percentile male THUMS mesh. Relative angles of each body part were computed from the previous body part wrt the same linkage.

For each body part, target surface nodes were rotated to match the relative angles computed previously (**Fig. 67**). Rotated target surface nodes were all merged in thoracic local coordinate system. Then, rotated target surface nodes were translated in the THUMS coordinate system and were rotated to fit the angle of the seatback (25°).

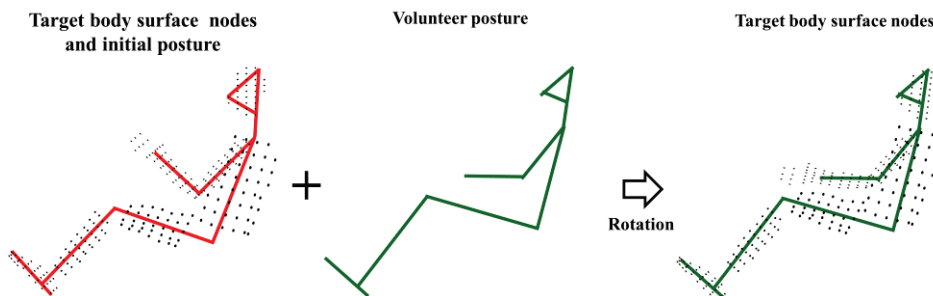


Fig. 67. Rotation of target surface nodes according to volunteer's posture.

2.2.4 Step 3: Mesh personalization using target surface nodes

Finally the interpolation of the entire mesh was performed by RBF using the target surface nodes as control points (**Fig. 68**). Prior to the interpolation, 15% of both initial and target surface nodes are removed in order to avoid excessive mesh distortion. Nodes removed correspond to the most extreme slices along the longitudinal axis of the body part and to the nodes needed in the definition of body part coordinates system.

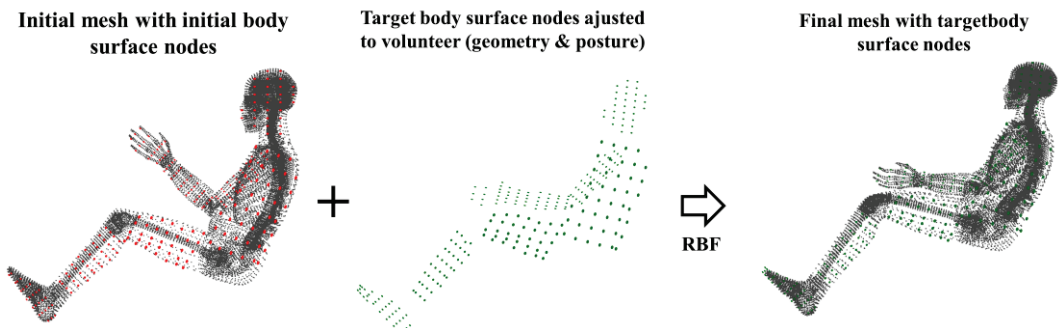


Fig. 68. Mesh interpolation by RBF using surface nodes.

2.3 Software

Personalization process was performed using scripts written in Matlab (R2007b, The MathWorks Inc., Natick, MA, USA). Cores of RBF scripts were already written by Raphaël Dumas (Dumas and Cheze, 2009). The host machine was a bi-core Intel Core2Duo, on Windows XP. LS-PREPOST (v3.0, LSTC, Livermore, CA, USA) was also used to display the whole body model and to check the geometry.

Each personalization was performed in 20 min.

3. Assessment of the geometrical personalization process

The geometrical personalization process was assessed using two volunteers (man, 33 years-old, 185 cm, 86 kg; woman, 40 years-old, 1m61, 54 kg). For each subject, 3 geometrically personalized THUMS model were computed using the three set of candidate's nodes as thoracic anatomical landmarks defined in **2.2.2.a**.

First, the influence of these candidate nodes as thoracic palpable points was assessed on the thoracic of the woman by comparing the personalized mesh with known reference geometry obtained by magnetic resonance imaging (MRI). Then, the assessment was performed on the whole body of both subjects by comparing the personalized mesh with anthropometric dimensions and mesh quality criteria.

3.1 Assessment of the thoracic geometrical personalization

3.1.1 Methods

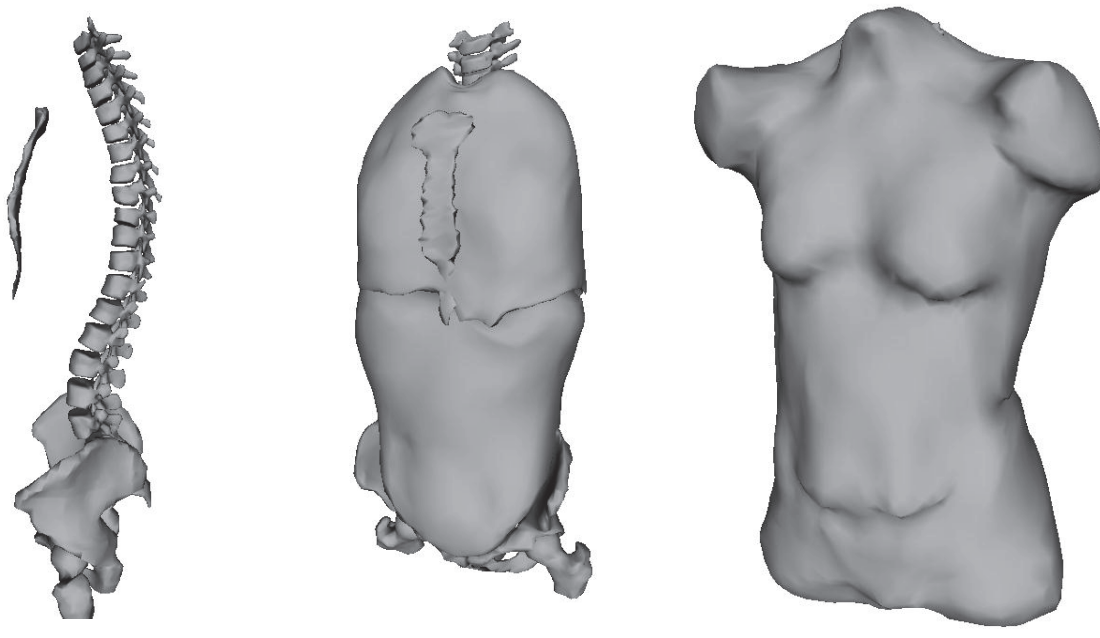
The personalized thoracic for the woman subject was geometrically compared to a known reference geometry built thanks to MRI scans (**Fig. 69**).

The MRI-scans of her thoracic were performed in a standing posture in the context of a previous study (Beillas et al., 2009).

As woman volunteer was standing, the arms over the shoulders during MRI-scans, the geometrical comparison was limited to the thorax and the upper part of the abdomen. The geometrical comparison is performed in the thoracic local coordinates frame (**Appendix 5**).

An “average distance”, S , is calculated between personalized thorax mesh and the reference geometry as the mean of the distance d_i found for each point of the reference geometry (~50000 points) to the closest point of the personalized thorax mesh (~35000 nodes) according to their location (sternum, ribcage, spine, mediastinum, abdomen, skin, whole thorax).

A d_i -value of 0 would mean that a point of the MRI-scan fits exactly a node of the personalized mesh of the woman.



a) Sternum and spine **b)** Ribcage, thoracic bag, **c)** Skin
abdomen

Fig. 69. MRI-scans used for the assessment of the thoracic geometrical personalization.

3.1.2 Results

3 geometrically personalized THUMS model obtained using the three different candidate nodes as thoracic palpable points were computed for the woman subject. Each personalized thorax mesh of the woman was geometrically compared to the thorax MRI scan. **Table 20** gives the mean distance S for the three different candidate nodes according to thorax parts.

Lower values of mean distance S correspond to the most similar geometrically personalized to MRI-scan.

Table 20. Results of woman personalized models with different candidate nodes as thoracic palpable points compared to MRI-scans.

Location	S-Score ($\text{♀-THUMS} \rightarrow \text{MRI-scan}$)		
	Thoracic skin set	Thoracic bone set	Thoracic bone & skin set
sternum	$4.9 \pm 2.1 \text{ mm}$	$5.9 \pm 3.3 \text{ mm}$	$5.8 \pm 2.7 \text{ mm}$
ribcage	$5.3 \pm 3.2 \text{ mm}$	$6.0 \pm 3.5 \text{ mm}$	$5.4 \pm 2.9 \text{ mm}$
spine	$5.0 \pm 4.3 \text{ mm}$	$5.0 \pm 3.9 \text{ mm}$	$5.3 \pm 3.2 \text{ mm}$
mediastinum	$6.1 \pm 3.1 \text{ mm}$	$7.0 \pm 3.3 \text{ mm}$	$6.1 \pm 2.9 \text{ mm}$
abdomen	$8.4 \pm 5.6 \text{ mm}$	$13.4 \pm 12.0 \text{ mm}$	$8.8 \pm 5.8 \text{ mm}$
skin	$20.2 \pm 17.5 \text{ mm}$	$23.5 \pm 23.9 \text{ mm}$	$21.6 \pm 18.7 \text{ mm}$
Total	$8.8 \pm 9.6 \text{ mm}$	$11.0 \pm 13.1 \text{ mm}$	$9.0 \pm 10.1 \text{ mm}$

Fig. 70 shows the distance d_i found for each of the 4000 skin points of the reference geometry MRI-scan to the closest point of the personalized thorax mesh. d_i -values are not homogeneous. Highest d_i -values (worst fit) are concentrated on the arms, on breast and on the posterior part of the pelvis. The position of the volunteer (pelvis in standing position, arm over the shoulders) can explain d_i -values for these respective parts. Bad fit for the breast is more likely to be linked to the intrinsic anatomic differences between both genders. As the initial geometry is based on a man, these anatomic differences cannot be reproduced. Finally as CT-scan were performed 3 years ago (2009), the geometry of the volunteer could have changed during this period.

In most of the case, the *thoracic skin set* gives the best results.

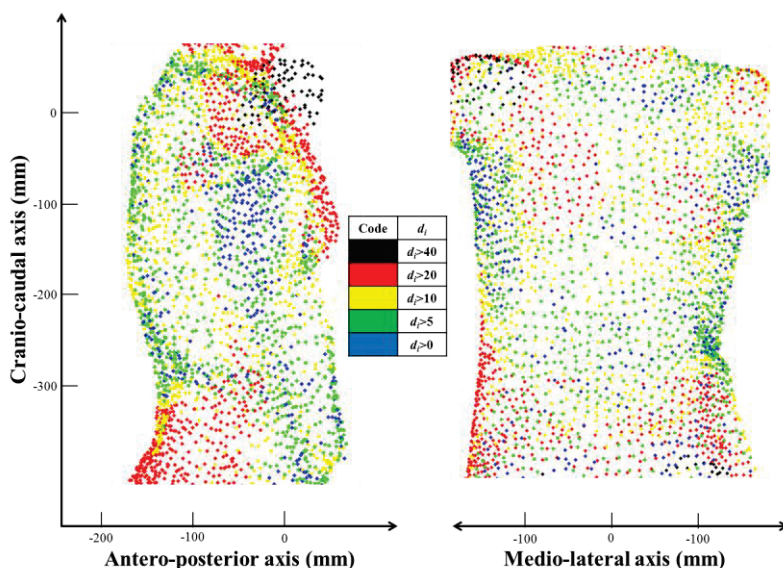


Fig. 70. View of the distance d_i found for skin point of the reference geometry CT-scan to the closest point of the personalized thorax mesh using *thoracic skin set*.

3.2 Assessment of the whole body geometrical personalization

3.2.1 Methods

Personalized model anthropometry dimensions for both subjects were compared to their anthropometry dimensions measured in vivo. In total, 15 thoracic dimensions and 17 general anthropometrical ones (including weight) were considered.

Mesh quality of each personalized body model was also evaluated using the “Element Quality” module included in LS-Prepost. Recommended value by the software was used in the limit for each criterion.

3.2.2 Results

The following tables give results of different set of candidate nodes as thoracic palpable points for different criterion: global anthropometries (**Table 22**), thoracic anthropometries (**Table 23**), weight (Table 24) and mesh quality (Table 25).

The set of candidate nodes as thoracic palpable points which optimized most both global and thoracic anthropometries is the *thoracic skin set*. With this set, the mean thoracic anthropometry difference between the volunteers and their respective personalized THUMS was below 4 % where it is 6% wrt standard THUMS for man volunteer and 21% for the woman volunteer. The mean body anthropometry difference was below 3% (standard THUMS: 5% for man volunteer, 13% for women volunteer). Similarly, mean weight difference was below 4% for both volunteers with this set.

It must be noticed that most of the time *thoracic bone set* implies massive difference with the anthropometry dimensions, in particular thoracic anthropometry and weight.

Finally, all personalized meshes tend to have a worse mesh quality than the initial one: about 1360 ± 366 additional elements violated the limitations for personalized meshes. Nevertheless, *thoracic skin set* and *thoracic bone&skin set* tend to have better score than *thoracic bone set*.

In conclusion, the selected set of thoracic palpable points for personalization is the *thoracic skin set*. Nodes definition is proposed in **Table 21**.

Table 21. Optimum set candidate nodes as thoracic palpable points.

Code	Thoracic skin set	Code	Thoracic skin set
CV_M_007	mid(8713006 - 8713013)	CLAV_R_004	mid(8984957 - 8984954)
TV_M_001	mid(8713013 - 8983045)	CLAV_R_005	8984276
TV_M_002	8983046	INF_L_001	8983840
TV_M_003	8983047	INF_L_002	8983831
TV_M_004	8983048	INF_L_003	8371930
TV_M_005	mid(8983050 - 8983049)	INF_R_001	8984804
TV_M_006	8983051	INF_R_002	8984795
TV_M_007	mid(8983052 - 8983053)	INF_R_003	8370764
TV_M_008	8983054	AXIL_L_001	8983235
TV_M_009	8983055	AXIL_L_002	8983247
TV_M_010	8983057	AXIL_L_003	8983863
TV_M_011	mid(8983058 - 8983057)	AXIL_R_001	8984237
TV_M_012	8983059	AXIL_R_002	8984249
STER_M_001	8984032	AXIL_R_003	8984825
STER_M_002	8983062	POST_L_001	8983149
STER_M_003	8983820	POST_L_003	8983926
ACRO_L_001	8983323	POST_L_002	mid(8983179 - 8983186)
CLAV_L_004	mid(8984002 - 8983999)	POST_R_003	8984881
CLAV_L_005	8983274	POST_R_002	mid(8984181 - 8984188)
ACRO_R_001	8984325	POST_R_004	8984891

Table 22. Results of man and woman personalization for different combination candidate nodes as thoracic palpable points on global anthropometry dimensions.

Code	Description	Reference values		THUMS 50th		THUMS skin set		THUMS Personalized with thoracic set below	
		♀	♂	Relative difference (♀)	Relative difference (♂)	Relative difference (♀)	Relative difference (♂)	Relative difference (♀)	Relative difference (♂)
ANTH_26a	Glabella - occiput lenght (mm)	185	197	11.6%	4.8%	0.1%	-0.4%	0.1%	-0.4%
ANTH_26b	Skull height auricular height (mm)	220	220	9.7%	9.7%	-0.4%	0.6%	0.8%	-0.5%
ANTH_26c	Head width (mm)	147	162	10.6%	0.3%	0.0%	0.0%	0.0%	0.0%
ANTH_19	Arm length (acromion - elbow) (mm)	350	380	10.6%	1.9%	-0.6%	2.7%	3.8%	1.0%
ANTH_44	Arm upper circumference (mm)	235	330	29.5%	7.8%	-0.2%	-0.5%	0.1%	-0.3%
ANTH_49	Arm bottom circumference (mm)	215	300	46.1%	4.7%	7.5%	10.9%	8.7%	13.5%
ANTH_18	Ulna length (mm)	260	280	9.4%	1.6%	-4.9%	-3.8%	-5.0%	-3.7%
ANTH_50	Greatest forearm circumference (mm)	215	265	28.6%	4.3%	2.3%	1.8%	2.7%	2.0%
ANTH_51	Smallest forearm circumference (mm)	135	165	21.1%	-0.9%	-5.6%	-4.8%	-5.4%	-4.7%
ANTH_06 - ANTH_07	Femur length (mm)	380	420	4.3%	-5.6%	0.3%	0.1%	0.3%	-0.1%
ANTH_36	Thigh upper circumference (mm)	510	580	3.9%	-8.6%	0.4%	4.7%	2.6%	1.8%
ANTH_37	Thigh bottom circumference (mm)	415	460	5.2%	-5.1%	-8.0%	-2.9%	-7.0%	-1.2%
ANTH_07 - ANTH_43	Tibia length (mm)	415	470	-4.6%	-15.8%	-4.4%	-4.6%	-4.1%	-4.3%
ANTH_39	Greatest calf circumference (mm)	340	395	6.6%	-8.3%	-6.6%	-6.9%	-6.3%	-6.2%
ANTH_40	Smallest ankle circumference (mm)	200	230	4.8%	-8.9%	-2.3%	-1.2%	-0.7%	-0.7%
ANTH_42	Greatest foot width (mm)	92	96	3.6%	-0.7%	-1.2%	0.4%	1.5%	-1.2%
ANTH_43	Greatest foot lenght (mm)	225	271	20.1%	-0.3%	-1.0%	-1.0%	-1.0%	-1.0%
Total (mean absolute difference)				13.6%	5.3%	2.7%	2.8%	2.7%	2.8%

Table 23. Results of man and woman personalization for different combination candidate nodes as thoracic palpable points on thoracic anthropometry dimensions.

Code	Description	Reference values		THUMS 50th		THUMS skin set		THUMS Personalized with thoracic set below	
		♀	♂	Relative difference (♀)	Relative difference (♂)	Relative difference (♀)	Relative difference (♂)	Relative difference (♀)	Relative difference (♂)
ANTH_15	Bi-acromial width (mm)	327	374	10.5%	-3.4%	-5.3%	1.3%	-1.1%	7.0%
RAM_15	Bi-deltoid width (mm)	400	510	8.4%	-15.0%	-4.3%	-6.6%	-6.4%	-6.0%
ANTH_20	Thoracic axillary width (mm)	282	349	32.0%	6.6%	1.7%	6.0%	16.4%	18.5%
ANTH_23	Thoracic sub-sternal width (mm)	264	338	29.8%	1.4%	3.8%	6.2%	15.8%	12.8%
ANTH_30	Abdominal width (mm)	267	327	14.0%	-6.9%	-4.0%	-2.5%	1.6%	3.8%
ANTH_38	Iliac bi-crest width (mm)	280	328	2.9%	-12.1%	-1.7%	-4.9%	-9.9%	-7.6%
ANTH_09	Bi-trochanter width (mm)	310	390	20.3%	-4.4%	5.5%	1.7%	9.9%	-2.0%
ANTH_21	Thoracic axillary thickness (mm)	158	220	39.5%	0.2%	5.8%	5.1%	39.5%	31.4%
ANTH_33	Abdominal thickness (mm)	180	241	31.0%	-2.1%	2.6%	3.6%	34.2%	31.9%
ANTH_24	Thoracic sub-sternal thickness (mm)	176	232	28.5%	-2.6%	-3.4%	2.2%	34.0%	29.1%
ANTH_46	Stemum length (mm)	180	240	23.2%	-7.6%	-0.2%	3.8%	-54.7%	9.3%
ANTH_47	Xiphoid angle (°)	79	103	35.6%	4.0%	-3.5%	-0.6%	-37.6%	-10.9%
ANTH_25	Thoracic sub-sternal circumference (mm)	800	960	12.8%	-6.0%	-5.7%	-1.4%	6.7%	11.8%
ANTH_22	Thoracic axillary circumference (mm)	870	1030	8.7%	-8.1%	-6.0%	-3.7%	0.0%	8.0%
ANTH_31	Abdominal circumference (mm)	720	960	18.4%	-11.2%	-5.5%	-6.6%	12.0%	7.6%
Total (mean absolute difference)				21.0%	6.1%	3.9%	3.8%	18.7%	7.4%

Table 24. Results of man and woman personalization for different combination candidate nodes as thoracic palpable points on weight.

Description	Reference values		THUMS 50th		Thoracic skin set		Thoracic bone set		Thoracic bone & skin set	
	♀	♂	Mass (kg)	Mass (kg)	Mass (kg)	Mass (kg)	♀	♂	Mass (kg)	Mass (kg)
Right Lower Ex*	-	-	-	-	12.9	10.9	16.0	11.1	16.4	10.9
Left Lower Ex*	-	-	-	-	12.9	10.9	16.1	11.1	16.4	11.0
Pelvic, Abdomen	-	-	-	-	14.6	9.7	17.2	13.0	21.8	10.2
Right Upper Ex*	-	-	-	-	3.6	2.0	3.8	2.1	4.0	2.0
Left Upper Ex*	-	-	-	-	3.6	2.0	3.8	2.1	4.0	2.1
Neck	-	-	-	-	1.1	0.8	1.0	0.9	1.2	0.8
Head	-	-	-	-	4.3	3.2	3.8	3.2	3.8	3.2
Thorax	-	-	-	-	22	13.9	26.1	18.0	34.7	14.4
Total	51.7	85.0	74.8	53.5	87.8	61.6	102.3	54.7	89.4	89.4
Relative difference	-	-	44.7%	-12.0%	3.6%	3.3%	19.1%	20.4%	5.8%	5.2%

Table 25. Results of man and woman personalization for different combination candidate nodes as thoracic palpable points on mesh quality.

Quality Name	Limit value	THUMS 50th		Thoracic skin set		Thoracic bone set		Thoracic bone & skin set	
		#Violated (%)	#Violated (%)	#Violated (%)	#Violated (%)	#Violated (%)	#Violated (%)	#Violated (%)	#Violated (%)
Min side length	1	2822 (3.8%)	2885 (3.9%)	2816 (3.8%)	2954 (4.0%)	2816 (3.8%)	2930 (4.0%)	2812 (3.8%)	2812 (3.8%)
Max side length	25	2801 (3.8%)	1858 (2.5%)	3929 (5.3%)	2471 (3.3%)	4940 (6.7%)	1847 (2.5%)	4154 (5.6%)	4154 (5.6%)
Aspect Ratio	10	717 (0.9%)	678 (0.9%)	680 (0.9%)	674 (0.9%)	723 (1.0%)	647 (0.9%)	671 (0.9%)	671 (0.9%)
Warpage	10	14772 (19.9%)	15064 (20.3%)	15248 (20.6%)	15555 (21.0%)	15661 (21.1%)	15136 (20.4%)	15255 (20.6%)	15255 (20.6%)
Min Quad Angle	45	1312 (1.8%)	1656 (2.2%)	1711 (2.3%)	1896 (2.6%)	1925 (2.6%)	1686 (2.3%)	1699 (2.3%)	1699 (2.3%)
Max Quad Angle	135	1828 (2.5%)	2185 (2.9%)	2244 (3.0%)	2426 (3.3%)	2394 (3.2%)	2278 (3.1%)	2227 (3.0%)	2227 (3.0%)
Min Tria Angle	30	2501 (3.4%)	2789 (3.7%)	2608 (3.5%)	2711 (3.7%)	2661 (3.6%)	2822 (3.8%)	2643 (3.6%)	2643 (3.6%)
Max Tria Angle	120	192 (0.3%)	247 (0.3%)	255 (0.3%)	300 (0.4%)	308 (0.4%)	250 (0.3%)	271 (0.4%)	271 (0.4%)
Taper	0.7	120 (0.16%)	165 (0.20%)	162 (0.2%)	224 (0.3%)	223 (0.3%)	144 (0.2%)	148 (0.2%)	148 (0.2%)
Skew	45	561 (0.8%)	774 (1.0%)	904 (1.2%)	946 (1.3%)	965 (1.3%)	867 (1.2%)	889 (1.2%)	889 (1.2%)
Jacobian	0.6	4388 (5.9%)	4809 (6.5%)	4881 (6.6%)	5098 (6.9%)	5124 (6.9%)	4821 (6.5%)	4803 (6.5%)	4803 (6.5%)
Char. length	1	2808 (3.8%)	2966 (4.0%)	2824 (3.8%)	3025 (4.1%)	2831 (3.8%)	2993 (4.0%)	2816 (3.8%)	2816 (3.8%)
Area	5	4731 (6.4%)	6245 (8.4%)	4488 (6.0%)	5925 (8.0%)	4249 (5.7%)	6157 (8.3%)	4329 (5.8%)	4329 (5.8%)
Feature angle	88	3469 (4.7%)	2940 (4.0%)	2921 (3.9%)	2935 (4.0%)	2934 (4.0%)	2963 (4.0%)	2983 (4.0%)	2983 (4.0%)
TimeStep	1.00E-06	275 (0.4%)	683 (0.9%)	370 (0.5%)	639 (0.9%)	378 (0.5%)	700 (0.9%)	358 (0.5%)	358 (0.5%)
Total failed (%)	26405 (35.6%)	27681 (37.4%)	27376 (36.9%)	28166 (38.0%)	28213 (38.1%)	27778 (37.5%)	27378 (36.9%)	27378 (36.9%)	27378 (36.9%)

4. Discussion

In this chapter, RBF method was applied to personalize THUMS model in posture and anthropometry with focus on thorax geometry, from in-vivo data. The process was validated by checking the mesh quality and comparing personalized model versus volunteer anthropometry and MRI-scans.

Although in-vivo data were too poor as control points for the personalization of THUMS, the geometrical personalization process using virtual control points permitted to handle both the thorax posture and the geometry personalization of the model without re-meshing. Moreover, this process permitted to keep a good mesh quality and THUMS characteristics (articular joint, ligament). Thus, as in-vivo data necessary for the geometrical personalization process are easy to obtain, this method is very efficient and very promising.

However, the resulting model is always more or less close to the initial geometry. In particular, genders difference cannot be reproduced. This could be corrected if the initial geometry used is the small female Total HUman Model for Safety (Kimpara et al. 2002). Moreover, pathological deformities of the thorax (pectus excavatum, pectus carinatum, pouter pigeon breast) and of the spine (lordosis, kyphosis) may not be reproduced in the current state of the process as thoracic anatomical landmarks are “cleaned” prior to the process. Deactivate the cleaning should deal with thorax and spine deformities but could imply large local mesh distortions and therefore additional post-processing work. However, an interesting alternative would be to increase the number of anatomical points in particular on the bone allowing for a better accuracy and therefore greater personalization power.

In **Chapter 4**, the personalization will be applied on specific subjects showing various anthropometries.

CHAPTER IV - INJURY RISK ON VULNERABLE INDIVIDUALS WITH PERSONALIZED HUMAN BODY FINITE ELEMENT MODELS

1. Introduction

In the present chapter, we provide the analysis of simulations using personalized THUMS models of six specific subjects. First, a validation of the models under a low pulse is presented. Then, simulations of more severe pulses are analysed to compare different levels of personalization on injury risk assessment.

2. Material and methods

2.1 Geometrically personalized FE models of human body

50th percentile male THUMS model was personalized in geometry using the method described in **Chapter 3**. Six geometric personalized models were created according to six volunteers. They are shown in **Fig. 71** and volunteers' anthropometries are available in **Table 26**. All volunteers were included for the sled test experiments described in **Chapter 2**.

Table 26. Anthropometric characteristics of volunteers subjected to THUMS personalization process.

ID	Gender	Age (yo)	Height (m)	Weight (kg)	BMI (kg/m ²)
806	M	21	1.96	88	23.1
957	F	23	1.55	58	24.5
442	M	35	1.75	86	28.0
370	F	20	1.70	90	31.1
948	M	25	1.69	73	25.6
118	M	65	1.67	75	27.0

Personalized models are identified by the volunteers' identification number. A version number was added in order to code their level of personalization:

- v 1.0.: geometrical personalization only
- v 1.1. and more: geometrical and material properties personalization.

Four geometrically personalized models represent young volunteers with various anthropometries (height, corpulence): a small woman with mid BMI (957) a mid-height

woman with high BMI (370), a mid-height man with high BMI (442), a tall man with mid BMI (806). No changes have been made in their material properties (v 1.0).

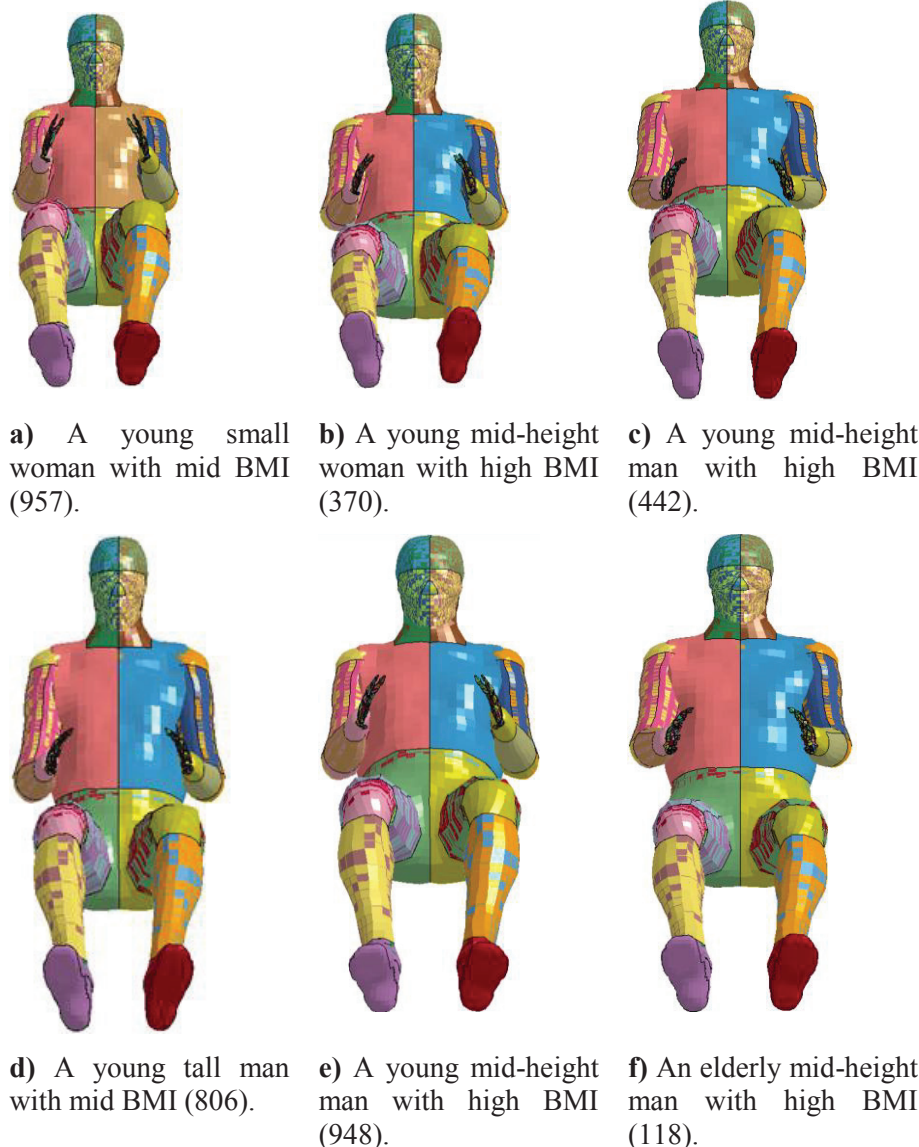


Fig. 71. Six geometrically personalized FE models.

The two others geometrically personalized models (948 & 118) represents 2 men of different age groups with similar corpulence and thoracic anthropometries (**Table 27**): the oldest is 118, the youngest 948.

Distribution of subjects for men (a) and women (b) are available in **Fig. 72**.

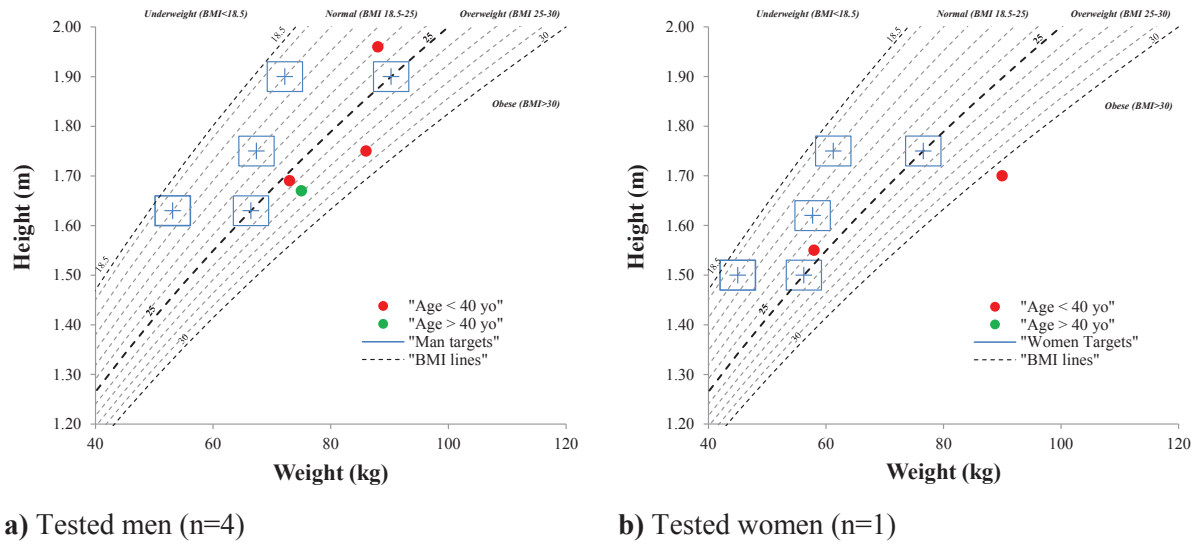


Fig. 72. Distribution of tested subjects compared to the initial targets based upon anthropometry charts (Jürgens et al., 1990).

Table 27. Thoracic anthropometries of volunteer 948 and 118

Code	Thoracic dimensions	Volunteer	
		948	118
ANTH_15	Bi-acromial width (mm)	390	384
RAM_15	Bi-deltoid width (mm)	450	448
ANTH_20	Thoracic axillary width (mm)	322	334
ANTH_23	Thoracic sub-sternal width (mm)	302	324
ANTH_30	Abdominal width (mm)	330	343
ANTH_08	Iliac bi-crest width (mm)	300	316
ANTH_09	Bi-trochanter width (mm)	345	337
ANTH_21	Thoracic axillary thickness (mm)	213	223
ANTH_33	Abdominal thickness (mm)	234	236
ANTH_24	Thoracic sub-sternal thickness (mm)	250	271
ANTH_46	Sternum length (mm)	190	195
ANTH_47	Xiphoid angle (°)	103	103
ANTH_25	Thoracic sub-sternal circumference (mm)	910	946
ANTH_22	Thoracic axillary circumference (mm)	920	970
ANTH_31	Abdominal circumference (mm)	970	1010

2.2 Material properties personalization considering aging

Material properties of the geometrically personalized models THUMS 948 and THUMS 118 were modified to correspond to the changes in bone material properties due to aging. Thus, material properties of cortical bone, trabecular bone, and cartilage for both rib and sternum and cortical thickness were decreased to correspond to an old subject.

Ito et al. developed adult (35 yr) and elderly (75 yr) human thorax FE models from H-model for evaluating thoracic skeletal injuries (Ito et al., 2009). Elderly material properties of the thoracic bones were estimated by applying the aging functions proposed for the femur bone

(Dokko et al., 2009). Cortical thickness of the elderly model was directly estimated on the basis of literature (Mohr et al., 2007).

Since H-model and THUMS material properties of the ribcage are both based on elastic-plastic formulation, the ratios applied by Ito to modify the yield stress, yield strain, ultimate strain, ultimate stress for their elderly model were reproduced on our personalized models. Extracted ratios are available in **Table 28** and material properties of the aged THUMS model in **Table 29**.

In the same way, cortical thickness ratio of rib and sternum are extracted from the ones applied by Ito et al. Cortical thickness used for aged THUMS models are available in **Table 30**.

Thus, different versions of THUMS 948 and THUMS 118 are developed according to the level of material personalization applied:

- v 1.0.: No material personalization
- v 1.1.: Thickness personalization
- v 1.2.: Cortical, Trabecular and Thickness personalization
- v 1.3.: Cartilage, Cortical, Trabecular and Thickness personalization

Levels of material property personalization and associated versions of personalized THUMS models are synthetized in **Table 31**.

Table 28. Ratio for personalization of material properties according to age from Ito et al. (2009).

Cortical bone				
	σ_y (MPa)	ϵ_y	σ_{max} (MPa)	ϵ_{max}
Adult (35 yo)	64.1	0.025	79.9	0.025
Elderly (70 yo)	54	0.021	68.3	0.021
Ratio elderly/adult	0.842	0.862	0.855	0.862
Trabecular bone				
	σ_y (MPa)	ϵ_y	σ_{max} (MPa)	ϵ_{max}
Adult (35 yo)	-	-	3.31	0.070
Elderly (70 yo)	-	-	1.25	0.078
Ratio elderly/adult			0.378	1.115
Cartilage				
	σ_y (MPa)	ϵ_y	σ_{max} (MPa)	ϵ_{max}
Adult (35 yo)	-	-	9.41	1.8%
Elderly (70 yo)	-	-	7.16	1.4%
Ratio elderly/adult			0.761	0.772

2.3 Solver and software

The solver used is LS-DYNA (mpp971sR3.2.1, LSTC, Livermore, CA, USA). The host machine is a multi-core Intel Xeon64, on Linux Red Hat 4. The pre and post processor used are LS-PREPOST (v3.0, LSTC, Livermore, CA, USA) and scripts written in Matlab (R2007b, The MathWorks Inc., Natick, MA, USA).

2.4 Sled configuration

The personalized THUMS models are positioned in a generic interior vehicle model representative of a sled test configuration, under action of gravity. The models were restrained by 3-point belt system with retractor pretensioner and load limiter representative of a mid-size sedan car. The footrest, seat and knee bolster are modeled as rigid bodies and adjusted to be in contact with the personalized THUMS at the beginning of the simulation, according to the volunteer adjustments during in vivo experiments. In addition the belt shape was deformed according to the thorax shape using RBF (Buhmann, 2000).

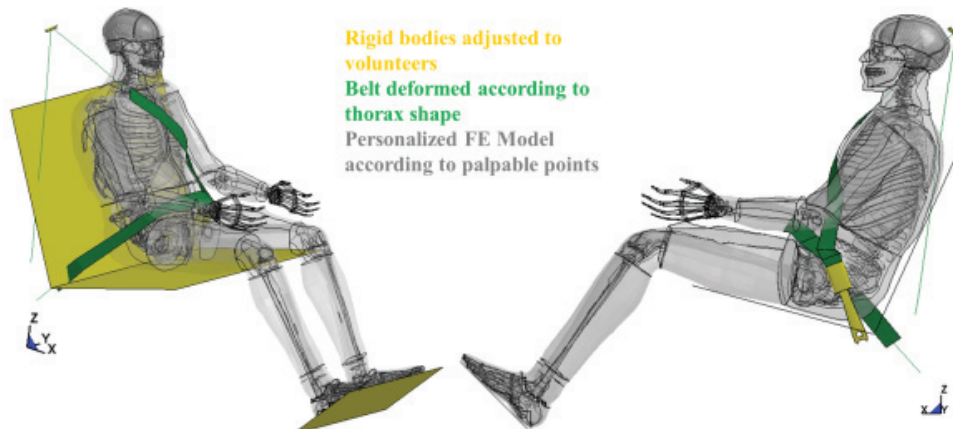


Fig. 73. Generic interior vehicle model with a personalized THUMS human body model.

Table 29. Material properties of the initial THUMS model (1) and the aged THUMS model (2).

	ρ (kg/m ³)	YM (MPa)	ϵ_{y1}	σ_{y1} (MPa)	ϵ_{y2}	σ_{y2} (MPa)	ϵ_{y3}	σ_{y3} (MPa)	ϵ_{y4}	σ_{y4} (MPa)	σ_{max} (MPa)	ϵ_{max}
Cartilage-1	1000	49.0	0.0000	4.8	0.1675	9.0	0.3296	10.0	-	-	-	0.3296
Cartilage-2	1000	49.0	0.0000	3.7	0.1293	6.8	0.2545	7.6	-	-	-	0.2545
Cortical-1	2000	13000	0.0000	93.5	0.0715	128.0	0.0185	150.0	-	-	-	0.0180
Cortical-2	2000	13000	0.0000	79.9	0.0617	109.4	0.0159	128.2	-	-	-	0.0154
Trabecular-1	862	40.0	0.0000	1.8	0.0500	3.8	0.0600	4.1	0.1000	5.0	-	0.1030
Trabecular-2	862	40.0	0.0000	0.7	0.0557	1.4	0.0669	1.5	0.1115	1.9	-	0.1148

Table 30. Cortical thickness of the initial THUMS model (1) and the aged THUMS model (2).

Code	Cortical thickness (mm)	Sternum thickness (mm)
Thickness-1	0.70	1.00
Thickness-2	0.60	0.86

Table 31. Level of material property personalization and associated versions of personalized THUMS models.

	Cartilage-1	Cartilage-2	Cortical-1	Cortical-2	Thickness-1	Thickness-2	Trabecular-1	Trabecular-2
Thums-118 v1.0	Yes	No	Yes	No	Yes	No	Yes	No
Thums-118 v1.1	Yes	No	Yes	No	Yes	Yes	Yes	No
Thums-118 v1.2	Yes	No	No	Yes	Yes	No	No	Yes
Thums-118 v1.3	No	Yes	No	Yes	No	Yes	No	Yes
Thums-948 v1.0	Yes	No	Yes	No	Yes	No	Yes	No
Thums-948 v1.1	Yes	No	Yes	No	Yes	Yes	Yes	No
Thums-948 v1.2	Yes	No	No	Yes	Yes	No	Yes	Yes
Thums-948 v1.3	No	Yes	No	Yes	No	Yes	No	Yes

The model and the sled were subjected first to a low-speed, non-injurious deceleration pulse similar to the one applied on volunteers (4g, 8km/h), coded IV8; then to a high-speed, injurious deceleration pulse (13 g, 40 km/h), coded IJ40 similar to literature (Lopez-Valdes et al., 2010). These deceleration pulses are shown in **Fig. 74**. The simulation duration time is 150 ms.

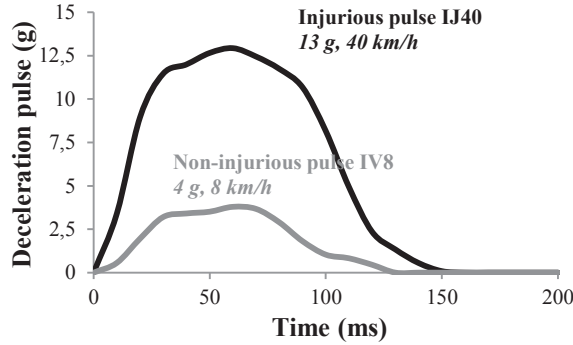


Fig. 74. Low speed (gray) and high speed (black) pulses used for the sled test simulations.

2.5 Simulation matrix

The six geometrically personalized models and the initial THUMS model were subjected to the low-speed sled test (IV8). The six geometrically personalized models correspond to six different volunteers subjected to in-vivo sled tests (**Chapter 2**). No material properties personalization was applied for low-speed simulations.

At high speed, the 6 geometrically personalized models and the initial THUMS model were subjected to high speed sled test (IV40). For 4 models (957, 370, 442, 806) and the initial THUMS, no material properties personalization was applied. A progressive material properties personalization was applied for 948 and 118 models.

Table 32 synthetizes the different simulations.

Table 32. Simulation tests matrix

Num	Model	Pulse
S0-1	AM50	IV8
S0-2	AM50	IJ40
S1-1	957 v 1.0	IV8
S1-2	957 v 1.0	IJ40
S2-1	370 v 1.0	IV8
S2-2	370 v 1.0	IJ40
S3-1	442 v 1.0	IV8
S3-2	442 v 1.0	IJ40
S4-1	806 v 1.0	IV8
S4-2	806 v 1.0	IJ40
S5-1	118 v 1.0	IV8
S5-2	118 v 1.0	IJ40
S5-3	118 v 1.1	IJ40
S5-4	118 v 1.2	IJ40
S5-5	118 v 1.3	IJ40
S6-1	948 v 1.0	IV8
S6-2	948 v 1.0	IJ40
S6-3	948 v 1.1	IJ40
S6-4	948 v 1.2	IJ40
S6-5	948 v 1.3	IJ40

2.6 Measurements

Thoracic excursions were measured at the 1st thoracic vertebral position (T1), at the 7th thoracic vertebral position (T7) and at the 4th lumbar vertebral position of the model (L4). They are reported as relative displacements from the sled along its longitudinal axis (x-sled).

The chest deflections were measured at mid-sternum and at four additional points taken directly on cartilage (**Fig. 75**). Two mid-sternum deflections were measured. The first one was measured using nodes taken on skin and the other directly on the bony structure of the sternum and the 7th thoracic vertebral spinous process. Midsternum deflection measured on skin corresponds to the one measured in vivo sled tests (**Chapter 2**). The multi-point deflections were measured directly on both side of the ribcage, at 5 cm to the sternum, on the cartilage of the 4th rib and between the 6th and the 7th rib. They are reported in an axis-direction parallel to the midsternum deflection.

Chest compressions were defined as the respective chest deflections divided by the initial thickness of the thorax measured on skin at midsternum level.

Similarly to Lau and Viano, a viscous response was defined by a time dependent function formed by the product of the instantaneous velocity of midsternum deflection measured on bone, and the instantaneous compression, defined as the midsternum deflection measured on bone divided by the initial thickness of the thorax measured on skin at midsternum level. The

viscous response peak $[VC]_{max}$ similar to the Viscous Criterion was computed consequently. This criterion is used to address the effect of velocity of deformation (Lau and Viano, 1986).

Contact forces between the human body model and the vehicle interior model (seat, backseat, footrest) and belt loads were computed in the binary outputs. Force-deflection curves were built using resultant shoulder belt force F_{Res} (see **Chapter 2**) and mid-sternum deflection.

Outputs were computed for each millisecond of the simulation and a global output (d3plot) was printed each 10 milliseconds.

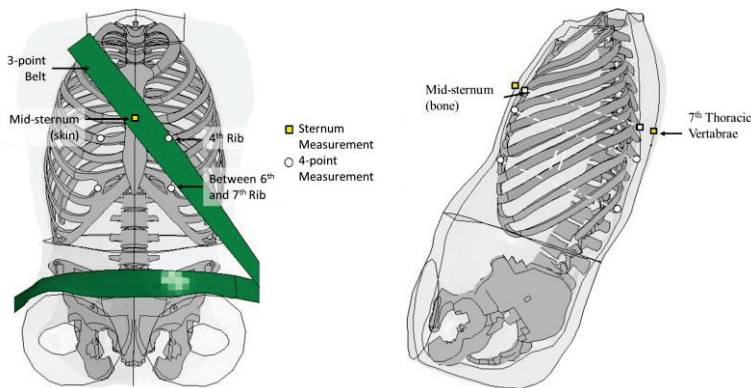


Fig. 75. Definition of the points used for chest deflection measurement during simulation.

2.7 Rib injury assessment

The ribs elements erased by the model were used to locate and quantify the number of fractured ribs (NFR) as shown in **Fig. 76**. An estimate torso AIS (TOAIS) was computed according to the number of fractured ribs and their location (**Table 33**). “Flail chest” is defined as three or more consecutive ribs fractured in more than one side. Costal cartilage fracture or tear is coded separately according the side which is injured.

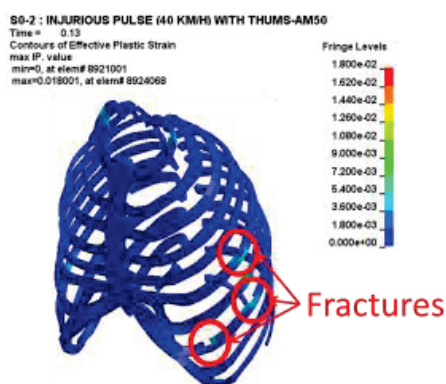


Fig. 76. Prediction of bone fractures in simulation.

Table 33. Computation of Torso Abbreviated Injury Scale (TOAIS) according to the number of fractured ribs and their location (AIS 2005).

Area	AIS2005	Description	AIS
Rib cage		multiple rib fractures	2
-	450210.2	fracture(s) without flail, any location unilateral or bilateral	1
-	450200.1	one rib	1
-	450201.1	two ribs	2
-	450202.2	≥ 3 ribs	3
-	450203.3	fractures with flail, NFS	3
-	450209.3	unilateral flail chest NFS	3
-	450211.3	$3\text{--}5$ flail ribs	3
-	450212.3	>5 flail ribs	4
-	450213.4	bilateral flail chest	5
-	450214.5	fracture	2
Sternum	450804.2		2
		TOAIS	Max(AIS)

3. Responses of geometrically personalized models at low speed

To use the geometrically personalized models as efficient prediction tool, it is important to validate it under dynamic conditions. Simulations outputs from geometrically personalized models were compared to outputs from initial model and to in-vivo sled test data. Results of these comparisons are synthetized in **Table 34**.

The comparison of the model-predicted and measured maximum relative excursions at different positions (T1, T7, L4) shows that in general, similar relative excursions were obtained between numerical and experimental even if they tend to be lower for the personalized models compared to the volunteer data.

Comparisons of the belt loads time histories between the model and the test data are illustrated in **Fig. 77**, **Fig. 78**, **Fig. 79** and **Fig. 80**. Similar curves were obtained between the responses of geometrically personalized models and real subjects.

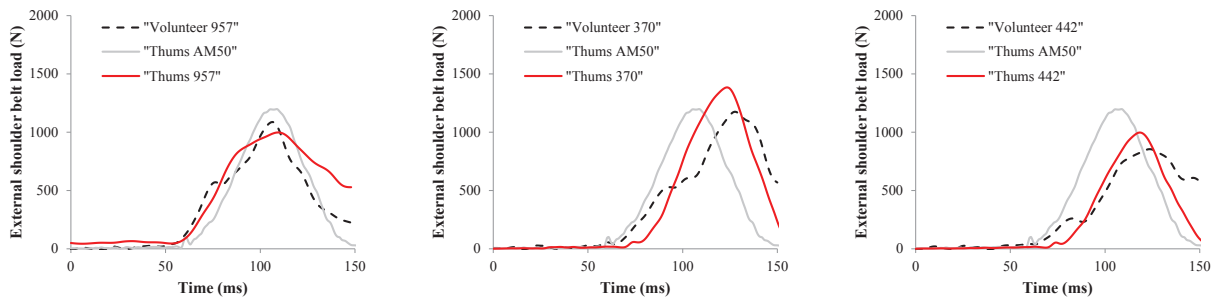
Fig. 81 and **Fig. 82** compare the model-predicted and measured histories of mid-sternum deflections and compression. In general, similar deflections were obtained between mid-sternum deflection measured on ribcage of geometrically personalized models and mid-sternum deflection measured on volunteer at low speed. Little variability was obtained for mid-sternal deflection measured on ribcage of geometrically personalized models. A significant difference was obtained between the mid-sternum deflection measured on skin model and the mid-sternum deflection measured directly on bony structure of the model.

Comparisons of the thoracic force-deflection responses between geometrically personalized models and thoracic force-deflection responses obtained on volunteers are shown in **Fig. 83**. The calculated thoracic responses to dynamic chest compression are almost similar with the experimental results.

As expected, no bone fracture was observed for all models at low speed.

Table 34. Thoracic mechanical characteristics obtained on geometrically personalized models and volunteers at low-speed (4g, 8km/h).

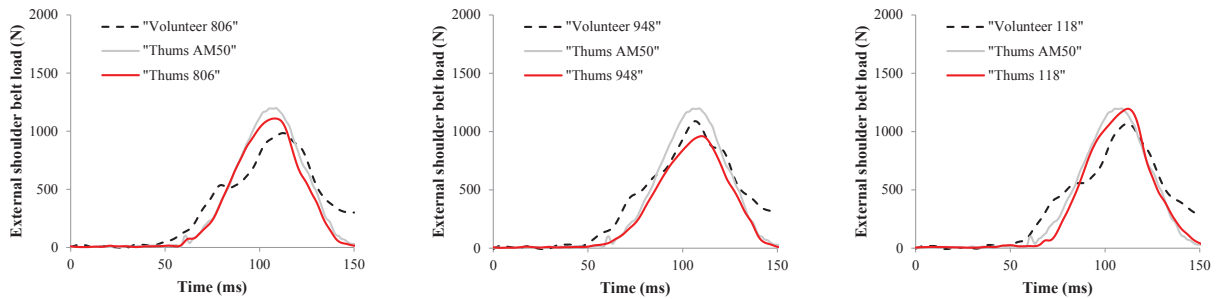
#ID	FB3 _{max} [N]	FB4 _{max} [N]	FB6 _{max} [N]	FRes _{max} [N]	Foot _{max} [N]	T1 X-Exc. [mm]	T7 X-Exc. [mm]	L4 X-Exc. [mm]
#ID	Volunteer	Simulation	Volunteer	Simulation	Volunteer	Simulation	Volunteer	Simulation
AM50 v1.0	-	1197	-	1220	-	551	-	880
957 v1.0	1090	997	1126	809	913	708	721	582
370 v1.0	1181	1383	1588	1690	897	787	884	1038
442 v1.0	856	996	930	1121	396	511	582	717
806 v1.0	986	1109	1113	1374	529	715	526	690
948 v1.0	1092	960	1138	1279	546	595	821	823
118 v1.0	1067	1195	1253	1157	641	659	726	818
AM50 v1.0	-	787	-	18.4	12.4	-	-	8.0%
957 v1.0	869	864	22.5	16.8	9.4	12.0%	8.7%	5.2%
370 v1.0	1028	861	19.5	24.7	10.9	8.9%	10.2%	4.5%
442 v1.0	1082	824	26.5	19.9	9.7	10.3%	7.7%	3.8%
806 v1.0	1275	826	14.1	24.7	10.0	6.5%	10.6%	4.3%
948 v1.0	1048	598	23.3	20.4	9.6	10.4%	8.3%	3.9%
118 v1.0	824	670	16.7	18.8	6.8	7.2%	7.7%	2.8%
AM50 v1.0	-	131.3	-	77.8	-	-	-	52.4
957 v1.0	146.9	116.4	93.0	77.8	63.7	80.3	84.2	68.9
370 v1.0	147.1	117.3	97.1	79.2	76.3	62.5	76.3	67.3
442 v1.0	145.2	111.9	106.6	73.2	64.6	67.3	64.6	70.9
806 v1.0	115.2	153.1	71.5	92.7	68.7	91.4	86.9	91.4
948 v1.0	108.2	112.5	84.9	75.8	68.7	70.9	82.3	88.2
118 v1.0	97.6	132.7	87.6	94.2	86.9	91.4	88.2	91.4



a) A young small woman with mid BMI (957).

b) A young mid-height woman with high BMI (370).

c) A young mid-height man with high BMI (442).

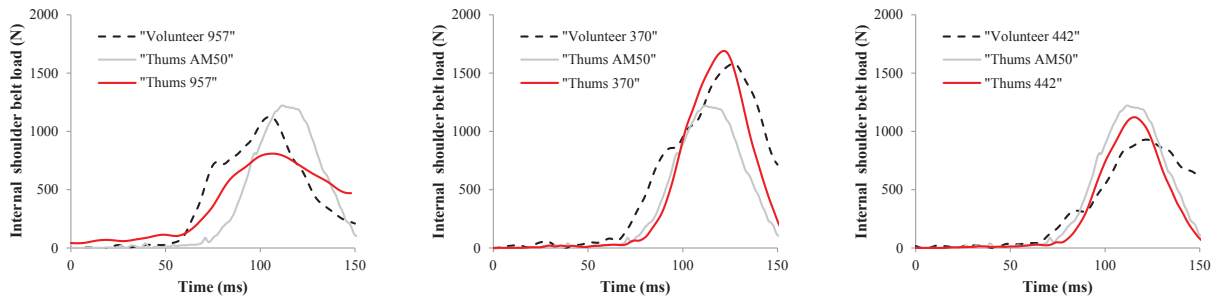


d) A young tall man with mid BMI (806).

e) A young mid-height man with high BMI (948).

f) An elderly mid-height man with high BMI (118).

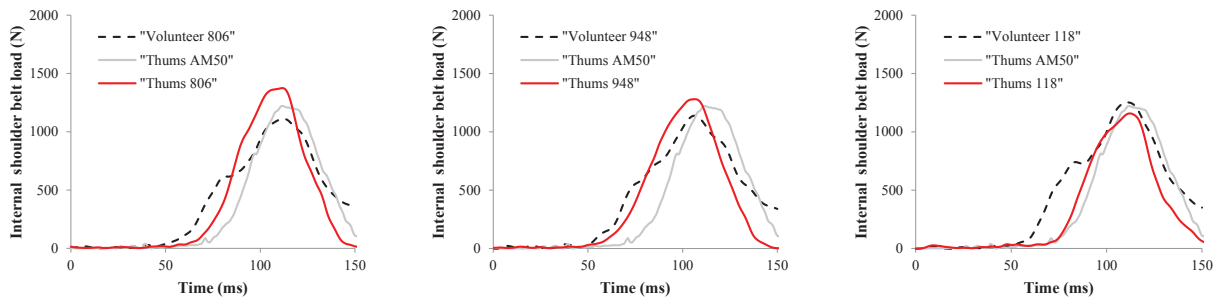
Fig. 77. Comparisons of external shoulder belt load FB3 between geometrically personalized models and in-vivo sled tests at low speed (4 g, 8 km/h).



a) A young small woman with mid BMI (957).

b) A young mid-height woman with high BMI (370).

c) A young mid-height man with high BMI (442).



d) A young tall man with mid BMI (806).

e) A young mid-height man with high BMI (948).

f) An elderly mid-height man with high BMI (118).

Fig. 78. Comparisons of internal shoulder belt load FB4 between geometrically personalized models and in-vivo sled tests (4 g, 8 km/h).

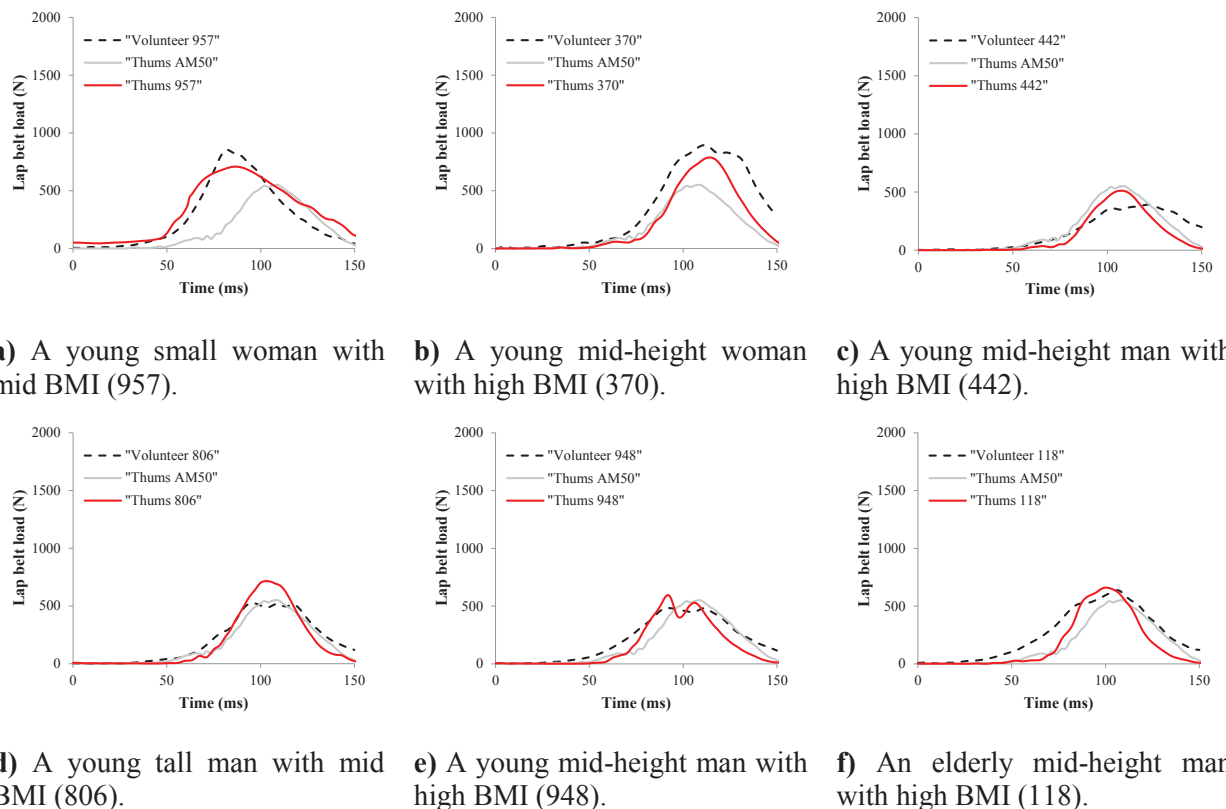


Fig. 79. Comparisons of the lap shoulder belt load FB6 between geometrically personalized models and in-vivo sled tests (4 g, 8 km/h).

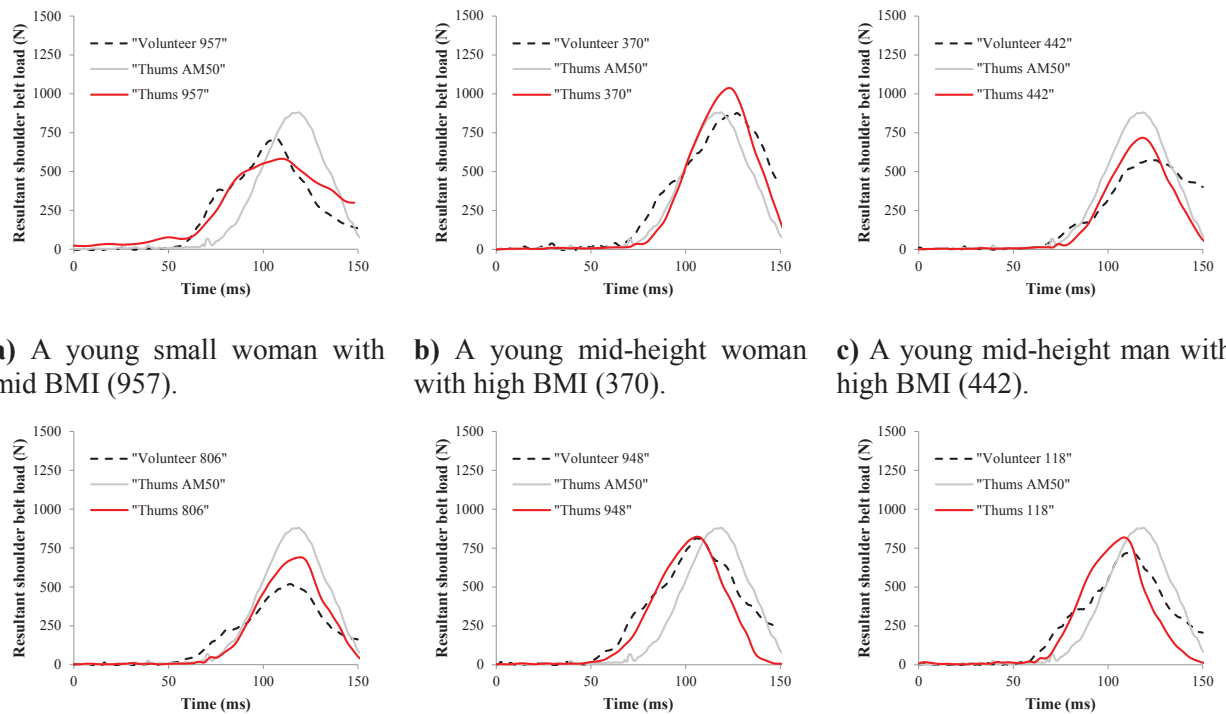
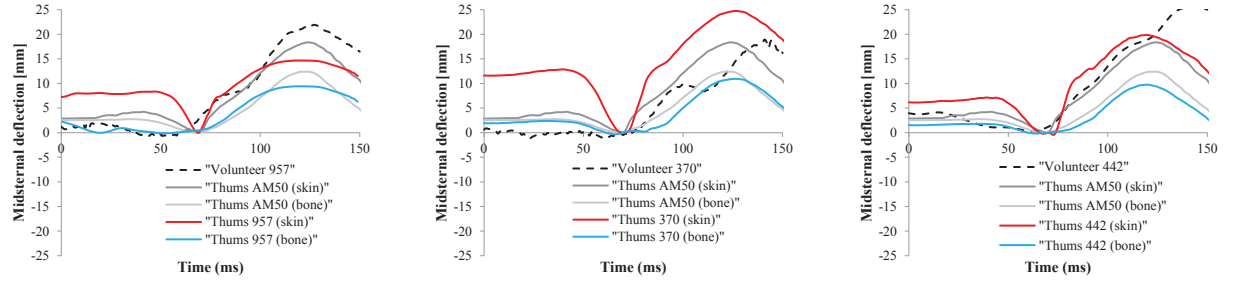


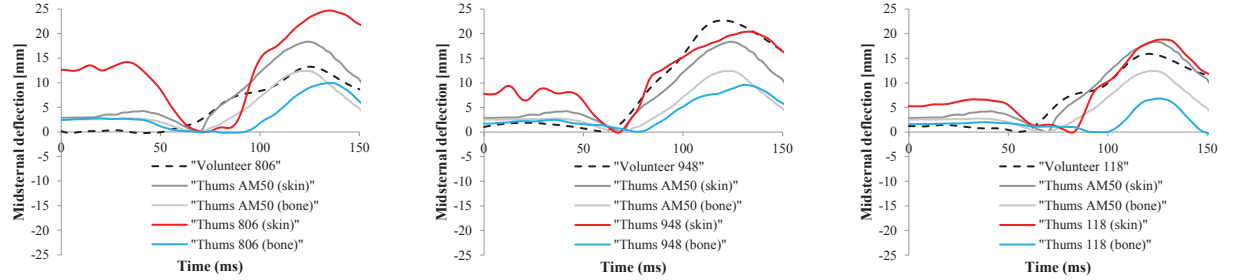
Fig. 80. Comparisons of the resultant shoulder belt load FRes between geometrically personalized models and in-vivo sled tests (4 g, 8 km/h).



a) A young small woman with mid BMI (957).

b) A young mid-height woman with high BMI (370).

c) A young mid-height man with high BMI (442).

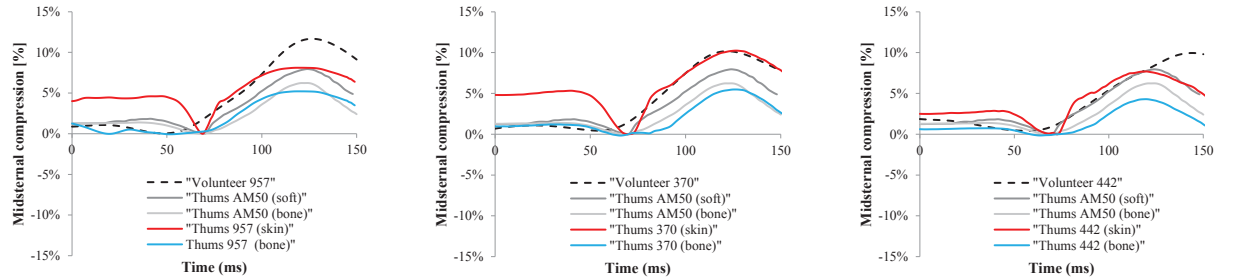


d) A young tall man with mid BMI (806).

e) A young mid-height man with high BMI (948).

f) An elderly mid-height man with high BMI (118).

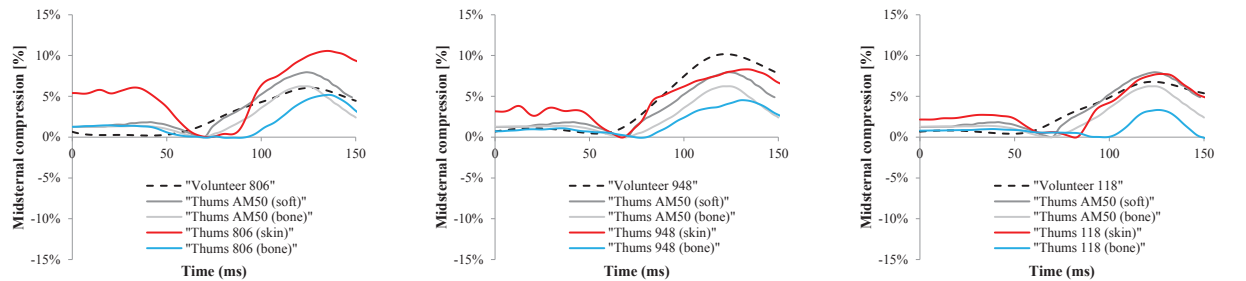
Fig. 81. Comparisons of mid-sternum deflections between geometrically personalized models and in-vivo sled tests (4 g, 8 km/h).



a) A young small woman with mid BMI (957).

b) A young mid-height woman with high BMI (370).

c) A young mid-height man with high BMI (442).



d) A young tall man with mid BMI (806).

e) A young mid-height man with high BMI (948).

f) An elderly mid-height man with high BMI (118).

Fig. 82. Comparisons of mid-sternum compression between geometrically personalized models and in-vivo sled tests (4 g, 8 km/h).

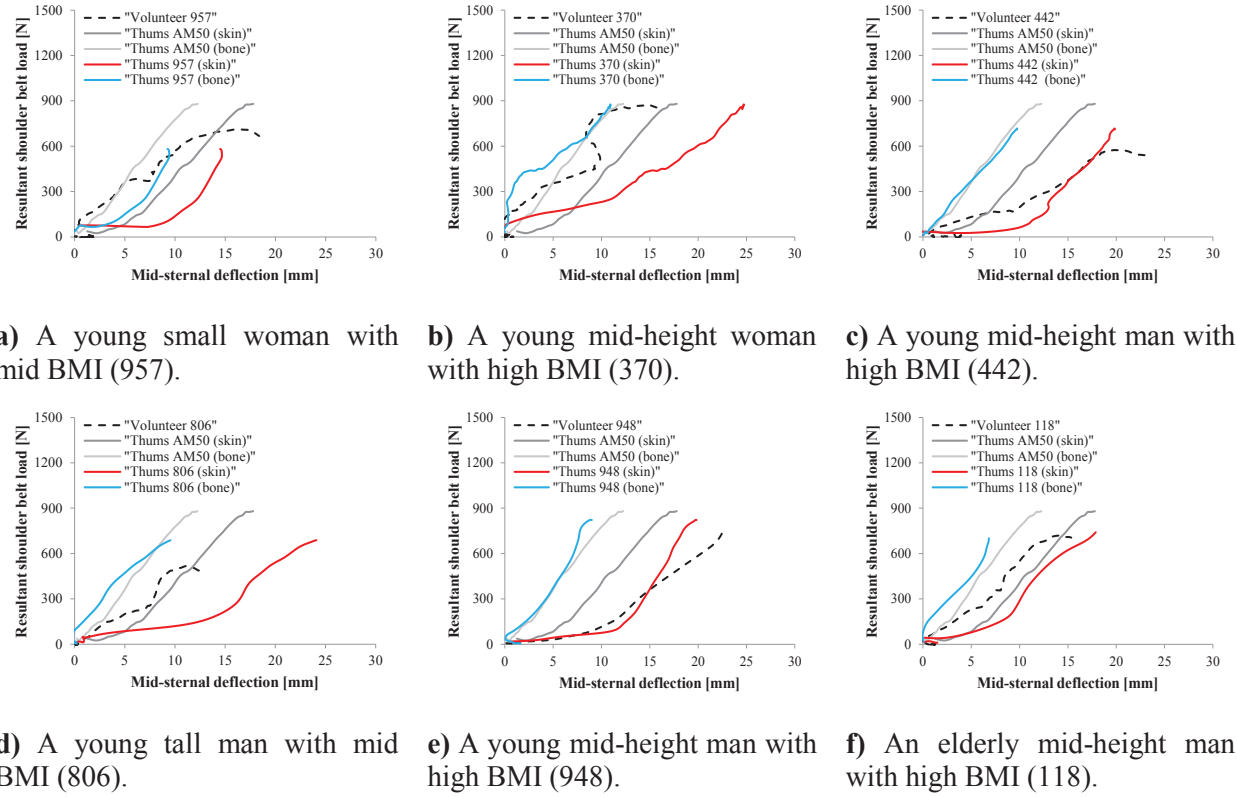


Fig. 83. Comparisons of the thoracic forces-deflection responses between geometrically personalized models and volunteers (4 g, 8 km/h).

4. Influence of personalization levels on thoracic injury risk prediction

4.1 Influence of geometrical personalization

Simulations maximal outputs from the four geometrically personalized models are available in **Table 35** and illustrated in **Fig. 84**. **Table 36** synthetizes the location of rib fractures and the number of elements erased during the simulations. Thoracic force-deflection responses obtained from geometrically personalized models and initial THUMS model are shown in **Fig. 85**.

The recess of the curves that appears after 4000 N corresponds to the action of the load limiter. The load limiter permits to limit the effect of thorax inertia on loading and thus the belt loads variability as observed in **Table 35**.

Fig. 86 shows the Von Mises stress distribution at maximum bony midsternal deflection time for the four geometrically personalized models. Stress concentration was observed at the left part of the rib cage and on sternum as expected for this configuration of belt loading. Nevertheless, stress distribution is quite variable between geometrically personalized models.

Thus, stresses are concentrated on sternum for THUMS 957 v1.0 while stresses are concentrated on ribs for THUMS 370 v1.0. These differences may be due to the difference in thorax shape. In addition, maximum midsternal deflection occurs at different times for the different geometrical personalized models (between 60 ms and 90 ms).

The number of rib fractures and their location also vary greatly among models. Thums 806 v1.0 is clearly the model most injured among all others counting the number of fractured ribs (14 ribs). In addition, as three or more consecutive ribs are fractured in both sides for this model, a bilateral flail chest is counted (TOAIS=5). An explanation for this phenomenon is due to the fact that the volunteer 806 has relatively heavy torso (28 kg on personalized model) because of his height (1.96 m). Thus, the thorax may self-chARGE more easily despite the opposing action of the force limiter. This hypothesis may be confirmed by the fact that model THUMS 370 v1.0 whose associate volunteer also has a heavy thorax (26 kg on personalized model), also suffered higher damage (8 ribs fractured).

In addition, some outputs seem to be correlated to the number of fractured ribs (NFR). In **Fig. 87**, the number of fractured ribs is displayed crossed upper right chest compression, Vcmax and midsternal deflection measured on bone. There is a link ($R^2=0.97$, $p< 0.01$) between the upper right chest compression and the number of fractured ribs. Similarly, there is a link ($R^2=0.78$; $p=0.05$) between the midsternal deflection measured on bone and NFR. These correlations imply that excessive rib injuries observed for extreme anthropometries (806 & 370) may be linked to higher crushing effect on ribcage especially on the side that bears the load (upper right). In addition, there is a link ($R^2=0.82$; $p=0.03$) between $[VC]_{max}$ and the number of fractured ribs. This correlation implies that excessive rib injuries observed for extreme anthropometries may be also associated with higher effect of velocity of deformation.

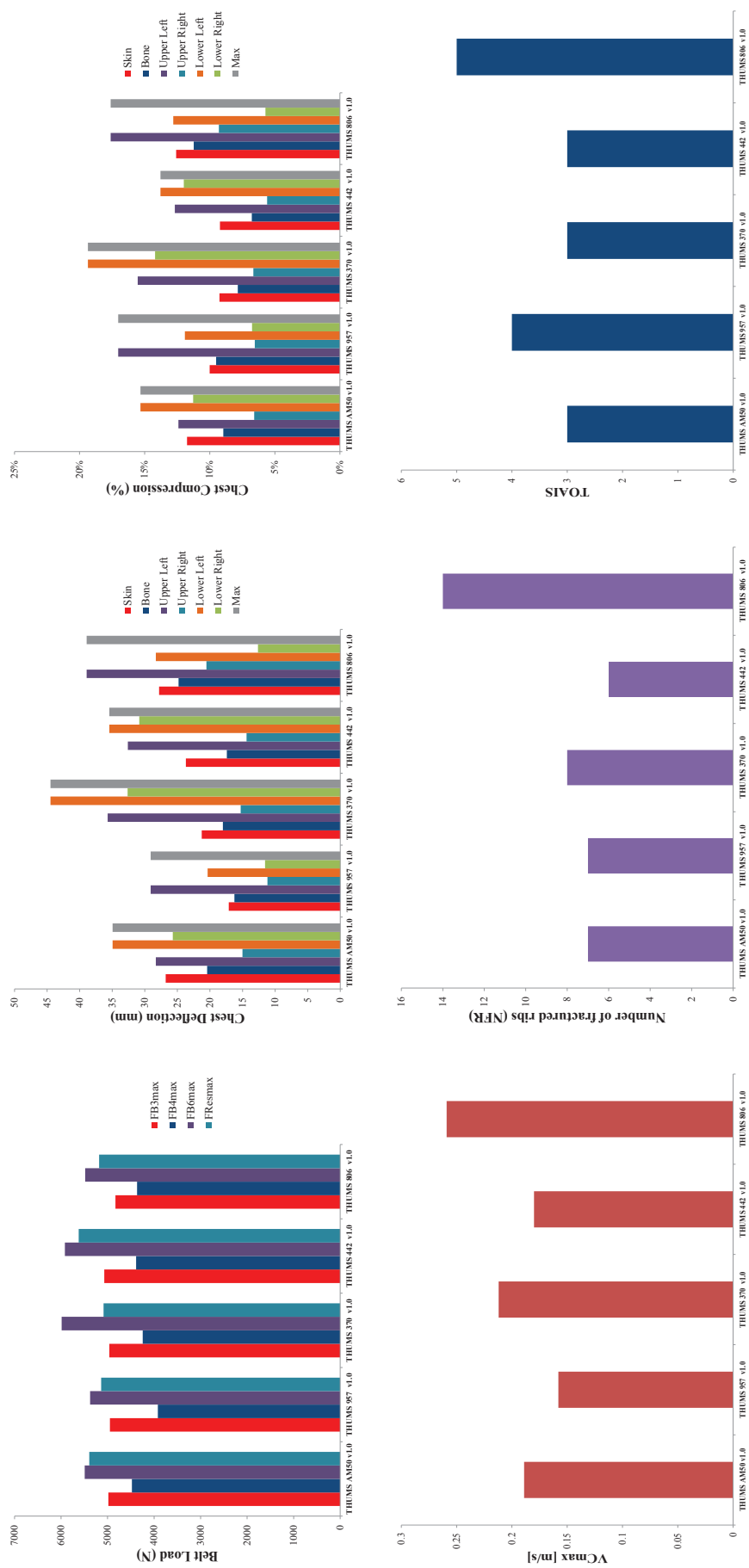


Fig. 84. Maximum outputs for different geometrically personalized models.

Table 35. Thoracic mechanical characteristics dataset obtained on geometrically personalized models at high-speed (13g, 40km/h).

Num	Model	Maximum belt loads peaks [N]				Chest Deflection [mm]					
		FB3 _{max}	FB4 _{max}	FB6 _{max}	FRes _{max}	Skin	Bone	Upper Left	Upper Right	Lower Left	Lower Right
S0-2	THUMS AM50 v1.0	4983	4477	5492	5393	26.8	20.4	28.3	15.0	34.9	25.7
S1-2	THUMS 957 v1.0	4950	3920	5375	5139	17.1	16.2	29.1	11.2	20.4	11.5
S2-2	THUMS 370 v1.0	4963	4243	5987	5086	21.3	18.0	35.7	15.3	44.5	32.6
S3-2	THUMS 442 v1.0	5071	4386	5917	5619	23.7	17.4	32.6	14.4	35.5	30.9
S4-2	THUMS 806 v1.0	4830	4367	5482	5181	27.8	24.7	38.6	20.2	28.7	12.9
Mean ± SD		4959 ± 87	4278 ± 278	5650 ± 221	5284 ± 280	23.3 ± 4.3	19.4 ± 3.4	32.9 ± 4.5	15.3 ± 3.4	32.7 ± 9.0	22.7 ± 10.0
Num	Model	Chest Compression [%]						VC _{max} [m/s]			
		Upper	Upper	Lower	Lower	Left	Right	Max	NFR	TOAIS	
S0-2	THUMS AM50 v1.0	11.8%	8.9%	12.4%	6.6%	15.3%	11.3%	15.3%	0.189	7	3
S1-2	THUMS 957 v1.0	10.0%	9.5%	17.0%	6.6%	11.9%	6.7%	17.0%	0.158	7	4
S2-2	THUMS 370 v1.0	9.3%	7.8%	15.5%	6.7%	19.4%	14.2%	19.4%	0.212	8	3
S3-2	THUMS 442 v1.0	9.2%	6.8%	12.7%	5.6%	13.8%	12.0%	13.8%	0.180	6	3
S4-2	THUMS 806 v1.0	12.6%	11.2%	17.5%	9.1%	13.0%	5.8%	17.5%	0.259	14	5
Mean ± SD		10.8 ± 2.0%	8.8 ± 2.0%	15.0 ± 1.7%	6.9 ± 1.3%	14.7 ± 2.4%	10 ± 3.6%	16.6 ± 2.9%	0.200 ± 2.1%	8.4 ± 0.038	3.6 ± 0.9

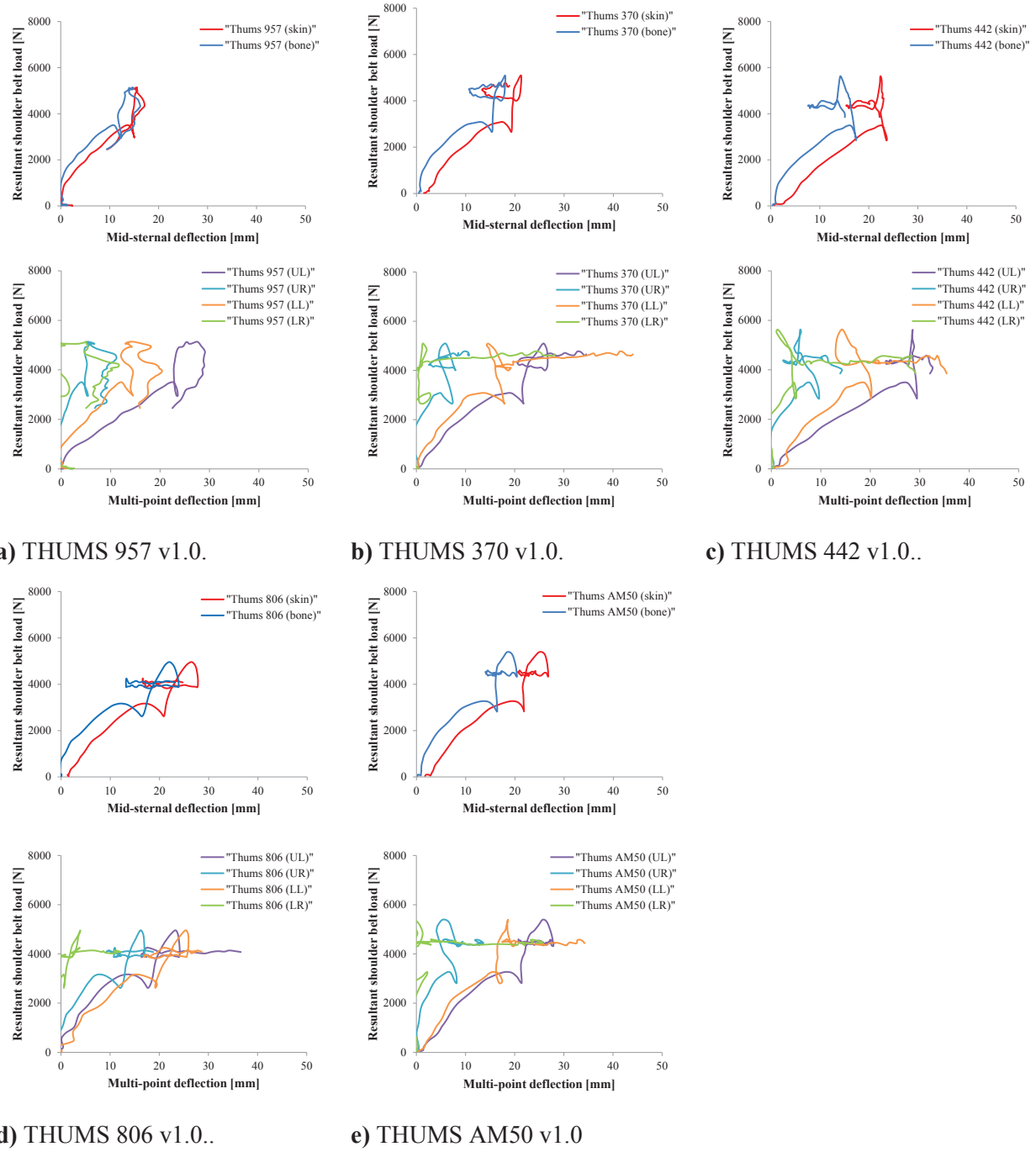


Fig. 85. Force-deflection obtained for geometrically personalized models at high speed (IJ40).

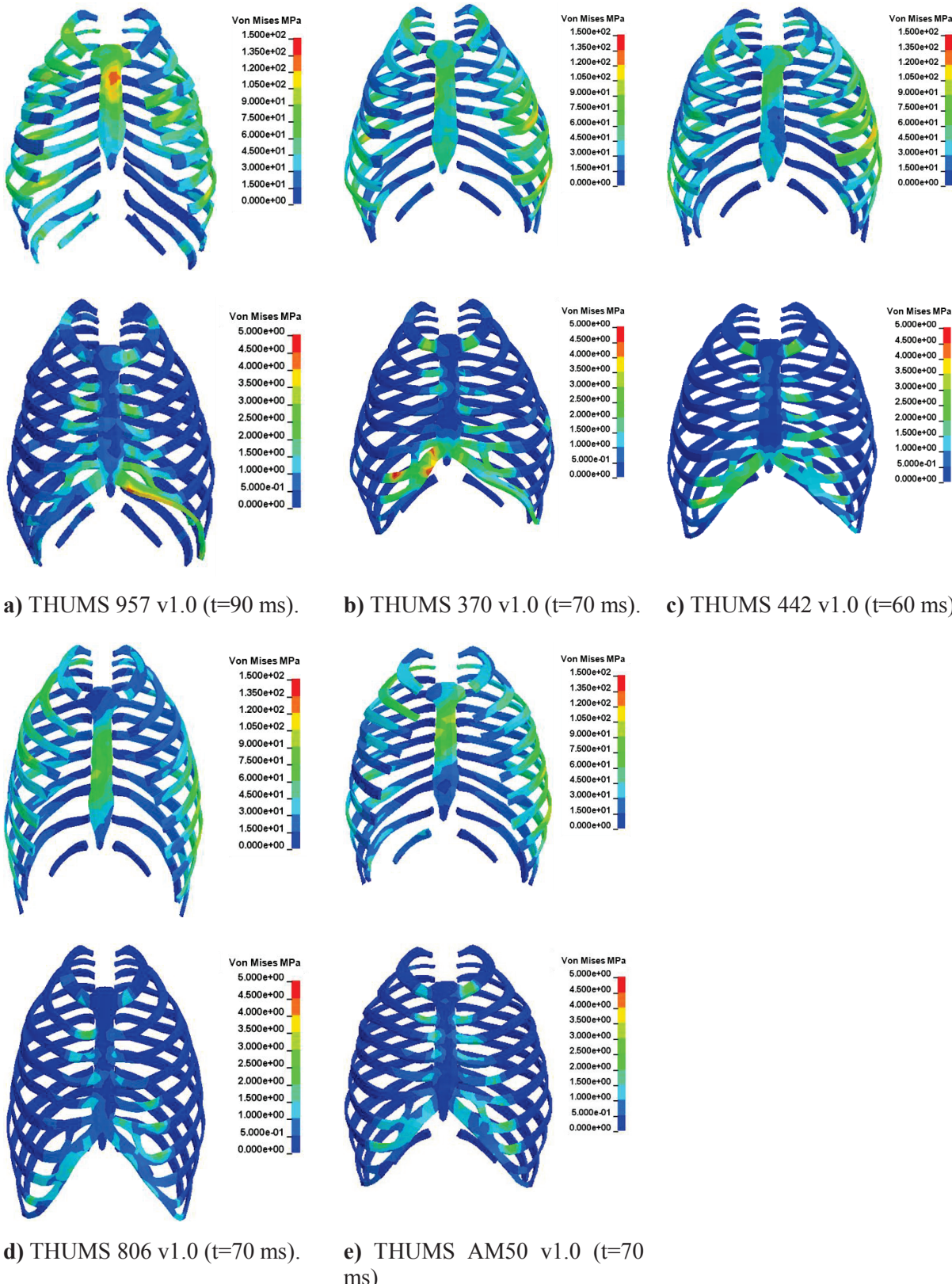


Fig. 86. Von Mises stress contour obtained for geometrically personalized models in high speed sled tests at maximum bony midsternal deflection time (upper: cortical, lower: cartilage & trabecular).

Table 36. Fractures summarize for geometrically personalized models at high speed (IJ40).

Code	Thums AIM50 v1.0			Thums 957 v1.0			Thums 370 v1.0			Thums 442 v1.0			Thums 806 v1.0		
	1 st occ. (ms)	N# elements	1 st occ. (ms)	N# elements	1 st occ. (ms)	N# elements	1 st occ. (ms)	N# elements	1 st occ. (ms)	N# elements	1 st occ. (ms)	N# elements	1 st occ. (ms)	N# elements	
L_rib01	94.6	1	-	-	80.3	1	140.6	3	112.1	53	-	-	-	-	
L_rib02	94.4	3	84.7	7	80.1	7	96.4	6	110.6	49	-	-	-	-	
L_rib03	-	-	120.3	1	-	-	-	-	109.9	78	-	-	-	-	
L_rib04	-	-	126.3	1	-	-	152.2	5	110.0	72	-	-	-	-	
L_rib05	85.6	4	75.9	15	140.4	1	135.7	3	112.1	43	-	-	-	-	
L_rib06	-	-	-	-	86.2	1	-	-	-	-	-	-	-	-	
L_rib07	96.3	2	-	-	86.6	6	-	-	108.0	2	-	-	-	-	
L_rib08	128.6	1	-	-	-	-	-	-	-	-	-	-	-	-	
L_rib09	-	-	-	-	-	-	-	-	83.6	5	-	-	-	-	
L_rib10	-	-	-	-	-	-	-	-	-	-	-	-	-	-	
L_rib11	-	-	-	-	-	-	-	-	-	-	-	-	-	-	
L_rib12	-	-	-	-	-	-	-	-	-	-	-	-	-	-	
R_rib01	119.0	6	107.3	8	105.3	9	117.4	3	112.7	1	-	-	-	-	
R_rib02	-	-	79.4	18	129.6	6	-	-	-	-	112.6	25	-	-	
R_rib03	-	-	103.2	1	-	-	-	-	-	-	112.1	79	-	-	
R_rib04	-	-	-	-	-	-	-	-	-	-	109.9	120	-	-	
R_rib05	-	-	-	-	-	-	-	-	-	-	112.3	50	-	-	
R_rib06	-	-	-	-	-	-	-	-	-	-	112.1	78	-	-	
R_rib07	102.9	4	-	-	82.6	3	-	-	-	-	112.1	82	-	-	
R_rib08	-	-	-	-	-	-	-	-	-	-	-	-	-	-	
R_rib09	-	-	-	-	-	-	-	-	-	-	-	-	-	-	
R_rib10	-	-	-	-	-	-	-	-	-	-	-	-	-	-	
R_rib11	-	-	-	-	-	-	-	-	-	-	-	-	-	-	
R_rib12	-	-	118.4	2	90.7	46	80.4	13	97.1	174	-	-	-	-	
Sternum	94.7	10	-	-	85.6	19	90.9	5	92.6	49	-	-	-	-	
L_cart	100.0	6	-	-	102.4	13	83.3	4	93.3	86	-	-	-	-	
R cart	111.9	7	102.2	20	-	-	-	-	-	-	-	-	-	-	

Table 37. Computation of Torso Abbreviated Injury Scale (TOAIS) according to the number of fractured ribs and their location for geometrically personalized models at high speed (IJ40).

Area	AIS2005	Description	AIS	THUMS AM50 v1.0	THUMS v1.0	THUMS 957 v1.0	THUMS 370 v1.0	THUMS 442 v1.0	THUMS 806 v1.0
Rib cage	450210.2	multiple rib fractures	2	1	1	1	1	1	1
-	450200.1	fracture(s) without flail, any location unilateral or bilateral	1	1	0	0	1	1	0
-	450201.1	one rib	1	1	0	0	1	1	0
-	450202.2	two ribs	2	1	0	0	1	1	0
-	450203.3	≥ 3 ribs	3	1	0	0	1	1	0
-	450209.3	fractures with flail, NFS	3	0	1	1	0	0	1
-	450211.3	unilateral flail chest NFS	3	0	1	1	0	0	0
-	450212.3	3-5 flail ribs	3	0	1	1	0	0	0
-	450213.4	> 5 flail ribs	4	0	1	0	0	0	0
-	450214.5	bilateral flail chest fracture	5	0	0	0	0	1	1
Sternum	450804.2		2	1	1	1	1	1	1
		TOAIS	3	4	3	3	3	3	5

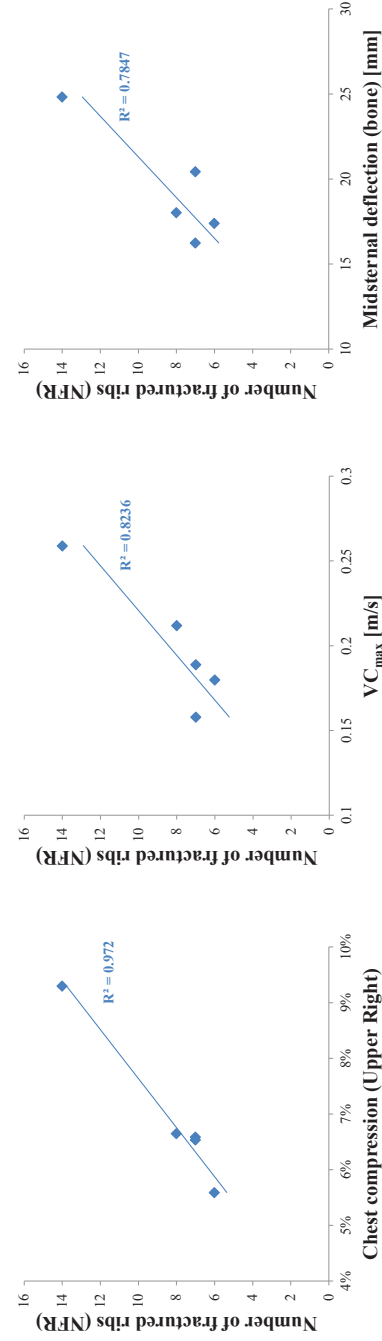


Fig. 87. Significant correlations of outputs with the number of fractured ribs.

4.2 Influence of material property modifications

Maximum outputs from personalized models 948 and 118 considering aging are available in **Table 38** and illustrated in **Fig. 88**. Thoracic force-deflection responses of personalized models considering aging are shown in **Fig. 89**. No significant difference was found in thoracic mechanical response between personalized models considering aging and geometrically personalized models only. Nevertheless, the number of fractured ribs and consequently the estimated Torso AIS (TOAIS) significantly increase as the material properties get personalized, significantly after cortical and trabecular material properties are updated (v1.2).

Fig. 90 shows the Von Mises contour at maximum bony midsternal deflection time for the personalized models considering aging. Stress concentration was observed at the left part of the rib cage and on sternum as expected for this configuration of belt loading. There is no clear difference between THUMS v1.0 (geometrical personalization only) and THUMS v1.1 (Cortical thickness decreasing) neither in the amount and nor in the location of Von Mises stress. There is a significant difference in the amount of Von Mises stress when material properties of cortical bone and trabecular are modified (v1.2 and more). Nevertheless, there is no clear difference between THUMS v1.2 (material properties of cortical and trabecular updated) and THUMS v1.3 (material properties of cartilage updated) neither in the amount and nor in the location of Von Mises stress.

Table 39 synthetized the location of rib fractures and the number of elements erased for the personalized models considering aging. The number of fractured ribs increases as the model get personalized considering aging. The number of fractured ribs slightly increased (≈ 1 fractured rib) when cortical thickness is personalized (v 1.1) and fractured ribs may occur slightly before. There is a significant increase of fractured ribs (≈ 5) when material properties of rib are personalized (v 1.2) and fractured ribs occur 7 ms before. The number of fractured ribs slightly increased (≈ 2 fractured rib) when material properties of the cartilage are finally personalized (v 1.3). As expected, a significant increase of the number of deleted cartilage elements is observed. It should be noted that for both personalized models (948 & 118), at least a flail chest with more than 5 ribs is counted when material properties of cortical bone and trabecular were modified (v1.2 and more).

In addition, there is no significant link between simulated outputs and NFR.

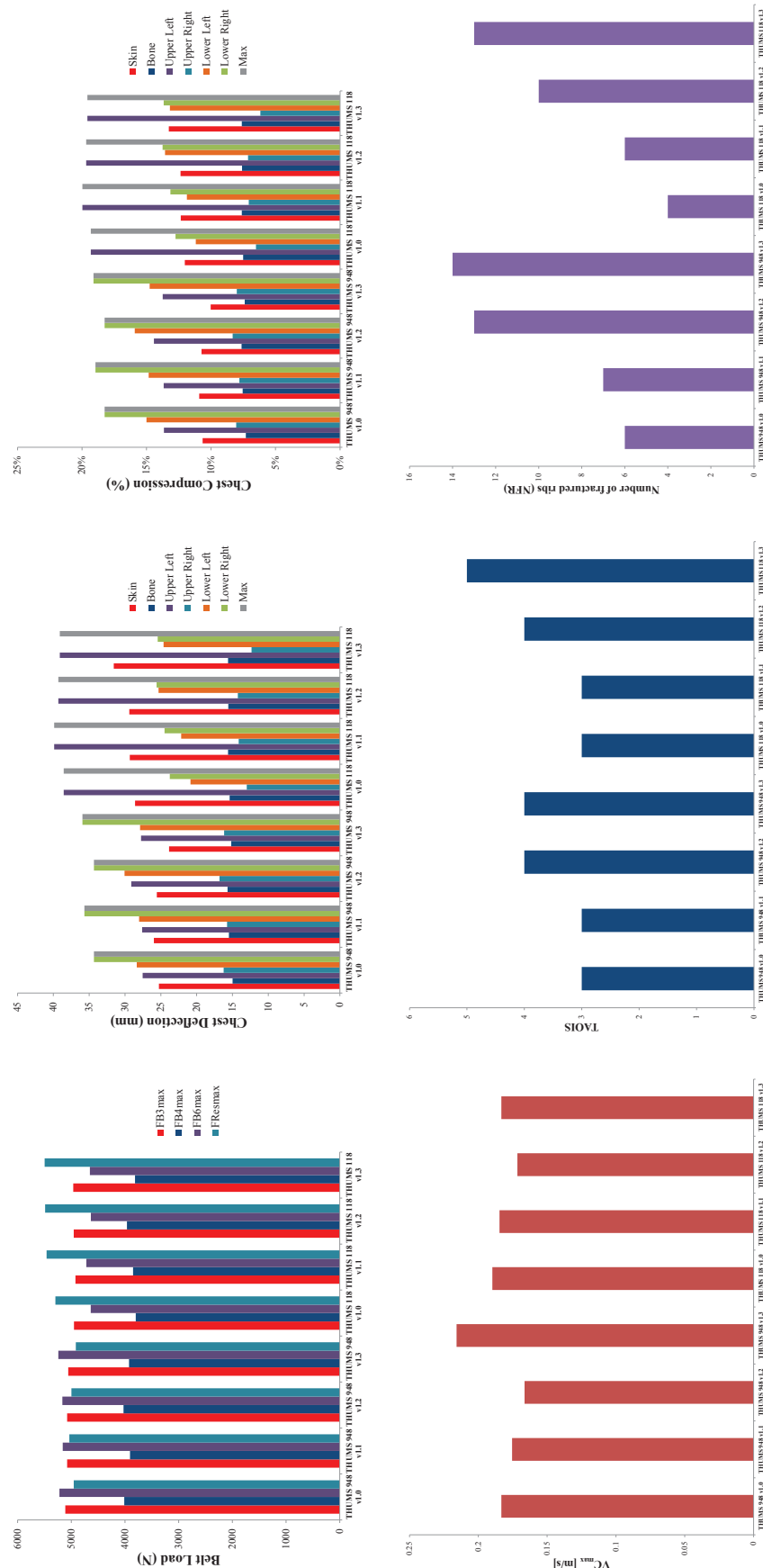


Fig. 88. Maximum outputs for different personalized models considering aging.

Table 38. Thoracic mechanical characteristics dataset obtained on personalized models considering aging at high-speed (13g, 40km/h).

Num	Model	Maximum belt loads peaks [N]				Chest Deflection [mm]					
		FB3 _{max}	FB4 _{max}	FB6 _{max}	FRes _{max}	Skin	Bone	Upper Left	Upper Right	Lower Left	Lower Right
S5-2	THUMS 948 v1.0	5110	4014	5220	4953	25.3	15.0	27.5	16.2	28.4	34.3
S5-3	THUMS 948 v1.1	5076	3907	5159	5036	26.0	15.5	27.6	15.8	28.0	35.7
S5-4	THUMS 948 v1.2	5076	4028	5166	4996	25.6	15.7	29.1	16.8	30.1	34.3
S5-5	THUMS 948 v1.3	5057	3924	5241	4916	23.9	15.2	27.8	16.2	27.9	35.9
Mean ± SD		5080 ± 22	3968 ± 61	5196 ± 40	4975 ± 52	25.2 ± 0.9	15.3 ± 0.3	28 ± 0.8	16.2 ± 0.4	28.6 ± 1	35.1 ± 0.9
S6-2	THUMS 118 v1.0	4950	3799	4638	5294	28.6	15.4	38.6	13.0	20.9	38.6
S6-3	THUMS 118 v1.1	4921	3848	4720	5459	29.3	15.6	39.9	14.1	22.2	39.9
S6-4	THUMS 118 v1.2	4954	3964	4635	5488	29.4	15.6	39.3	14.3	25.3	39.3
S6-5	THUMS 118 v1.3	4964	3814	4654	5496	31.6	15.6	39.1	12.3	24.6	39.1
Mean ± SD		4947 ± 18	3856 ± 75	4662 ± 40	5434 ± 95	29.7 ± 1.3	15.6 ± 0.1	39.2 ± 0.5	13.4 ± 0.9	23.2 ± 2.1	39.2 ± 0.5
Chest Compression [%]											
Num	Model	Skin	Bone	Upper Left	Upper Right	Lower Left	Lower Right	Max	Max	VC _{max} [m/s]	NFR
S5-2	THUMS 948 v1.0	10.7%	6.3%	11.6%	6.8%	12.0%	14.5%	14.5%	14.5%	0.1833	6
S5-3	THUMS 948 v1.1	10.9%	6.5%	11.6%	6.6%	11.8%	15.0%	15.0%	15.0%	0.1755	7
S5-4	THUMS 948 v1.2	10.8%	6.6%	12.2%	7.1%	12.6%	14.4%	14.4%	14.4%	0.1664	13
S5-5	THUMS 948 v1.3	10.0%	6.4%	11.7%	6.8%	11.7%	15.1%	15.1%	15.1%	0.2158	14
Mean ± SD		10.6 ± 0.5	6.5 ± 0.1	11.8 ± 0.3	6.8 ± 0.2	12.0 ± 0.4	14.7 ± 0.4	14.7 ± 0.4	14.7 ± 0.4	0.185 ± 0.022	3.5 ± 0.6
S6-2	THUMS 118 v1.0	12.0%	6.5%	16.2%	5.5%	8.8%	10.0%	16.2%	16.2%	0.1898	4
S6-3	THUMS 118 v1.1	12.3%	6.6%	16.8%	5.9%	9.3%	10.3%	16.8%	16.8%	0.1846	6
S6-4	THUMS 118 v1.2	12.4%	6.6%	16.5%	6.0%	10.6%	10.8%	16.5%	16.5%	0.1716	4
S6-5	THUMS 118 v1.3	13.3%	6.6%	16.4%	5.2%	10.3%	10.7%	16.4%	16.4%	0.1833	13
Mean ± SD		12.5 ± 0.5	6.5 ± 0.2	16.5 ± 0.4	9.8 ± 0.4	10.4 ± 0.4	16.5 ± 0.4	16.5 ± 0.4	16.5 ± 0.4	0.182 ± 0.008	3.8 ± 1.0

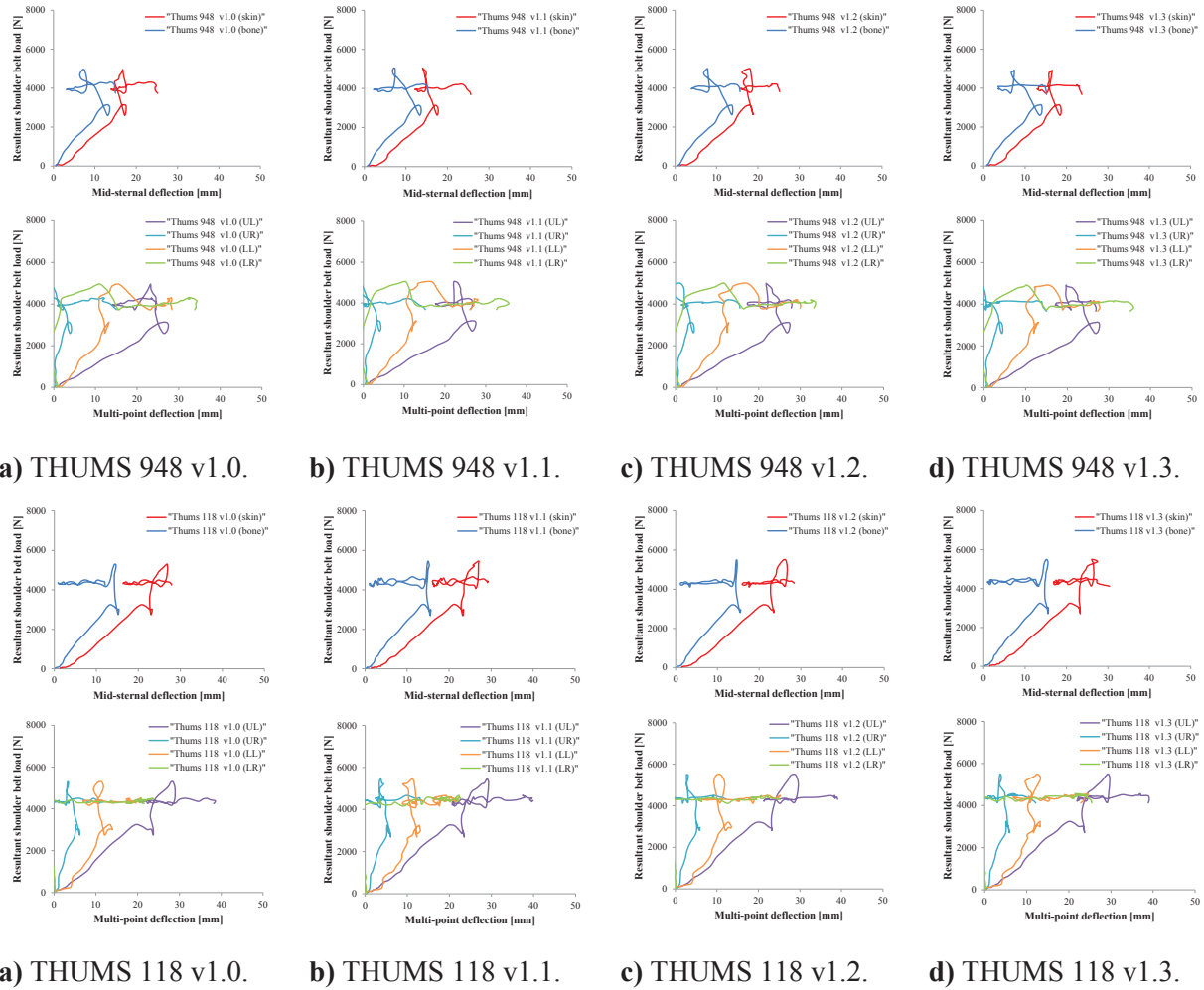


Fig. 89. Force-deflection obtained for personalized models considering aging at high speed (13 g, 40 km/h).

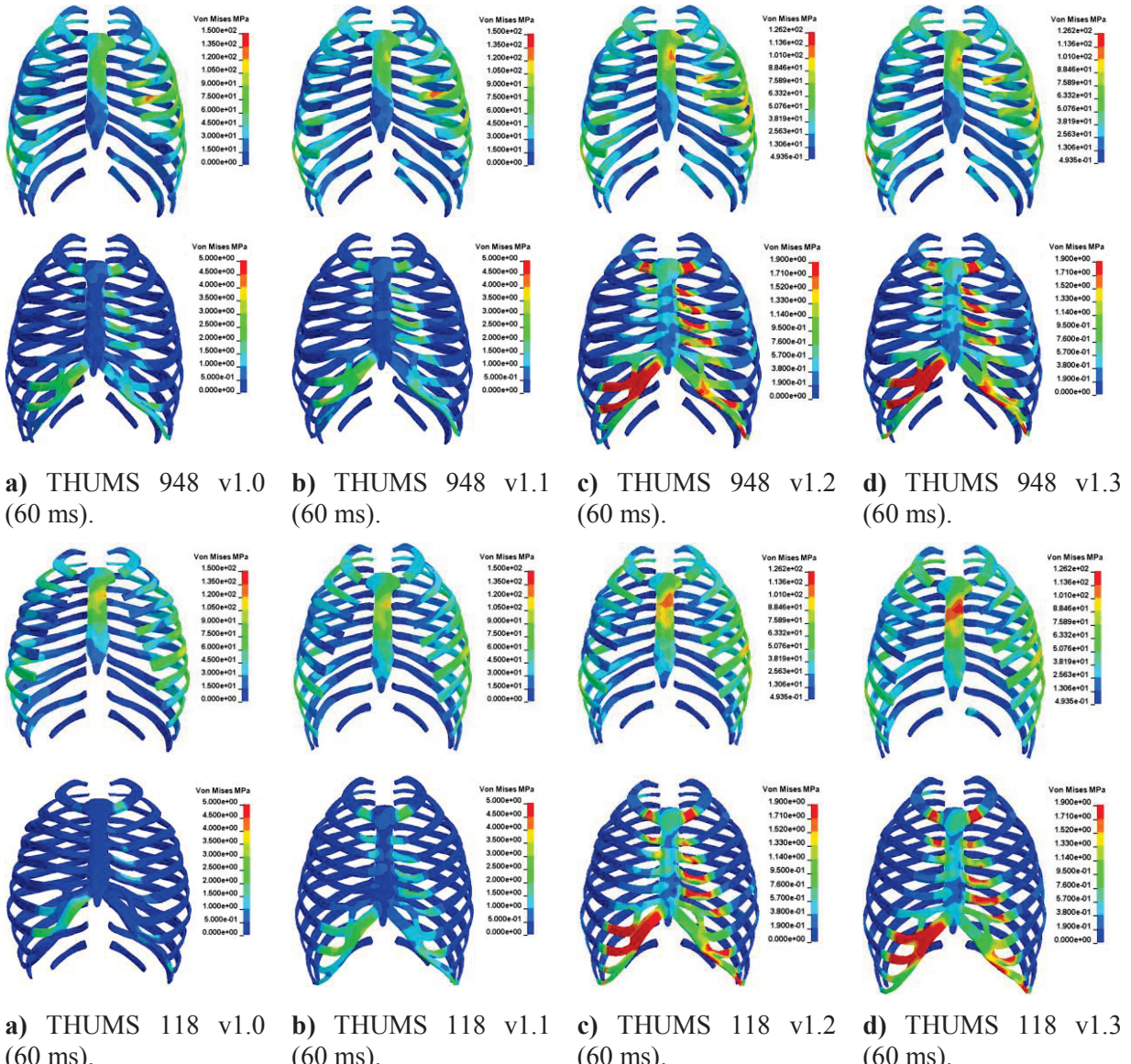


Fig. 90. Von Mises stress contour obtained for personalized models considering aging in high speed sled tests at maximum bony midsternal deflection time (upper: cortical, lower: cartilage & trabecular).

Table 39. Fractures summarize for the personalized models considering aging

Code	Thums 948 v1.0			Thums 948 v1.1			Thums 948 v1.2			Thums 948 v1.3			Thums 118 v1.0			Thums 118 v1.1			Thums 118 v1.2		
	1 st occ.	N# elements	1 st occ. (ms)	N# elements	1 st occ.	N# elements (ms)	occ.	N# elements (ms)	occ.	N# elements (ms)	occ.	N# elements (ms)	occ.	N# elements (ms)	occ.	N# elements (ms)	occ.	N# elements (ms)	occ.	N# elements (ms)	
L_rib01	85.7	4	82.6	5	81.1	9	85.1	5	-	-	-	-	95.2	1	96.2	1	96.2	1	96.2	5	
L_rib02	-	-	95.2	4	79.5	9	76.6	11	88.3	5	82.2	9	78.5	11	77.4	15	-	-	-	-	
L_rib03	76.3	4	74.3	4	73.1	7	71.7	11	-	-	-	-	100.5	11	99.8	10	-	-	-	-	
L_rib04	71.4	14	70.9	5	68.7	11	67.9	11	-	-	-	-	94.9	4	97.7	5	76.5	6	76.5	6	
L_rib05	95.1	8	97.2	4	91.5	5	94.2	4	102.9	4	101.3	4	93.2	1	90.9	3	91.3	23	91.3	36	
L_rib06	-	-	-	-	104.7	1	121.7	1	-	-	93.2	1	90.9	3	94.7	10	93.7	14	-	-	
L_rib07	-	-	-	-	95.1	6	102.0	3	98.7	7	94.6	14	95.2	14	-	-	-	-	-	-	
L_rib08	-	-	-	-	-	-	106.0	5	-	-	-	-	94.7	10	93.7	14	-	-	-	-	
L_rib09	-	-	-	-	-	-	-	-	-	-	97.9	8	92.7	14	-	-	-	-	-	-	
L_rib10	-	-	-	-	91.0	3	127.1	25	-	-	148.9	2	-	-	-	-	-	-	-	-	
L_rib11	85.7	4	82.6	5	81.1	8	85.1	4	-	-	-	-	-	-	-	-	-	-	-	-	
L_rib12	-	-	-	-	-	-	-	-	-	-	-	-	-	-	-	-	-	-	-	-	
R_rib01	113.4	2	110.0	3	86.6	8	105.3	7	109.9	6	111.6	4	103.2	6	105.2	6	-	-	-	-	
R_rib02	-	-	-	-	-	-	-	-	-	-	-	-	-	-	-	-	-	-	-	-	
R_rib03	-	-	-	-	-	-	96.5	1	-	-	-	-	-	-	90.5	1	92.3	4	-	-	
R_rib04	-	-	-	-	-	-	97.1	1	-	-	-	-	-	-	-	-	-	-	-	-	
R_rib05	97.1	2	-	-	-	-	-	-	-	-	-	-	-	-	-	-	-	-	-	-	
R_rib06	-	-	-	-	-	-	98.9	4	100.4	3	-	-	-	-	-	-	-	-	-	-	
R_rib07	-	-	-	-	104.0	1	85.6	3	86.1	3	-	-	-	-	-	-	-	-	-	-	
R_rib08	-	-	-	-	-	-	-	-	-	-	-	-	-	-	-	-	-	-	-	-	
R_rib09	-	-	-	-	-	-	-	-	-	-	-	-	-	-	-	-	-	-	-	-	
R_rib10	-	-	-	-	-	-	-	-	-	-	-	-	-	-	-	-	-	-	-	-	
R_rib11	-	-	-	-	-	-	-	-	-	-	-	-	-	-	-	-	-	-	-	-	
R_rib12	-	-	-	-	-	-	-	-	-	-	-	-	-	-	-	-	-	-	-	-	
Sternum	82.7	2	80.8	5	79.9	11	79.4	19	91.7	14	95.6	12	84.3	38	84.5	50	-	-	-	-	
L_cart	118.1	3	-	-	77.9	11	87.1	9	93.5	11	91.7	9	89.5	23	90.2	34	-	-	-	-	
R_cart	100.4	3	90.8	5	84.3	9	77.2	10	109.1	4	109.9	3	85.0	5	85.3	23	-	-	-	-	

Table 40. Computation of Torso Abbreviated Injury Scale (TOAIS) according to the number of fractured ribs and their location for the personalized models considering aging.

Area	AIS2005	Description	AIS	THUMS 948 v1.0	THUMS 948 v1.1	THUMS 948 v1.2	THUMS 948 v1.3	THUMS 118 v1.0	THUMS 118 v1.1	THUMS 118 v1.2	THUMS 118 v1.3
Rib cage	450210.2	multiple rib fractures fracture(s) without flail, any location unilateral or bilateral	2	1	1	1	1	1	1	1	1
-	450200.1		1	0	0	0	0	1	0	0	0
-	450201.1	one rib	1	0	0	0	0	1	0	0	0
-	450202.2	two ribs	2	0	0	0	0	1	0	0	0
-	450203.3	≥ 3 ribs	3	0	0	0	0	1	0	0	0
-	450209.3	fractures with flail, NFS	3	1	1	1	1	0	1	1	1
-	450211.3	unilateral flail chest NFS	3	1	1	1	1	0	1	0	0
-	450212.3	3-5 flail ribs	3	1	1	0	0	0	1	0	0
-	450213.4	>5 flail ribs	4	0	0	1	1	0	1	0	0
-	450214.5	bilateral flail chest	5	0	0	0	0	0	0	0	1
Sternum	450804.2	fracture	2	1	1	1	1	1	1	1	1
	TOAIS		3	3	4	4	3	3	4	5	5

5. Discussion

In this chapter, geometrically personalized models of six specific subjects of various anthropometries and age were developed from THUMS, based on vivo data and the geometrical personalization process described in **Chapter 3**.

A validation of the six geometrically personalized models was performed against in vivo sled tests at low speed. The comparison was carried out for belt loads, mid-sternum, chest excursions and thoracic force deflection curves. Similar maximum peak and time histories were obtained between personalized models and experiments. Nevertheless, this comparison is qualitative and it could be improved by using an objective rating method as proposed by (Hovenga et al., 2005).

The influence of geometrical personalization on thoracic injury risk prediction was evaluated at high speed on four geometrically personalized models of various anthropometries. Thoracic mechanical response was found sensitive to these various anthropometries. Extreme anthropometries (obese or tall subject) were found to be the most substantially injured relatively to other anthropometries. A higher crushing effect on ribcage and a higher effect of velocity of deformation may imply the excessive rib injuries observed for extreme anthropometries. Nevertheless, other simulations with different anthropometries are needed to confirm this tendency.

The influence of material property modifications related to the effect of aging on thoracic injury risk prediction was evaluated at high speed on two geometrically personalized models of similar anthropometries and thorax morphotypes. Thus, cortical thickness, material properties of cortical bone, trabecular bone, and cartilage were progressively decreased to correspond to an old subject. The simulations indicated that changes in bone material parameters could substantially affect the FE model predictions of rib fractures. The number of fractured ribs was found more sensitive to changes in bone material properties (cortical and trabecular) than in cortical thickness decreasing.

Nevertheless, the influence of cortical thickness on thoracic injury risk prediction may be underestimated in our study. In initial THUMS model, ribs are modeled with cortical shell elements with constant thickness (1 mm). While real cortical thickness distributions may vary differently along the rib with aging, the assignment of a constant cortical thickness in the rib models limits this study. Cortical shell elements with variable thickness reflected more the

local thickness variations in the rib cortical, and therefore may provide more sensitive predictions of rib structural responses when their thicknesses are modified.

In this study, material properties of cortical and trabecular bone were modified at the same time. Thus, the influence of each part of the rib structure is not clear. Nevertheless, it was found that for bending test on isolated ribs, variations in trabecular bone properties produced negligible influence on model results (Li et al., 2010). So a lesser influence of material properties of trabecular bone is expected in high speed sled tests.

It was assumed that according to the rib orientation, the applied force causes rib deformations and rotations at various degrees (Kent et al. 2005). Thus, when rib deformations are majority, i.e. when the load force acts straight in the plane of the ribs, an increased structural stiffness and a decreased thoracic deflection tolerance are expected. The influence of costovertebral joint properties on thoracic injury risk prediction could be an interesting point to focus on since it may modify the amount of rib rotation and rib deformations. On THUMS, as each articular joint was modeled anatomically by bone-to-bone contacts, the personalization of joints would imply to re-mesh locally the joint bones and to change their contact properties.

The number of fractured ribs obtained in simulations seemed overestimated considering the recorder amount of chest compression and VC_{max} . According to Kent and Patrie, 50% risk of probability of more than six rib fractures occurs at 33% chest compression for a 70-year-old, but at 43% for a 30-year-old (Kent and Patrie, 2005). Similarly, according to Lau and Viano, 25% risk of probability of $AIS \geq 4$ occurs at $VC_{max} = 1.0$ m/s (Lau and Viano, 1986). Differences in chest compression and VC_{max} may due to the way to define chest deflection and compression. In our study, due to in vivo experiment limitations, chest compression was defined from the relative displacement of the midsternum to the 7th vertebrae, easy to get on volunteer using the scapular tip but this tends to underestimate chest deflection, chest compression and consequently VC_{max} . In Mroz et al. study, the chest deflection was defined as the posterior displacement of the sternum relative in the x-direction of a local coordinate system rigidly connected to the 10th thoracic vertebrae (Mroz et al., 2010).

Thus, it seems that THUMS tends to overestimate the number of fractured ribs (Mroz et al., 2010; Pipkorn and Mroz, 2009). However, we consider that the increased risk of injury highlighted in this study for different level of personalization is still valid as it was defined relatively to baseline simulations.

CONCLUSION

In the context presented in introduction, a literature analysis related to the knowledge of thorax anatomy and its injury mechanisms is performed. Then, a summary of the biomechanical tests performed on thorax and a summary of the existing thoracic injury criteria is presented. It led to the conclusion that a thoracic injury assessment tool accounting for differences in anatomical features and biological material properties that are observed between adults and elderly was needed. From that state of the art, it appeared that personalized models which represent all the population in corpulence and in age could be useful as thoracic injury assessment tools.

To develop such models is needed. First, experimental data are needed to validate the personalized models in real-world conditions. And also, a choice of the level of personalization of the model must be made and the sensibility of the model response to this personalization must be assessed to predict thoracic injury risk.

To answer these questions, we performed *in vivo* sled tests involving adults of various anthropometries and age to understand thoracic mechanical response and we developed and used customized FE models to carry out the same analysis in the injurious domain. The statistical analysis of the experiments on 30 subjects showed that:

- The thoracic stiffness was significantly higher for 40-years old group especially for older women with no overweight, less for older people with high BMI
- The young subjects were more compliant (lower K-values) than the others especially the thin ones.
- The overweight volunteers' group seems to have a higher viscous thoracic behavior than the subjects in the normal group especially older people with high BMI.

These results suggest that both age and overweight have an influence on thoracic mechanical response.

In vivo experiments bring needed data and but present some limitations:

- The number of available subjects and especially over 40-years-old subject was limited. A larger amount of subjects, especially elderly would allow to perform a finer analysis of the results concerning the role of age, and BMI in thoracic mechanical response variability. In

addition, tested older subjects were not representative of their age group in term of bone quality since they were recruited if only if they have no osteopenia (total femoral and lumbar Tscore >-1). In a next protocol, this criterion should be reassessed in order to include elderly easily.

- Although most representative of a real crash situation, sled tests have the disadvantage of not being able to control the force applied by the belt on the thorax. Thus, thorax is self-loaded by its own inertia which limits comparison of thoracic mechanical behavior. Compression tests as proposed by Cesari and Bouquet 1990 allow to control the force applied by the belt on the thorax. Nevertheless, this protocol implies that the subject is in supine position, which is less representative of a real crash situation where spine excursion is not limited.
- In our study, volunteers were subjected to one low-speed pulse, defined from two public crash simulators and similar to other pulses used in literature. In a next protocol involving in vivo sled tests, using different set of pulses should allow to check the relevance of spring-dashpot-model parameters K , μ at different initial speed. However, the different pulses must be sufficiently severe to study thoracic mechanical response without presenting a risk to the volunteers.
- The kinematics of landmarks additionally placed to the left and right side of chest and on the inferior contour of the ribcage have not been exploited in our analysis because of soft tissue artifacts. Increased superficial tissue depthtissue and arm excursions obstruct the visual field of the camera. In a next protocol, a solution would be to integrate a chestband device to get contours of both sides of the thorax. Additional cameras covering the scene could also help and the use of optoelectronical system as VICON® instead of standard high speed camera would be interesting (Arbogast et al., 2009; Lopez-Valdes et al., 2010; Kemper et al., 2011).

Nevertheless, the question of whether these thoracic mechanical differences between volunteers have implications on thoracic injury risk was to be studied numerically. To use customized FE models for simulation in the injurious domain, the initial mesh of THUMS 50th percentile male FE model was modified using RBF, towards the geometry and the posture of the volunteers tested in vivo. The geometrical personalization process was validated by checking the mesh quality and comparing personalized model versus volunteer anthropometry and MRI-scans for one subject. From this validation, it appeared that:

- The geometrical personalization process using virtual control points allows both the thorax posture and the geometry personalization of the model without re-meshing.
- This process permits to keep a good mesh quality and other FE features.

Concerning the personalization of the FE model, the limitations of our work are the following:

- For the material property personalization considering aging, the fact that cortical thickness is constant in THUMS limits the potential of cortical thickness personalization. Using a FE model with variable cortical thickness along the rib would permit to go beyond this limitation. Nevertheless, *in vivo* data of cortical thickness variation along the rib are very limited, especially for young subjects. The development of ultrasound methods for rib cortical bone assessment should fill this lack (Tran et al., 2011).
- The personalization of costovertebral joint properties on thoracic injury risk prediction could be an interesting point to focus on since it may modify the amount of rib rotation and rib deformations. On THUMS, as each articular joint was modeled anatomically by bone-to-bone contacts, the personalization of joints would imply to change their properties (contact, ligaments). Nevertheless, *in vivo* data on ribcage mobility must be acquired for the personalization of joints. The Elderly project in which has been this thesis conducted also includes ribcage mobility. The volunteers tested during *in vivo* sled tests are also subjected to a protocol of breathing movement recording. It would be interesting to exploit these data in this goal.
- After personalization, the resulted model is always more or less close to the initial geometry (male, 50th percentile) in term of shape. In particular, genders difference and pathological deformities of the thorax cannot be reproduced. A solution would be to increase the number of thoracic palpable landmarks allowing for a better accuracy. Another solution would be to use numerous anatomical points acquired for MRI-scans or EOS ultra-low dose scans instead of thoracic anatomical points (Humbert et al., 2009). These scans have significant accuracy but these *in vivo* methods are expensive and difficult to implement on a large population. An alternate option could be to use specific initial mesh more representative of the target population. Thus, using an initial female mesh would be more suitable for the building of female personalized FE models.

Hence, geometrical personalization process was applied on six specific subjects of various anthropometries and age subjected to *in vivo* sled tests. A validation of the six geometrical

models was performed against in vivo sled tests at low speed. The calculated thoracic responses were similar to the experimental results at low speed.

From the prediction of injury risk, it appeared that:

- Extreme anthropometries (obese or tall subject) were found to be the most substantially injured relatively to other anthropometries.
- Changes in either various anthropometries or bone material parameters could substantially affect the FE model predictions of rib fractures.
- Considering the personalization with aging, the number of fractured ribs was more sensitive to changes in bone material property than cortical thickness.

Thus, this work puts forward the potential of personalized models as improved thoracic injury assessment tools. Personalized model should also include multi-scale personalization: geometrical material properties updating since both affect thoracic injury outcome.

Concerning the simulations, the limitations are:

- The number of personalized models especially considering aging was very limited. A parametric study including a larger amount of personalized models with various anthropometries and different levels of personalization considering aging would allow to explore more finely the role of different levels of personalization on thoracic injury risk assessment.
- Personalized FE models were subjected to a unique high-speed pulse, defined from literature. Using different set of high-speed pulses should allow to study the evolution of thoracic injury risk for different severities and levels of personalization investigated.

To conclude, when considering previous works dealing with the thorax some progresses have been made:

- Thoracic mechanical responses of subjects of both genders, of different age and corpulence subjected to frontal sled tests are supplied whereas experimental data concerning sled tests in literature are very limited in anthropometry, age and sex.
- The influences of various anthropometries, cortical bone thickness and bone material properties on thoracic injury outcome were evaluated whereas simulations data were seldom in the literature due to available personalized models.

This contribution should help to better estimate the injury risk for car occupants. It should help to propose personalized human body models as attractive thoracic injury assessment tool of vulnerable individuals.

BIBLIOGRAPHY

- Abdel-Aziz, Y. and H. Karara (1971).** Direct linear transformation from comparator coordinates into object space coordinates in close-range photogrammetry. In *Proceedings of the Symposium on Close-Range photogrammetry*, Volume 1, pp. 18.
- Arbogast, K., S. Balasubramanian, T. Seacrist, M. Maltese, J. García-España, T. Hopely, E. Constans, F. Lopez-Valdes, R. Kent, H. Tanji, et al. (2009).** Comparison of kinematic responses of the head and spine for children and adults in low-speed frontal sled tests. *Stapp car crash journal* 53, 329.
- Armstrong, R., H. Waters, and J. Stapp (1968).** Human muscular restraint during sled deceleration. In *Proceedings of Twelfth Stapp Car Crash Conference*, Volume 680793.
- Backaitis, S. and A. St-Laurent (1986).** Chest deflection characteristics of volunteers and hybrid iii dummies. In S. Inc (Ed.), *30th Stapp Car Crash Conference Proceedings*, Volume 30, San Diego, California., pp. 157–166. SAE International.
- Bass, C., K. Darvish, B. Bush, J. Crandall, S. Srinivasan, C. Tribble, S. Fiser, L. Tourret, J. Evans, J. Patrie, et al. (2001).** Material properties for modeling traumatic aortic rupture. *Stapp car crash journal* 45, 143.
- Beillas, P., Y. Lafon, and F. Smith (2009).** The effects of posture and subject-to-subject variations on the position, shape and volume of abdominal and thoracic organs. *Stapp car crash journal* 53, 127.
- Berthet, F., P. Vezin, L. Cheze, and J. Verriest (2005).** Assessment and analysis of the human rib lateral slopes. *Computer Methods in Biomechanics and Biomedical Engineering* 8(S1), 35–36.
- Bertrand, S., W. Skalli, L. Delacherie, D. Bonneau, G. Kalifa, and D. Mitton (2006).** External and internal geometry of european adults. *Ergonomics* 49(15), 1547–1564.
- Besnault, B., H. Guillemot, S. Robin, F. Lavaste, and J. Le Coz (1998).** Morphometric study of the human pelvis. *Journal of Biomechanics* 31(1), 9–9.
- Boulanger, B., D. Milzman, K. Mitchell, and A. Rodriguez (1992).** Body habitus as a predictor of injury pattern after blunt trauma. *The Journal of trauma* 33(2), 228.

- Buhmann, M. (2000).** Radial basis functions. *Acta numerica* 9, 1–38.
- Burstein, A., D. Reilly, M. Martens, et al. (1976).** Aging of bone tissue: mechanical properties. *The Journal of bone and joint surgery. American volume* 58(1), 82.
- Cavanaugh, J. (1993).** The biomechanics of thoracic trauma. *Accidental injury: biomechanics and prevention* 26, 362.
- Cavanaugh, J., Y. Zhu, Y. Huang, and A. King (1993).** Injury and response of the thorax in side impact cadaveric tests. In *Proceedings of the 37 th Stapp Car Crash Conference*, Volume 933127.
- Cesari, D. and R. Bouquet (1990).** Behaviour of human surrogates thorax under belt loading. In *Proc. of the 34th Stapp Car Crash Conference*.
- Charpail, E. (2006).** *Analyse du comportement mécanique des côtes humaines en dynamique*. Ph. D. thesis, ENSAM.
- Chawla, A., S. Mukherjee, D. Mohan, and S. Jain (2005).** Validation of the cervical spine model in thums. In *Proceedings of the 19th International Technical Conference on the Enhanced Safety of Vehicles Washington DC USA*.
- Chen, P. et al. (1978).** Finite element dynamic structural model of the human thorax for chest impact response and injury studies. *Aviation, space, and environmental medicine* 49(1 Pt. 2), 143.
- Compigne, S., Y. Caire, T. Quesnel, and J. Verriest (2004).** Non-injurious and injurious impact response of the human shoulder tree-dimensional analysis of kinematics and determination of injury threshold. *Stapp car crash journal* 48, 89–125.
- Cowin, S. (2001).** *Bone Biomechanics Handbooks*. CRC Press, New York.
- Crandall, J., W. Pilkey, G. Klopp, B. Pilkey, R. Morgan, R. Eppinger, S. Kuppa, and C. Sharpless (1994).** A comparison of two and three point belt restraint systems. In *Proceedings joint AAAM-IRCOBI special session. September 22 1994, Lyon France*.
- Creasy, J., C. Chiles, W. Routh, and R. Dyer (1997).** Overview of traumatic injury of the thoracic aorta. *Radiographics* 17(1), 27–45.
- De Onis, M. and J. Habicht (1996).** Anthropometric reference data for international use: recommendations from a world health organization expert committee. *The American journal of clinical nutrition* 64(4), 650–658.

- Deng, Y., W. Kong, and H. Ho (1999).** Development of a finite element human thorax model for impact injury studies. Technical report, SAE International.
- Dokko, Y., O. Ito, and K. Ohashi (2009).** Development of human lower limb and pelvis fe models for adult and the elderly. Technical Report 2009-01-0396, SAE.
- Dumas, R. and L. Cheze (2009).** Soft tissue artifact compensation by linear 3d interpolation and approximation methods. *Journal of Biomechanics* 42(13), 2214–2217.
- Eckert, M., M. Fayet, L. Cheze, R. Bouquet, E. Voiglio, and J. Verriest (2000).** Costovertebral joint behaviour during frontal loading of the thoracic cage. In *Proceedings of the 2000 International Ircobi conference on the biomechanics of Impact, September 20-22, 2000, Montpellier, France*.
- Eickhoff, B., W. Schrenk, H. Zellmer, and M. Meywerk (2011).** Optimization of seat belt buckle motion for reducing chest deflection, using rib eye sensors. In *Proceedings of the 22nd International Technical Conference on the Enhanced Safety of Vehicles (ESV)*.
- El-Jawahri, R., T. Laituri, J. Ruan, S. Rouhana, and S. Barbat (2010).** Development and validation of age-dependent fe human models of a mid-sized male thorax. *Stapp car crash journal* 54, 407.
- Eppinger, R., E. Sun, F. Bandak, M. Haffner, N. Khaewpong, M. Maltese, S. Kuppa, T. Nguyen, E. Takhounts, R. Tannous, et al. (1999).** Development of improved injury criteria for the assessment of advanced automotive restraint systems–ii. Technical report, National Highway Traffic Safety Administration.
- Foret-Bruno, J., X. Trosseille, J. Le Coz, F. Bendjellal, C. Steyer, T. Phalempin, D. Villeforceix, and P. Dandres (1998).** Thoracic injury risk in frontal car crashes with occupant restrained with belt load limiter. In *Proceedings of the 42nd Stapp Car Crash Conference*.
- Foret-Bruno, J., X. Trosseille, Y. Page, J. Huere, J. Le Coz, F. Bendjellal, A. Diboine, T. Phalempin, D. Villeforceix, P. Baudrit, et al. (2001).** Comparison of thoracic injury risk in frontal car crashes for occupant restrained without belt load limiters and those restrained with 6 kn and 4 kn belt load limiters. *Stapp car crash journal* 45, 205.
- Forman, J. (2010).** *The structural characteristics of the costal cartilage: The roles of calcification and the perichondrium, and the representation of the costal cartilage in finite element models of the human body*. Ph. D. thesis, University of Virginia.

- Forman, J., F. Lopez-Valdes, D. Lessley, M. Kindig, R. Kent, and O. Bostrom (2009).** The effect of obesity on the restraint of automobile occupants. In *Annual Proceedings/Association for the Advancement of Automotive Medicine*, Volume 53, pp. 25. Association for the Advancement of Automotive Medicine.
- Fung, Y. and M. Yen (1984).** Experimental investigation of lung injury mechanisms. Technical report, US Army Medical Research and Development Command.
- Gayzik, F., M. Yin, K. Danielson, D. Slice, and J. Stitzel (2008).** Quantification of age-related shape change of the human rib cage through geometric morphometrics. *Journal of Biomechanics* 41(7), 1545 – 1554.
- Gray, H. (1918).** *Anatomy of the human body*. Lea & Febiger.
- Gutierrez-Fisac, J., E. Lopez, J. Banegas, A. Graciani, and F. Rodriguez-Artalejo (2004).** Prevalence of overweight and obesity in elderly people in spain. *Obesity* 12(4), 710–715.
- Haug, E., H. Choi, S. Robin, and M. Beaugonin (2004).** Human models for crash and impact simulation. *Handbook of Numerical Analysis* 12, 231–452.
- Holden, M. (2008).** A review of geometric transformations for nonrigid body registration. *Medical Imaging, IEEE Transactions on* 27(1), 111–128.
- Hovenga, P., H. Spit, M. Uijidert, and A. Dalenoort (2005).** Improved prediction of hybrid-iii injury values using advanced multibody techniques and objective rating. *SAE transactions* 114(6), 1578–1590.
- Huang, Y., A. King, and J. Cavanaugh (1994).** Finite element modeling of gross motion of human cadavers in side impact. In *Proceedings of the 38th Stapp Car Crash Conference, October 31-November 4, 1994, Fort Lauderdale, Florida, USA*.
- Humbert, L., J. De Guise, B. Aubert, B. Godbout, and W. Skalli (2009).** 3d reconstruction of the spine from biplanar x-rays using parametric models based on transversal and longitudinal inferences. *Medical engineering & physics* 31(6), 681–687.
- Ito, O., Y. Dokko, and K. Ohashi (2009).** Development of adult and elderly fe thorax skeletal models. Technical report, SAE International.
- Iwamoto, M., Y. Kisanuki, I. Watanabe, K. Furusu, K. Miki, and J. Hasegawa (2002).** Development of a finite element model of the total human model for safety (thums) and

- application to injury reconstruction. In *Proceedings of the International IRCOBI Conference*.
- Iwamoto, M., K. Miki, M. Mohammad, A. Nayef, K. Yang, P. Begeman, and A. King (2000).** Development of a finite element model of the human shoulder. *Stapp car crash journal* 44, 281.
- Kallieris, D., A. Rizzetti, R. Mattern, R. Morgan, R. Eppinger, and L. Keenan (1995).** On the synergism of the driver air bag and the 3-point belt in frontal collisions. In *Proceedings of the 39th Stapp Car Crash Conference, November 8-10, 1995, San Diego, California, USA*.
- Kallieris, D., K. Stein, R. Mattern, R. Morgan, and R. Eppinger (1994).** The performance of active and passive driver restraint systems in simulated frontal collisions. In *Proceedings of the 38th Stapp Car Crash Conference, October 31-November 4, 1994, Fort Lauderdale, Florida, USA*.
- Kapandji, A. (2009).** *Anatomie fonctionnelle*. Maloine.
- Kemper, A., S. Beeman, and S. Duma (2011).** Effects of pre-impact bracing on chest compression of human occupants in low-speed frontal sled tests. In *17th Tech. Conference on the Enhanced Safety of Vehicles*, Number 11-0193, pp. 1–6. SAE International.
- Kent, R., C. Bass, W. Woods, R. Salzar, S. Lee, and J. Melvin (2006).** The role of muscle tensing on the force-deflection response of the thorax and a reassessment of frontal impact thoracic biofidelity corridors. *Proceedings of the Institution of Mechanical Engineers, Part D: Journal of Automobile Engineering* 220(7), 853–868.
- Kent, R., J. Funk, and J. Crandall (2003).** How future trends in societal aging, air bag availability, seat belt use, and fleet composition will affect serious injury risk and occurrence in the united states. *Traffic Injury Prevention* 4(1), 24–32.
- Kent, R., S. Lee, K. Darvish, S. Wang, C. Poster, A. Lange, C. Brede, D. Lange, and F. Matsuoka (2005).** Structural and material changes in the aging thorax and their role in crash protection for older occupants. *Stapp car crash journal* 49, 231.
- Kent, R., D. Lessley, and C. Sherwood (2004).** Thoracic response to dynamic, non-impact loading from a hub, distributed belt, diagonal belt, and double diagonal belts. *Stapp car crash journal* 48, 495.

- Kent, R. and J. Patrie (2005).** Chest deflection tolerance to blunt anterior loading is sensitive to age but not load distribution. *Forensic Science International* 149(2–3), 121 – 128.
- Kent, R., C. Sherwood, D. Lessley, B. Overby, and F. Matsuoka (2003).** Age-related changes in the effective stiffness of the human thorax using four loading conditions. In *Proc. of International Research Council on the Biomechanics of Impact*, Lisbon (Portugal), pp. 249–263.
- Kimpara, H., M. Iwamoto, and K. Miki (2002).** Development of a small female fem model. In *Proc. JSAE spring congress, Issue*, Number 59-02, pp. 1–4.
- Kimpara, H., J. Lee, K. Yang, A. King, M. Iwamoto, I. Watanabe, and K. Miki (2005).** Development of a three-dimensional finite element chest model for the 5 (th) percentile female. *Stapp car crash journal* 49, 251.
- Klanner, W. (2001).** Status report and future development of the euro ncap program. In *17th Tech. Conference on the Enhanced Safety of Vehicles*. SAE International.
- Kleinberger, M. and U. S. N. H. T. S. Administration (1998).** Development of improved injury criteria for the assessment of advanced automotive restraint systems.
- Krige, D. G. (1951).** A statistical approach to some basic mine valuation problems on the witwatersrand. *Journal of the Chemical, Metallurgical and Mining Society of South Africa* 52, 119–139.
- Kroell, C., D. Schneider, and A. Nahum (1974).** Impact tolerance and response of the human thorax ii. (SAE# 741187).
- Kroell C.K., Schneider D.C., N. A. (1971).** Impact tolerance and response of the human thorax. biomechanics of impact injury and injury tolerances of the thorax-shoulder complex. In *Proc. of the 15th Stapp Car Crash Conference*.
- Kuppa, S. and R. Eppinger (1998).** Development of an improved thoracic injury criterion.
- L'Abbe, R., D. Dainty, and J. Newman (1982).** An experimental analysis of thoracic deflection response to belt loading. In *Proc. of the IRCOBI Conference, Cologne (Germany)*, pp. 184–194.
- Lafont, S. and B. Laumon (2003).** Vieillissement et gravité des atteintes lesionnelles des victimes d'accident de la circulation routière: Ageing and injury severity among road traffic accident victims. *Recherche-Transports-Sécurité* 79, 121–133.

- Lau, I. and D. Viano (1986).** The viscous criterion-bases and applications of an injury severity index for soft tissues. In *Proc. of International Research Council on the Biomechanics of Impact*, Number 861882. SAE International.
- Li, Z., M. Kindig, D. Subit, and R. Kent (2010).** Influence of mesh density, cortical thickness and material properties on human rib fracture prediction. *Medical engineering & physics* 32(9), 998–1008.
- Lizée, E., S. Robin, E. Song, N. Bertholon, J. Le Coz, B. Besnault, and F. Lavaste (1998).** Development of a 3d finite element model of the human body. (P-337, 983152).
- Lobdell, T., C. Kroell, D. Schneider, W. Hering, and A. Nahum (1973).** Impact response of the human thorax. *Human Impact Response Measurement and Simulation*, 201–245.
- Lopez-Valdes, F. (2009).** Optical measurement of 6-dof kinematics of internal body structures during frontal impact restraint loading. In *Proceedings of the JSAE Annual Congress*. Inc. Pacifico Yokohama, Japan.
- Lopez-Valdes, F., A. Lau, J. Lamp, P. Riley, D. Lessley, A. Damon, M. Kindig, R. Kent, S. Balasubramanian, T. Seacrist, et al. (2010).** Analysis of spinal motion and loads during frontal impacts. comparison between pmhs and atd. In *Annals of advances in automotive medicine/Annual Scientific Conference... Association for the Advancement of Automotive Medicine. Association for the Advancement of Automotive Medicine. Scientific Conference*, Volume 54, pp. 61.
- McCalден, R., J. McGeough, M. Barker, et al. (1993).** Age-related changes in the tensile properties of cortical bone. The relative importance of changes in porosity, mineralization, and microstructure. *The Journal of bone and joint surgery. American volume* 75(8), 1193.
- Melvin, J., D. Mohan, and R. Stalnaker (1975).** Occupant injury assessment criteria.
- Mertz, H. (1993).** Anthropomorphic test devices. *Accidental injury: Biomechanics and prevention*, 66–84.
- Mertz, H. and C. Gadd (1971).** Thoracic tolerance to whole-body deceleration. In *Proc. of the 15th Stapp Car Crash Conference*. SAE International.
- Mertz, H., J. Horsch, G. Horn, and R. Lowne (1991).** Hybrid III sternal deflection association with thoracic injury severities of occupants restrained with force limiting

- belts biomechanics of impact injury and injury tolerances of the thorax-shoulder complex. In *SAE PT-92*.
- Mock, C., D. Grossman, R. Kaufman, C. Mack, and F. Rivara (2002).** The relationship between body weight and risk of death and serious injury in motor vehicle crashes. *Accident analysis and prevention* 34(2), 221–228.
- Mohr, M., E. Abrams, C. Engel, W. Long, and M. Bottlang (2007).** Geometry of human ribs pertinent to orthopedic chest-wall reconstruction. *Journal of biomechanics* 40(6), 1310–1317.
- Moss, S., Z. Wang, M. Salloum, M. Reed, M. Van Ratingen, D. Cesari, R. Scherer, T. Uchimura, and M. Beusenberg (2000).** Anthropometry for worldsid, a world-harmonized midsize male side impact crash dummy.
- Mroz, K., O. Boström, B. Pipkorn, J. Wismans, and K. Brolin (2010).** Comparison of hybrid iii and human body models in evaluating thoracic response for various seat belt and airbag loading conditions.
- Nahum, A., C. Gadd, and D. Schneider (1970).** Deflection of the human thorax under sternal impact.
- Nahum, A.M. and J. Melvin (2002).** Accidental injury: biomechanics and prevention.
- Nahum, A.M., Schneider D.C., K. C. (1975).** Cadaver skeletal response to blunt thoracic impact. In *Proc. of the 19th Stapp Car Crash Conference*.
- Ndiaye, A. and M. Chiron (2009).** Thorax vulnerability of female car users reported by the road accident field. Rapport Work Package 1., UMRESTTE, 0901. Confidential.
- Neathery, R. (1974).** Analysis of chest impact response data and scaled performance recommendations. In *Stapp Car Crash Conference Proceedings*, Volume 18.
- Oshita, F., K. Omori, Y. Nakahira, and K. Miki (2002).** Development of a finite element model of the human body. In *7th International LS-DYNA Users Conference*, pp. 19–21.
- Patrick, L. (1981).** Impact force-deflection of the human thorax. In I. SAE (Ed.), *Proceedings of 25th Stapp car crash conference*, Volume 25, pp. 471. Internaltion Research Committe on Biokinetics of Impacts: SAE, Inc.
- Petitjean, A., P. Baudrit, and X. Trosseille (2003).** Thoracic injury criterion for frontal crash applicable to all restraint systems. pp. 323–348.

- Pipkorn, B. and K. Mroz (2009).** Validation of a human body model for frontal crash and its use for chest injury prediction. *SAE International Journal of Passenger Cars-Mechanical Systems* 1(1), 1094–1117.
- Plank, G. and R. Eppinger (1989).** Computed dynamic response of the human thorax from a finite element model.
- Plank, G. and R. Eppinger (1991).** An improved finite element model of the human thorax.
- Plank, G., M. Kleinberger, and R. Eppinger (1994).** Finite element modelling and analysis of thorax/restraint system interaction. (94-S1-O-16).
- Poulard, D., K. Bruyere, S. Compigne, and F. Bermond (2011).** In-vivo test protocol for analysis of thorax response under belt loading. In *In Proceedings of IRCOBI, Krakow, Poland, 2011.*, Number IRC-11-59, Krakow, Poland.
- Roberts, J., J. O'Connor, and E. Ward (2005).** Modeling the effect of nonpenetrating ballistic impact as a means of detecting behind-armor blunt trauma. *The Journal of trauma* 58(6), 1241.
- Roberts, S. and P. Chen (1972).** Global geometric characteristics of typical human ribs. *Journal of Biomechanics* 5(2), 191–201.
- Robin, S. (2001).** Humos: Human model for safety—a joint effort towards the development of refined human like car occupant models.
- Ruan, J., R. El-Jawahri, L. Chai, S. Barbat, and P. Prasad (2003).** Prediction and analysis of human thoracic impact responses and injuries in cadaver impacts using a full human body finite element model. *Stapp car crash journal* 47, 299.
- Sandoz, B., E. Vajda, F. Alonso, K. Bruyere, and F. Bermond (2009).** Mechanical properties assessment of child trunk. In *Proceedings of the XXII Congress of the International Society of Biomechanics.*, Cape Town, Afrique du Sud.
- Schmitt, K., P. Niederer, M. Muser, and F. Walz (2009).** *Trauma biomechanics: accidental injury in traffic and sports.* Springer Verlag.
- Schneider, L. (1983).** Development of anthropometrically based design specifications for an advanced adult anthropomorphic dummy family, volume 1. final report.

- Serre, T., C. Brunet, K. Bruyere, J. Verriest, D. Mitton, S. Bertrand, W. Skalli, and T. Bekkour (2006).** Humos(human model for safety) geometry: From one specimen to the 5 th and 95 th percentile.
- Shah, C., K. Yang, W. Hardy, H. Wang, and A. King (2001).** Development of a computer model to predict aortic rupture due to impact loading. *Stapp car crash journal* 45, 161.
- Shams, T., N. Rangarajan, J. McDonald, Y. Wang, G. Platten, C. Spade, P. Pope, and M. Haffner (2005).** Development of thor nt: Enhancement of thor alpha-the nhtsa advanced frontal dummy. In *Proceedings of the 19th International Technical Conference on the Enhanced Safety of Vehicles, Paper*, Volume 540455.
- Shaw, J., R. Herriott, J. McFadden, B. Donnelly, J. Bolte, et al. (2006).** Oblique and lateral impact response of the pmhs thorax. *Stapp car crash journal* 50, 147.
- Shen, W., Y. Niu, L. Bykanova, P. Laurence, and N. Link (2010).** Characterizing the interaction among bullet, body armor, and human and surrogate targets. *Journal of biomechanical engineering* 132, 121001.
- Song, E., X. Trosseille, and P. Baudrit (2009).** Evaluation of thoracic deflection as an injury criterion for side impact using a finite elements thorax model. *Stapp car crash journal* 53, 155.
- Song, E., X. Trosseille, and L. E. (2010).** Injury criteria. In *THORAX FP7 Workshop*.
- Stalnaker, R. and D. Mohan (1974).** Human chest impact protection criteria. Technical report, report SAE 740589.
- Stein, I. and G. Granik (1976).** Rib structure and bending strength: an autopsy study. *Calcified Tissue International* 20(1), 61–73.
- Stitzel, J., J. Cormier, J. Barretta, E. Kennedy, E. Smith, A. Rath, S. Duma, and F. Matsuoka (2003).** Defining regional variation in the material properties of human rib cortical bone and its effect on fracture prediction. *Stapp car crash journal* 47, 243.
- Sundaram, S. and C. Feng (1977).** Finite element analysis of the human thorax. *Journal of biomechanics* 10(8), 505–516.
- Talantikite, Y., R. Bouquet, M. Rarnet, H. Guillernot, S. Robin, and E. Voiglio (1998).** Human thorax behaviour for side impact-influence of impact mass and velocities. pp. 98–S7.

- Tamura, A., I. Watanabe, and K. Miki (2005).** Elderly human thoracic fe model development and validation. In *Proceedings of the 19th ESV Conference, European Enhanced Safety of Vehicle*.
- Tran, D., K. Bruyere-Garnier, A. Didier, J. Minonzio, J. Foiret, N. Vilayphiou, M. Talmant, P. Laugier, and D. Mitton (2011).** Non-invasive assessment of human ribs mechanical properties. *Computer Methods in Biomechanics and Biomedical Engineering* 14(sup1), 195–196.
- Vezin, P. and F. Berthet (2009).** Structural characterization of human rib cage behavior under dynamic loading. *Stapp car crash journal* 53, 93.
- Vezin, P. and J. Verriest (2005).** Development of a set of numerical human models for safety.
- Viano, D. (1989).** Biomechanical responses and injuries in blunt lateral impact.
- Wilhelm, M. (2003).** A biomechanical assessment of female body armor.
- Yamada, H. (1970).** *Strength of Biological Materials*. The Williams & Wikins Company, Baltimore.
- Yang, K., J. Hu, N. White, A. King, C. Chou, and P. Prasad (2006).** Development of numerical models for injury biomechanics research: a review of 50 years of publications in the stapp car crash conference. *Stapp car crash journal* 50, 429.
- Yoganandan, N., F. Pintar, D. Skrade, W. Chmiel, J. Reinartz, and A. Sances Jr (1993).** Thoracic biomechanics with air bag restraint.
- Yoganandan, N., D. Skrade, F. Pintar, J. Reinartz, and J. A. Sances (1991).** Thoracic deformation contours in a frontal impact. In *Proceedings of the 35th Stapp Car Crash Conference*.
- Zhao, J. and G. Narwani (2005).** Development of a human body finite element model for restraint system r&d applications. In *The 19th International Technical Conference on the Enhanced Safety of Vehicles (ESV), Paper*, Number 05-0399.
- Zhou, Q., S. Rouhana, and J. Melvin (1996).** Age effects on thoracic injury tolerance. In *Proc. of the 40th Stapp Car Crash Conference*. SAE International.

Publications

Poulard D., Bermond F, Bruyere K., and Compigne S., 2012. In-vivo analysis of thorax mechanical response under belt loading: the role of BMI in thorax stiffness. *Journal of Biomechanics*. Accepted.

Conferences

Poulard, D., K. Bruyere, S. Compigne, and F. Bermond 2011. In-vivo test protocol for analysis of thorax response under belt loading. In *Proceedings of IRCOBI, Krakow, Poland, 2011*. Number IRC-11-59, Krakow, Poland.

Poulard D., Bruyere K., Bermond F., Dumas R., and Compigne S. 2012. Geometrical personalization of human FE model using palpable markers on volunteers. *Computer Methods in Biomechanics and Biomedical Engineering, volume 15, supplement 1, pages 298–300. Taylor & Francis, DOI: 10.1080/10255842.2012.713669*

APPENDIX 1: DEFINITION OF A NON-INJURIOUS LOW DECELERATION PULSE PROTOCOL FOR ANALYSIS OF THORAX RESPONSE UNDER BELT LOADING

A1.1. Introduction

A non-injurious low deceleration protocol was defined for which two public crash simulators were tested and Ifsttar sled was modified. From the sled tests tri-dimensional sternal deflection was measured on Hybrid III 50th and 5th percentiles using stereovision and preliminary thorax force-deflection curves were obtained on two volunteers.

This appendix is based on the article submitted to IRCOBI 2011 (Poulard et al., 2011).

A1.2. Methods

A1.2.1. Test devices

Three shock devices were investigated for establishing the protocol: two public crash simulators and a laboratory sled. The first public crash simulator, named Autochoc, is designed to simulate an emergency braking on dry pavement at 5 km/h (**Fig. 91**) and has been used by French insurer MACIF since 1998. The second public crash simulator, named Testochoc, is designed to raise awareness towards seatbelt use. It is a two-seated sled sliding on a horizontal raceway up to 6 km/h frequently used by French Road Safety in public events and in schools (**Fig. 92**).

Ifsttar shock sled simulates a standard sedan car environment of a front passenger restrained by a 3-point belt (**Fig. 93**). The propelling system of Ifsttar sled was modified to allow low impact velocities with a good repeatability in pulses and to limit the maximum impact speed (12 km/h). Two rubber bands (Sandows®) of diameter 20 mm were mounted on each side of the sled. The sled was pulled rearward by an electrical winch until reaching 165% of the two rubber bands' initial length. An impact speed of 8 km/h was obtained. The stopping system uses the energy of deformation of an elastomeric tube penetrated by a spear to dissipate the

kinetic energy of the sled. In this case, only one tube (hardness 95 SHA, 46.5 mm diameter spear) was needed to stop the sled at a maximum deceleration of 3.8 g and during 120 ms.



Fig. 91. Autochoc, crash simulator of MACIF.



Fig. 92. Testochoc, crash simulator of French Road Safety.



Fig. 93. Ifsttar sled.

5.1.1 Subjects and Test matrix

Volunteer's main characteristics are listed as identifier code, gender, age, height, weight and BMI (S01, woman, 36 yo, 162 cm, 54 kg, 20.5 ; S02, man, 21 yo, 175 cm, 75 kg, 24.5 ; S03, man, 47, 177 cm, 64 kg, 20.4).

Ten and eight tests using volunteers (S01 and S02) were performed on Autochoc and Testochoc respectively. Five and seven tests were performed on Hybrid III 50th percentile male (HIII AM50) and Hybrid III 5th percentile female (HIII AF05) respectively to check repeatability of the pulse and accuracy of the stereovision. Four sled tests were performed on volunteers (S01 and S03) to evaluate measurement sensitivity.

A1.2.2. Instrumentation

All data were acquired at 10 kHz and filtered using CFC Butterworth filters according to the standard norm SAE J211.

A1.2.2.1. Sled

The longitudinal deceleration of each device was recorded by using an uniaxial accelerometer mounted on it. Belt webbing load cells were installed on the shoulder belt, above subject's and dummy's shoulder, and on the external lap belt side. Additional measurements were performed on Ifsttar sled: reaction forces were measured by 1-axis load cells placed under each footrest and under the seat pan. Three markers were placed on the pillar where seat belt external anchorage points were mounted in order to follow sled displacement.

A1.2.2.2. Subjects

Markers were placed on volunteers' chest at anatomical landmarks: on sternum at jugular notch, sternal angle, xiphoid process, on spinous process of 7th cervical vertebra, 2nd, 4th,

6th, 8th, 10th and 12th thoracic vertebrae. As the thorax was partially hidden by the shoulder belt, markers were also placed on the shoulder belt in particular at sternum level for deflection measurement.

A1.2.2.3. Dummies

Markers were placed on dummy sternum, spine box and shoulder belt in addition to dummy standard channels.

A1.2.3. Cameras

Four high speed cameras were positioned around the sled for recording at 1000 fps the position of markers placed on subjects, dummies and sled. Time zero was given by a flash visible by all cameras and synchronised with the data acquisition system. After the tests, the scene was calibrated by using a calibration object and the three dimensional coordinates of the subjects and dummies markers were computed using the Direct Linear Transformation (stereovision) method [8]. 3D trajectories were filtered at CFC-60 Butterworth. Spatial interpolation of 3D coordinates was performed by using vertebra neighbour markers in the case of missing vertebra markers.

A1.2.4. Data analysis

On volunteers and dummies, the sternal deflection was calculated as the distance variation between belt markers placed at the mid-sternum location and the 8th thoracic vertebra spinous process for subjects or equivalent height on spine for dummies. Force-deflection curves were drawn using shoulder belt force and sternum deflection. In dummy tests with Hybrid III, the sternum deflection was also measured by the chest potentiometer of the dummy and compared with the deflection obtained by the stereovision in order to assess its accuracy. Note that the markers were placed at the dummy sensor measurement position and the check was performed without the dummy jacket.

A1.3. Results

A1.3.1. Test devices severity and repeatability

The deceleration of the Autochoc reached a peak of 0.97 ± 0.38 g (2 SD) with a pulse duration of 200 ms. Testochoc deceleration reached a peak of 9.98 ± 0.44 g with a pulse

duration of 45 ms. Ifsttar sled deceleration reached a peak of 3.75 ± 0.27 g for a pulse duration of 120 ms (**Fig. 94**).

A1.3.2. Stereovision accuracy

Maximum sternal deflections, without dummy jacket, computed by stereovision were 4.85 ± 0.39 mm for HIII AM50 and 3.14 ± 0.43 mm for HIII AF05. At the same time, sternal deflections measured by dummy chest potentiometer were to 4.66 ± 1.03 mm and 2.66 ± 0.75 mm on HIII AM50 and HIII AF05 respectively. The Mean deflection difference across time was 0.31 ± 0.56 mm between stereovision and dummy internal deflection sensor (**Fig. 95**). The maximum difference was 1.22 mm.

A1.3.3. Dummy and volunteer readings

A1.3.3.1. Belt load

Shoulder belt loads of 69 ± 50 N for S01 and 110 ± 88 N for S02 were measured with Autochoc. Shoulder belt loads of 726 ± 82 N and 956 ± 128 N were measured respectively for S01 and S02 with Testochoc. Using Ifsttar sled, shoulder belt loads of 1365 ± 173 N and 547 ± 42 N were measured respectively with HIII AM50 and HIII AF05. On volunteers, the maximum shoulder belt loads were 559 ± 20 N and 859 ± 116 N for S01 and S03 respectively.

A1.3.3.2. Spine trajectories and excursion

Spine's landmark trajectories are shown in **Fig. 97** in the x-z plane of the sled. The maximum of X-axis excursion for the T8 landmark was 84.3 ± 4.8 mm for S01 and 80.5 ± 1.3 mm for S03. Similarly the maximum of Z-axis excursion for the T8 landmark was 83.8 ± 3.6 mm and 33.4 ± 2.2 mm for S01 and S03 respectively.

A1.3.3.3. Sternal deflection

On volunteers, the maximum sternal deflections were 25.6 ± 4.5 mm for S01 and 16.6 ± 5.3 mm for S03 (**Fig. 96**). S03 and S01 thoraces exhibited different deflection-force response. S03 initial slope was two times stiffer than S01. Furthermore, S03 sternal deflection decreased almost right after maximum shoulder belt force was reached while S01 sternal deflection continued to increase under maximum shoulder belt load.

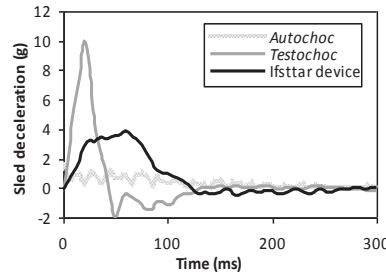


Fig. 94. Mean deceleration pulses of the three devices.

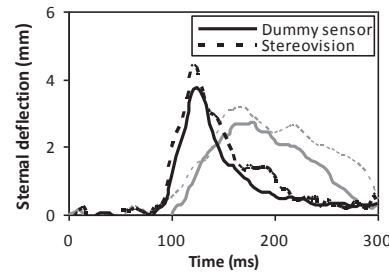


Fig. 95. HIII AM50 (black) and HIII AF 05 (grey) sternal deflection measured by internal dummy sensor (solid lines) and stereovision (dotted lines).

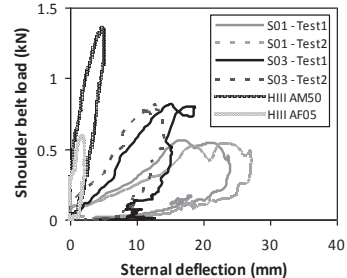


Fig. 96. Thorax mechanical responses of two volunteers (S01 in grey, S03 in black) overlaid with Dummy ones. (thick lines)

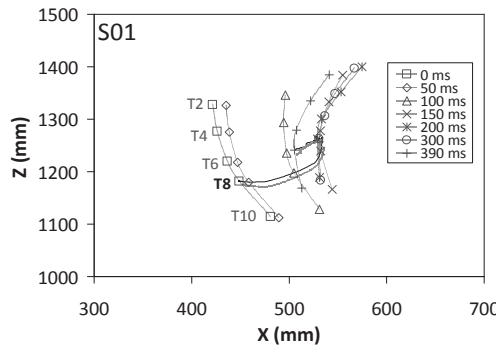


Fig. 97. Side view of spine kinematics of S01 (left) and S03 (right) subjects relative to the sled. 2D trajectory of T8 is shown in black line.

A1.4. Discussion

It appeared that while the severity of Autochoc was too low to observe any effect on subject thorax, Testochoc pulse was felt too severe by the two volunteers. Finally, Ifsttar device was selected to replicate a pulse between Autochoc and Testochoc pulses with 3.75 g peak and 120 ms duration. This pulse was found similar to the one of a recent study (Arbogast et al., 2009).

The total sled mass (including subject) was kept constant whatever subject mass by adding or removing weights attached to the sled. A good repeatability of the pulse (3.75 ± 0.27 g) was obtained.

Intrinsic error of stereovision (0.31 ± 0.56 mm) was judged acceptable compared to the volunteer lowest maximum sternal deflection (14.6 mm, 6%). Deflection measurements in this study consisted of soft tissue and bone deflections. It also included the error by soft tissue movements. Unfortunately, this error could neither be quantified nor corrected. Lopez-Valdes evaluated it between 15 and 20% in tests performed at 40 km/h with PMHS (Lopez-Valdes, 2009). At 8 km/h, a smaller error could be expected.

Subjects displayed high variation (60 %) of the maximum excursion in the Z-axis for the eight thoracic vertebrae.

Intra-subject sternal deflection varied between 9 and 13 %, whereas inter-subject deflection difference was 36 %.

APPENDIX 2: DEFINITION OF PALPABLE LANDMARKS

A2.1. Sled tests

Table 41. Definition of landmarks acquired on volunteer (front & back) during sled tests (1/3).

Code	Description
STER_M_001	Jugular notch (incisa jugularis)
STER_M_004	Midpoint between STER_M_001 and STER_M_003
STER_M_003	Midpoint between STER_M_001 and STER_M_005
STER_M_005	Midpoint between STER_M_003 and STER_M_005
STER_M_002	Xiphisternal joint
ACRO_L_001	Left acromioclavicular joint
CLAV_L_001	Left lateral convexity
CLAV_L_002	Left lateral concavity
CLAV_L_003	Midpoint between CLAV_L_001 and CLAV_L_002
CLAV_L_004	Midpoint between CLAV_L_001 and CLAV_L_003
CLAV_L_005	Midpoint between CLAV_R_002 and CLAV_L_003
ACRO_R_001	Right acromioclavicular joint
CLAV_R_001	Right lateral convexity
CLAV_R_002	Right lateral concavity
CLAV_R_003	Midpoint between CLAV_R_001 and CLAV_R_002
CLAV_R_004	Midpoint between CLAV_R_001 and CLAV_R_003
CLAV_R_005	Midpoint between CLAV_R_002 and CLAV_R_003
INF_L_001	Left anterior extremity of the left free rib 11
INF_L_002	Left inferior contour of the ribcage, 2 equi distant points from xyphoid to INF_L_001
INF_L_003	
INF_R_001	Left anterior extremity of the right free rib 11
INF_R_002	Left inferior contour of the ribcage, 2 equi distant points from xyphoid to INF_R_001
INF_R_003	
RIB_L_001	Vertical line at 5 cm left of STER_M_001
RIB_L_002	Vertical line at 5 cm left of STER_M_002
RIB_L_003	Vertical line at 5 cm left of STER_M_003
RIB_L_004	Vertical line at 5 cm left of STER_M_004
RIB_L_005	Vertical line at 5 cm left of STER_M_005
RIB_L_101	Vertical line at 10 cm left of STER_M_001
RIB_L_102	Vertical line at 10 cm left of STER_M_002
RIB_L_103	Vertical line at 10 cm left of STER_M_003
RIB_L_104	Vertical line at 10 cm left of STER_M_004
RIB_L_105	Vertical line at 10 cm left of STER_M_005
RIB_R_001	Vertical line at 5 cm right of STER_M_001
RIB_R_002	Vertical line at 5 cm right of STER_M_002
RIB_R_003	Vertical line at 5 cm right of STER_M_003
RIB_R_004	Vertical line at 5 cm right of STER_M_004
RIB_R_005	Vertical line at 5 cm right of STER_M_005
RIB_R_101	Vertical line at 10 cm right of STER_M_001
RIB_R_102	Vertical line at 10 cm right of STER_M_002

Table 41. Definition of landmarks acquired on volunteer (front & back) during sled tests (2/3).

RIB_R_103	Vertical line at 10 cm right of STER_M_003
RIB_R_104	Vertical line at 10 cm right of STER_M_004
RIB_R_105	Vertical line at 10 cm right of STER_M_005
SPINE_CV07_M_001	Spinous process of the cervical vertebrae 7
SPINE_LV04_M_001	Spinous process of the lumbar vertebrae 4 (same level of iliac crest)
SPINE_TV01_M_001	Spinous process of the thoracic vertebrae 1
SPINE_TV07_M_001	Spinous process of the thoracic vertebrae 7 (scapular tip)
SPINE_00X	Landmarks along the spine
RIB_L_201	Vertical line at 5 cm left of SPINE_001
RIB_L_202	Vertical line at 5 cm left of SPINE_002
RIB_L_203	Vertical line at 5 cm left of SPINE_003
RIB_L_204	Vertical line at 5 cm left of SPINE_004
RIB_L_205	Vertical line at 5 cm left of SPINE_005
RIB_L_301	Vertical line at 10 cm left of SPINE_001
RIB_L_302	Vertical line at 10 cm left of SPINE_002
RIB_L_303	Vertical line at 10 cm left of SPINE_003
RIB_L_304	Vertical line at 10 cm left of SPINE_004
RIB_L_305	Vertical line at 10 cm left of SPINE_005
RIB_R_201	Vertical line at 5 cm right of SPINE_001
RIB_R_202	Vertical line at 5 cm right of SPINE_002
RIB_R_203	Vertical line at 5 cm right of SPINE_003
RIB_R_204	Vertical line at 5 cm right of SPINE_004
RIB_R_205	Vertical line at 5 cm right of SPINE_005
RIB_R_301	Vertical line at 10 cm right of SPINE_001
RIB_R_302	Vertical line at 10 cm right of SPINE_002
RIB_R_303	Vertical line at 10 cm right of SPINE_003
RIB_R_304	Vertical line at 10 cm right of SPINE_004
RIB_R_305	Vertical line at 10 cm right of SPINE_005
INF_L_101	Vertical line of RIB_L_205, most inferior point of the ribcage
INF_L_102	Vertical line of RIB_L_305, most inferior point of the ribcage
INF_L_103	From INF_L_102, same distance between INF_L_101 and INF_L_102 on the contour
INF_R_101	Vertical line of RIB_R_205, most inferior point of the ribcage
INF_R_102	Vertical line of RIB_R_305, most inferior point of the ribcage
INF_R_103	From INF_R_102, same distance between INF_R_101 and INF_R_102 on the contour
HEAD_L_001	Nasion
HEAD_L_002	Vertex
HEAD_L_003	Gonion of the mandible
HUME_L_001	Humerus greater tubercle
HUME_L_002	Lateral epicondyle
HUME_L_003	Middle of the humerus
ULNA_L_001	Ulnar styloid process
ULNA_L_002	Olecranon posterior face superior border
ULNA_L_003	Middle of the ulna
FEMU_L_001	Greater trochanter
FEMU_L_002	Femoral lateral condyle
FEMU_L_003	Middle of the femur
TIBI_L_001	Tibia lateral condyle
TIBI_L_002	Lateral malleolus
TIBI_L_003	Middle of the tibia
FOOT_L_001	Lateral malleolus : Ankle

Table 41. Definition of landmarks acquired on volunteer (front & back) during sled tests (3/3).

FOOT_L_002	Anterior extremity of shoes
FOOT_L_002	Ball of foot (on shoes)
HEAD_L_001	Nasion
HEAD_L_002	Vertex
HEAD_L_003	Gonion of the mandible
HUME_L_001	Humerus greater tubercle
HUME_L_002	Lateral epicondyle

Table 42. Definition of the anatomical landmarks acquired on left side of the volunteer during sled tests.

Code	Description
HEAD_001	Nasion
HEAD_002	Vertex
HEAD_003	Gonion of the mandible
ACRO_L_001	Left acromioclavicular joint
HUME_001	Humerus greater tubercle
HUME_002	Lateral epicondyle
HUME_003	Middle of the humerus
ULNA_001	Ulnar styloid process
ULNA_002	Olecranon posterior face superior border
ULNA_003	Middle of the ulna
FEMU_001	Greater trochanter
FEMU_002	Femoral lateral condyle
FEMU_003	Middle of the femur
TIBI_001	Tibia lateral condyle
TIBI_002	Lateral malleolus
TIBI_003	Middle of the tibia
FOOT_001	Lateral malleolus : Ankle
FOOT_002	Anterior extremity of shoes
FOOT_003	Ball of foot (on shoes)

A2.2. Geometrical personalization

Table 43. Definition of the thorax anatomical landmarks acquired on thorax volunteer for geometrical personalization process.

Code	Description
	Vertebrae
CV_M_007	Spinous process of the cervical vertebrae 7
TV_M_001	Spinous process of the thoracic vertebrae 1
TV_M_002	Spinous process of the thoracic vertebrae 2
TV_M_003	Spinous process of the thoracic vertebrae 3
TV_M_004	Spinous process of the thoracic vertebrae 4
TV_M_005	Spinous process of the thoracic vertebrae 5
TV_M_006	Spinous process of the thoracic vertebrae 6
TV_M_007	Spinous process of the thoracic vertebrae 7
TV_M_008	Spinous process of the thoracic vertebrae 8
TV_M_009	Spinous process of the thoracic vertebrae 9
TV_M_010	Spinous process of the thoracic vertebrae 10
TV_M_011	Spinous process of the thoracic vertebrae 11
TV_M_012	Spinous process of the thoracic vertebrae 12
	Sternum
STER_M_001	Jugular notch
STER_M_002	Midpoint between STER_M_001 and STER_M_003
STER_M_003	Xiphisternal joint
	Clavicle
ACRO_L_001	Left acromioclavicular joint
CLAV_L_001	Left lateral convexity
CLAV_L_002	Left lateral concavity
ACRO_R_001	Right acromioclavicular joint
CLAV_R_001	Right lateral convexity
CLAV_R_002	Right lateral concavity
	Ribcage – inferior contour lines
INF_L_001	Left anterior extremity of the left free rib 11
INF_L_002	Left inferior contour of the ribcage, 2 equi distant points from xyphoid to INF_L_001
INF_L_003	
INF_R_001	Right anterior extremity of the right free rib 11
INF_R_002	Right inferior contour of the ribcage, 2 equi distant points from xyphoid to INF_R_001
INF_R_003	
	Ribcage – axillary lines
AXIL_L_003	Vertical line on the left axillary region : most inferior point of the ribcage
AXIL_L_001	Vertical line on the left axillary region : xyphoid level
AXIL_L_002	Vertical line on the left axillary region of the thorax : mid-point
AXIL_R_003	Vertical line on the right axillary region : most inferior point of the ribcage
AXIL_R_001	Vertical line on the right axillary region : xyphoid level
AXIL_R_002	Vertical line on the right axillary region of the thorax : mid-point
	Ribcage – posterior lines
POST_L_001	Left inferior angle of the scapula
POST_L_003	Most inferior point of the ribcage along the vertical line from the left inferior angle of the scapula
POST_L_002	Midpoint between POST_L_001 & POST_L_003
POST_L_004	Midpoint between POST_L_003 & AXIL_L_001
POST_R_001	Right inferior angle of the scapula
POST_R_003	Most inferior point of the ribcage along the vertical line from the right inferior angle of the scapula
POST_R_002	Midpoint between POST_R_001 & POST_R_003

Table 44. Definition of the anatomical landmarks acquired on THUMS geometry.

Code	Thorax skin set	Thorax bone set	Thorax bone& skin set
CV_M_007	mid(8713006 - 8713013)	8711784	mid(8713006 - 8713013)
TV_M_001	mid(8713013 - 8983045)	mid(8910006 - 8910007)	mid(8713013 - 8983045)
TV_M_002	8983046	mid(8910462 - 8910461)	8983046
TV_M_003	8983047	mid(8910895 - 8910907)	8983047
TV_M_004	8983048	mid(8911290 - 8911289)	8983048
TV_M_005	mid(8983050 - 8983049)	mid(8911686 - 8911685)	mid(8983050 - 8983049)
TV_M_006	8983051	mid(8912114 - 8912177)	8983051
TV_M_007	mid(8983052 - 8983053)	8912672	mid(8983052 - 8983053)
TV_M_008	8983054	mid(8912914 - 8912916)	8983054
TV_M_009	8983055	8913249	8983055
TV_M_010	8983057	mid(8913637 - 8913597)	8983057
TV_M_011	mid(8983058 - 8983057)	8914281	mid(8983058 - 8983057)
TV_M_012	8983059	mid(8914741-8914745)	8983059
STER_M_001	8984032	8925020	8925020
STER_M_002	8983062	8925069	8925069
STER_M_003	8983820	8925044	8925044
ACRO_L_001	8983323	8650010	8650010
CLAV_L_004	mid(8984002 - 8983999)	8650190	8650190
CLAV_L_005	8983274	8650070	8650070
ACRO_R_001	8984325	8550010	8550010
CLAV_R_004	mid(8984957 - 8984954)	8550190	8550190
CLAV_R_005	8984276	8550070	8550070
INF_L_001	8983840	8924741	8983840
INF_L_002	8983831	8924753	8983831
INF_L_003	8371930	8923427	8371930
INF_R_001	8984804	8924286	8984804
INF_R_002	8984795	8924248	8984795
INF_R_003	8370764	8921427	8370764
AXIL_L_001	8983235	8923110	8983235
AXIL_L_002	8983247	8923303	8983247
AXIL_L_003	8983863	8923419	8983863
AXIL_R_001	8984237	8921110	8984237
AXIL_R_002	8984249	8921303	8984249
AXIL_R_003	8984825	8921419	8984825
POST_L_001	8983149	8651001	8983149
POST_L_003	8983926	8941221	8983926
POST_L_002	mid(8983179 - 8983186)	mid(8923449 - 8923394)	mid(8983179 - 8983186)
POST_L_004	8983936	8923564	8983936
POST_R_001	8984151	8551001	8984151
POST_R_003	8984881	8940020	8984881
POST_R_002	mid(8984181 - 8984188)	mid(8921449 - 8921394)	mid(8984181 - 8984188)
POST_R_004	8984891	8921564	8984891

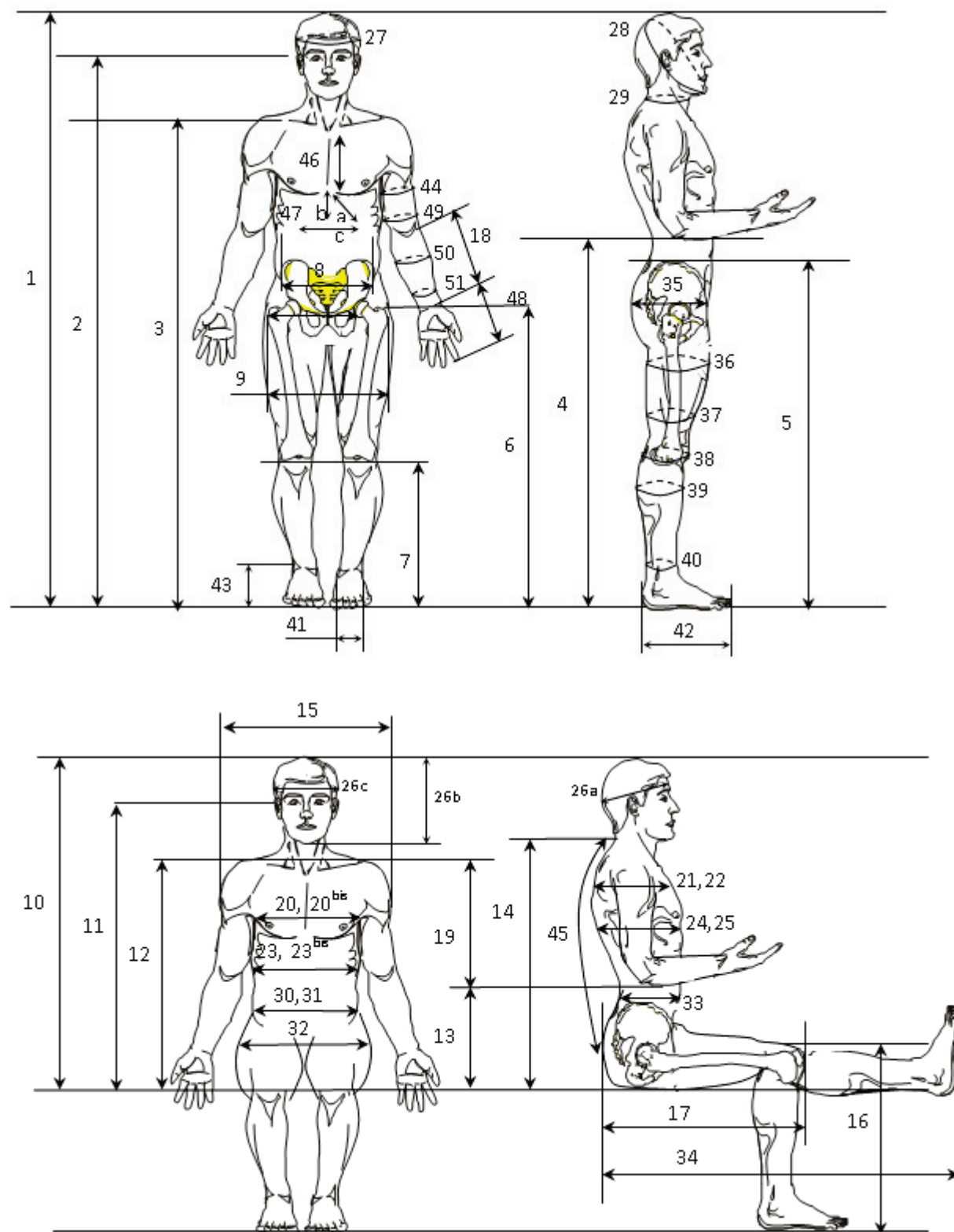


Fig. 98. External anthropometric measurements taken on volunteers.

Table 45. Definition of the anthropometric measurements taken on volunteers.

Code	Description
ANTH_01	Height
ANTH_02	Eyes - ground height (Francfort's plane parallel to the ground)
ANTH_03	Acromion - ground height
ANTH_04	Elbow - ground height
ANTH_05	Anterior-superior iliac spine - ground height
ANTH_06	Greater trochanter top - ground height
ANTH_07	Knee articular interline spacing - ground height
ANTH_08	Iliac bi-crest width
ANTH_09	Bi-trochanter width
ANTH_10	Sitting height (vertex)
ANTH_11	Eyes - seat height (Francfort's plane parallel to the ground)
ANTH_12	Acromion - seat height
ANTH_13	Elbow - seat height
ANTH_14	Cervical (C7) - seat height
ANTH_15	bi-acromial width
ANTH_16	Knee - ground height
ANTH_17	Buttock - Knee lenght
ANTH_18	Radius lenght
ANTH_19	Arm lenght (acromion - elbow)
ANTH_20	Thoracic axillary width
ANTH_21	Thoracic axillary thickness
ANTH_22	Thoracic axillary circumference
ANTH_23	Thoracic sub-sternal width
ANTH_24	Thoracic sub-sternal thickness
ANTH_25	Thoracic sub-sternal circumference
ANTH_26a	Head lenght = glabella - occiput lenght
ANTH_26b	Porion height (for skull height)
ANTH_26c	Head maximum width
ANTH_27	Head circumference passing over the glabella and through the occiput
ANTH_28	Chin - occipital circumference (with lower jaw closed from the dentary articulate)
ANTH_29	Neck circumference under the thyroid cartilage
ANTH_30	Abdominal width (navel)
ANTH_31	Abdominal circumference (navel)
ANTH_33	Abdominal thickness (navel)
ANTH_34	Buttock - heel lenght (tense leg)
ANTH_35	Low pelvic circumference (going through the trochanters)
ANTH_36	Thigh upper circumference (superior third)
ANTH_37	Thigh bottom circumference (inferior third)
ANTH_38	Knee circumference (interline spacing level)
ANTH_39	Greatest calf circumference
ANTH_40	Smallest ankle circumference
ANTH_41	Greatest foot width
ANTH_42	Greatest foot lenght
ANTH_43	Internal maleolus bottom - ground height
ANTH_43b	Internal maleolus - ground height
ANTH_44	Arm upper circumference (superior third)
ANTH_45	Cervical (C7) – seat height
ANTH_46	Sternum lenght
ANTH_47	Xiphoid angle
ANTH_48	Hand lenght
ANTH_49	Arm bottom circumference (inferior third)
ANTH_50	Greatest forearm circumference
ANTH_51	Smallest forearm circumference
ANTH_52	Seat height
RAM_07	Neck length (sternum – gnathion)
RAM_11	Chin height (for head height)
RAM_15	Bi-deltoid width

APPENDIX 3: DEFINITION OF BODY COORDINATES SYSTEMS USED IN GEOMETRICAL PERSONALIZATION PROCESS

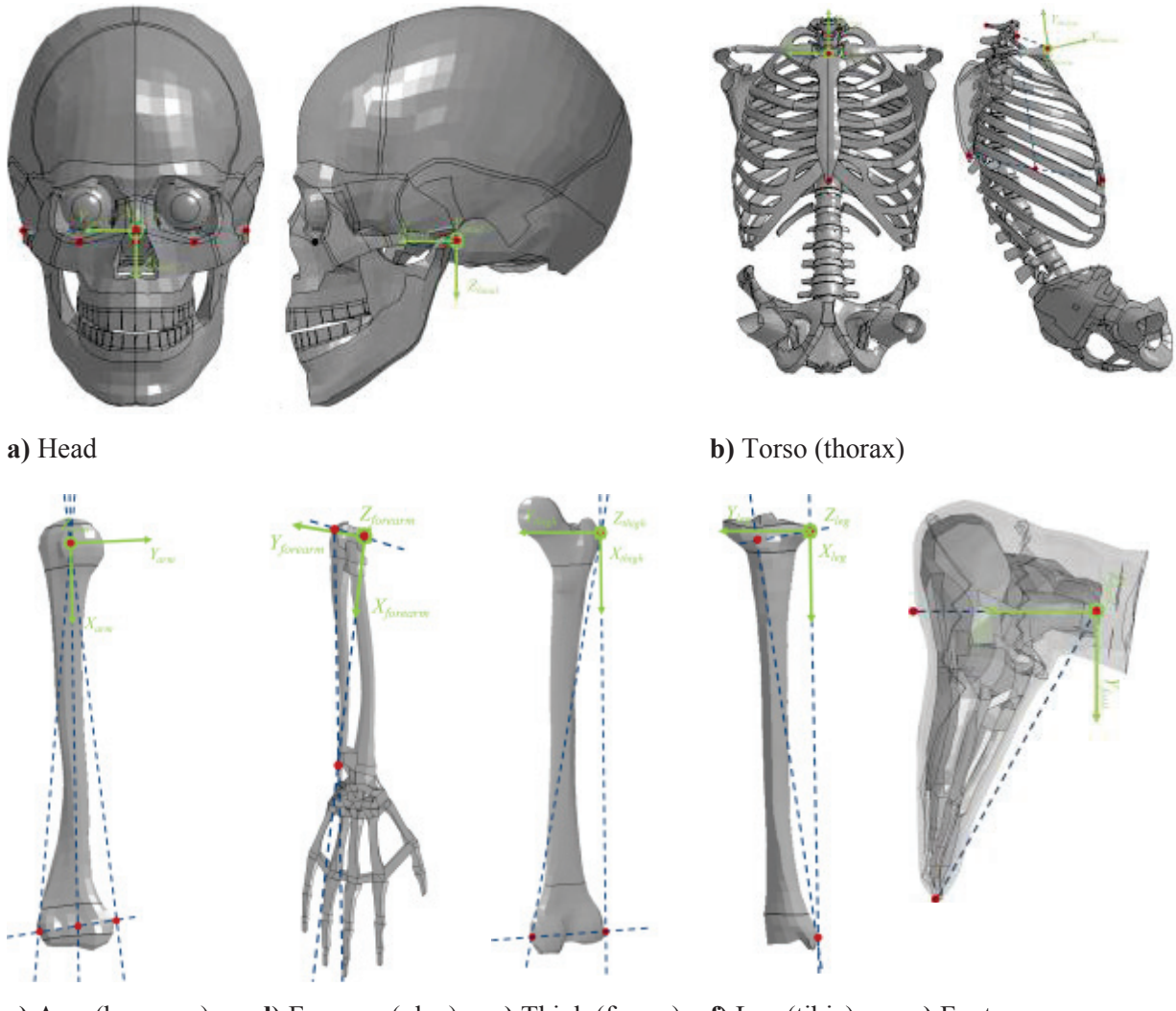


Fig. 99. Body coordinates system.

A3.1.1. Head coordinates system O_{head} , X_{head} , Y_{head} , Z_{head}

- O_{head} : The origin coincident with the middle of the two porions
 - X_{head} : The line connecting the middle of the two infraorbital point and the middle of the two porions, pointing forwards

- Y_{head} : The line connecting the right porion and the middle of the two porions, pointing to the right
- Z_{head} : The common line perpendicular to the X_{head} - and Y_{head} -axis, pointing downwards.

A3.1.2. Thorax coordinates system $\mathbf{O}_{\text{thorax}}, \mathbf{X}_{\text{thorax}}, \mathbf{Y}_{\text{thorax}}, \mathbf{Z}_{\text{thorax}}$

- O_{thorax} : The origin coincident with Incisura Jugulais
- Y_{thorax} : The line connecting the midpoint between Xiphoidus Process and T8 and the midpoint between Incisura Jugulais and C7, pointing upward.
- Z_{thorax} : The line perpendicular to the plane formed by IJ, C7, and the midpoint between PX and T8, pointing to the right.
- X_{thorax} : The common line perpendicular to the Z_{thorax} - and Y_{thorax} -axis, pointing forwards.

A3.1.3. Arm (humerus) coordinates system $\mathbf{O}_{\text{arm}}, \mathbf{X}_{\text{arm}}, \mathbf{Y}_{\text{arm}}, \mathbf{Z}_{\text{arm}}$

- O_{arm} : The origin coincident with the center of the head of humerus
- X_{arm} : The line connecting the middle of the two epicondyles and the center of the head of humerus, pointing upward.
- Y_{arm} : The line connecting the most medial point of the medial epicondyle and the center of the head of humerus, pointing to the right.
- Z_{arm} : The common line perpendicular to the X_{arm} - and Y_{arm} -axis, pointing forwards.

A3.1.4. Forearm (ulna) coordinates system $\mathbf{O}_{\text{forearm}}, \mathbf{X}_{\text{forearm}}, \mathbf{Y}_{\text{forearm}}, \mathbf{Z}_{\text{forearm}}$

- O_{forearm} : The origin coincident with the olecranon rostrum top
- X_{forearm} : The line connecting the ulnar styloid process top and the olecranon rostrum top.
- Y_{forearm} : The line connecting the point of the most cranial of the olecranon posterior face and the center of the head of humerus, pointing to the right.

- $Z_{forearm}$: The common line perpendicular to the $X_{forearm}$ - and $Y_{forearm}$ -axis, pointing forwards.

A3.1.5. Thigh (femur) coordinates system $\mathbf{O}_{thigh}, \mathbf{X}_{thigh}, \mathbf{Y}_{thigh}, \mathbf{Z}_{thigh}$

- O_{thigh} : The origin coincident with the most lateral of the greater trochanter
- X_{thigh} : The line connecting the epicondyle lateral top and the most lateral of the greater trochanter.
- Y_{thigh} : The line connecting the epicondyle medial top and the center of the most lateral of the greater trochanter.
- Z_{thigh} : The common line perpendicular to the X_{thigh} - and Y_{thigh} -axis, pointing forwards.

A3.1.6. Leg (tibia) coordinates system $\mathbf{O}_{leg}, \mathbf{X}_{leg}, \mathbf{Y}_{leg}, \mathbf{Z}_{leg}$

- O_{leg} : The origin coincident with the most caudal point of the medial condyle (on the medial edge)
- X_{leg} : The line connecting the median of the point most lateral of the tibial articular surface posterior edge and the point most lateral of the tibial articular surface anterior edge crossing the medial face of the medial malleolus and the most caudal point of the medial condyle (on the medial edge)
- Y_{leg} : The line connecting the tibial tuberosity top and the most caudal point of the medial condyle (on the medial edge).
- Z_{leg} : The common line perpendicular to the X_{leg} - and Y_{leg} -axis, pointing forwards.

A3.1.7. Foot coordinates system $\mathbf{O}_{foot}, \mathbf{X}_{foot}, \mathbf{Y}_{foot}, \mathbf{Z}_{foot}$

- O_{foot} : The origin coincident with the median of the point most lateral of the tibial articular surface posterior edge and the point most lateral of the tibial articular surface anterior edge crossing the medial face of the medial malleolus
- X_{foot} : The line connecting the most distal point of the tibial sole (on the foot skin) and O_{foot}

- Y_{foot} : The line connecting the most anterior point of the foot (on the skin) and O_{foot} .
- Z_{foot} : The common line perpendicular to the X_{foot} - and Y_{foot} -axis, pointing forwards.

APPENDIX 4: THE RADIAL BASIS FUNCTIONS (RBF), A NON-RIGID TRANSFORMATION METHOD FOR SCALING AN INITIAL MESH USING A SET OF CONTROL POINTS (BUHMANN, 2000)

A4.1. Introduction

The objective of this appendix is to briefly introduce RBF in the context of geometrical personalization. This appendix is based on the lecture given by Raphaël Dumas, in the M.Sc. of Biomechanics at the University of Lyon and on its article (Dumas and Cheze, 2009).

A4.2. Context

The Radial Basis Functions (RBF) are used as many different methods for determining the correspondence between points in two meshes, by convention between the initial and the target mesh. To determine correspondences, it is necessary to find the geometrical spatial transformation applied to the initial mesh so that it aligns with the target mesh. Transformations that preserve the distance between all nodes in the mesh are termed rigid-body transformations. They are equivalent to a change from one Cartesian system of coordinates to another one which differs by shift and rotation. Transformations that allow for a global change of scale and shear are referred to as affine transformations.

In contrast, nonrigid transformations as RBF convert straight lines to curves. There are many different nonrigid transformation models. In general, they can be divided into two categories: physical based models and function representations. The physical models in general, are derived from the theory of continuum mechanics. Function representations, as RBF, originate from interpolation and approximation theory.

A comprehensive and quantitative review of spatial transformations models is available in (Holden, 2008).

A4.3. Theoretical background

For each coordinate x_p^j, y_p^j, z_p^j of a control point p from the initial mesh i to the final mesh j , RBF corresponds to the linear decomposition on a basis of m functions of the Euclidean distances between the control point p and some centers ($\|\vec{x}_p^i - \vec{c}_f\|$) plus a linear polynomial a :

$$\begin{aligned} x_p^j &= \sum_{q=1}^m w_f^x h_f(\|\vec{x}_p^i - \vec{c}_f\|) + a(x_p^j, y_p^j, z_p^j) \\ y_p^j &= \sum_{q=1}^m w_f^y h_f(\|\vec{x}_p^i - \vec{c}_f\|) + a(x_p^j, y_p^j, z_p^j) \\ z_p^j &= \sum_{q=1}^m w_f^z h_f(\|\vec{x}_p^i - \vec{c}_f\|) + a(x_p^j, y_p^j, z_p^j) \end{aligned} \quad \text{Equation A-1}$$

where h_f are chosen functions, \vec{c}_f are called the centers of these functions and w are their respective weights. The centers can be arbitrarily fixed but are more generally selected out of the n points of the cluster (Buhmann, 2000). The number m of the functions of the basis is dependent on these selected centers and therefore $m \leq n$. The chosen function can be the same or different for each center. Thus, a RBF is a weighed sum of translations of a radially symmetric basic function augmented by a polynomial term.

Given a selected basis of m functions h_f (with their m corresponding centers), the $3 \times (m + 4)$ coefficients a and w can be found altogether by resolving a system of $3 \times (n + 4)$ linear equations for the n points of the cluster ($n \geq 5$):

$$\begin{bmatrix} \mathbf{H} & \bar{\mathbf{X}}^i \\ (\bar{\mathbf{C}})^T & \mathbf{0} \end{bmatrix} \begin{bmatrix} \mathbf{W} \\ \mathbf{A} \end{bmatrix} = \begin{bmatrix} \mathbf{X}^j \\ \mathbf{0} \end{bmatrix} \quad \text{Equation A-2}$$

with

$$\bar{\mathbf{C}}_{(m \times 4)} = \begin{bmatrix} 1 & x_1^i & y_1^i & z_1^i \\ \dots & \dots & \dots & \dots \\ 1 & x_f^i & y_f^i & z_f^i \\ \dots & \dots & \dots & \dots \\ 1 & x_m^i & y_m^i & z_m^i \end{bmatrix}, \mathbf{W}_{(m \times 3)} = \begin{bmatrix} w_1^x & w_1^y & w_1^z \\ \dots & \dots & \dots \\ w_f^x & w_f^y & w_f^z \\ \dots & \dots & \dots \\ w_m^x & w_m^y & w_m^z \end{bmatrix} \quad \text{Equation A-3}$$

and where the elements (p, f) of the matrix $\mathbf{H}_{(n \times m)}$ are $h_f(\|\vec{x}_p^i - \vec{c}_f\|)$.

The result for \mathbf{A} and \mathbf{W} is dependent on the chosen basis of functions. These functions and their corresponding centers can be selected by the user or by minimizing a cost function that

including the interpolation errors and a controlled smoothing effect (Dumas and Cheze, 2009). In a context of geometrical personalization, it was chosen to use the minimum cost function because an arbitrary choice of functions can generate large errors for RBF in mesh regions with a low landmark density (Holden, 2008). No smoothing effect was applied since we want to impose that RBF fit exactly the control points coordinates. The initial values of \mathbf{A} were computed using least squared methods and the initial residual that will be minimized was the residual from the least squared methods.

The coefficients a of the linear polynomial represent geometrical information (translation \vec{t}_0^{ij} , rotation \mathbf{R}^{ij} , homothety \mathbf{H}^{ij} and stretch \mathbf{S}^{ij}) can be computed from the coefficients of \mathbf{A} using a Single Value Decomposition (SVD):

$$\begin{bmatrix} a_0^x \\ a_0^y \\ a_0^z \end{bmatrix} = \vec{t}_0^{ij} \text{ and } \begin{bmatrix} a_1^x & a_2^x & a_3^x \\ a_1^y & a_2^y & a_3^y \\ a_1^z & a_2^z & a_3^z \end{bmatrix} = \mathbf{R}^{ij} \times \mathbf{H}^{ij} \times \mathbf{S}^{ij} \quad \text{Equation A-4}$$

APPENDIX 5: FRENCH SUMMARY OF THE MANUSCRIPT

A5.1. Introduction

Cette étude aborde le problème de l'aggravation du risque de fractures de côtes chez les automobilistes âgés en choc frontal. L'objectif de ce travail était d'étudier l'influence de l'âge et du morphotype sur la réponse mécanique du thorax en choc frontal.

La méthodologie retenue est la suivante. Des expérimentations *in vivo* en choc léger ont été réalisées sur des volontaires ceinturés, de différents âges et anthropométries. Ces expérimentations permirent d'étudier l'influence de l'âge et de la corpulence sur la réponse mécanique du thorax. Ces corridors permirent en outre l'obtention de corridors nécessaires à la validation de modèles EF personnalisés. Ensuite, simulations numériques effectuées dans le domaine lésionnel ont été effectuées avec des modèles personnalisés. Nous avons choisi pour cela d'utiliser des modèles EF personnalisés pour la simulation d'essais chariots dans le domaine lésionnel. Ce processus de personnalisation s'est divisé en une partie personnalisation géométrique et un vieillissement de la cage thoracique. Les simulations numériques permirent d'évaluer l'influence de ces deux niveaux de modifications sur le risque de fracture de côtes.

A5.2. Etat de l'art

A5.2.1. Anatomie

Le thorax humain est la partie supérieure du tronc compris entre le cou et l'abdomen. La région thoracique est limitée en haut par la ceinture scapulaire et la première paire de côtes, en arrière par la colonne vertébrale thoracique et l'arc postérieur des côtes, latéralement par les côtes et en avant par le plastron sterno-costal. Le segment thoracique se compose de:

- la structure osseuse du thorax ou cage thoracique dont le rôle est de protéger les viscères qui y sont contenues,
- la musculature et la peau qui constituent l'enveloppe extérieure de ce segment,
- les viscères intra-thoraciques (cœur, poumons, vaisseaux sanguins ...).

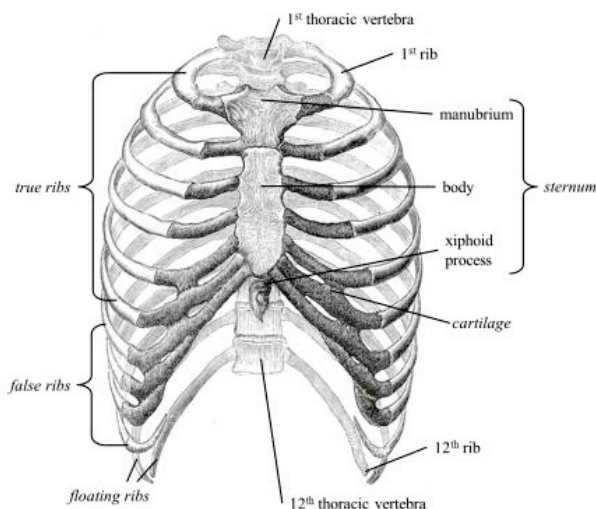


Fig. 100. Anatomie de la cage thoracique (Gray, 1918).

A5.2.2. Les lésions thoraciques

Dans le cadre des accidents automobiles, les blessures thoraciques sont fréquentes : le thorax apparaît comme étant la région anatomique la plus touchée en cas de choc frontal (Lafont and Laumon, 2003). Dans ce contexte, la blessure du thorax la plus fréquente est la fracture de côte particulièrement pour les personnes âgées (Ndiaye and Chiron, 2009).

A5.2.3. Réponse mécanique du thorax en chargement antéro-postérieur et critères de tolérance

Des essais expérimentaux ont permis de mieux connaître sa réponse au choc du thorax en chargement antéro-postérieur. Les premières études, réalisées sur sujets anatomiques, avaient pour objectif de développer des corridors force-déflexion du thorax à l'aide d'impacteurs (Kroell C.K., 1971; Lobdell et al., 1973; Nahum A.M., 1975; Neathery, 1974). Ces corridors ont été utilisés pour le développement des mannequins de choc et la définition de critère tolérance.

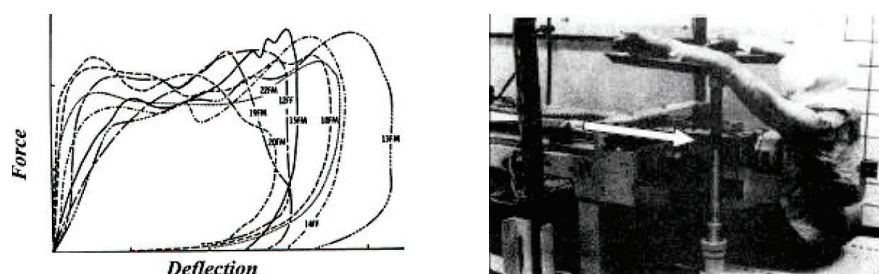


Fig. 101. Réponses mécaniques du thorax évaluées sur impacteurs (Kroell C.K., 1971) ; (Nahum A.M., 1975; Neathery, 1974).

Les critères et les seuils de tolérance thoraciques pour les essais avec mannequins en choc frontal sont :

- L'accélération max au niveau du thorax ou de la colonne qui reflète la sévérité globale :
 - Accélération max de 60 g au niveau de la colonne
- La compression du thorax qui reflète les lésions locales au niveau du squelette et souligne les blessures aux tissus mous causées par l'écrasement
 - C_{max} entre la paroi thoracique et la colonne de 30-35%
- Le critère visqueux qui reflète les blessures aux tissus mous dépendantes de la vitesse de chargement et, aussi, les fractures
 - VC_{max} de 1.0 à 1.3 m/s

Cependant, les corridors force-déflexion du thorax ont été jugés fortement dépendants de la répartition de la charge, en particulier sur la zone anatomique qui la supporte (Kent et al., 2003).

De plus, la réponse mécanique du thorax dépend fortement des caractéristiques géométriques de la cage thoracique et des propriétés de ses matériaux biologiques. Des auteurs s'accordent que la déformation de la cage thoracique sous un chargement antérieur-postérieur est divisée en rotation et déformation des côtes (Kent et al., 2005). Plus précisément, on suppose que, conformément à l'orientation thoracique, la force appliquée provoque des déformations de côtes et des rotations à des degrés divers. Ainsi, pour un individu avec une cage thoracique "verticale", un chargement antéro-postérieur produit à la fois des rotations et des déformations de côtes alors que pour un individu avec une cage thoracique "horizontale", la force agit directement dans le plan des côtes et implique principalement de la déformation. Ainsi, il semble que les caractéristiques géométriques de la cage thoracique peuvent prédisposer les fractures de côtes.

A5.2.4. Influence de l'âge sur la tolérance thoracique

Il est bien établi que la tolérance du thorax humain sous chargement dynamique diminue à mesure que l'âge augmente (Zhou et al., 1996). Les phénomènes physiologiques liés au vieillissement pourraient être décrits comme la combinaison de modifications mécaniques et structurales associés à une diminution de la tolérance à la déformation thoracique.

Le module élastique et la résistance à la rupture des os humains diminuent avec le vieillissement (Burstein et al., 1976). De même, une diminution de la résistance à la rupture du cartilage hyalin costal et de l'épaisseur corticale dans les sections de côtes a été observée (Yamada, 1970).

Les changements liés à l'âge dans la forme du thorax ont également été étudiés et des auteurs ont supposé que les côtes deviennent plus horizontales avec l'âge et l'inclinaison des côtes dans le plan sagittal diminue avec l'âge.

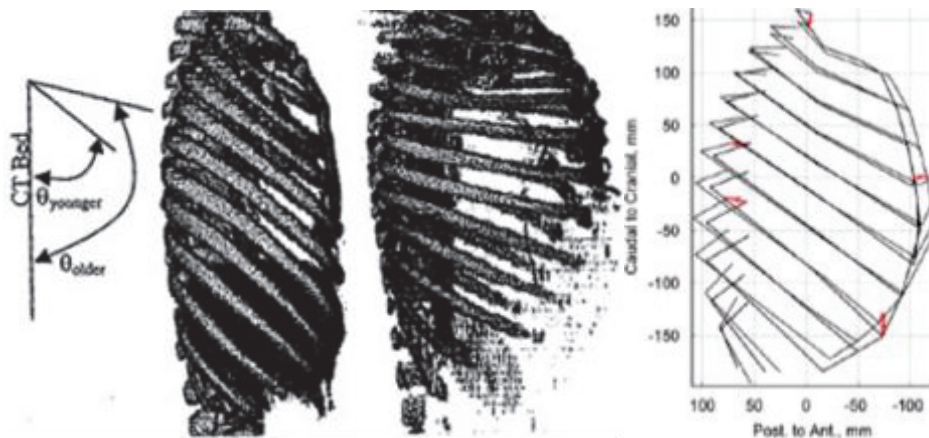


Fig. 102. Relèvement costal chez les personnes âgées (Gayzik et al., 2008; Kent et al., 2003).

Pourtant, certains auteurs ont également constaté une corrélation entre l'IMC et la forme du thorax. L'Indice de masse corporelle (IMC) a été associé à un risque accru de mortalité et un risque accru de blessures graves au thorax avec une prédominance de fractures des côtes et de contusions pulmonaires. Dans la grande majorité des pays développés, la prévalence du surpoids et de l'obésité dans la population âgée est très élevée.

A5.2.5. Potentiel des modèles éléments finis personnalisés du corps humain comme outils améliorés de prédiction de blessures

Les modèles éléments finis du corps humain ont été développées dans le but d'aider le développement de dispositifs de protection pour les usagers automobiles. Les modèles éléments finis existants (Robin, 2001 ; Iwamoto et al., 2002 ; Haug et al., 2004 ; Zhao and Narwani, 2005; Shen et al., 2010) sont validés par rapport aux essais expérimentaux existants mais ont l'inconvénient de représenter un homme moyen ($50^{\text{ème}}$ percentile).

Des modèles représentant des anthropométries extrêmes (Kimpara et al., 2002 ; Vezin and Verriest, 2005) ou des personnes âgées (Kimpara et al., 2005 ; Ito et al., 2009) ont été développées mais étaient limités aux données disponibles lors de leur validation.

A5.2.6. Conclusion

L'analyse de la bibliographie fait ressortir que les moyens actuels d'évaluation du risque de fractures ne permettent pas de prendre en compte les différences anatomiques et de propriétés mécaniques du thorax observées chez les personnes âgées. Les modèles éléments finis (EF) personnalisés du corps humain offrent un grand potentiel en tant qu'outil avancé d'évaluation du risque de blessures. Toutefois, des données expérimentales sont nécessaires pour valider ces modèles dans des conditions réalistes. De plus, le choix du niveau de personnalisation et la sensibilité de la réponse du modèle à celle-ci doivent être évaluées.

A5.3. Analyse in-vivo de la réponse mécanique du thorax lors d'un chargement ceinture

Des expérimentations in vivo menés sur des volontaires ceinturés en choc léger, de différents âges et anthropométries, ont été réalisées. Le but était d'évaluer l'influence de l'âge du surpoids ($IMC \geq 25 \text{ kg} / \text{m}^2$) sur la réponse mécanique thoracique.

A5.3.1. Matériel et méthodes

30 volontaires ont été testés. Ils étaient âgés entre 19 et 65 ans, hommes et femmes et furent sélectionnés sur des critères de poids et de taille selon des critères d'anthropométries.

Les essais ont été réalisés sur chariot représentant l'environnement d'un passager avant retenu par une ceinture 3-point. Le pulse utilisé lors des essais (4 g, 8 km/h) a été défini à partir d'essais préliminaires sur des démonstrateurs tout public avec des volontaires et des mannequins de chocs. Les moyens de mesures principaux étaient :

- un accéléromètre et capteurs de force situés sur le chariot
- un capteur laser mesurant la vitesse instantanée au moment du choc

De plus, des mires réfléchissantes étaient collées sur les volontaires et leur suivi par caméras vidéo rapides (1000 images/seconde) a permis l'obtention des trajectoires de ces marqueurs.

Un effort ceinture épaule résultant F_{Res} a été calculé en utilisant les efforts ceintures épaules externe et interne baudriers la géométrie de la ceinture. La déflection mid-sternale a été calculée comme la variation de distance entre les marqueurs placés au midsternum et le processus épineux de la 7ème vertèbre thoracique du sujet. Les courbes force-déflexion ont été construits en utilisant l'effort ceinture épaule résultant et la déflection mid-sternale.

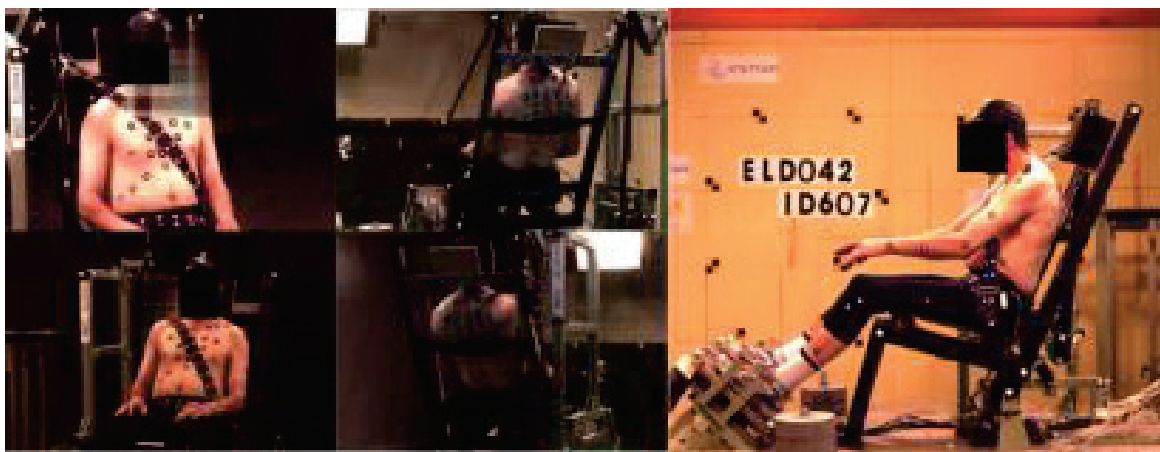


Fig. 103. Vue globale du dispositif.

Des raideurs thoraciques ont été identifiées sur les courbes force-déflexion. La raideur dynamique (DS) représente le comportement thoracique au début du chargement. La raideur effective (ES) représente son comportement sans prendre en compte l'historique du chargement. De plus, un modèle ressort-amortisseur a été identifié sur les courbes force-déflexion avec comme paramètres K et μ respectivement la raideur linéaire et l'amortissement du modèle.

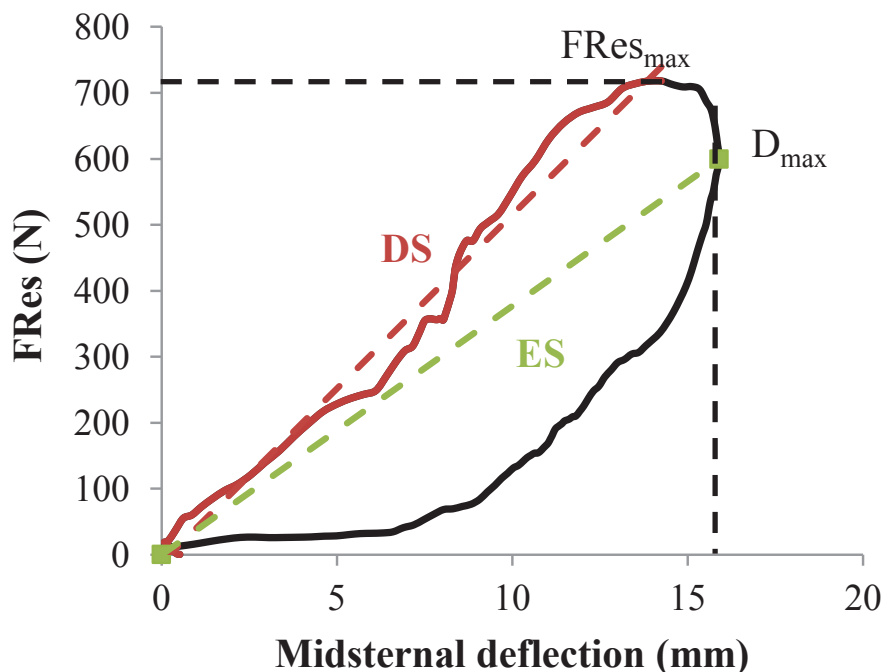


Fig. 104. Définition des raideurs thoraciques DS et ES.

A5.3.2. Résultats

Les réponses mécaniques obtenues dans ce protocole sont similaires à ceux obtenus dans la littérature (Kemper et al., 2011). La variabilité de la réponse mécanique thoracique est plus

élevée dans notre étude que dans la littérature, où seuls les hommes moyens avaient été pris en compte.

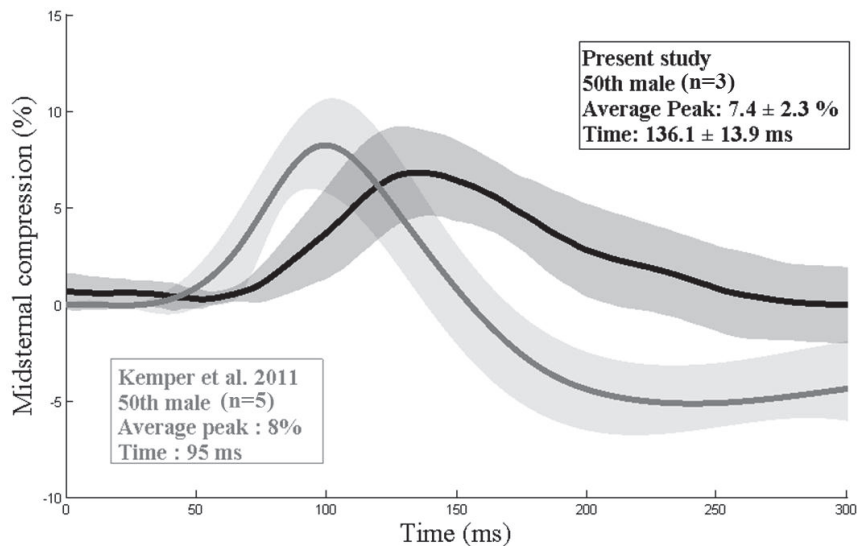


Fig. 105. Comparaison de corridors de compressions pour des volontaires proche du 50ème percentile homme entre cette étude ($n=3$) et Kemper et al. (2011; $n=5$).

Le groupe des volontaires en surpoids montre nettement une plus grande excursion du sternum dans le plan crano-caudal que les sujets du groupe normal. Ce phénomène peut être provoqué par un rôle accru des erreurs de mesures dues aux tissus mous. En outre, aucune différence significative n'a été observée pour le maximum de compression thoracique chez le groupe des volontaires en surpoids. Toutefois, il peut y avoir une tendance que les volontaires en surpoids ont un effet visqueux plus important dans leur comportement thoracique (μ plus élevée).

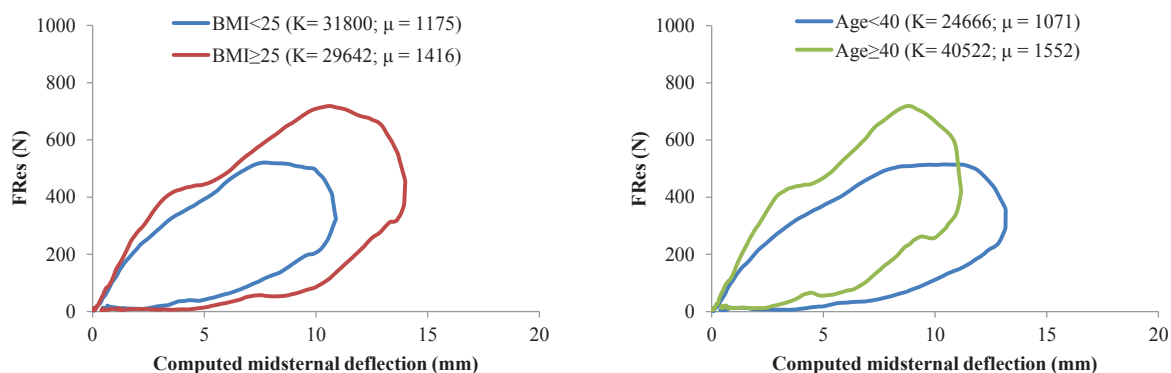


Fig. 106. Courbe de force-déflexion thoracique pour différents groupes d'âge et de BMI.

Le groupe des volontaires des plus de 40 ans montre nettement un maximum de compression thoracique plus faible que le groupe des volontaires plus jeunes. En outre, la raideur

thoracique était significativement plus élevée chez le groupe des volontaires des plus de 40 ans. une classification hiérarchique ascendante a montré que la plus grande valeur de raideur thoracique a été observée chez les femmes âgées sans surpoids, tandis que les valeurs les plus faibles du groupe ont été trouvées pour les personnes âgées ayant un IMC élevé. En outre, les personnes âgées ayant un IMC élevé semblaient avoir un effet visqueux plus important dans leur comportement thoracique. Le thorax des sujets jeunes étaient plus compliant surtout chez les plus minces.

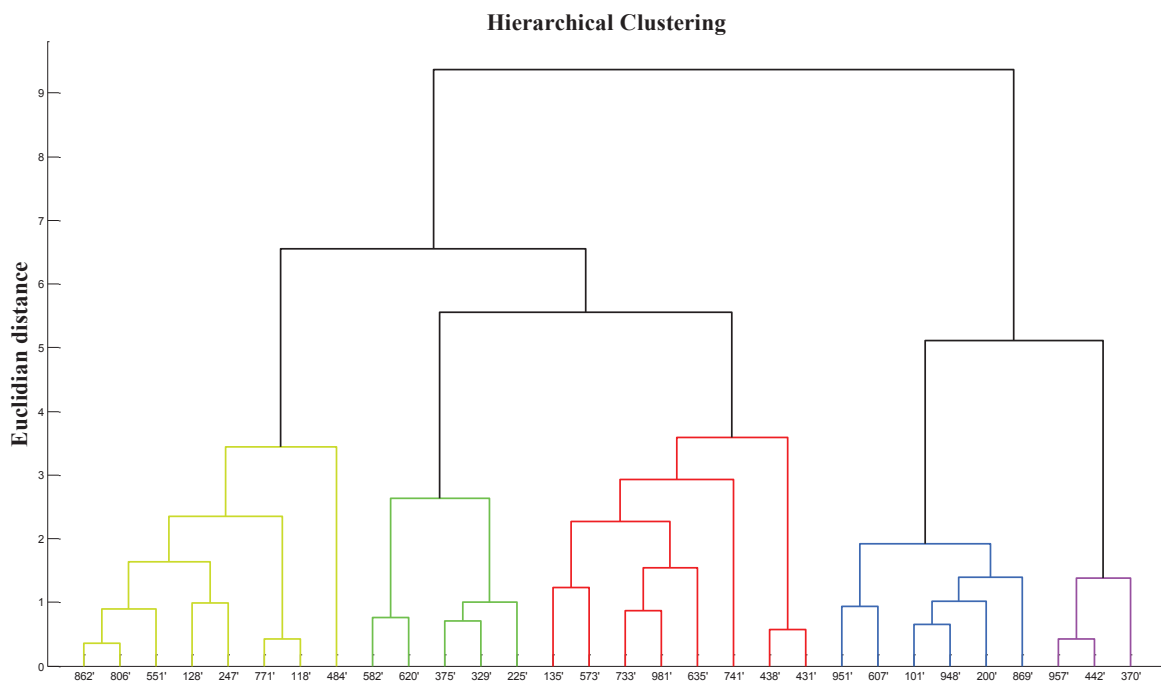


Fig. 107. Dendrogramme illustrant la répartition des groupes produit par la classification hiérarchique ascendante.

Néanmoins, la question si ces différences de réponses mécaniques entre volontaires ont des conséquences sur le risqué de blessures reste ouverte. Nous avons choisi pour cela d'utiliser des modèles EF personnalisés pour la simulation d'essais chariots dans le domaine lésionnel. Ce processus de personnalisation s'est divisé en une partie personnalisation géométrique et un vieillissement de la cage thoracique.

A5.4. Personnalisation géométrique d'un modèle humain numérique

Dans ce chapitre, nous présentons la méthodologie utilisée pour personnaliser la géométrie et la posture du modèle THUMS en utilisant des marqueurs externes pris sur le thorax et des mesures anthropométriques pris sur volontaires et sa posture. Le processus a été évalué sur un

sujet en comparant des IRM et le thorax personnalisé géométriquement et sur deux sujets en comparant des mesures anthropométriques.

A5.4.1. Matériel et méthodes

La personnalisation géométrique du modèle THUMS a été effectuée en utilisant la méthode Radial Basis Function (RBF; Buhmann, 2000) qui est fréquemment utilisée dans la littérature pour personnaliser des modèles EF avec des points de contrôle (Bertrand et al., 2006; Besnault et al., 1998; Serre et al., 2006; Vezin and Berthet, 2009).

Dans notre cas, la création de ces points de contrôle à la fois sur la géométrie initiale (THUMS 50ème percentile homme) et de la géométrie ciblée a demandé un traitement conséquent en amont.

Sur le modèle THUMS 50ème percentile homme, les points de contrôle initiaux ont été extrait selon le processus suivant. Pour chaque segment un repère local cylindrique est défini et chaque segment a été découpé en 10 tranches réparties le long de son axe longitudinal. Un balayage de long de cet axe a permis d'extraire les nœuds les plus distants: ce sont les points de contrôle initiaux.

Les points de contrôle initiaux ont ensuite été adaptés à la géométrie et la posture du volontaire. Les points de contrôle initiaux du thorax ont été déformés en utilisant 42 marqueurs externes pris sur le thorax. Ces marqueurs palpables thoraciques ont été identifiés aussi sur le maillage du THUMS 50ème percentile homme afin de réaliser cette opération. Difficile à localiser sur le maillage, ce sont au total 3 sets de nœuds potentiellement candidats qui ont été extraits du maillage initial du thorax.



Fig. 108. Données invivo utilisés pour personnaliser le modèle EF.

Les points de contrôle initiaux des autres segments ont été déformés en utilisant des mesures anthropométriques pris sur le volontaire. L'orientation de ces points de contrôle a été ensuite adaptée à la posture du volontaire acquis durant les essais sled.

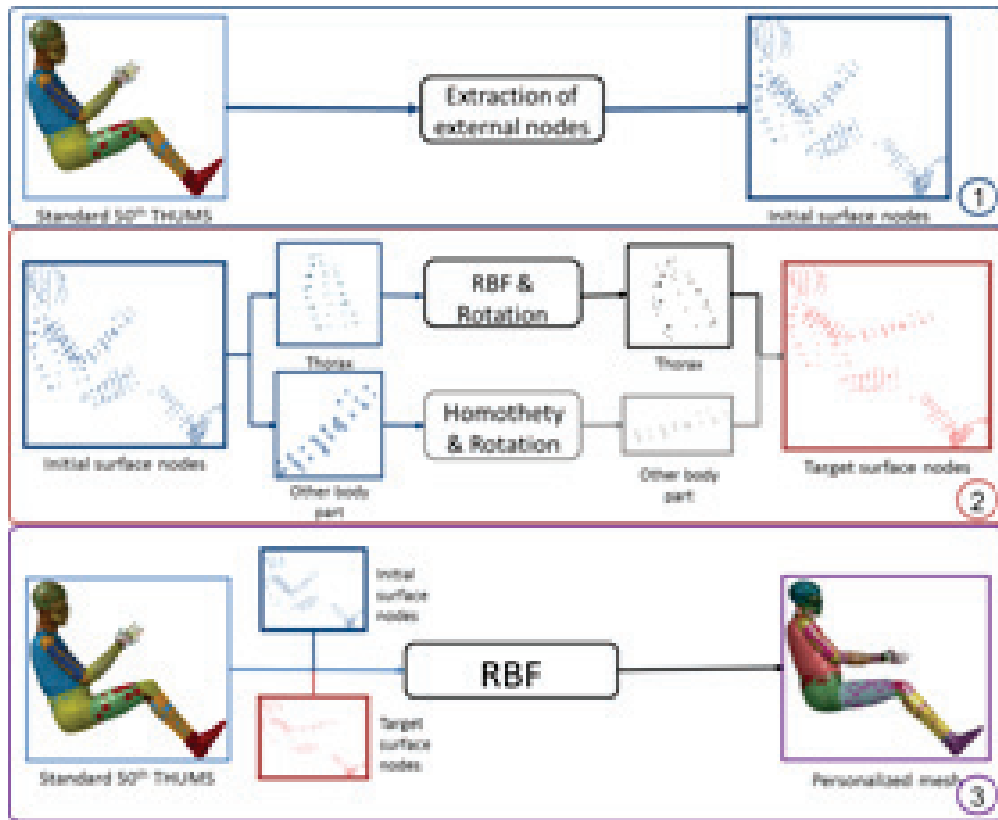
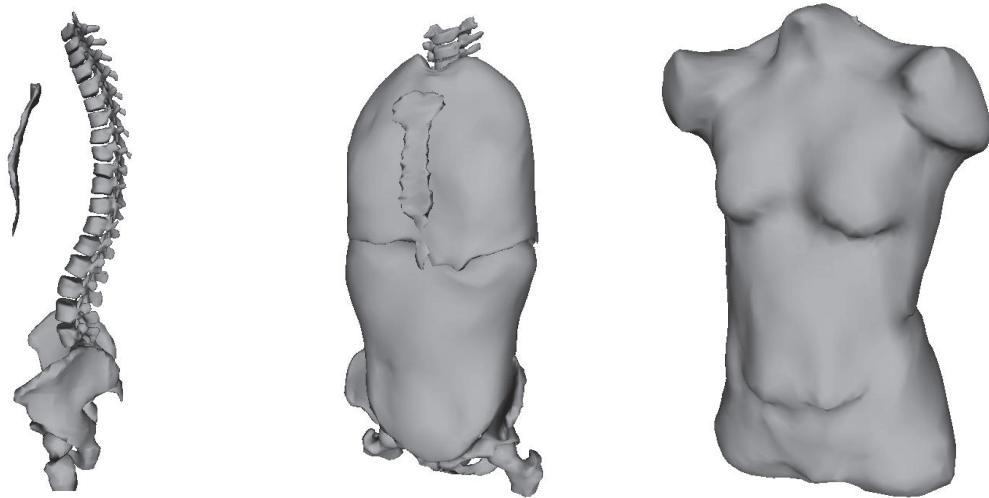


Fig. 109. Synthèse du processus de personnalisation géométrique.

A5.4.2. Résultats

Ce processus de personnalisation géométrique a été évalué premièrement sur le thorax en comparant le modèle personnalisé d'une femme et des IRM réalisées dans le cadre d'une étude précédente (Beillas et al., 2009; Lafont et al. 2010). Une distance moyenne nœuds à nœuds entre le modèle personnalisé et l'IRM appelée S-Score a été définie pour quantifier leur similitude.



a) Sternum et colonne vertébrale b) Cage thoracique, Poumons, Abdomen

Fig. 110. IRM utilisés dans l'évaluation du processus de personnalisation géométrique.

Le tableau ci-contre rapporte le S-Score obtenus pour différents modèles selon les nœuds candidats utilisés comme marqueurs palpables thoraciques. Les nœuds candidats pris sur la peau donnent les meilleurs résultats.

Table 46. Résultats des modèles personnalisés géométriquement pour différents jeux de noeuds comme marqueurs palpable thoraciques comparés aux IRMs.

Location	S-Score (♀-THUMS → MRI-scan)		
	Peau	Os	Combinaison
sternum	4.9 ± 2.1 mm	5.9 ± 3.3 mm	5.8 ± 2.7 mm
ribcage	5.3 ± 3.2 mm	6.0 ± 3.5 mm	5.4 ± 2.9 mm
spine	5.0 ± 4.3 mm	5.0 ± 3.9 mm	5.3 ± 3.2 mm
mediastinum	6.1 ± 3.1 mm	7.0 ± 3.3 mm	6.1 ± 2.9 mm
abdomen	8.4 ± 5.6 mm	13.4 ± 12.0 mm	8.8 ± 5.8 mm
skin	20.2 ± 17.5 mm	23.5 ± 23.9 mm	21.6 ± 18.7 mm
Total	8.8 ± 9.6 mm	11.0 ± 13.1 mm	9.0 ± 10.1 mm

Ce processus a été évalué en deuxième sur deux sujets en comparant des mesures anthropométriques et l'évolution de la qualité du maillage.

Le tableau ci-contre rapporte les différences relatives entre les mesures anthropométriques mesurées in vivo et sur les modèles éléments finis.

Table 47. Résultats des modèles personnalisés géométriquement pour différents jeux de noeuds comme marqueurs palpable thoraciques comparés à des dimensions anthropométriques.

Critères	Initial		Peau		Os		Combinaison	
	♀	♂	♀	♂	♀	♂	♀	♂
Corps entier	13.6%	5.3%	2.7%	2.8%	2.7%	3.0%	2.8%	2.8%
Thorax	21.0%	6.1%	3.9%	3.8%	18.7%	12.4%	7.4%	5.2%
Poids	44.7%	-12.0%	3.6%	3.3%	19.1%	20.4%	5.8%	5.2%

On remarque un réel apport de la personnalisation géométrique par rapport au maillage initial. Toutefois, parmi les modèles personnalisées, les modèles générées à partir de marqueurs palpables pris directement sur l'os n'ont pas été satisfaisant.

Bien que les données *in vivo* soient très limitées, le processus de personnalisation géométrique permet de gérer la posture et la géométrie sans remaillage. De plus ce processus permet de conserver une bonne qualité de maillage et les caractéristiques du modèle (liaisons articulaires, ligaments). Comme les données *in vivo* utilisées peuvent être obtenues de manière aisée, ce processus est très efficace et très prometteur.

A5.5. Risque de blessures thoraciques sur personnes vulnérables avec des modèles éléments finis personnalisés

Dans ce chapitre, nous présentons l'analyse de simulations avec des six modèles personnalisées. Premièrement, les modèles personnalisés ont été soumis à un pulse similaire aux essais *invivo* et leur réponse comparée à celle des volontaires. Ensuite, les modèles ont été soumis à un pulse plus sévère et l'influence du niveau de personnalisation sur le risque de lésion a été évalué.

A5.5.1. Réponse des modèles personnalisés géométriquement soumis à un pulse similaire aux essais *invivo*

Six modèles personnalisés géométriquement soumis à un pulse similaire aux essais *invivo*. Les modèles ont été positionnés en tant que passager avant dans un intérieur générique adapté géométriquement. Les modèles étaient retenus par une ceinture 3-points et soumis à l'action de la gravité et d'un pulse similaire aux essais volontaires (4g, 8km/h).



a) Une petite femme jeune de BMI moyen (957). **b)** Une jeune femme obèse (370). **c)** Un jeune homme en surpoids (442).



d) Un homme jeune de grande taille (806).

e) Un jeune homme de taille moyenne en surpoids (948).

f) Un homme âgé de taille moyenne en surpoids (948).

Fig. 111. Modèles personnalisés géométriquement soumis à un pulse similaire aux essais invivo

La comparaison a été effectuée sur les efforts ceintures, les excursions thoraciques et les courbes de force-déflexion. Les courbes obtenues par simulation étaient similaires à celles obtenues invivo.

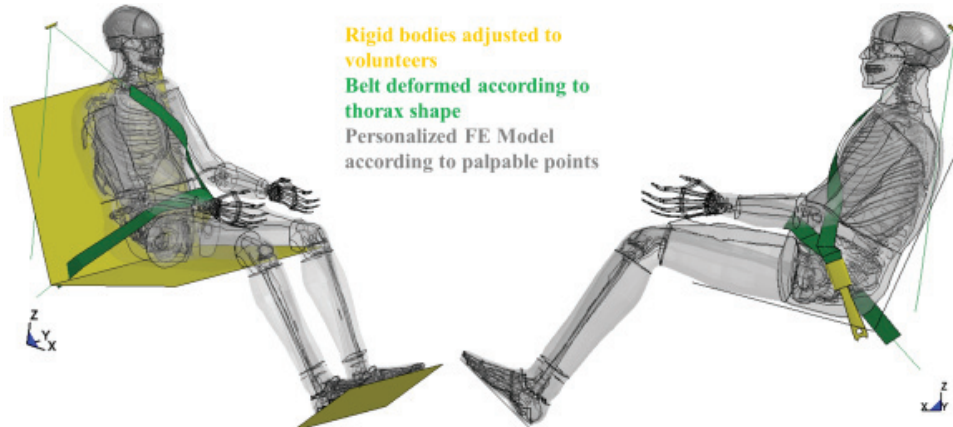
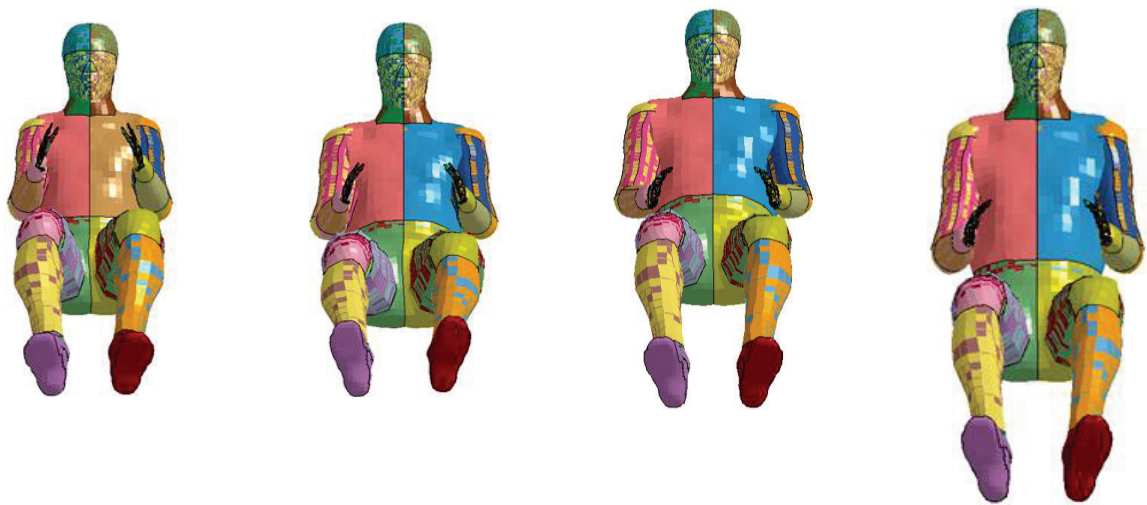


Fig. 112. Modélisation d'un intérieur générique adapté au modèle THUMS personnalisé géométriquement placé en position passager.

A5.5.2. Influence de la personnalisation géométrique

L'influence de la personnalisation géométrique sur le risque de blessure thoracique a été évaluée à grande vitesse sur quatre modèles personnalisés géométriquement de différentes anthropométries.



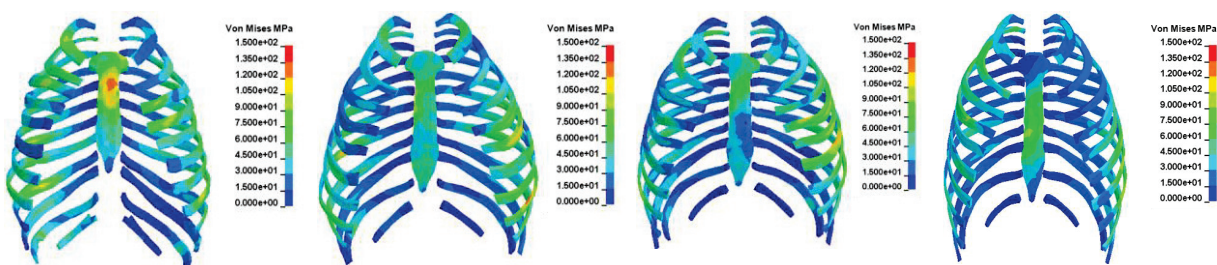
a) Une petite femme jeune de BMI moyen (957). **b)** Une jeune femme obète (370). **c)** Un jeune homme en surpoids (442). **d)** Un homme jeune de grande taille (806).

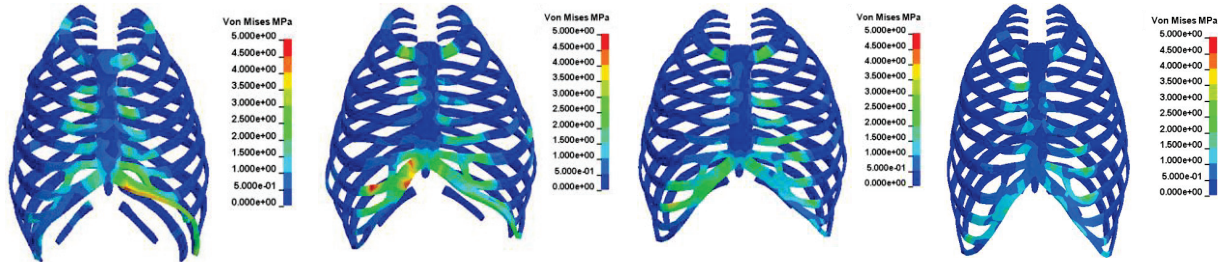
Fig. 113. Modèles personnalisés géométriquement pour l'étude de l'influence de la personnalisation géométrique

Les modèles ont été positionnés dans un intérieur générique adapté géométriquement identique aux simulations précédentes. Les modèles étaient retenus par une ceinture 3-points et soumis à l'action de la gravité et d'un pulse sévère reconnu pour générer des lésions (13g, 40 km/h).

Les éléments de côtes effacés lors de la simulation ont été utilisés pour localiser et quantifier le nombre de côtes fracturées (NFR). Une échelle de sévérité spécifique au thorax TOAIS a été ensuite calculée à partir de ces informations

Une concentration de contraintes a été observée sur la partie gauche de la cage thoracique et sur le sternum comme on pouvait s'y attendre dans une telle configuration. Néanmoins il a été observé une certaine variabilité de répartition entre les différents modèles personnalisés géométriquement.





a) Une petite femme jeune de BMI moyen (957). **b)** Une jeune femme obèse (370). **c)** Un jeune homme en surpoids (442). **d)** Un homme jeune de grande taille (806).

Fig. 114. Contraintes d Von Mises stress obtenus pour quatre modèles personnalisés géométriquement soumis à un pulse de 13g à 40 km/h (haut: cortical, bas: cartilage & trabeculae)

Le nombre et la localisation des fractures de côtes varient considérablement d'un modèle personnalisé géométriquement à un autre. Thums 806 a été clairement beaucoup plus blessé d'un point de vue du nombre de fractures de côtes (14). Une explication à ce phénomène pourrait être un thorax plus lourd (28 kg dans ce cas). Ce thorax plus lourd pourrait ainsi s'auto-charger plus facilement malgré la présence d'un limiteur d'effort.

A5.5.3. Influence du vieillissement de la cage thoracique

Après cette analyse sur différents modèles personnalisés géométriquement, nous avons souhaité connaître l'influence d'un vieillissement des matériaux de la cage thoracique sur le risque de fractures.

Nous avons souhaité effectuer ce vieillissement de manière progressive en incorporant séquentiellement une diminution de l'épaisseur cortical (Mohr et al., 2007), une diminution des propriétés mécaniques de l'os (cortical et trabéculaire) et enfin une diminution des propriétés du cartilage. La diminution des propriétés a été définie à partir des ratios appliqués par Ito et al., 2009.

Ce processus a été appliqué sur deux modèles personnalisés géométriquement correspondant à deux individus 118 et 948 d'âge différent et de taille moyenne et de corpulence supérieure.

Table 48. Level of material property personalization and associated versions of personalized THUMS models.

	Cartilage-1	Cartilage-2	Cortical-1	Cortical-2	Thickness-1	Thickness-2	Trabecular-1	Trabecular-2
Thums-118 v1.0	Yes	No	Yes	No	Yes	No	Yes	No
Thums-118 v1.1	Yes	No	Yes	No	No	Yes	Yes	No
Thums-118 v1.2	Yes	No	No	Yes	No	Yes	No	Yes
Thums-118 v1.3	No	Yes	No	Yes	No	Yes	No	Yes
Thums-948 v1.0	Yes	No	Yes	No	Yes	No	Yes	No
Thums-948 v1.1	Yes	No	Yes	No	No	Yes	Yes	No
Thums-948 v1.2	Yes	No	No	Yes	No	Yes	No	Yes
Thums-948 v1.3	No	Yes	No	Yes	No	Yes	No	Yes

Table 49. Material properties of the initial THUMS model (1) and the aged THUMS model (2).

	ρ (kg/m ³)	YM (MPa)	ϵ_{y1}	σ_{y1} (MPa)	ϵ_{y2}	σ_{y2} (MPa)	ϵ_{y3}	σ_{y3} (MPa)	ϵ_{y4}	σ_{y4} (MPa)	σ_{max} (MPa)	ϵ_{max}
Cartilage-1	1000	49.0	0.0000	4.8	0.1675	9.0	0.3296	10.0	-	-	-	0.3296
Cartilage-2	1000	49.0	0.0000	3.7	0.1293	6.8	0.2545	7.6	-	-	-	0.2545
Cortical-1	2000	13000	0.0000	93.5	0.0715	128.0	0.0185	150.0	-	-	-	0.0180
Cortical-2	2000	13000	0.0000	79.9	0.0617	109.4	0.0159	128.2	-	-	-	0.0154
Trabecular-1	862	40.0	0.0000	1.8	0.0500	3.8	0.0600	4.1	0.1000	5.0	-	0.1030
Trabecular-2	862	40.0	0.0000	0.7	0.0557	1.4	0.0669	1.5	0.1115	1.9	-	0.1148

Table 50. Cortical thickness of the initial THUMS model (1) and the aged THUMS model (2).

Code	Cortical thickness (mm)	Sternum thickness (mm)
Thickness-1	0.70	1.00
Thickness-2	0.60	0.86

Les modèles ont été positionnés dans un intérieur générique adapté géométriquement identique aux simulations précédentes. Les modèles étaient retenus par une ceinture 3-points et soumis à l'action de la gravité et d'un pulse sévère reconnu pour générer des lésions (13g, 40 km/h).

Les éléments de côtes effacés lors de la simulation ont été utilisés pour localiser et quantifier le nombre de côtes fracturées (NFR). Une échelle de sévérité spécifique au thorax TOAIS a été ensuite calculée à partir de ces informations

Le nombre de côtes fracturés NFR a cru substantiellement au fur et à mesure que les propriétés de la cage thoracique eurent été modifiées. Particulièrement, le fait de diminuer les propriétés mécaniques de l'os (cortical et trabéculaire) a été plus influent sur l'aggravation des lésions.

A5.6. Conclusion

Cette étude aborde le problème de l'aggravation du risque de fractures de côtes chez les automobilistes âgés en choc frontal. L'analyse de la bibliographie fait ressortir que les moyens actuels d'évaluation du risque de fractures ne permettent pas de prendre en compte les différences anatomiques et de propriétés mécaniques du thorax observées chez les personnes âgées. Les modèles éléments finis (EF) personnalisés du corps humain offrent un grand potentiel en tant qu'outil avancé d'évaluation du risque de blessures. Toutefois, des données expérimentales sont nécessaires pour valider ces modèles dans des conditions réalistes. De plus, le choix du niveau de personnalisation et la sensibilité de la réponse du modèle à celle-ci doivent être évaluées.

Pour répondre à ces questions, nous avons effectué des essais de type chariot sur des volontaires adultes de différents âge et anthropométries afin d'étudier la variabilité de réponse mécanique du thorax et nous avons développé des modèles éléments finis personnalisés afin d'étudier cette variabilité dans le domaine lésionnel.

L'analyse statistique sur 30 volontaires a montré que la raideur thoracique était significativement plus élevée chez les volontaires âgés de plus de 40 ans, particulièrement chez les femmes âgées minces et dans une moindre mesure chez les personnes en surpoids. Ces résultats suggèrent ainsi qu'âge et corpulence ont une influence sur la réponse mécanique du thorax. De plus une classification hiérarchique ascendante a permis de définir 5 groupes de réponse mécanique différente dont certains avaient des anthropométries spécifiques.

Ces expérimentations *in vivo* ont apporté de nouvelles données sur la variabilité biomécanique humaine mais présentent toutefois certaines limitations:

- Une plus grande quantité de sujets, notamment des personnes âgées permettrait d'effectuer une analyse plus fine des résultats concernant le rôle de l'âge, de la corpulence et de la variabilité de la réponse mécanique du thorax. En outre, les sujets âgés testés ne sont pas forcément représentatifs de leur groupe d'âge, car ils ont été recrutés sur un critère strict d'absence d'ostéopénie, ce qui représente moins de la population de plus de 40 ans.
- Bien que plus représentatif d'une situation d'accident réel, les tests de type sled ont l'inconvénient de ne pas permettre un contrôle de la force exercée par la ceinture sur le thorax. Ainsi, le thorax est auto-chargée par sa propre inertie ce qui limite la comparaison du comportement mécanique thoracique. Des essais de compression tel que proposé par Cesari et Bouquet 1990 permettent de contrôler la force appliquée par la ceinture sur le thorax. Néanmoins, ce protocole implique que le sujet est en décubitus dorsal, qui est moins représentatif d'une situation d'accident réel, où l'excursion de la colonne vertébrale n'est pas limitée.
- Dans notre étude, les volontaires ont été soumis à un pulse défini à partir de deux démonstrateurs public et similaire à d'autres pulses utilisés dans la littérature. Dans un prochain protocole impliquant dans des tests *in vivo* de type sled, utiliser un ensemble de différents pulses devrait permettre de vérifier la pertinence du modèle ressort amortisseur défini pour la réponse mécanique du thorax. Cependant, ces différents pulses devront être suffisamment violents pour étudier une différence de réponse mécanique thoracique sans toutefois présenter un risque pour les volontaires.

Néanmoins, la question de savoir si ces différences de réponses mécaniques du thorax entre volontaires impliquent des répercussions sur le risque de blessure au thorax devait être étudiée numériquement. Nous avons choisi pour cela d'utiliser des modèles EF personnalisés pour la simulation d'essais chariots dans le domaine lésionnel. Ce processus de personnalisation s'est divisé en une partie personnalisation géométrique et un vieillissement de la cage thoracique.

La géométrie et la posture du modèle EF THUMS 50^{ème} percentile a été modifiée à l'aide de données acquises sur les volontaires testés *in vivo*. Le processus de personnalisation géométrique a été validé en comparant la géométrie obtenue sur un modèle personnalisé et celle acquise sur un volontaire par IRM et de mesures anthropométriques globales sur deux volontaires. De cette validation, il est apparu que le processus de personnalisation permet à la fois d'adapter géométrie et posture sans remaillage. Ce processus permet en outre de conserver une bonne qualité de maillage et les caractéristiques du modèle.

Ce processus de personnalisation géométrique a été appliqué pour personnaliser le modèle THUMS à partir des données issues de quatre volontaires de différentes anthropométries. Une validation de ces modèles personnalisés géométriquement a été effectuée dans le domaine non lésionnel en comparaison des réponses obtenues expérimentalement. Les réponses simulées étaient semblables aux résultats expérimentaux à faible vitesse. Ensuite des simulations dans le domaine lésionnel ont montré une influence de cette personnalisation géométrique sur le risque de fractures de côtes. Ainsi, les anthropométries les plus extrêmes ont été les plus gravement lésées.

Toutefois, le modèle final est toujours plus ou moins proche de la géométrie initiale en termes de forme. En particulier, les différences anatomiques spécifiques dues au sexe et des déformations pathologiques du thorax ne purent être reproduites. Une solution serait d'augmenter le nombre de marqueurs palpables du thorax pour augmenter la précision. Une autre solution serait d'avoir une information sur la géométrie interne du volontaire à partir d'un système radiographie basse dose (EOS) ou d'IRM. Enfin il pourrait être bénéfique d'utiliser des géométries initiales plus représentatives de la population cible. Ainsi, utiliser une géométrie initiale d'un modèle EF féminin serait plus approprié pour la construction de modèles EF féminins personnalisés géométriquement.

Ensuite un processus de vieillissement de la cage thoracique a été appliqué sur deux modèles d'anthropométrie similaires. Le vieillissement a été appliqué de manière progressive en incorporant séquentiellement une diminution de l'épaisseur cortical, une diminution des

propriétés mécaniques de l'os (cortical et trabéculaire) et enfin une diminution des propriétés du cartilage issus de la littérature. Des simulations numériques dans le domaine lésionnel ont montré que le risque de fractures était particulièrement sensible à une modification des propriétés osseuses.

Toutefois, ce processus de vieillissement a été appliqué sur un nombre réduit de modèles personnalisés géométriquement, il pourrait être intéressant de reproduire ce travail sur des modèles personnalisés géométriquement représentatifs d'anthropométries extrêmes. De plus, ce processus de vieillissement devrait être idéalement appliqué en fonction de données acquises sur volontaire afin de personnaliser le thorax du modèle EF en fonction de l'âge. Il n'existe pas actuellement de techniques permettant d'extraire ces données bien que les méthodes de transmission d'ondes ultrasonores dans les côtes ont un fort potentiel (Tran et al., 2010).

En conclusion, lors de l'examen des travaux antérieurs portant sur le thorax certains progrès ont été réalisés:

- Des réponses mécaniques du thorax de volontaires de différentes anthropométries et d'âges sont fournis alors que les données expérimentales concernant ce type d'essai dans la littérature sont très limitées d'un point de vue variabilité.
- Les influences d'une personnalisation géométrique et d'un vieillissement de la cage thoracique sur le risque de fractures de côtes ont été évaluées conjointement alors que les études similaires sont limitées à un seul de ces aspects.

Cette étude devrait permettre de mieux estimer le risque de blessure pour les automobilistes vulnérables. Elle devrait contribuer ainsi à promouvoir les modèles personnalisés du corps humain comme outil avancé d'évaluation du risque de blessures.

INFLUENCE DE L'AGE ET DU MORPHOTYPE SUR LA REPONSE MECANIQUE DU THORAX : ETUDE EXPERIMENTALE IN VIVO ET ANALYSE NUMERIQUE A L'AIDE DE MODELES EF PERSONNALISES DU CORPS HUMAIN

Cette étude aborde le problème de l'aggravation du risque de fractures de côtes chez les automobilistes âgés en choc frontal. L'analyse de la bibliographie fait ressortir que les moyens actuels d'évaluation du risque de fractures ne permettent pas de prendre en compte les différences anatomiques et de propriétés mécaniques du thorax observées chez les personnes âgées. Les modèles éléments finis (EF) personnalisés du corps humain offrent un grand potentiel en tant qu'outil avancé d'évaluation du risque de blessures. Toutefois, des données expérimentales sont nécessaires pour valider ces modèles dans des conditions réalistes. De plus, le choix du niveau de personnalisation et la sensibilité de la réponse du modèle à celle-ci doivent être évaluées.

Des expérimentations in vivo menés sur des volontaires ceinturés en choc léger, de différents âges et anthropométries, ont été réalisées. Ces tests ont permis d'étudier l'influence de l'âge et de la corpulence sur la réponse mécanique du thorax et ont permis l'obtention de corridors nécessaires à la validation de modèles EF personnalisés. La géométrie du modèle numérique THUMS a été adaptée à celle des volontaires et les propriétés mécaniques du thorax ont été modifiées au vu du vieillissement pour effectuer une analyse similaire dans le domaine lésionnel. Les simulations numériques ont mis en évidence un risque accru de fracture de côtes pour certains modèles personnalisés.

Cette étude devrait permettre de mieux estimer le risque de blessure pour les automobilistes vulnérables. Elle devrait contribuer ainsi à promouvoir les modèles personnalisés du corps humain comme outil avancé d'évaluation du risque de blessures.

AGE AND MORPHOTYPE INFLUENCE ON THORACIC MECHANICAL RESPONSE: IN VIVO EXPERIMENTAL STUDY AND NUMERICAL ANALYSIS USING PERSONALIZED HUMAN BODY FE MODELS

This study deals with the topic of increased risk of rib fractures among elderly drivers in frontal impact. The analysis of the literature reveals that actual thorax injury assessment tools do not take into account for the differences in anatomical features and biological material properties observed between adults and elderly. Personalized human body finite element (FE) models have great potential as improved thorax injury assessment tools. However, experimental data are needed to validate these models under real-world conditions. In addition, the choice of the level of personalization of the model and the sensibility of the model response to this personalization must be assessed to predict thoracic injury risk.

In vivo sled tests were performed on belted volunteers of various anthropometries and age. These tests were used to assess the influence of age and corpulence on thorax mechanical response and allowed to obtain corridor responses needed to validate personalized FE models. The geometry of the FE model THUMS was adapted to the volunteers and the thorax material properties were modified considering aging to carry out a similar analysis in the injurious domain. Numerical simulations highlighted an increased risk of rib fractures for specific personalized models.

This study should help to better estimate the injury risk for car occupants. It should contribute to promote personalized human body models as attractive thorax injury assessment tool of vulnerable individuals.

DISCIPLINE Mécanique

MOTS-CLES

Biomécanique, Choc frontal, Thorax, Vieillissement, Volontaires, Modèles EF personnalisés.

INTITULE ET ADRESSE DU LABORATOIRE :

Laboratoire de Biomécanique et Mécanique des Chocs LBMC UMR_T 9406 (Ifsttar / UCBL),
Ifsttar — Institut Français des Sciences et Technologies des Transports, de l'Aménagement et des
Réseaux, UCBL — Université Claude Bernard Lyon 1.

Cité des Mobilités, 25 Avenue François Mitterrand, Case 24, 69675 BRON Cedex France